Helium-based cryogenic infrastructure and payload cooling concept for the Einstein Telescope

Zur Erlangung des akademischen Grades eines

DOKTORS DER INGENIEURWISSENSCHAFTEN

von der KIT-Fakultät für Chemieingenieurwesen und Verfahrenstechnik des
Karlsruher Instituts für Technologie (KIT)
genehmigte

DISSERTATION

von

Lennard Niclas Busch

aus Kiel

Tag der mündlichen Prüfung: 22.01.2026

Erstgutachter: Prof. Dr.-Ing. Steffen Grohmann

Zweitgutachter: Prof. dr. ir. Srinivas Vanapalli

Für meine Mutter Elisabeth.

"After all this time?"
"Always,"

Joanne Kathleen Rowling:
Harry Potter and the Deathly Hallows

Abstract

The Einstein Telescope (ET) is a proposed third-generation gravitational-wave detector (GWD) based on interferometers. It aims at significantly enhancing detection sensitivity compared to second-generation detectors, particularly in the low-frequency range below ca. 30 Hz. The sensitivity evolution requires cooling the suspended interferometer mirrors to between 10 K and 20 K to minimize thermally induced noise. This necessitates the development of an advanced technological approach to the cryogenic cooling system integration in the detector framework.

In fact, different technological approaches for implementing cryogenics into GWDs exist, each ultimately aimed at minimizing thermal noise without compromising detector sensitivity by introduction of other noise sources such as seismic noise. These approaches rely on the use of cryocoolers, sorption coolers, exclusive thermal radiation, or superfluid helium. The cooling system interface to the interferometric payload must be adapted for each of these strategies. Several R&D projects on cryogenic payload cooling have been initiated using cryocoolers, sorption coolers, or exclusively thermal radiation. Each of these concepts, none of which is yet mature enough to meet the ET cryogenic payload cooling requirements, is accounted for and outlined in this thesis. The focus, however, is specifically on the superfluid helium approach, thereby contributing to its application in cryogenic cooling for gravitational-wave detectors.

With helium-based cooling for ET as leitmotif, this work focuses on four pivotal aspects: heat extraction from the cryogenic payloads via an integrated interface design, a helium supply infrastructure for the payloads and all other consumers, an architecture for the innermost thermal shield around the cold payloads as well as configurations for low-noise heat extraction paths from both, the payloads and the corresponding thermal shields.

The first critical challenge addressed is the integration of the helium cooling system interface within the payload, while ensuring that the performance of the highly sensitive interferometer is not compromised. This work explores a double-walled tube as the suspension geometry for the cryogenic mirror marionette. The tube carries helium as coolant and represents the least-invasive cooling system interface geometry possible. Thermodynamic analyses show that suitable tube geometries enable steady-state operating temperatures of the mirrors down to ~17.5 K with marionettes kept at ~2 K superfluid helium temperature. Additionally, the suspension tube is shown to facilitate sufficiently fast mirror cooldowns in approximately two weeks. In detail, the analyses demonstrate an accelerated initial cooldown of silicon mirrors due to their higher emissivity compared to the steel- or aluminum-based marionette.

Following the examination of the cryogenic payloads as the critical consumers of cooling power in ET, this thesis elaborates on the design of a helium-based cryogenic infrastructure. This system ensures the provision of refrigeration capacity to all consumers within the ET installation, including thermal shields, cooled optical baffles, and cryopumps. The presented concept introduces a large-scale helium infrastructure based on a closed refrigeration loop, with coldboxes at central underground locations and surface compressor stations. This system ensures transport of helium at different temperature levels (5 K and 80 K). Based on the outlined system, the scale of required electrical input power to the complete ET cryogenic infrastructure is determined as 3×850 kW, considering the developed concept comprising three cryoplants, which is adapted to an existing triangular total detector layout plan.

Building upon both the helium infrastructure and the superfluid helium approach for payload cooling, an innermost thermal shield architecture is presented, which is designed to maintain the low temperatures required for the payload. The presented geometry enables rapid cooldowns in a few hours and minimizes thermal gradients across the structure during steady-state operation at ~2 K. The thermal shield's design further considers low mechanical vibration transfer, with structural resonant frequencies kept outside the relevant gravitational-wave detection band, ensuring that the shield's motion does not interfere with the sensitive measurement system. In the context of both, thermal shield- and payload cooling, particular attention is given to the investigation of He II phase front propagation speed from remote heat sinks to interfaces within the interferometer. In exemplary connection geometries for ET, conversion of He I to He II is calculated via a numerical model to be achievable within minutes.

Finally, potential arrangements for the connecting heat extraction geometries from both the payload and thermal shield are presented, seamlessly integrating the cooling interfaces into the comprehensive cryogenic infrastructure concept. This is envisioned to be realized by means of thin tubes measuring 10 m in length. Exemplary tube arrays identified to meet thermal and hydraulic requirements for payload cooling provision of 1 W at approximately 2 K consist of 10 to 40 tubes in total, with inner diameters decreasing from 5.0 mm to 2.5 mm as the tube count increases. The helium tube investigations conducted in this work include the consideration of various vibration attenuation strategies, such as the incorporation of designated heat link vibration isolation systems, small-scale bellows, and auxiliary super-attenuators. Each of these contributes to minimizing vibration transmission from the ambiance along the heat extraction path.

The results presented in this thesis demonstrate the feasibility of the developed helium cooling system aspects to meet the operational- and thermal requirements of ET and therefore set the stage for future engineering work, which will translate the extensively investigated concepts into a practical and operational system. Besides novel concept development and detailed modeling of pioneering tailor-made cooling system parts, this PhD project made major contributions to envisioning tangible future testing, laying the groundwork for an experimental proof-of-concept of the proposed superfluid helium cooling approach in interferometric gravitational-wave detectors.

German abstract — Zusammenfassung

Das Einstein-Teleskop (ET) ist ein in Planung befindlicher interferometerbasierter Gravitationswellendetektor der dritten Generation, dessen Ziel es ist, die Nachweisempfindlichkeit gegenüber der derzeitigen, zweiten Detektorgeneration signifikant zu erhöhen. Dies gilt insbesondere für den niederfrequenten Bereich unterhalb von etwa 30 Hz. Die vorgesehene Weiterentwicklung der Detektorempfindlichkeit erfordert die Absenkung der thermisch bedingten Beiträge zum Detektorrauschen durch Kühlung der an Pendelenden aufgehängten Interferometerspiegel auf Temperaturen zwischen 10 K und 20 K. Dies bedingt die Entwicklung eines technologisch anspruchsvollen Konzepts zur Integration eines kryogenen Kühlsystems innerhalb der komplexen Detektorarchitektur. Das Design dieser Architektur wird maßgeblich durch Anforderungen bestimmt, die sich aus der Notwendigkeit zur extremen Unterdrückung des Messrauschens in den hochsensiblen Interferometern ergeben.

Es existieren mehrere technologische Ansätze zur Integration kryogener Kühlung in Gravitationswellendetektoren (GWDs), deren Ziel jeweils darin besteht, thermisch bedingtes Rauschen zu minimieren, ohne durch andere Störquellen wie seismische Vibrationen die Gesamtleistung des Detektors zu beeinträchtigen. Die Strategien stützen sich auf den Einsatz von Kleinkühlern, Sorptionskühlern, reiner Strahlungskühlung oder suprafluidem Helium (He II). Die jeweilige Schnittstelle zwischen Kühlsystem und interferometrischem Nutzlastsystem ('Payload') im Herzen des Detektors muss hochpräzise an die spezifischen Anforderungen des gewählten Ansatzes angepasst werden. Mehrere Projekte zur Kühlung kryogener Nutzlasten, die Kleinkühler, Sorptionskühler oder ausschließlich Strahlungskühlung einsetzen, wurden in jüngster Vergangenheit in die Wege geleitet. Jedem dieser Ansätze, von denen keiner bislang ausreichend ausgereift ist, um die Anforderungen der kryogenen Nutzlastkühlung gänzlich zu erfüllen, wird in dieser Arbeit in einer bündigen Darstellung Rechnung getragen. Der Schwerpunkt dieser Dissertation liegt allerdings auf dem Einsatz von suprafluidem Helium und einer rein heliumbasierten kryogenen Infrastruktur für ET insgesamt. Dieser Ansatz erweist sich als äußerst vielversprechend hinsichtlich geringem Rauscheintrag, Kälteleistung und Betriebseffizienz im Vergleich zu anderen Methoden und wird hier detailliert auf seine Anwendbarkeit in interferometrischen Gravitationswellendetektoren untersucht.

Mit der heliumbasierten Kühlung für ET als Leitmotiv widmet sich das vorliegende Werk vier grundlegenden Aspekten einer entsprechenden Systemkonzeption. Zunächst wird die effektive Wärmeabfuhr von den kryogenen Nutzlasten mittels einer Schnittstellengestaltung betrachtet. Weiterhin wird die Auslegung einer Heliumversorgungsinfrastruktur für die Nutzlasten sowie andere relevante Kälteleistungsverbraucher untersucht. Ein zusätzlicher Schwerpunkt liegt auf dem Design eines innersten thermischen Schilds zur schützenden Einhausung der kalten Nutzlasten. Schließlich wird die Konzeption geeigneter Geometrien zur rauscharmen Wärmeabfuhr sowohl aus den Payloads als auch aus den zugehörigen thermischen Schilden behandelt.

Der zunächst thematisierte technische Aspekt ist die Integration der Schnittstelle zum heliumbasierten Kühlsystem in die Payloadstruktur unter der Randbedingung, dass die angestrebte Interferometersensitivität nicht beeinträchtigt wird. Hierfür wird eine doppelwandige Rohrstruktur als kombinierte Aufhängungs- und Wärmeableitungsgeometrie der sogenannten Interferometerspiegelmarionette vorgesehen. Das Rohr führt in seinem Inneren Helium als Kühlmittel und stellt gleichzeitig im Vergleich zu existierenden, bei Raumtemperatur betriebenen GWDs eine geringinvasive Lösung zur Implementierung einer Kühlsystemschnittstelle in Payloads dar. Thermodynamische Modellierungen und Simulationen belegen, dass durch geeignete Dimensionierung der Rohrgeometrie stationäre Betriebstemperaturen der Spiegel von bis zu $\sim$17.5 K erreichbar sind, während die Marionetten bei ca. 2 K in Kontakt mit suprafluidem Helium betrieben werden können. Darüber hinaus zeigen instationäre Analysen, dass mit dem gewählten Designansatz die Spiegel innerhalb von etwa zwei Wochen von Umgebungs- auf Betriebstemperatur abgekühlt werden können.

Im Anschluss ist, aufbauend auf der Betrachtung der Payloads als prominente Kälteleistungsverbraucher innerhalb des Detektorgesamtsystems, die Gestaltung einer umfassenden Heliuminfrastruktur beschrieben, die sämtliche Verbraucher innerhalb des ET-Systems versorgt. Hierzu zählen neben den Payloads auch thermische Schilde, bei kryogener Temperatur betriebene optische Blenden, sowie leistungsstarke Kryopumpen. Das vorgestellte Infrastrukturkonzept basiert auf einer geschlossenen Kältemittelkreislaufarchitektur mit zentral gelegenen unterirdischen Coldboxen und oberirdisch installierten Verdichterstationen. Innerhalb des Konzepts wird die Verteilung von Helium über Transferleitungen auf zwei wesentlichen Temperaturniveaus, 5 K und 80 K, ermöglicht. Basierend auf dieser Systemarchitektur ergibt sich ein elektrischer Eingangsleistungsbedarf der gesamten kryogenen Infrastruktur im stationären Betrieb von 3×850 kW. Dieser Wert basiert auf der Auslegung mit drei Kühlanlagen, angepasst an ein existierendes dreieckiges Detektorlayout des ET.

Weiterhin wird unter Nutzung der Erkenntnisse aus den Untersuchungen zur kryogenen Infrastruktur und zur Payloadkühlung ein Konzept für die Gestaltung des innersten thermischen Schilds vorgestellt. Dieses gewährleistet eine homogene, konstante Umgebungstemperatur von $\sim$2 K für die Payloads und minimiert somit die Wärmelast auf die letzteren. Die vorgesehene Schildgeometrie ermöglicht ein vollständiges Kaltfahren desselben in wenigen Stunden und sorgt für geringe thermische Gradienten während des stationären Betriebs. Gezielte strukturelle Maßnahmen stellen sicher, dass die Eigenfrequenzen des Schilds außerhalb des relevanten Frequenzspektrums für die Gravitationswellendetektion liegen, wodurch stochastische Bewegungen die Messgenauigkeit des Interferometers nicht beeinträchtigen. Im Zusammenhang mit der Kühlung sowohl der thermischen Schilde, als auch der Payloads wird die Ausbreitungsgeschwindigkeit von He II-Phasengrenzen in exemplarischen Geometrien für ET analysiert. Ein entwickeltes numerisches Modell zeigt, dass die Umwandlung von He I zu He II innerhalb von Minuten erfolgen kann, selbst bei Entfernungen $\geq$10 m der externen Wärmesenke zur Schnittstelle im Payload.

Abschließend werden verschiedene Konfigurationen zur Anbindung der Subsysteme zur Wärmeableitung aus Payload und innerstem thermischem Schild erörtert. Diese fügen sich nahtlos in das übergeordnete Heliuminfrastrukturkonzept ein. Die konkrete Umsetzung kann durch dünnwandige Rohre mit einer exemplarischen Länge von 10 m realisiert werden. Beispielhafte Rohrkonfigurationen, die den thermischen und hydraulischen Anforderungen zur Kühlung eines Payloads mit 1 W bei ca. 2 K entsprechen, bestehen aus insgesamt 10 bis 40 Rohren. Innerhalb dieses Intervalls nimmt der Innendurchmesser mit steigender Rohranzahl von 5.0 mm auf 2.5 mm ab. Weiterhin beinhalten die Untersuchungen Maßnahmen zur Verringerung der mechanischen Kopplung zwischen Payloads bzw. Schilden und deren Umgebung über die Rohrbündel. Hierzu zählen mehrstufige Entkopplungseinheiten, kleinskalige Metallbälge, sowie ergänzend implementaierte pendelbasierte Dämpfungen.

Die in dieser Arbeit präsentierten Ergebnisse belegen die prinzipielle Umsetzbarkeit der entwickelten, heliumbasierten kryogenen Infrastruktur. Ebenso wird die Realisierbarkeit des darin eingebetteten Konzepts zur Kühlung der Payloads und innersten thermischen Schilde zur Erfüllung der betrieblichen Anforderungen im Einstein-Teleskop nachgewiesen. Damit wird die Grundlage für spezifische Entwicklungsarbeiten zur Überführung der umfassend untersuchten Konzepte in ein physisch realisierbares und betriebssicheres System gelegt. Neben der Konzeption und detaillierten Modellierung neuartiger Bauteile eines maßgeschneiderten Kühlsystems leistet die Arbeit einen wesentlichen Beitrag zur Vorbereitung zukünftiger zielgerichteter Testkampagnen. Auf diese Weise werden die Voraussetzungen für die Durchführung experimenteller Machbarkeitsnachweise des suprafluiden Heliumkühlkonzepts in interferometrischen Gravitationswellendetektoren geschaffen.

Contents

Notation and acronyms

Latin symbols

Symbol	Description	Unit
A	area	m^2
C	constant	m
c	specific heat capacity	$\mathrm{J\,kg^{-1}\,K^{-1}}$
COP	coefficient of performance	–
D	dilution factor	–
d	diameter	m
E	Young's modulus	$\mathrm{N\,m^{-2}}$
F	force	N
f	frequency	$\mathrm{s^{-1}}$
g_{peak}	empirical function [1]	$\mathrm{W^{3.4}\,m^{5.8}\,K^{-1}}$
H	height	m
H	enthalpy	J
h	specific enthalpy	$\mathrm{J\,kg^{-1}}$
h	empirical function [1]	–
h_{s}	dissipation depth	m
I	area moment of inertia	m^4
i	indexed variable	–
j	indexed variable	–
k	spring constant	$\mathrm{N\,m^{-1}}$
k_{e}	elastic fiber wave number	$\mathrm{m^{-1}}$
k_{s}	flexural stiffness wave number	$\mathrm{m^{-1}}$
L	length	m
l	specific energy demand of a thermodynamic process	$\mathrm{J\,kg^{-1}}$
M	mass	kg

Symbol	Description	Unit
m	Gorter-Mellink exponent	–
$\dot{M}$	mass flow rate	$\mathrm{kg\,s^{-1}}$
$\dot{m}$	mass flux	$\mathrm{kg\,s^{-1}\,m^{-2}}$
N	number of discretization elements	–
n	number	–
P	power	W
p	pressure	$\mathrm{N\,m^{-2}}$
$\dot{Q}$	heat flow rate	W
$\dot{q}$	heat flux	$\mathrm{W\,m^{-2}}$
$\dot{Q}_\mathrm{c}$	cooling power	W
Q_m	mechanical quality factor	–
R	thermal contact resistance	$\mathrm{K\,m^2\,W^{-1}}$
s	specific entropy	$\mathrm{J\,kg^{-1}\,K^{-1}}$
s	wall thickness	m
S_xx	displacement spectral density	$\mathrm{m^2\,Hz^{-1}}$
T	temperature	K
t	time	s
$\overline{T}$	average temperature	K
V	volume	$\mathrm{m^3}$
v	velocity	$\mathrm{m\,s^{-1}}$
$\dot{V}$	volume flow rate	$\mathrm{m\,s^{-3}}$
w	flow velocity	$\mathrm{m\,s^{-1}}$
X	displacement in the frequency domain	m
x	displacement in the time domain	m
x	longitudinal coordinate	m
Y	mechanical admittance	$\mathrm{m\,N^{-1}\,s^{-1}}$
y	vapor quality	–
Z	mechanical impedance	$\mathrm{N\,m^{-1}\,s}$
z	longitudinal coordinate	m
z	redshift	–

Greek symbols

Symbol	Description	Unit
α_{HT}	heat transfer coefficient	$\mathrm{W\,m^{-2}\,K^{-1}}$
α_{surf}	surface loss parameter	m
α_{TE}	linear thermal expansion coefficient	$\mathrm{K^{-1}}$
β	thermal elastic coefficient	$\mathrm{K^{-1}}$
γ	bulk fluid expansivity	$\mathrm{K^{-1}}$
Δ	difference	–
ϵ	effective emissivity	–
η	efficiency	–
η	dynamic viscosity	Pa s
θ_{s}	scattering angle	°
θ_{vh}	vertical-to-horizontal coupling factor	–
λ	thermal conductivity	$\mathrm{W\,m^{-1}\,K^{-1}}$
λ_{bp}	bending point position	m
μ_{JT}	Joule-Thomson coefficient	$\mathrm{K\,Pa^{-1}}$
μ	geometry factor	–
ξ	friction coefficient	–
ρ	volumetric mass density	$\mathrm{kg\,m^{-3}}$
σ_{m}	tension	N
$\sigma_{\mathrm{m,max}}$	ultimate tensile strength	$\mathrm{N\,m^{-2}}$
σ_{y}	yield strength	$\mathrm{N\,m^{-2}}$
τ	thermal diffusion time	s
ϕ	loss angle	–
φ	view factor	–
χ	relative spatial distortion	–
ψ	isothermal bulk compressibility	$\mathrm{Pa^{-1}}$
ω	angular frequency	$\mathrm{s^{-1}}$
ω_0	angular frequency at resonance	$\mathrm{s^{-1}}$

Dimensionless numbers

Number	Name
Nu	Nusselt number
Pr	Prandtl number
Re	Reynolds number

Subscripts

Subscript	Description
$\odot$	solar
00	lowest-order mode
λ	He I–He II transition
amb	ambient conditions ($T = 293.15\,\mathrm{K}$, $p = 1.013\,\mathrm{bar(a)}$)
arm	ET interferometer arm
bulk	bulk material property
C	Carnot
c	cooling
crit	critical
cross	cross-sectional
CTL	cryogenic transfer line
cx	complex
eff	effective
el	elastic
eq	equivalent
fr	frame
g	gravitational
h	hydraulic
horz	horizontal
HT	heat transfer
i	inner
in	inlet
join	jointing
liq	liquefaction

Subscript	**Description**
MA	marionette
ma	marionette suspension
min	minimum
nc	normalfluid component
o	outer
out	outlet
p	isobaric
pend	pendulum
r	reservoir
rad	radiative
refr	refrigeration
Sa	Sapphire
sat	saturation
sc	superfluid component
sh	thermal shield
Si	Silicon
ST	suspension tube
sup	supply
surf	surface
susp	suspension
therm	thermoelastic
TL	thermal link
TM	test mass
tm	test mass suspension
vap	evaporation
vert	vertical

Physical constants

Symbol	Description	Value	Unit
σ	Stefan-Boltzmann constant	$5.6704 \cdot 10^{-8}$	$\mathrm{W\,m^{-2}\,K^{-4}}$
g_0	standard acceleration of gravity	9.8067	$\mathrm{m\,s^{-2}}$
k_B	Boltzmann constant	$1.3806 \cdot 10^{-23}$	$\mathrm{m^2\,kg\,s^{-2}\,K^{-1}}$

Acronyms

Abbreviation	Description
1D	one-dimensional
2D	two-dimensional
2G	second-generation
3D	three-dimensional
3G	third-generation
5N	five-nines (refers to $\geq 99.999\,\%$ purity)
6N	six-nines (refers to $\geq 99.9999\,\%$ purity)
7N	seven-nines (refers to $\geq 99.99999\,\%$ purity)
AdVirgo	Advanced Virgo
aLIGO	Advanced LIGO
ARC	Amaldi Research Center
BBH	binary black hole
BNS	binary neutron star
BS	beam splitter
CA	actuation cage
CAD	computer aided design
CE	Cosmic Explorer
CERN	European Organization for Nuclear Research
CFD	computational fluid dynamics
CFHX	counterflow heat exchanger
CLIO	Cryogenic Laser Interferometer Observatory
CP	cryopump/cryotrap
CSU	cryogenic supply unit
CTL	cryogenic transfer line
DoF	degree of freedom
E-TEST	Einstein Telescope Euregio Meuse-Rhine Site and Technology
EH	electric heater

Abbreviation	Description
ET	Einstein Telescope
ET-D	Einstein Telescope design sensitivity curve option [2]
ET-HF	the high-frequency interferometer array in ET
ET-LF	the low-frequency interferometer array in ET
ETM	end test mass
FDT	fluctuation-dissipation theorem
FEA	finite element analysis
FEM	finite element method
FVM	finite volume method
GAS	geometric anti-spring
GFRP	glass-fiber reinforced plastic
GRB	gamma-ray burst
GW	gravitational wave
GWD	gravitational-wave detector
GWOSC	Gravitational Wave Open Science Center
HCB	hydroxide catalysis bonding
HF	high-frequency
HLVIS	heat link vibration isolation system
HX	heat exchanger
HXCT	cryotrap heat exchanger
HXIS	inner thermal shield heat exchanger
HXOS	outer thermal shield heat exchanger
HXPL	payload heat exchanger
ICB	interconnection box
IM	intermediate mass
IMBH	intermediate massive back hole
INFN	Istituto Nazionale di Fisica Nucleare (Italian: ‘National Institute for Nuclear Physics’)
IOP	Institute of Physics
ITM	input test mass
JT	Joule-Thomson
KAGRA	Kamioka gravitational-wave detector
KIT	Karlsruhe Institute of Technology
KSETA	Karlsruhe School of Elementary Particle and Astroparticle Physics: Science and Technology
LF	low-frequency
LHC	Large Hadron Collider
LIGO	Laser Interferometer Gravitational-Wave Observatory
LN_2	liquid nitrogen

Abbreviation	**Description**
MA	marionette
ma	marionette suspension
MLI	multilayer insulation
MUMPS	multifrontal massively parallel sparse direct solver
NIST	National Institute of Standards and Technology
NN	Newtonian noise
P	vacuum pump
PBH	primordial black hole
PF	platform/steering filter
PFD	process flow diagram
PRD	pressure relief device
PRM	power recycling mirror
PTC	pulse tube cryocooler
QRPN	quantum radiation pressure noise
R&D	research and development
REFPROP	reference fluid thermodynamic and transport properties [3]
RNG	renormalization group
RRR	residual resistivity ratio
SA	super-attenuator
Sa	sapphire
SF	safety factor
SNR	signal-to-noise ratio
SRM	signal recycling mirror
ST	suspension tube
STN	suspension thermal noise
TL	thermal-/heat link
TM	test mass
tm	test mass suspension
TMS	transmission monitor system
UHV	ultra-high vacuum
V	valve
VRS	vibration reduction stage
XHV	extreme high vacuum ($p < 10^{-12}$ mbar)

List of figures

List of tables

1 Introduction

In June 1916, Albert Einstein published an article titled “Approximate integration of the field equations of gravitation” [4]. In this work, he developed the weak-field linearized theory of general relativity determining the appropriate coordinate condition, and, consequently, predicted the existence of gravitational waves.

Gravitational waves

Gravitational waves (GWs) physically manifest themselves as time-dependent distortions $\chi = {}^{\partial L}/_{L}$ in spacetime, where L denotes the distance between two reference points in space and ∂L the induced displacement along this baseline L. These distortions travel through the universe at the speed of light.

Einstein’s general relativity predicts that the induced χ is perpendicular to the GW propagation axis and is quadrupolar. Specifically, for a wave traveling along the z-axis, one polarization stretches and then compresses the path along the x-axis, while simultaneously shrinking and then stretching the path along the y-axis. For the orthogonal polarization, this elongation and compression occurs along axes rotated 45° relative to the x- and y-axes.

Every accelerating physical object with a changing quadrupole moment generates GWs. However, the masses and accelerations of objects found on Earth are insufficient by far to produce GWs strong enough to be detected by existing instruments, due to the vanishing magnitudes of χ. To identify sources capable of generating GWs with sufficiently large χ, the observational horizon must be extended well beyond the boundaries of our solar system.

Generally, GW signals are anticipated to occur across a broad frequency range, approximately $f \approx 10^{-17}...10^{4}$ Hz. Figure 1.1 presents the complete gravitational-wave spectrum and displays the corresponding source spectra. Gravitational waves are assigned to three main categories, which are briefly described in the following [9–11].

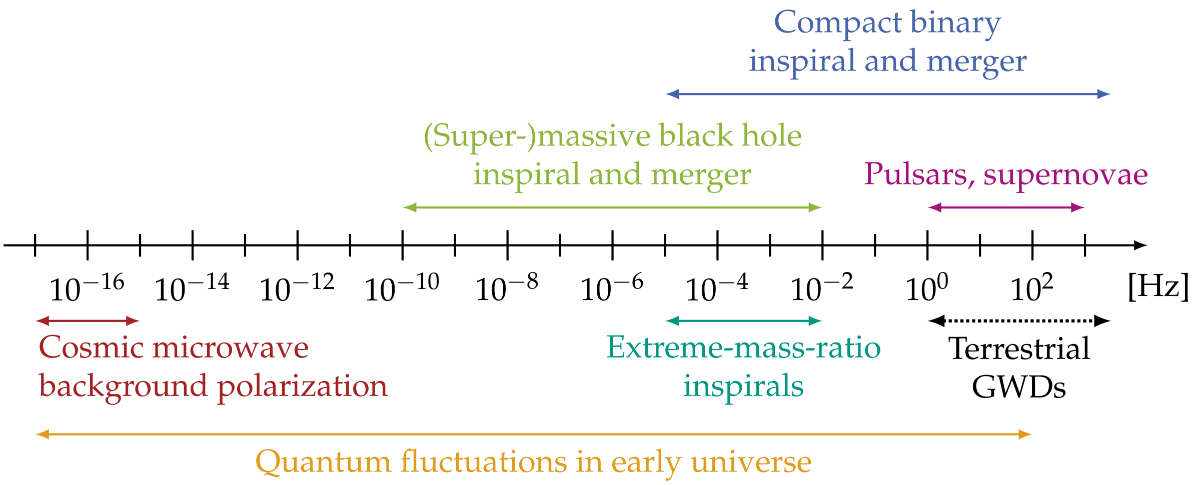

Figure 1.1: Gravitational-wave spectrum with potential sources and detection band of terrestrial gravitational-wave detectors (GWDs). Range data composed from [5–8].

Continuous gravitational waves are perpetually emitted by a source over a period significantly longer than the observation time, maintaining a nearly constant frequency or set of frequencies. Such sources are rotating systems where the rotational motion occurs at a specific, steady frequency. In the low-frequency (LF)-GW bands, continuous GWs are generated by orbiting white dwarf binary systems and supermassive black hole binaries, while in the high-frequency (HF) band, principal sources of continuous GW signals are non-axisymmetric pulsars.

Gravitational-wave bursts are episodes of gravitational radiation that are relatively brief compared to the observation time. Burst radiation is typically produced in violent astronomical events such as supernovae or binary coalescences, specifically the orbital decays and collisions of compact binary systems. These comprise binary black holes (BBHs), binary neutron stars (BNSs) and neutron star-black hole binaries. A result of these events is the emission of GWs across various frequency bands.

The *stochastic gravitational-wave background* is characterized by the aggregate of numerous gravitational waves, forming a stochastic signal. GWs from a large variety of sources overlap in both time and frequency, rendering it virtually impossible to attribute waves to their specific origin. Allen [12] and Maggiore [13] present commendable reviews of the gravitational-wave background.

Although Einstein himself predicted their existence, he was convinced it would never be possible to measure gravitational waves. Nevertheless, since his famous theoretical work over a century ago, there have been numerous attempts of physicists all over the world to do so. Recently, these decades-long efforts have led to considerable success, opening up an era of unprecedented GW astronomy.

1.1 Motivation and history of gravitational-wave detection

Before the advent of gravitational-wave detection, scientists had predominantly depended on electromagnetic radiation and neutrinos to study the universe. Each of these information 'messengers' provides scientists with a distinct yet complementary perspective on the universe. Gravitational waves, in contrast, are fundamentally unrelated to electromagnetic radiation. They interact extremely weakly with matter, traveling through the universe with minimal obstruction, and convey information about their origins without distortion. Hence, GWs serve as invaluable instruments for comprehending the behavior of matter and geometry under extreme conditions of density, temperature, magnetic fields, and relativistic motion. In particular, gravitational-wave observation will help explore a variety of invaluable and fundamental questions in astrophysics and cosmology [14]:

- ☐ What is the physics of stellar core collapse? How frequently do core-collapse supernovae occur [15, 16]?
- ☐ What is the equation of state, and what are the radii, of neutron stars [17, 18]?
- ☐ What are the multi-messenger emission mechanisms of high-energy transients (gamma-ray bursts and kilonovae) [19]?
- ☐ How do BBHs of tens of solar masses form and evolve [20, 21]?
- ☐ How did super-massive black holes at the cores of galactic nuclei form and evolve, and what were their seeds and demographics [22]?
- ☐ Are black hole spacetimes as predicted by general relativity [23]?
- ☐ Are there any signatures of horizon structure or other manifestations of quantum gravity accessible to gravitational-wave observations [24]?
- ☐ Is dark matter composed, in part, of primordial black holes (PBHs), or must it be composed solely from exotic matter such as axions or dark fermions [24]?
- ☐ What is the expansion rate of the universe [11]?
- ☐ What is the nature of dark energy and dark matter [11, 25]?
- ☐ Is there a measurable gravitational-wave stochastic background due to phase transitions in the early universe? If so, what were its properties [13, 26, 27]?
- ☐ How does gravity behave in the strong/highly dynamical regime [28–31]?
- ☐ Do we live in a universe with large extra dimensions [32]?
- ☐ Are black holes, neutron stars and white dwarfs the only compact objects in our universe, or are there even more exotic objects [33]?

Consequently, the scientific imperative for the development and operation of GWDs is profound. Among the different types of GWDs constructed, the initial ones were cylindrical resonant mass detectors, often referred to as 'bar' detectors, in the 1980s and 1990s. They are set into oscillation by GWs that are near the natural frequency of a large metal bar, and it is these oscillations that are measured. Bar detectors are responsive to GWs with relatively high frequencies $f = 0.1...1\,\text{kHz}$, thus, their sensitivity is rather narrow-band [34–36].

While some bar detectors are still operational, emphasis nowadays is primarily on GWDs utilizing laser interferometry (cf. Section 1.2). The first generation of these interferometric detectors ('GEO600' [37], 'LIGO' [38], 'Virgo' [39] and 'TAMA' [40]) effectively showcased the proof-of-principle and allowed inference of constraints on the anticipated gravitational-wave emissions from multiple sources. The detector output includes many noise events and non-stationarities alongside the fundamental Gaussian component. Hence, detecting gravitational wave events requires observing signals in multiple detectors to minimize the considerable number of false alarms caused by instrumental or environmental disturbances.

The subsequent generation of interferometric detectors ('aLIGO' and 'AdVirgo') were constructed until 2015. The enhancement in sensitivity achieved through the upgrade of GWDs from their first to the second generation finally enabled the first ever direct detection of gravitational waves on September 14, 2015 [41]. In recognition of this landmark achievement, the Nobel Prize in Physics 2017 was awarded to key members of the LIGO/Virgo collaboration "for decisive contributions to the LIGO detector and the observation of gravitational waves" [42].

1.2 Present gravitational-wave detectors

The sensitivity increase that resulted from the upgrade of the GWDs LIGO and Virgo from their first to the second (advanced) generation (2G) [43, 44] not only led to the first ever direct detection of gravitational waves, but allowed further detections of a large number of coalescing binaries in the subsequent observation runs. These brought groundbreaking scientific results and new insights into astrophysical processes. The latest (2G) gravitational-wave detectors are terrestrial observatories that explore the HF portion of the gravitational-wave spectrum from $\sim$10 Hz to $\sim$10 kHz. This segment of the GW spectrum is dominated by stellar-mass compact sources, such as coalescing BBHs and neutron star systems, as well as supernovae and isolated neutron stars, which have yet to be observed.

All 2G detectors rely on enhanced Michelson interferometry with suspended mirrors to directly measure a GW's phase and amplitude. Figure 1.2 schematically shows such a laser interferometer gravitational-wave detector. Michelson interferometers are ideally suited for measuring the effect of distortions χ in spacetime caused by GWs. A laser beam is divided into two partial beams, directed along the so-called interferometer arms, where it undergoes a phase shift due to the gravitational wave's effect on the metric. These beams are then reflected at the end test masses (ETMs) and directed back to the beam splitter, where they are recombined. The interference condition at the beam splitter, specifically the phase relationship between the two returning beams, dictates the intensity detected by the output photodiode. Therefore, the relative length change of the interferometer arms can be tracked by measurements of the output power. Together with the ETMs, the input test masses (ITMs) positioned near

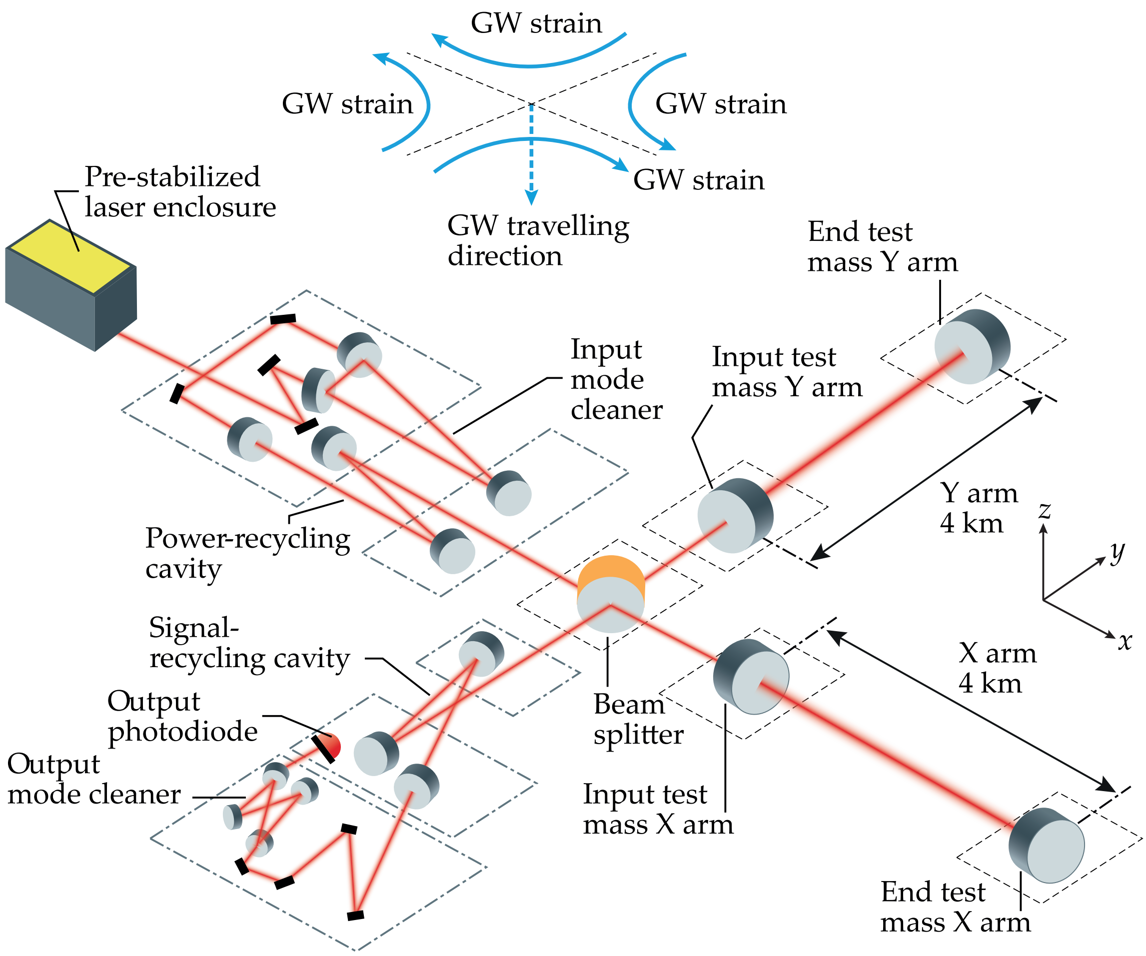

Figure 1.2: A simplified representation of the 2G aLIGO interferometer (adapted from [14] with permission of Springer Nature), illustrating the optical setup including the laser, input mode cleaner, power-recycling and signal-recycling cavities, the 4-kilometer-long arm cavities and the output mode cleaner. The gravitational-wave signal is captured by the output photodiode following the corresponding mode cleaner.

the beam splitter create optical resonators, i.e. *Fabry-Pérot cavities*. Optical resonance is a result of the light undergoing multiple round trips between an ITM and ETM, progressively amplifying the gravitational-wave signal with each pass. In this manner, the European-based Advanced Virgo (AdVirgo) detector amplifies a gravitational-wave signal by a factor of around 290 [45].

Among current-generation detectors, the two aLIGO detectors in the USA [44] exhibit arm lengths of $L = 4\,\text{km}$, while AdVirgo [43] and the Japan-based KAGRA [46, 47] feature $L = 3\,\text{km}$ arms. Typical values of χ from astrophysical sources are on the order of 10^{-21} or less. Consequently, test mass (TM) displacement sensitivities ∂L of less than $\sim 10^{-18}\,\text{m}$ are required to detect gravitational waves with sufficient signal-to-noise ratio (SNR) [14]. To put this miniscule displacement magnitude in perspective, consider for example that the radius of a proton is $\sim 10^{-15}\,\text{m}$. Hence, while the underlying measurement principle may be straightforward, achieving the best possible GW observation sensitivity requires minimizing detector noise by drastic limitation of all influences that alter the geometrical or optical interferometer arm length or induce signals in the detected photo-current resembling a gravitational wave. This necessity is the core driver of the development of highly sophisticated and complex instruments.

The TMs are suspended from multi-stage pendulum systems such that above the resonant frequencies of the suspension system (typically around 1 Hz), they can be effectively treated as in free fall (i.e. in a local inertial frame) in the direction of light propagation. These suspensions and accompanying seismic isolation systems reduce the undesired test-mass movement induced by ambient ground motion by about a factor of 10^{12} in the frequency range from 1 Hz to 10 Hz [43, 48]. Figure 1.3 schematically shows the respective, existing TM suspension apparatus in Virgo, a so-called 'super-attenuator' (SA), which combines an inverted pendulum with a multi-stage vertical vibration filter chain. The 'payload', which is the last stage of the suspension, is hung from the lowest filter of the chain ('platform'). The payload is designed as a double pendulum, in which the TM is suspended from a penultimate body referred to as 'marionette'. In AdVirgo, the double pendulum is surrounded by a cage (suspended to the platform), which acts as a reference mass [49]. Among other vital parts, the cage is equipped with sensors and actuators for TM positioning control.

Besides *seismic noise* (I), three less intuitive primary noise sources currently limit interferometer sensitivity [14]:

(II) *Thermal noise* inducing random displacements of the mirror surfaces caused by thermally fluctuating stresses in the interferometer mirror coatings, substrates and suspensions [51],

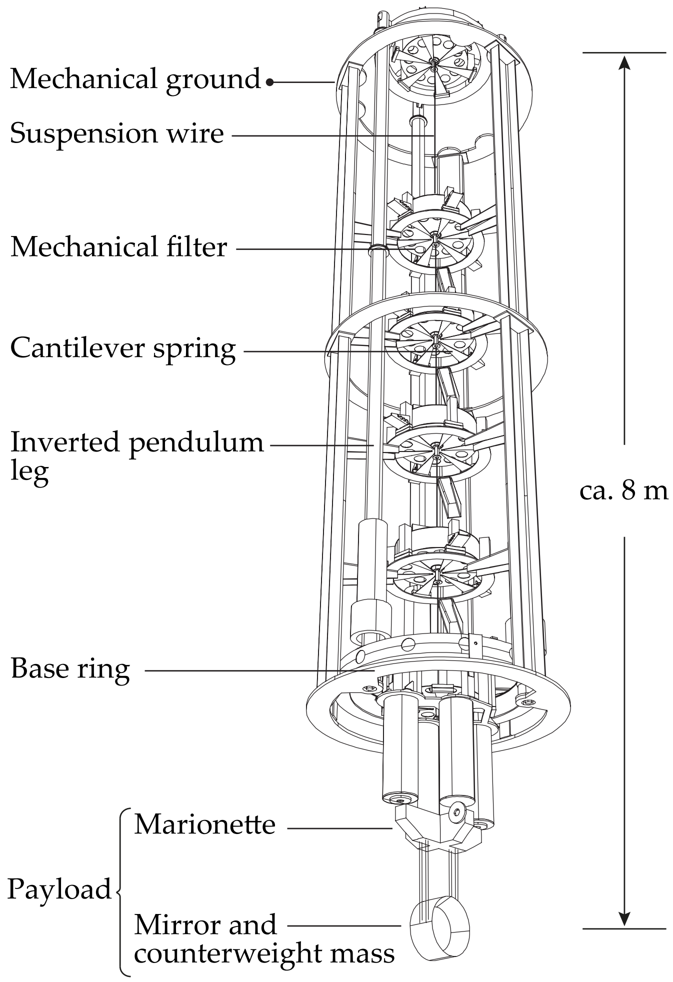

Figure 1.3: Illustration of a Virgo superattenuator (adapted from [50] with permission of Elsevier).

(III) *Newtonian (or dynamic gravity gradient) noise* induced by perturbations in the Earth's ground and atmospheric density, directly exerting dynamic forces on the mirrors via gravitational coupling [52] and

(IV) *Quantum noise* resulting from both vacuum fluctuations of the electromagnetic field limiting phase resolution in the readout photodetector (known as 'shot noise') and displacements of the mirrors caused by 'quantum radiation pressure noise' (QRPN), which induces stochastic impulses on the optics due to the random arrival time of momentum-carrying photons [53].

The effect of QRPN diminishes as the mirror mass increases, and both QRPN and shot noise can be reduced by injecting quantum-engineered squeezed vacuum states of light into the interferometer [54]. In turn, thermal noise manifests itself in a variety of ways [55]. It can be understood from a statistical mechanics perspective as infinitesimal internal motions of macroscopic objects at non-zero temperatures causing intrinsic dissipation, i.e. 'mechanical loss' in the system.

In addition to these fundamental noise sources, a large number of technical noises must be identified and overcome, which broadly group into laser frequency and intensity noises, acoustically and seismically driven scattered light noises, sensor and actuator noises, stochastic forces from electrical and magnetic fields, and, potentially, energy deposited by energetic particles [56, 57].

In order to deliver a maximum of scientific output, a network of interferometers distributed worldwide, acting as a unified detector, plays a key role. The aLIGO and AdVirgo detectors have collectively scanned the gravitational-wave sky through a meticulously coordinated effort during a sequence of observing runs conducted between 2015 and 2020. Figure 1.4 illustrates the total cumulative count of detected events by the two GWDs. During the 'O3' run, the detectors reached sufficient sensitivities to detect BBH mergers on a weekly basis [59]. Further, the plot clearly indicates how upgrades to aLIGO and AdVirgo between O2 and O3, including increased laser power, squeezed light injection, improved vibration isolation, and enhancements in optics and control systems, significantly improved detector sensitivity and led to a substantial increase in the GW detection rate [60, 61].

In turn, Figure 1.5 shows the interferometer sensitivity of AdVirgo in the O3 run. The displayed sensitivity is characterized by the amplitude spectral density of the calibrated output of χ, i.e. the strain per unit square root of frequency (derivation: e.g. in [63]). The stable, narrow spectral features arise from mechanical resonances and electrical coupling which are well distinguishable at 50 Hz and 60 Hz. Towards lower frequencies, noise is primarily caused by scattered laser light, seismic activities and interferometer controls. In the mid-band, the dominant source of noise is the thermal noise in the mirrors' dielectric coatings. At high frequencies, quantum noise limits sensitivity [64].

KAGRA recently joined LIGO and Virgo, forming the LIGO-Virgo-KAGRA network [65]. The LIGO-India [66] interferometer will join the network later in this decade, significantly enhancing the GWD-network's capability to confidently detect and locate GW events [67]. Further, this addition will offer new methods to test alternative theories of gravity by improving the resolution of GW polarizations [68].

Compared to other existing laser interferometers, KAGRA is technologically unique in two key features. First, it is located in an underground site at depths $\geq$ 200 m to minimize seismic noise. Second, KAGRA's test masses are sapphire mirrors which are designed to be operated at cryogenic temperatures ($\sim$20 K) in order to reduce thermal noise [47]. The future European gravitational-wave detector, the *Einstein Telescope*, will further reduce fundamental noises by advancing both of these approaches [69].

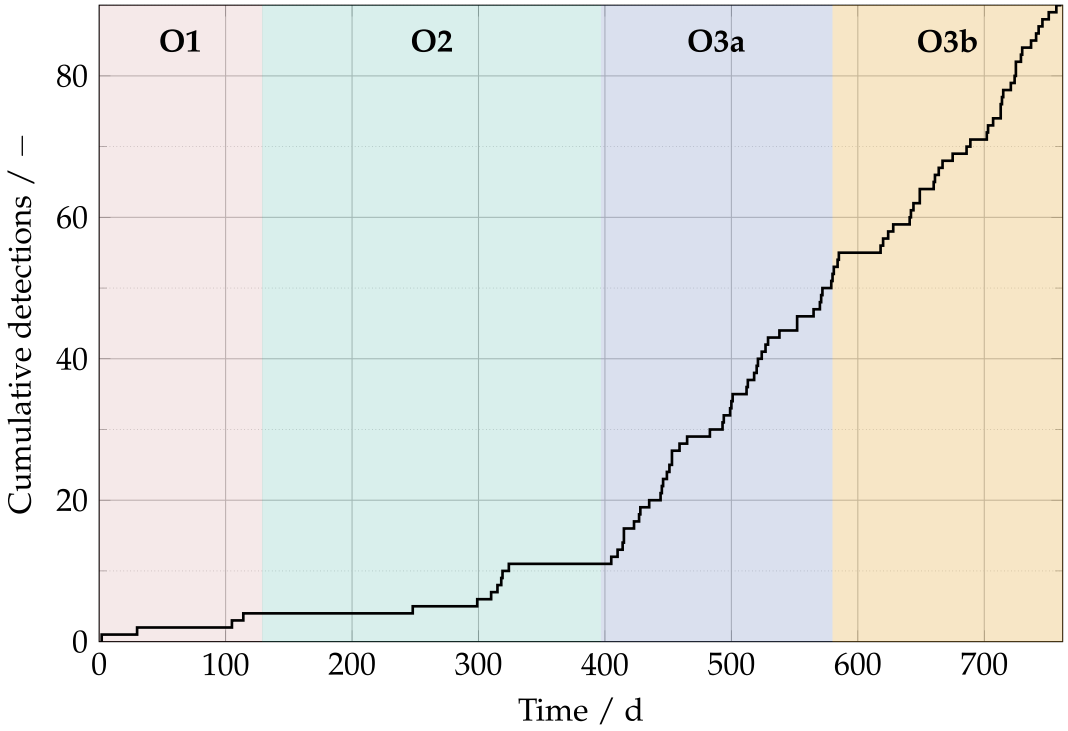

Figure 1.4: Cumulative number of GW detections during observing runs by aLIGO (O1–O3b) and AdVirgo (O2–O3b). Data accessible via the public LIGO document control center (DCC) [58].

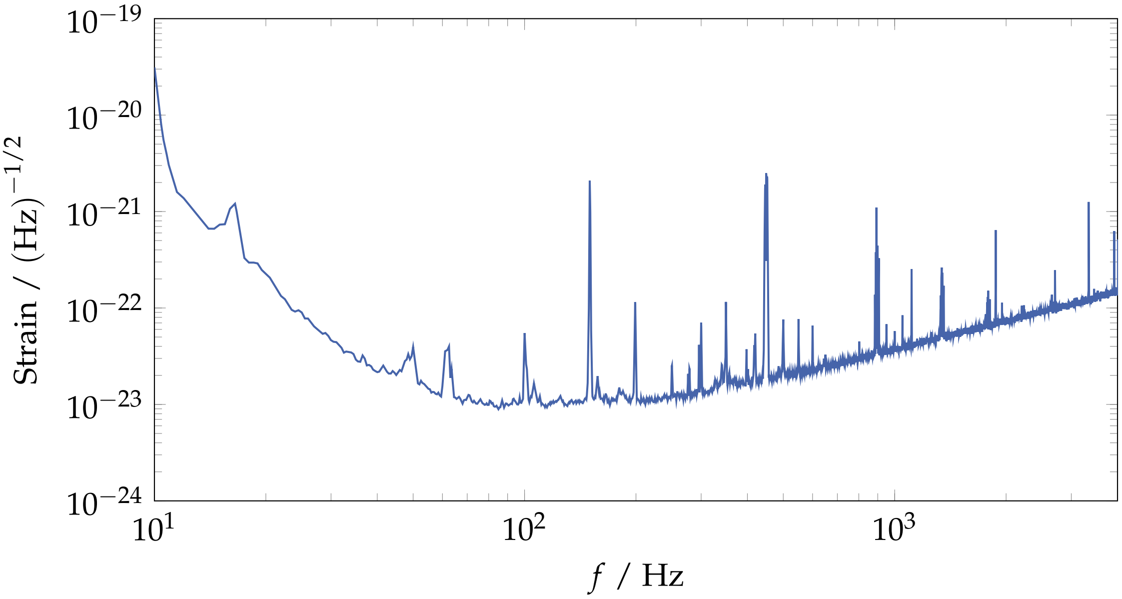

Figure 1.5: Representative amplitude spectral density of the AdVirgo strain sensitivity during the O3b run on 9 February 2020 at 01:16:00 UTC. Data accessible via the Gravitational Wave Open Science Center (GWOSC) [62].

1.3 Design parameters of the Einstein Telescope

Well before the first gravitational-wave detection in 2015, the GW-community started investigating a new (third) generation (3G) of detectors. Notably, the European Commission supported the European GW community in conducting a conceptual design study from 2008 to 2011, under the Seventh Framework Programme (FP7-Capacities) [70]. The primary objective of the 2G-detectors had been the detection of gravitational waves. Recently, there has been a shift in focus of the scientific community towards astrophysical *observations*. In this context, with significantly enhanced sensitivity, third-generation (3G) detectors will usher in the era of precision gravitational-wave astronomy [2].

Constructing a 3G gravitational-wave observatory with substantially enhanced sensitivity requires overcoming the technological limitations present in current interferometers. In fact, to achieve the scientific goals of the Einstein-Telescope (ET) as stated in [71], the sensitivity in comparison to the second generation of GWDs must be improved by about an order of magnitude over the entire detection frequency band accessible to ground-based detectors (cf. Figures 1.1 and 1.5). Frequent and precise observation of low-frequency sources such as intermediate massive back holes (IMBHs) additionally requires an extension of the detection range towards lower frequencies [72].

Figure 1.6 shows the target detector sensitivity curve of ET (cf. [2, 71]) including limiting primary noise sources as presented in Section 1.2. Generally, the ambitious sensitivity objective for ET is motivated by the necessity to achieve frequent, high-SNR events for regular precision gravitational-wave astronomy. High-frequency sensitivity is determined by the maximum feasible laser power in the interferometer arms, while the mid-frequency range is influenced mainly by Newtonian- and thermal noises. Approaching the lower-frequency limit of the detection band, the dominating noise source is seismic noise [2]. Therefore, the limiting noise sources targeted in the development of ET are expected to be comparable to those encountered in 2G detectors.

As Figure 1.6 further reveals, one of the major advancements of ET with respect to 2G-GWDs is its composition of two individual detectors, a low-frequency detector (ET-LF) and a high-frequency detector (ET-HF). This allows to pursue different strategies in optimizing the noise for each frequency range, resulting in an improved sensitivity across a wide detection band with ET-LF and ET-HF covering the intervals $f \approx 3...30\,\text{Hz}$ and $f \approx 30...10^4\,\text{Hz}$, respectively [73].

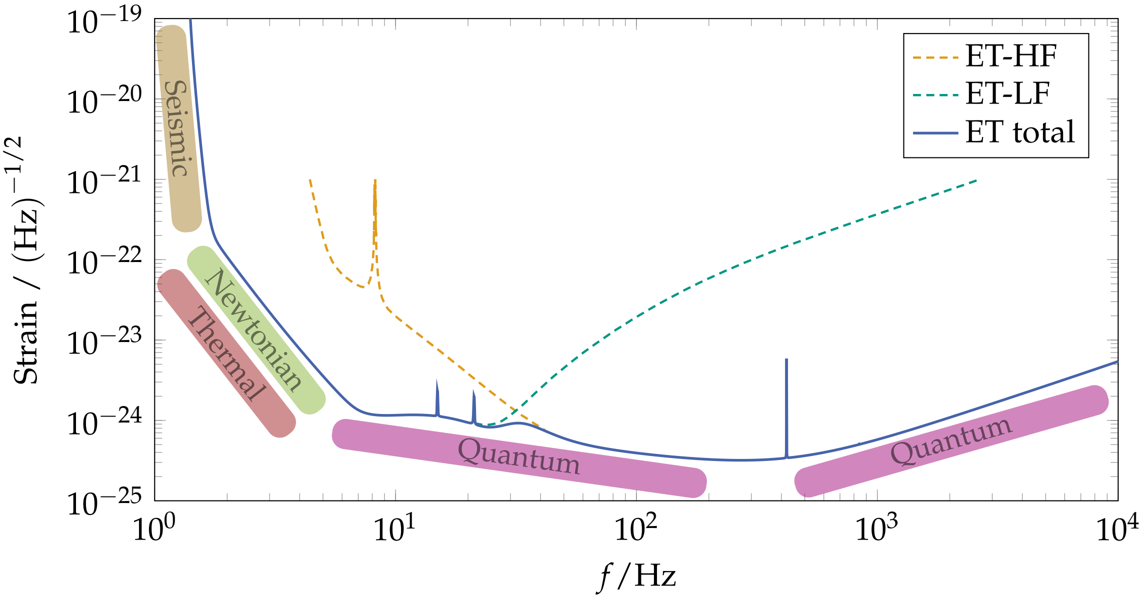

Figure 1.6: Sensitivity of the Einstein Telescope in the ‘xylophone’-configuration including limiting noise sources and distinction between ET-LF and ET-HF. Data source: [2, 71].

ET-LF and ET-HF are considered to be arranged in a so-called ‘xylophone’ configuration [73]. Specifically, extensive ET reports envisage a nested observatory comprised of three LF and three HF interferometers with a 60° opening angle, arranged in the shape of a triangle [2, 71]. Figure 1.7 presents the scheme of such a triangular detector configuration. Compared to any of the 2G GWDs, the interferometer arm length in the triangular layout is aimed to be significantly extended to $\geq$10 km. This increase is essential to suppress the impact of unavoidable displacement noises to a tolerable level for this next-generation detector [2]. The sensitivity achieved relative to a single 90° detector varies depending on both the GW source’s position in the sky and its orientation. However, on average, the sensitivity of a triple 60° detector is slightly superior to that of an optimally positioned single 90° detector [71]. Nevertheless, ET configurations based on perpendicularly aligned interferometers are also being explored. Recently, comprehensive investigations of different detector layout configurations such as two spatially separated detectors with 15 km arm lengths at an opening angle of 90° were presented [72].

Additionally, ET will introduce considerably improved QRPN by means of an increased TM mass. In fact, a minimum mass of around 200 kg is proposed for the TMs of both ET-LF and ET-HF [2, 71]. The higher mirror masses imply enlarged TM dimensions, which facilitates the use of larger beam spots on the mirror surfaces to reduce the impact of thermal noise. In this context, the HF-LF configuration presents a sophisticated solution to the dilemma that QRPN and shot noise scale oppositely with light power and cannot be individually optimized in a single interferometer [71].

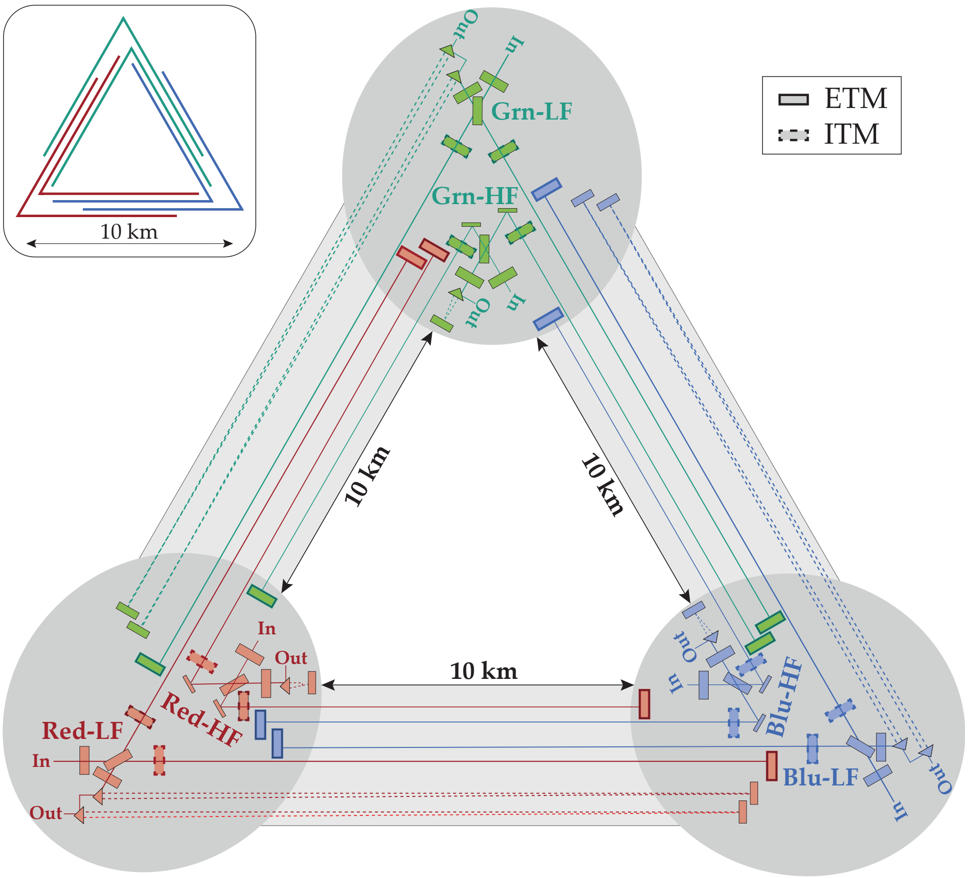

Figure 1.7: Triangular xylophone configuration for ET with three pairs of nested LF and HF interferometers. Solid lines denote the main laser beams, whereas dashed lines correspond to squeezed-light beams (adapted from [74], © IOP Publishing. Reproduced with permission. All rights reserved.).

Another major advancement of ET with respect to 2G-GWDs will have to be a significantly improved mitigation of Newtonian noise (cf. Section 1.2). As Figure 1.6 shows, it is one of the limiting noise sources in ET-LF at frequencies $f < 10\,\mathrm{Hz}$ [2]. Newtonian gravitational interactions between the detector optics and their surroundings directly couple ground motion to the test masses of the interferometer. Since the resulting gravity gradients cannot be shielded from the mirrors, it is imperative to find a location where seismic motion is minimal and the ambient structure is as uniform as possible. Newtonian noise in the LF range induced by surface waves supports the need for construction of ET in the underground. Accordingly, the corresponding noise mitigation objective can be met by choosing a subterranean site in a region with low seismic activity [71]. Studies indicate that a depth of several hundred meters in a remote area with sparse human population offers sufficiently low seismic activity [75, 76].

Figure 1.8 shows a detailed artist's 3D impression of such an underground installation of ET with the triangular xylophone configuration. The vacuum beam pipes of ET-

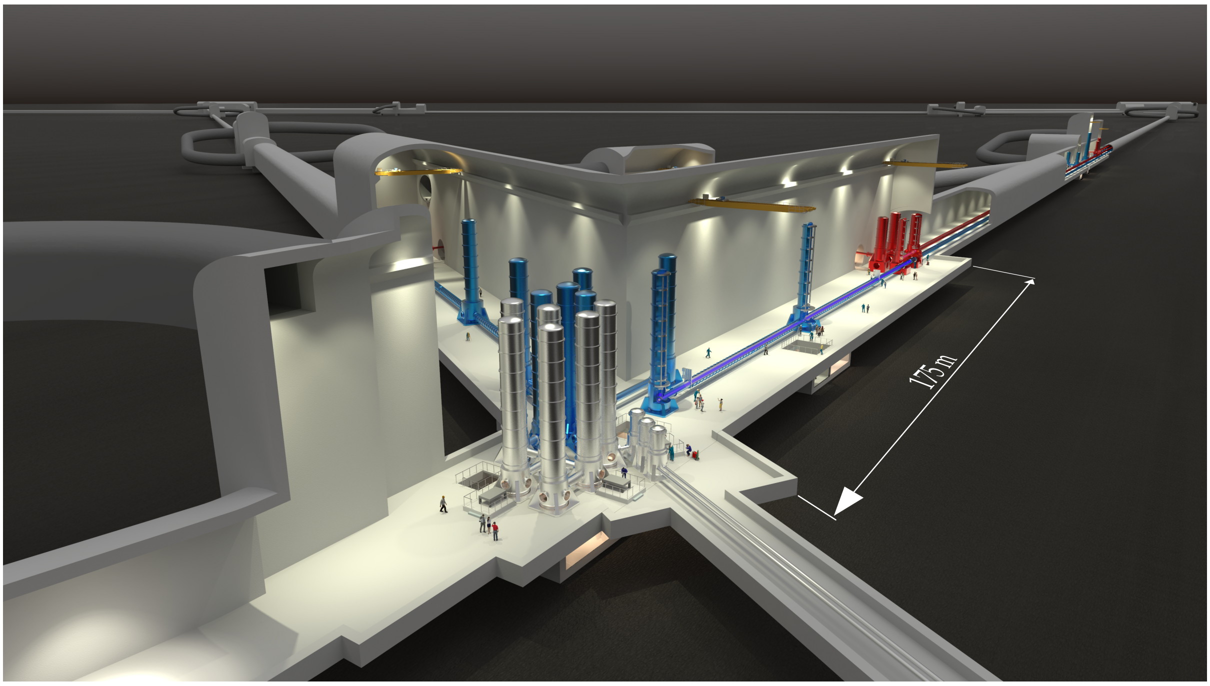

Figure 1.8: Artists' impression of the ET design. View inside an underground vertex cavern for a triangular xylophone detector configuration. © Marco Kraan/Nikhef [77] (annotated).

LF (blue) and ET-HF (red) are displayed, as well as the respective tall vacuum towers housing the SAs adapted from the Virgo design (cf. Figure 1.3). The towers hosting the optics for the input- and output mode cleaning (cf. Figure 1.2) of ET-LF are distinguishable by means of their silver color. The required height of the SAs and vacuum vessels containing the optics implies underground caverns between 12 m and 30 m in height [71]. Moreover, in the large vertex cavern's vicinity, three smaller auxiliary caverns are indicated. The two caverns along the 10 km beam pipes contain ETMs of the opposing interferometers (cf. Figure 1.7), while the auxiliary vertex cavern accomodates an ET-HF beam splitter and the respective input- and output mode cleaning optics' towers.

Further, compared to current GWDs, the Einstein Telescope will have to exhibit notably improved thermal noise mitigation in order to reach low-frequency (LF) sensitivities as depicted in Figure 1.6 [2, 71, 74]. Significant levels of signal distortion in the differential interferometer arm length due to thermal noise occur within both the TMs and their suspensions. In the frequency range of 2 Hz to 10 Hz, the dominant fundamental noise source, apart from Newtonian noise, is suspension thermal noise (STN). Reaching the LF sensitivity target of ET therefore requires its effective suppression. This can be achieved by cooling the TM suspensions to cryogenic temperatures, which significantly reduces thermal noise due to its dependence on both temperature and mechanical losses. The latter virtually vanish within low-temperature intervals, particularly in crystalline materials [14]. Along with their connected suspensions, the test masses themselves are cooled. This contributes to the total required suppression of mirror thermal noise, which can be attributed to both the TM substrate and its coating. Consequently, the ET sensitivity goal for low frequencies can only be met through the combined implementation of cryogenic TM operation and underground detector installation.

Motivated by the aforementioned advantages in gravitational-wave detection sensitivities, there are existing examples of the incorporation of cryogenics in GWDs. The Japanese Cryogenic Laser Interferometer Observatory (CLIO) project, for example, effectively showcased the functionality of a laser interferometer operating at cryogenic temperatures [78]. Building upon the CLIO prototype, KAGRA recently accomplished the first simultaneous cooldown of four TMs [79].

In ET-HF operating at room temperature T_{amb}, on the other hand, the various thermal noise contributions either do not play a significant role or can be sufficiently reduced by increasing the beam size on the test masses and the use of higher-order Laguerre-Gauss beam shapes [80] or so-called 'Mesa beams' [81].

The above noted advancements of ET with respect to current-generation GWDs imply significantly altered design parameters. Table 1.1 provides a concise comparison of the parameters most relevant to this thesis. The ET 'conceptual design study' from 2011 [2] as well as the recently completed ET 'design report update' [71] offer in-depth, comprehensive surveys of the ET design beyond the brief presentation here.

Table 1.1: Selected design parameters of ET in comparison with current interferometric gravitational-wave detectors.

Parameter	ET-LF	ET-HF	aLIGO	AdVirgo	KAGRA
Arm length	10 km [71]	10 km [71]	4 km [44]	3 km [43]	3 km [47]
Arm power	18 kW [71]	3 MW [71]	750 kW [44]	650 kW [82]	400 kW [83]
TM operating temperature	10...20 K [71]	290 K [71]	T_{amb} [84]	T_{amb} [82]	22 K [85]
TM material	silicon [71]	fused silica [71]	fused silica [44]	fused silica [43]	sapphire [47]
TM diameter	45 cm [71]	62 cm [71]	34 cm [44]	35 cm [43]	22 cm [85]
TM thickness	57 cm [71]	30 cm [71]	20 cm [44]	20 cm [43]	15 cm [85]
TM mass	211 kg [71]	200 kg [71]	40 kg [44]	42 kg [43]	23 kg [85]

Among other parameters, Table 1.1 lists the levels of optical power stored in the interferometer arms. ET-HF incorporates an arm power multiple times higher than that of currently existing GWDs, because the high-frequency sensitivity is determined by the maximum feasible laser power in the interferometer arms [71]. On the other hand, ET-LF exhibits merely 18 kW arm power, a value more than two orders of magnitude lower. This characteristic arises from the inherent limitations of even the most advanced mirror coatings produced by state-of-the-art technology. Despite achieving low residual absorption levels on the order of one part per million (ppm), circulating light power reaching the scale of megawatts, as is the case for ET-HF, would cause several watts of heat load in the cryogenic ET-LF TMs [71]. Consequently, the thickness of the suspension fibers necessary to extract this heat would compromise the performance of the ultra-low-loss (cf. Section 1.2) test mass suspensions.

Additionally, Table 1.1 displays the choice of TM materials in the detectors. Fused silica, which is an eligible material for TMs operated at T_{amb}, exhibits high mechanical losses at low temperatures, leading to excessive thermal noise contributions. Therefore, it is unsuitable as substrate material for cryogenic test masses [86, 87]. Silicon and sapphire show excellent low-temperature behavior and are the envisaged candidates for cryogenic GWDs [71]. The linear thermal expansion coefficient of silicon $\alpha_{\mathrm{TE,Si}}$ has roots at two particular temperatures ($\alpha_{\mathrm{TE,Si}}(T \approx 18\,\mathrm{K}) = \alpha_{\mathrm{TE,Si}}(T \approx 125\,\mathrm{K}) = 0$ [88]), while values of $\alpha_{\mathrm{TE,Sa}}$ become extremely small ($\alpha_{\mathrm{TE,Sa}}(T < 20\,\mathrm{K}) < 10^{-8}\,\mathrm{K}^{-1}$ [89]). Due to this fact, at temperatures below 20 K, the otherwise significant contribution of *thermo-elastic noise* to the sum of thermal noises virtually vanishes for both materials [2, 90]. Thus, the TM operating temperature of ET-LF is foreseen to be between 10 K and 20 K (cf. Table 1.1). Moreover, the advanced semiconductor industry ensures an ample supply of silicon in large quantities and with high purity. Consequently, silicon is a particularly promising material for the ET-LF optics and its consideration is hence prioritized in this thesis.

The following main chapters contribute to different aspects of the macroscopic technological improvement in interferometric gravitational-wave detection by cryogenically operated TMs. It shall be emphasized here that this is generally a new technology in GWDs. The present work showcases corresponding technological approaches in relation to the Einstein Telescope project. Constraints on the introduction of cryogenics into the overall detector system as well as on any other subsystem development are virtually exclusively defined via the total noise curve in Figure 1.6. Tangible design parameters suitable as boundary conditions are yet scarce. Consequently, assumptions are required in numerous of the presented calculations in subsequent chapters to determine parameter magnitudes. Given that the cryogenic developments for ET in this thesis are presented from their fundamental basis, the technological approaches may well be adapted to other current and future interferometric GWDs.

2 Overview of cryogenic detector developments

The payload system described in Section 1.2 is designed to couple the test mass to the super-attenuator (SA) chain, in order to compensate the residual seismic noise and to steer the test mass through internal forces exerted from the last SA element (cf. Figure 1.3) [91]. In contrast to 2G GWDs, the suspension chain's upper part will be at T_{amb}, while the payload is maintained at cryogenic temperatures in ET-LF.

The long steel suspension chain in the SA represents a poor thermal conductor, particularly at low temperatures, where the thermal conductivity of steels decreases significantly [92]. Thus, sufficient heat extraction from a cryogenic payload via a cooled SA suspension wire is impractical. Consequently, the interface with the cooling system (cf. Chapter 3) has to be integrated at the bottom end of the suspension chain, i.e. within the payload itself. This, however, poses a significant design challenge due to the fact that the presence of the interface must not spoil the noise isolation efforts provided by the sophisticated multi-stage upper suspension chain.

Thus, common techniques for providing thermal contact with a heat sink, such as rigid links composed of highly thermally conductive metal or flanged pipes carrying a refrigerant, are unsuitable for heat extraction from cryogenic payloads. Instead, a careful integration of the cooling system interface into the payload, fitting the extreme requirements of detector noise isolation, must be found. Presently, four distinct approaches to this challenge are being followed in the GW community, differing fundamentally in the technology used to extract the heat load from the payload:

(I) cryocoolers

(II) sorption coolers

(III) exclusive thermal radiation

(IV) (superfluid) helium

The cooling system interface needs to be adapted for either of these technological strategies. In this context, the following sections address the above approaches, in order to provide a comprehensive overview of all existing developments towards cryogenic cooling of GWDs. It is pertinent to note that the advancements in options (I), (II), and (III) are the work of other groups, whereas this thesis is dedicated to describing the author's contributions to the study of the approach using superfluid helium (IV).

2.1 Cooling concept using cryocoolers

As mentioned in the previous chapter, KAGRA is a currently operating gravitational-wave detector. Its target sensitivity is in a similar range to aLIGO and AdVirgo [47]. The design of KAGRA is similar to the 2G detectors, but it is located underground and incorporates cryogenically operated test masses composed of sapphire ($T \approx 20\,\mathrm{K}$). Due to these significant technological advancements, KAGRA is often referred to as a '2.5G' detector.

The overall layout of KAGRA is 'L'-shaped. Like LIGO and Virgo, it consists of a single Michelson interferometer with Fabry-Pérot cavities of $L = 3\,\mathrm{km}$ [47]. Thus, in the entire facility, four TMs have to be cooled, i.e. two ITMs and two ETMs.

KAGRA relies on pulse tube cryocoolers (PTCs) exclusively to ensure its cryogenic operation. Figure 2.1 representatively displays the cooling system scheme for one TM. The TM cryostat has a cylindrical shape with $d_\mathrm{o} \approx 2.6\,\mathrm{m}$ and $H_\mathrm{o} \approx 4.3\,\mathrm{m}$. Tokoku et al. [94] present the dimensions as well as estimated and roughly measured thermal budgets of the system. In order to extract the heat load, for every TM cryostat, six cryocoolers are required. The outer radiation shield at 80 K is cooled by four PTCs (first stages), while the inner shield (8 K) is cooled by two PTC second stages. Two further second stages provide cooling capacity for the payload ($\dot{Q}_\mathrm{c} \approx 1\,\mathrm{W}$). Two cryogenic duct shields, either of which is cooled to 120 K by a single-stage cryocooler, are located at both sides of the cryostat along the interferometer laser beam pipe. The tubular shields ($L = 5\,\mathrm{m}$, $d_\mathrm{i} = 37\,\mathrm{cm}$) are required to sufficiently limit the thermal radiation on the TMs passing through the large cryostat radiation shield openings, which are necessary for the laser beam to traverse the interferometer mirror [95].

The sole use of PTCs for cooling power provision implies that, unlike in a cooling system where cryogenic fluids can be distributed to the consumers (cf. Chapter 4), heat sinks are spatially confined to the extents of the cryocooler cold heads. As a consequence, solid links have to be used to conduct heat from all cryogenic consumers

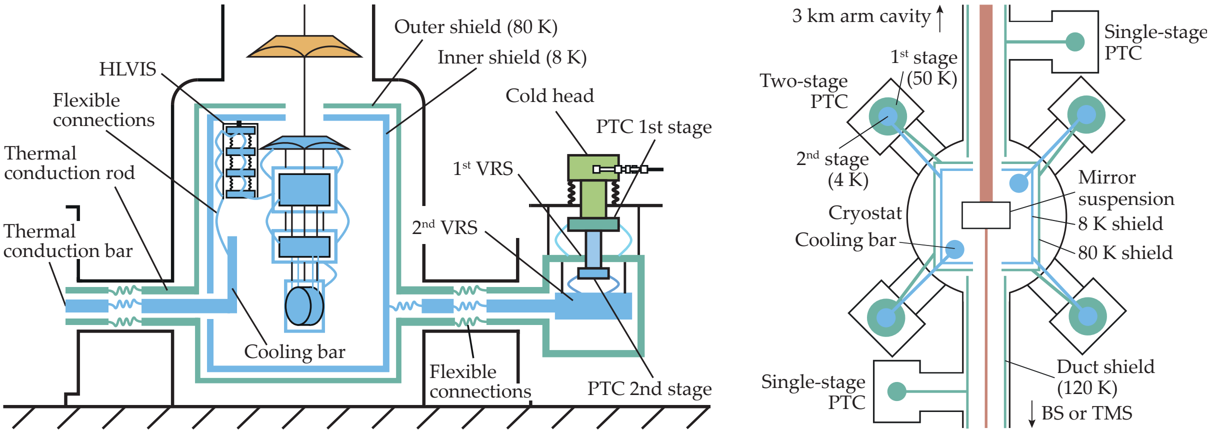

Figure 2.1: Representative scheme of the KAGRA cooling system (not to scale). *Left:* side view of a TM cryostat from an angle of 30° from the beam axis (adapted from [85], licensed under CC BY 4.0). *Right:* simplified view from above showing all cryocoolers required for operation (adapted from [93], © IOP Publishing. Reproduced with permission. All rights reserved.).

to the relatively small heat sink geometries. In KAGRA, these solid links are made out of high-purity copper and high-purity aluminum [94], both of which exhibit high thermal conductivity at cryogenic temperatures.

The working principle of PTCs relies on the control of a phase shift between the oscillating mass flow and pressure waves of the helium inside the cold head tubes. Thus, intrinsically, the PTCs generate acoustic noise within the provided heat sinks that are the stages of the cold head. Therefore, the solid connections by means of which heat is to be extracted from the cryogenic consumers in KAGRA must be designed so as to sufficiently mitigate the vibration transmission from the cold head stages into the cooled, extremely sensitive interferometer parts. These attenuation efforts are indicated schematically in Figure 2.1 (*left*).

To begin with, two vibration reduction stages (VRSs) are rigidly fixed to the ancillary cryocooler vacuum vessel by thermally insulating rods. The cold head 1st stages are connected to the 80 K thermal conduction bar by way of a first VRS, and the 2nd cold head stages are connected to the 8 K thermal conduction bars by means of a 2nd VRS. Between the VRSs and each cold head stage, there are flexible thermal links made of stranded wire of annealed Cu7N [94]. As the extremely high-purity copper wires are rather soft, these thermal links are chosen not only to conduct heat efficiently but also to attenuate the vibrations from the cold head as they propagate along the heat extraction path.

Further, there are flexible connections towards the end of the thermal conduction paths facing the payload cryostat, where layers of Al5N8 pure aluminum ($\geq$99.9998 % purity) are used for the same purpose as the stranded copper wires of the VRSs. Figure 2.2 shows these aspects in more detail. The PTCs are installed with remote motor option, thus, the valve unit is structurally isolated from the cold head and vacuum vessel. The cold head itself is clamped to a platform connected to the cryostat by a bellow in order to provide mechanical decoupling from the cryostat flange.

Finally, in addition to the attenuation efforts discussed above, a heat link vibration isolation system (HLVIS) is connected to the thermal conduction bars, inside the inner thermal shield (cf. Figure 2.1 (*left*)). This supplementary system is of paramount importance to sufficiently attenuate transmitted vibrations via heat links into the payload [96]. Due to the fact that it must be connected to the inner thermal shield to avoid running the integrated, cold heat links through an environment at higher temperature, shield vibrations couple into the payload as well [97]. This issue is addressed in further detail in Section 5.2.

Within the payload itself, the heat extraction path is continued by means of flexible connections ('heat links') that are implemented as strands of multiple, thin wires out of Al6N [98, 99]. These are visible in the KAGRA cryogenic payload depiction in Figure 2.3. In this illustration, the heat links directly connect the cooling bar to the marionette recoil mass, the HLVISs indicated in Figure 2.1 are not included. The links

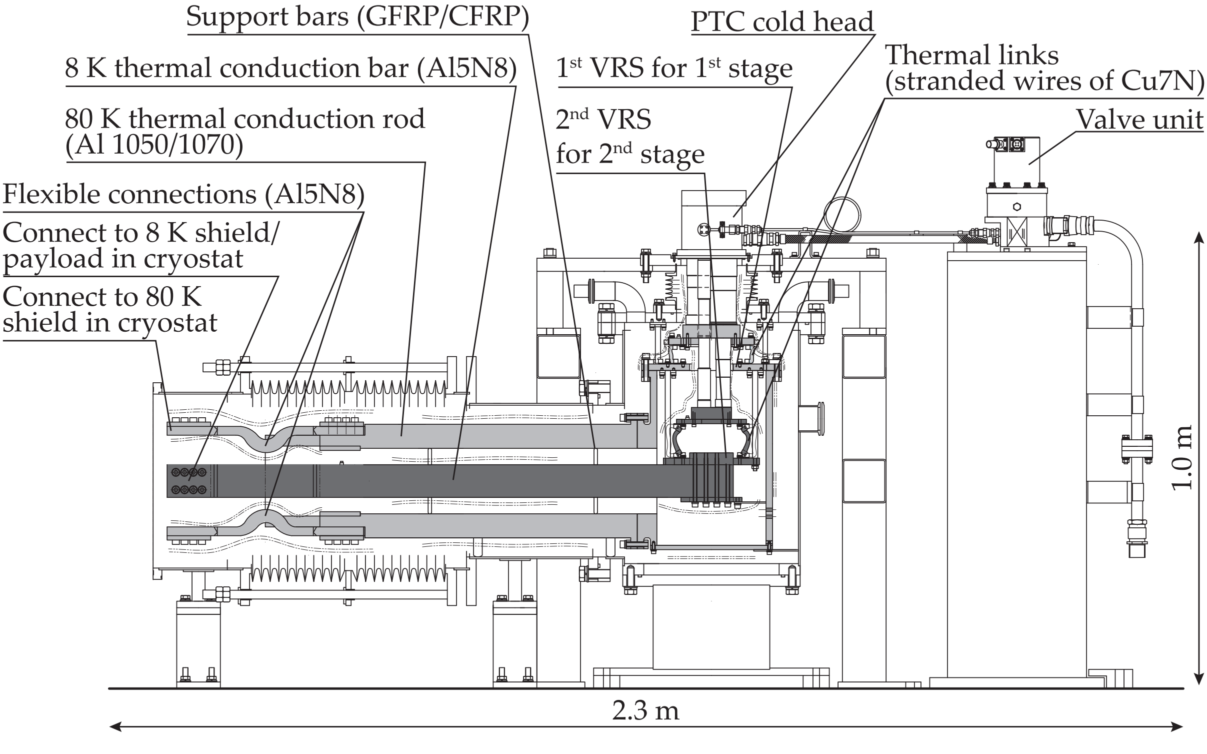

Figure 2.2: Detailed cross-sectional drawing of a KAGRA payload cryostat heat extraction unit. Reprinted from [94] with the permission of AIP publishing.

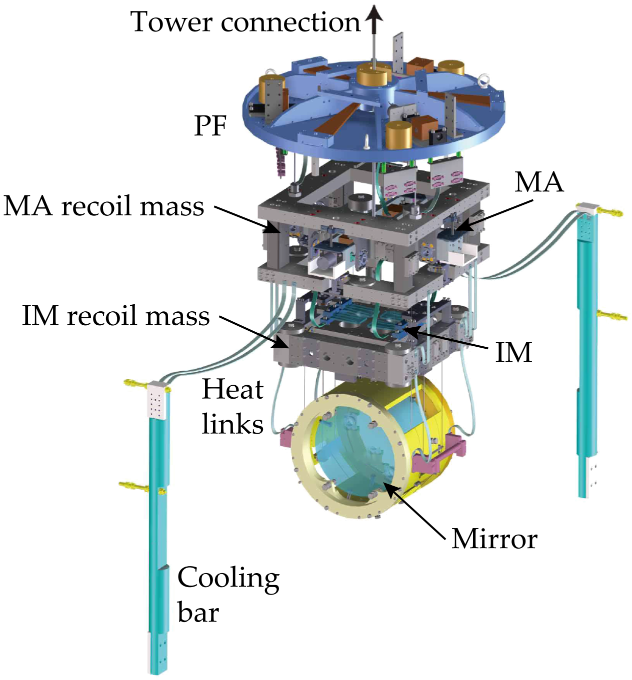

Figure 2.3: CAD model depiction of a cryogenic payload in KAGRA (adapted from [93, 99], © IOP Publishing. Reproduced with permission. All rights reserved.).

thermally couple the different payload masses towards the test mass in the following order [93]:

- marionette (MA) recoil mass
- platform/steering filter (PF)
- marionette (MA)
- intermediate mass (IM)
- mirror/intermediate mass (IM)

The IM suspends the test mass by sapphire fibers, which enable efficient heat extraction via conduction. Additional heat links are used to thermally interconnect the reaction chain composed of MA recoil mass, IM recoil mass and TM recoil mass.

For transient payload cooldown, the heat extraction path described above is used, including superimposed thermal radiation to the surrounding cold thermal shield. In this manner, subsequently to evacuating the payload cryostat, it takes ca. 27 days for TMs in KAGRA to reach their minimum temperature of 23 K [100]. In the end of the transient TM cooldown, along the solid heat extraction paths, temperatures of 15 K in the marionette recoil mass, 9 K in the cooling bar and 8 K at the PTC 2$^{\text{nd}}$ stage (cf.

Figure 2.1 (*left*)) are reached [100]. There are ongoing efforts to improve the process in order to shorten detector downtimes after system warmups.

The KAGRA cooling system performance in general is carefully considered in the developments towards the Einstein Telescope. In evaluating the suitability of cryocooler-based detector cooling for ET, the importance of finding solutions to enhance the corresponding TM cooldown performance is emphasized. This is due to the fact that the TMs in the Einstein Telescope have an increased weight by around one order of magnitude with respect to KAGRA (cf. Table 1.1). Further, due to the considerably higher detector sensitivity, yet, a comprehensive investigation is still necessary in order to evaluate if similar techniques may render a cryocooler-based cooling solution also applicable for ET. In fact, inspired by the cooling approach followed by KAGRA, there are significant developments in the scope of ET [101, 102]. A prototype of a solid conduction cooling-line equipped with two pulse tube cryocoolers was designed and commissioned at the Amaldi Research Center (ARC) in Rome. Figure 2.4 presents a respective photo. The macroscopic structure is consistent with the heat extraction path designs of KAGRA discussed above. The right-hand side shows the ancillary cryostat for the cold heads. Attached to its side is the duct containing a thermal conduction bar and, later on, flexible links envisaged to be made out of Al6N. The thermal conduction bar will be suspended at an intermediate position to provide further seismic isolation. Finally, at the left-hand side end of the cooling line, an experimental chamber for cryogenic operation- and vibration tests is connected.

Another significant unresolved issue in the scope of the cryogenically operated test masses in KAGRA is the high rate of ice formation ('frost') on the mirror surfaces.

Figure 2.4: Mechanical assembly of a cryocooler-based cooling duct prototype developed at ARC (reproduced from [101], licensed under CC BY-NC-ND 4.0).

It is induced by adsorption of residual molecules from within the payload cryostat as well as molecules traversing through the beam pipe openings towards the TM. The build-up time of one monolayer of adsorbed molecules was found to be $\sim$15 min [103]. Further, it has been confirmed that, due to frost layer growth, cryogenic test masses experience both a decrease in reflectivity [103–105] and an increase in thermal noise [106], ultimately leading to a considerable deterioration of detector sensitivity. A proposed resolution strategy is a stepwise adsorption of residual gas components on the thermal shield and duct shield surfaces around the payload cryostats in KAGRA [107]. This approach, however, implicates greatly increased cooldown times on the order of 2 months. In contrast, for ET, the foreseen long cryopumps (cf. Section 4.3.1) ensure a satisfactorily increased frost monolayer accumulation time of $\Delta t \approx 2\,\mathrm{yr}$ [108].

An additional factor that potentially perturbs detector sensitivity in the context of the cooling system is excessive Newtonian noise (cf. Section 1.2). Cryocooler operation leads to an oscillation of gravity force by causing vibrations of the relatively heavy cooling system components in close proximity to the test masses. Newtonian noise estimations in KAGRA show, that without further mitigation efforts, it can be expected to deteriorate the sensitivity of the Einstein Telescope. An approach yet to be investigated is the use of Wiener filters using cryogenic accelerometers to subtract cooling system Newtonian noise from detector data [109].

A hitherto unaddressed complication of the cryocooler-based cooling approach for ET is the substantial power dissipation in the underground caverns. Two cooling lines as depicted in Figure 2.4 are required in order to supply sufficient cooling power to a payload cryostat ca. 75 % the size estimated for ET (cf. Section 5.1). Considering the fact that each prototype cooling line hosts two PTCs of the Cryomech PT420 model [110], it is to be expected that a full size ET payload cryostat is to be supplied with cooling power by $n \geq 5$ such PTCs in total. One Cryomech PT420 cryocooler consumes $P_{\mathrm{input}} = 11.5\,\mathrm{kW}$ electrical power [111]. This amounts to a total consumption of around 60 kW per TM cryostat and thus, 240 kW per ET vertex (cf. Figure 1.7). ET-wide, this corresponds to an underground power dissipation of 720 kW, excluding the operation of cryopumps, which are the main cryogenic consumers. The power, ultimately dissipated in the form of heat, needs to be extracted from the caverns by means of cooling water circuits and air conditioning systems. In existing GWDs, ventilation and air conditioning systems have been found to be remarkable sources of seismic and acoustic noise. Moreover, flowing cooling water induces vibrations, often amplified by a turbulent flow regime, which can be transferred into sensitive detector parts via the cooling targets [112]. Therefore, the specific application of such measures to remove the dissipated heat from underground in the case of ET is to be carefully investigated.

This issue is mitigated within the purely helium-based cooling system concept (cf. Chapter 4) since virtually all refrigeration power is generated on the surface by a compressor system. The approach to cool all ET-LF test mass payloads with superfluid helium during detector operation as introduced in Section 2.4 is embedded in this concept.

2.2 Cooling concept using sorption coolers

A proposed alternative approach to payload refrigeration in GWDs utilizes sorption-based Joule-Thomson (JT) coolers [113, 114]. The application of the technology shall be assessed in ETpathfinder, a research facility with the objective of supporting the development and testing of essential new technologies needed for designing and operating future gravitational-wave detectors [115].

Figure 2.5 illustrates the basic scheme of a typical sorption-based JT cooler. The sys-

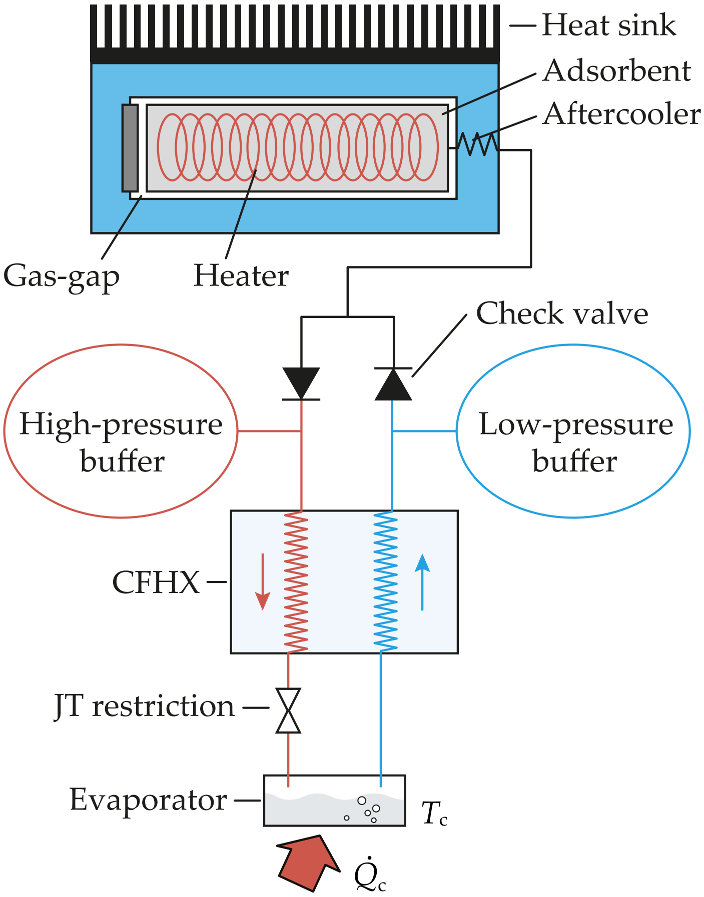

Figure 2.5: Schematic process visualization of a sorption-based JT cooler (adapted from [116], licensed under CC BY 3.0).

tem comprises a sorption compressor cell, depicted at the top of the figure, two buffer volumes, and a pair of passive valves. A sorption cell includes a container filled with an adsorbent material, such as activated carbon. The gas follows a path from a low-pressure buffer to a high-pressure buffer through the sorption cell driven by two primary processes involving cyclic heating and cooling of the adsorbent within the cell. After reaching the high-pressure buffer, the gas then traverses a counterflow heat exchanger (CFHX) before passing the JT flow restriction. At this stage, the gas undergoes an isenthalpic expansion to the low-pressure level, resulting in a temperature decrease and potentially leading to liquefaction in case of a negative Joule-Thomson coefficient. The expanded fluid absorbs heat from its surroundings and returns through the CFHX, exchanging heat with the incoming high-pressure flow. JT coolers utilizing sorption technology can be run using sorption compressors comprising one or more cells. Operating based on thermal principles, these compressors regulate gas flow direction through passive valves, allowing for the maintenance of nearly continuous gas flow through a JT cold stage. Thus, aside from passive valves, sorption coolers lack moving parts, which enables a reliable, low-vibration operation and extended lifetime [117].

By arranging multiple sorption coolers in a cooling cascade, a chain can be engineered, which enables the provision of refrigeration power at cryogenic temperatures. Using liquid nitrogen for precooling, the cascade is necessary to stepwise lower the coolant temperatures below their inversion temperature, ensuring that the JT expansion produces a cooling effect rather than heating. Such a cooler chain is being developed for ETpathfinder, adapted to its cryogenic payload thermal environment [113]. Table 2.1 lists the respective heat load specifications. Further, the working fluids providing the required cooling power are stated. The sorption cooler chain is composed of three stages, helium, hydrogen and neon. A total of 26 sorption compressor cells provide

Table 2.1: ETpathfinder payload cryostat baseline heat load specifications and sorption cooler chain design parameters [113, 114].

Parameter	Thermal shields Outer	 Intermediate	 Inner	Payload
$T_{\text{interface}}$ / K	77	40	15	8
$\dot{Q}_{\text{c,design}}$ / W	200	2.5	0.5	0.05
			Sorption chain	
Working fluid	N_2	Ne	H_2	He
Number of compressor cells	n/a	15	5	6

refrigeration capacity for an intermediate and an inner thermal shield as well as the ETpathfinder cryogenic payload itself.

Stringent vacuum requirements in the ETpathfinder experiment prohibit the use of multilayer insulation (MLI), which gives rise to a comparatively high heat load of 200 W intercepted by an outer thermal shield at ~80 K. The use of a liquid nitrogen bath at 77 K is foreseen to provide the necessary cooling power [113]. The respective aluminum vessel is envisaged to be connected rigidly to the bottom of the shield via an indium contact. In order to avoid excessive detector noise introduction, several measures to prevent nucleate boiling in the vessel, such as coating the inner surfaces with Teflon® are planned to be tested in the facility. In the same context, wide lines for the gaseous nitrogen return are anticipated with sintered bronze vapor limiters to mitigate the suction of liquid droplets into the exhaust.

Heat extraction from the payload itself is intended to be enabled by the so-called 'jellyfish' design. This refers to the use of manifold thin thermal links connecting different parts within the payload. Figure 2.6 visualizes this concept. The heat sink within the payload is the cold finger. It is decoupled from the thermal shields but rigidly linked to the cryostat mechanical structure, which causes it to exhibit a virtually identical dis-

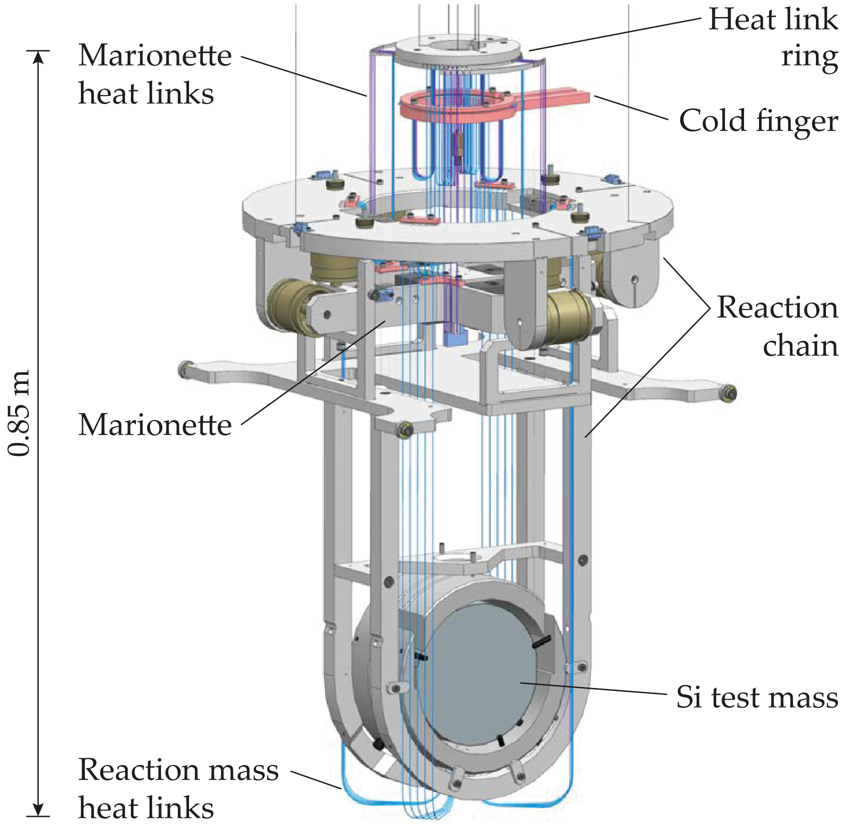

Figure 2.6: Complete model of the ETpathfinder cryogenic payload employing the 'jellyfish' design (adapted from [113, 114], licensed under CC BY 4.0).

placement spectral density as the ground. A total of 32 Al6N wires with $d = 0.15\,\mathrm{mm}$ are connected to the cold finger in order to enable sufficient thermal conduction from the warmer payload components while simultaneously attenuating excessive cold finger displacements. An intermediate body ('heat link ring') suspended from the steering filter at T_{amb} is placed between these components and the cold finger to provide a passive filtering stage for the vibrations of the cryostat.

Connected to the heat link ring, the Al wires are used to enable heat transfer throughout the complete payload, including the reaction chain. The only exception is the test mass pendulum stage, which is cooled exclusively via crystalline silicon suspension fibers in order to ensure the desired thermal noise performance [113]. The design of the heat extraction path beyond the cold finger, which needs to be thermally connected to the evaporator of the helium sorption cooler stage as well as the equivalent heat exchangers for the inner and intermediate thermal shield is under development.

Concerning the transient cooldown process, preliminary modelling results indicate that the desired TM operating temperature of $T = 18\,\mathrm{K}$ cannot be reached, even after more than 40 d [113]. This applies to the aforementioned hybrid refrigeration system composed of sorption-based JT coolers and LN_2 bath cooling. When additionally considering the small TM weight of $M_{\mathrm{TM}} = 3.5\,\mathrm{kg}$ in comparison to ET-LF or KAGRA (cf. Table 1.1), the criticality of finding technological solutions for this issue becomes particularly evident.

The introduction of an additional helium-based cooling circuit is proposed for accelerated cooldown of cold finger, inner- and intermediate thermal shield. The circuit is estimated to lower $\Delta t_{\mathrm{cooldown}}$ to about 2 to 3 weeks [118]. In order to avoid excessive vibration transmission into the payload caused by flowing helium in contact with the cold finger, this additional cooler has to be switched off for steady-state operation of the interferometer facility.

2.3 Cooling concept using exclusive thermal radiation

Another approach to cooling cryogenic payloads in GWDs is to resort to pure thermal radiation. Radiation-only cooling is arguably the most intuitive solution to refrigerate GWD test masses. This is because the primary mechanical coupling to the cooling system occurs solely through the ground, from which the TMs are isolated by means of super-attenuators (cf. Section 1.2), thereby offering a substantial advantage in terms of noise suppression. The LIGO Voyager upgrade is planned to make use of this advantage to avoid complicating the test mass suspensions by introducing additional demands for thermal conduction [119]. The U.S.-based next-generation GWD, Cosmic Explorer (CE), is anticipated to follow this approach [120].

However, a drawback of radiative cooling is the substantial reduction of the heat transfer rate as the temperature of the TM decreases, which is attributed to the T^4-dependence of thermal radiation coupling. In the case of LIGO Voyager and CE, this is a manageable impairment due to the comparatively high test mass operating temperature of $T_{\mathrm{TM}} = 123\,\mathrm{K}$.

For the Einstein Telescope, this approach gives rise to significant implications. The ET-LF test mass operating temperature $T_{\mathrm{TM}} = 10...20\,\mathrm{K}$ strongly limits the possible radiative heat flux to an even colder ambiance. Considering the *Gedankenexperiment* of a test mass at $T = 20\,\mathrm{K}$ with $\epsilon = 1.0$ being perfectly enclosed by a black body at $T = 0\,\mathrm{K}$ yields the asymptotic upper limit of $\dot{q} \approx 9\,\mathrm{mW\,m^{-2}}$ for the extractable heat flux. Taking into account a total heat load in ET-LF of $\dot{Q}_{\mathrm{c}} = 1.0\,\mathrm{W}$ (cf. Table 4.3), this implies a warm surface area of $A \gtrsim 112\,\mathrm{m}^2$. In comparison, the total combined surface area of marionette and test mass in the baseline design for ET-LF (cf. Figure 3.2) is ca. $2.3\,\mathrm{m}^2$.

The overall radiative cooling principle is investigated as part of the Einstein Telescope Euregio Meuse-Rhine Site and Technology (E-TEST) activities [121]. In this scope, an experimental setup is designed, the main purpose of which is the provision of a framework for developments of

❏ low-temperature vibration control systems, which involves vacuum- and cryogenic technologies, active vibration isolation and the design of a seismic isolation apparatus, and

❏ optical engineering designs including the manufacturing and testing of silicon mirrors, lasers and optics at 2 µm wavelength as well as the assembly and validation of the whole setup.

Figure 2.7 depicts a scheme of the E-TEST prototype cryostat, reduced to the parts of relevance for the radiative cooling principle. Centrally located within the vacuum vessel and suspended from an above marionette and damping platform at T_{amb} are a cold platform and a silicon mirror. These are foreseen to be operated at 20 K [121]. The cold platform is a cryogenic testbed for sensors such as superconducting inertial sensors [123, 124]. Suspended from the platform by silicon rods is the mirror with $M = 100\,\mathrm{kg}$.

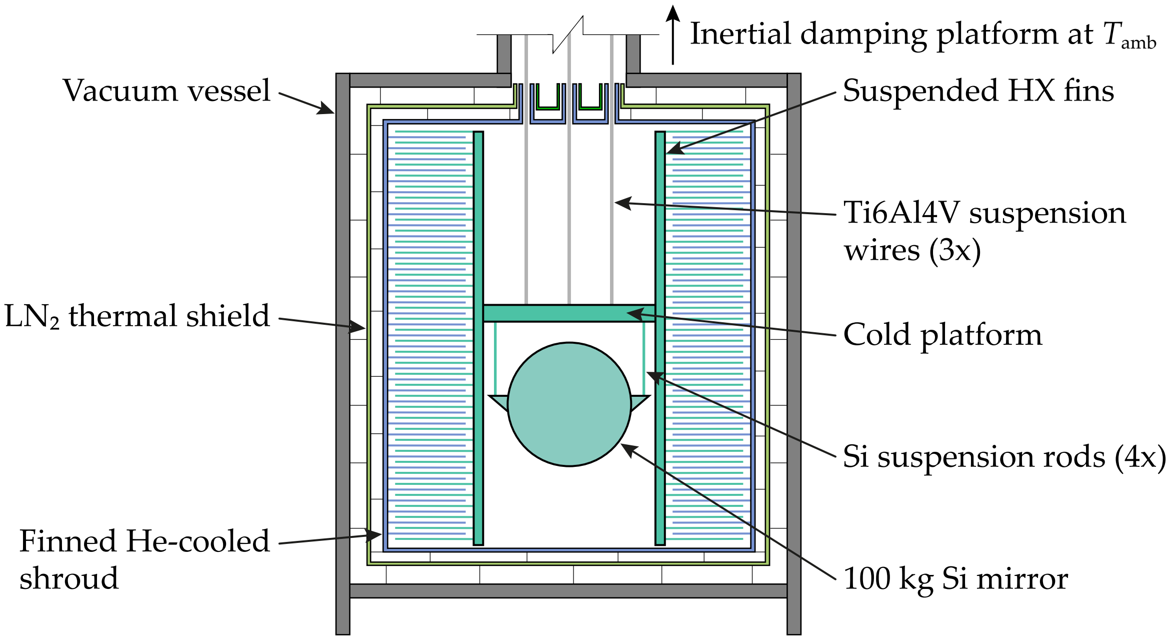

Figure 2.7: Basic scheme of the E-TEST prototype cryostat with the main features for radiative cooling of all suspended elements (not to scale, adapted from [122], licensed under CC BY 4.0).

The E-TEST design refrigeration capacity via exclusive thermal radiation for the cold platform and mirror is $\dot{Q}_c = 0.3\,\mathrm{W}$ in steady-state [121]. The required heat sink is provided by means of a shroud completely surrounding the platform and mirror cooled via forced convection with gaseous helium from a closed-loop refrigerator. To increase the area of heat transfer, the chosen strategy is to implement horizontal fins for both the cold suspended platform and the shroud. The fins overlay alternately, forming a large stack which establishes $A_{\mathrm{HT}} \approx 70\,\mathrm{m}^2$ within a total volume of ca. $8\,\mathrm{m}^3$, surrounding platform and mirror on all sides. High-emissivity polyurethane coating is applied to the fin surfaces in order to increase thermal radiation efficiency [122]. Further, for thermal conduction through the thin geometries with tolerable temperature gradients, aluminum has been chosen as fin material.

Ray-tracing simulations based on the Monte-Carlo method show that for a coating emissivity $\epsilon = 0.4$ and an average shroud temperature $\overline{T} = 20\,\mathrm{K}$, a steady-state mirror temperature of $\sim$27 K can be reached [122]. Achieving $T_{\mathrm{mirror}} = 20\,\mathrm{K}$ with a liquid helium-cooled shroud at 4 K is estimated to require $A_{\mathrm{HT}} \approx 100\,\mathrm{m}^2$. While the shroud temperature is estimated to be lowered from T_{amb} to 20 K in about 12 h, the cooldown of the system composed of mirror, platform and its attached fins ($M_{\mathrm{total}} \approx 400\,\mathrm{kg}$) will take $\sim$13 d [121].

In the E-TEST prototype cryostat, the innermost shield is thus utilized as the exclusive heat sink for mirror cooling. As for the case of ET-LF, besides complementing the payload cooling aspects which are presented in Section 3.1, the thermal shielding design must consider further constraints. This is addressed in Chapter 5. The overall concept remains subject to open questions regarding the extent to which such large payload surfaces are compatible with the noise and vacuum requirements in ET-LF.

2.4 Cooling concept using superfluid helium

Finally, a promising emerging approach to supplying cooling power to GWD payloads utilizes superfluid helium. This method constitutes the physical cooling principle with the lowest noise, which can be integrated in the cryogenic payloads with minimal coupling. Following its introduction here, the concept is examined in detail in all subsequent chapters.

Since its discovery around ninety years ago [125], this distinct state of ^{4}He has been established as an effective technical refrigerant not only for high-field superconducting devices, but also in laboratory experiments and large-scale research projects. Central to the technological approach of introducing superfluid helium to cryogenic GWDs is the implementation of a heat sink within the payload itself. This can be achieved by engineering the marionette suspension as a tube, the bottom of which is inserted in the bulk marionette material. Figure 2.8 visualizes the concept. The suspension tube serves a dual purpose. It allows cooldown of the payload via forced convection with supercritical helium and liquid He I via an inner guiding tube. Further, in steady-state cryogenic GWD operation, it is completely filled with a static column of superfluid He II. The use of superfluid helium as a cooling fluid is predominantly motivated by two key properties, its low operating temperature and its exceptional heat transfer properties, which are elaborated upon in this chapter.

Figure 2.9 marks the state conditions of ^{4}He under which He II occurs. When liquid He I is cooled below a transition temperature T_λ, Bose-Einstein condensation of helium atoms commences. The notion that superfluidity must be connected with the formation of a Bose-Einstein condensate was suggested first by London in 1938 [127]. This marked a particularly significant discovery, as a quantum-mechanical process could be perceived via its macroscopic consequence, i.e. a second-order phase transition in which no latent heat is generated [128], but extraordinary fluid property changes are triggered. These comprise a sharp peak of the specific isobaric heat $c_p\left(T\right)$ around T_λ, which forms a shape resembling the letter 'λ' [129]. Due to the fact that $T_\lambda = f\left(p\right)$, in the ^{4}He phase diagram, the division between the two liquid phases He I and superfluid He II forms the 'λ line'. At a pressure $p = 1\,\mathrm{atm}$, the transition temperature is $T_\lambda \approx 2.17\,\mathrm{K}$.

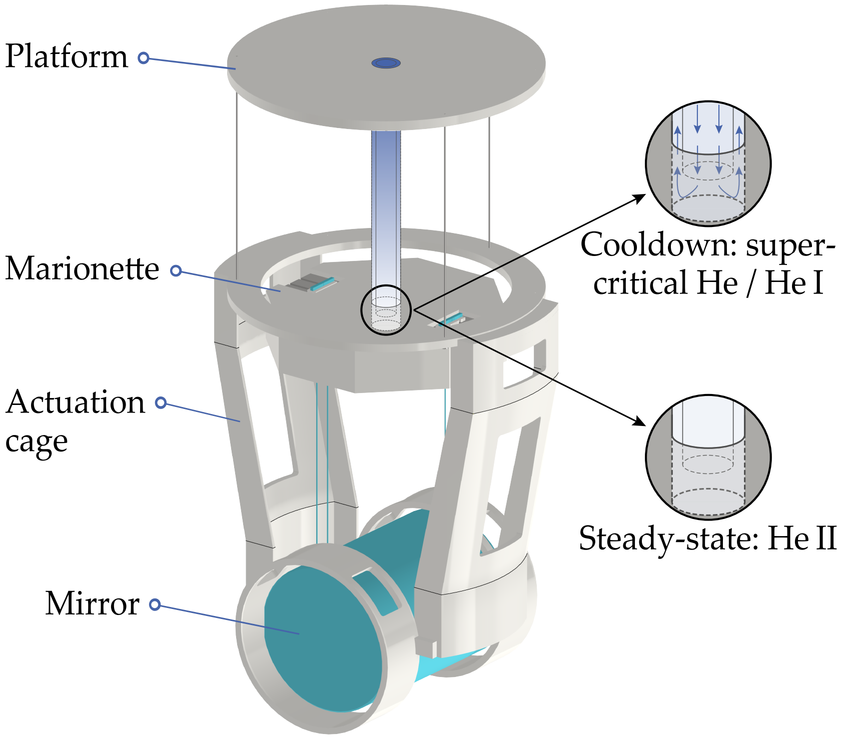

Figure 2.8: Schematic depiction of superfluid helium introduction into GWD payloads via a marionette suspension tube.

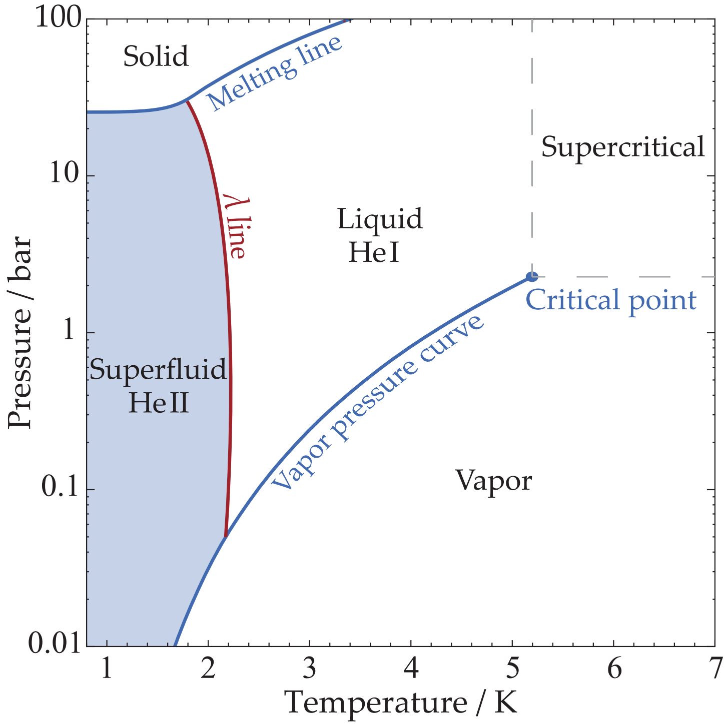

Figure 2.9: Phase diagram of ^{4}He with highlighted conditions under which superfluidity occurs. Thermophysical property data from [126].

At temperatures $T < T_\lambda$, He II is composed of both a normal- and a superfluid component, as described by the two-fluid model [130, 131]. This is owed to the fact that the proportion of superfluid increases from zero at the transition temperature to unity at $T \to 0$. Thus, below T_λ, both fluid components coexist in the same bulk liquid phase, interpenetrating each other and thereby constituting the macroscopic quantum fluid that is He II. In particular, the two-fluid model describes the He II density as made up of these two component densities,

$$\rho = \rho_{\mathrm{nc}} + \rho_{\mathrm{sc}} \,, \tag{2.1}$$

with both the density of the normal fluid component ρ_{nc} and the superfluid component ρ_{sc} being strongly dependent on temperature. Due to this dependence, the superfluid component composes about 99% of He II at $T = 1\,\mathrm{K}$. Similar to the density, the total liquid momentum flux of He II is the sum of the two components,

$$\rho v = \rho_{\mathrm{nc}} v_{\mathrm{nc}} + \rho_{\mathrm{sc}} v_{\mathrm{sc}} \,, \tag{2.2}$$

where v_{nc} and v_{sc} denote the velocities of the normal fluid and superfluid component. The superfluid component behaves as a Bose-Einstein condensate, exhibiting zero viscosity ($\eta_{\mathrm{sc}} = 0$). It flows through even the finest capillaries, driven solely by a difference in chemical potential, which depends on the relative proportions of the superfluid and normal fluid components. Further, the superfluid component carries no entropy ($s_{\mathrm{sc}} = 0$). The complete entropy s of the macroscopic He II phase is attributed to the normal fluid component, which behaves as an ordinary liquid with conventional viscosity η_{nc}. Thus, a postulated kinetic model describes the heat flux transported through He II by motion of the normal fluid as

$$\dot{q} = \rho s T v_{\mathrm{nc}} \tag{2.3}$$

for the case of zero net mass flow at $v = 0$ [132]. As the normal fluid component is viscous, its flow near a solid boundary is influenced by shear forces. Following this kinetic model, in stationary He II ($v = 0$), the temperature-gradient-induced velocity of the normal fluid is counterbalanced by the motion of the superfluid component, as described by Equation (2.2). This condition, known as 'thermal counterflow', is considered to account for the exceptionally high thermal conductivity of He II. Measurements of the latter were first published by Allen, Peierls and Uddin in 1937 [133]. They observed that the thermal conductivity of He II, as conventionally defined, was dependent on the temperature gradient and appeared to approach infinity as the temperature gradient diminished to near zero.

In thermal counterflow, above a certain critical value of the relative velocity $\mid v_{\mathrm{sc}} - v_{\mathrm{nc}} \mid$ on the order of a few $\mathrm{mm\,s^{-1}}$, turbulence develops within He II [132]. This turbulence can manifest in two forms. The normal fluid component may transition to turbulence at a Reynolds number comparable to that of classical fluids,

$$Re_{\mathrm{crit}} = \frac{\rho v_{\mathrm{nc}} d_{\mathrm{h}}}{\eta_{\mathrm{nc}}} \approx 1200\,, \tag{2.4}$$

where d_{h} is the hydraulic diameter of the channel containing the He II. Further, the superfluid component may also exhibit turbulence. However, owing to its inviscid behavior, this turbulence materializes as quantized vortex lines that extend throughout the fluid. Feynman [134] discovered the possibility of their existence in his influential theoretical work in 1955. Subsequently, a theoretical treatment of the phenomenon was developed, which yielded good quantitative agreement with experiments [135]. Later, even photographs of quantized vortex lines in He II were successfully captured [136].

Consequently, the thermal conductivity of He II is not only a function of fluid- but also of system properties, i.e. d_{h} and $\dot{q}$. Therefore, in order to compare heat transfer characteristics of He II to other materials, an effective thermal conductivity λ_{eff} is communicated. Figure 2.10 shows typical values of λ_{eff} in comparison to ultra-pure annealed copper. It is evident that λ_{eff} of He II exceeds the thermal conductivity of even the purest copper, which is among the best heat-conducting solids known. At $T \approx 1.9\,\mathrm{K}$, λ_{eff} rises to nearly $2{\cdot}10^5\,\mathrm{W\,m^{-1}\,K^{-1}}$, while the thermal conductivity of 5N-Cu stays well below its peak value $\lambda_{\mathrm{5N-Cu}}(T \approx 10\,\mathrm{K}) \approx 1 \cdot 10^4\,\mathrm{W\,m^{-1}\,K^{-1}}$ at slightly elevated temperature [92]. When nominal operation is set to temperatures moderately

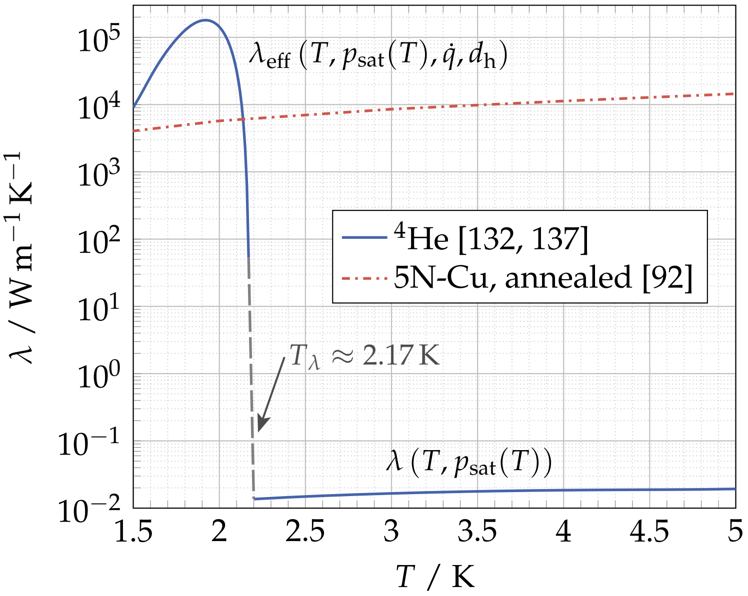

Figure 2.10: Thermal conductivity of ^{4}He across T_λ at saturation pressures in comparison to highly pure, well-annealed copper. Typical helium system property values of $\dot{q} = 10\,\mathrm{kW\,m^{-2}}$ and $d_{\mathrm{h}} = 1\,\mathrm{mm}$ were chosen.

below the peak in λ_{eff}, He II demonstrates an exceptional ability to compensate large transient heat loads, making it especially useful for maintaining thermal stability in sensitive systems.

Given values of helium thermal conductivity in Figure 2.10 are at saturation pressure $p_{\text{sat}}(T)$. An examination of the phase diagram of helium in Figure 2.9 shows the working domains of He II, reached by gradually lowering the pressure to below 50 mbar along the vapor pressure curve. Pressurized He II, on the other hand, is obtained by sub-cooling liquid helium at any pressure above saturation, most commonly at atmospheric pressure. While cooling via pressurized He II requires an additional level of heat transfer and extra processing equipment, notably a pressurized-to-saturated He II-heat exchanger, it offers several significant established technical advantages [138]. In the context of gravitational-wave detector cooling, refrigeration through pressurized He II avoids the necessity to pump directly on the static liquid column situated in the marionette suspension tube (cf. Section 4.2). Thus, further seismic noise decoupling potential is offered. The following chapters comprehensively examine various aspects of the overarching cooling concept utilizing superfluid helium, beginning with an evaluation of the influence on detector noise by implementing a marionette suspension designed as a hollow tube rather than a solid fiber. Investigations into potential adverse effects by the postulated thermal counterflow in He II as outlined above on GWD sensitivity will be the subject of extensive future experimental studies to the planning of which the author has significantly contributed [139].

3 Cryogenic payloads for the Einstein Telescope

The supply of helium to the cryogenic payloads of ET-LF (cf. Section 2.4) calls for an integrated design which meets a multitude of of thermodynamic, mechanical and operational requirements. Ultimately, this system, located at the cores of each ET-LF interferometer, will be the central element to enable the low-frequency design sensitivity of the Einstein Telescope as presented in Figure 1.6. The following publication presents the first development of a baseline cryogenic payload design for ET-LF. Of the technological approaches to supply cooling power to the payload described in the preceding chapter, the options (I)/cryocoolers, (II)/sorption coolers and (IV)/(superfluid) helium are compatible with the latter. A key focus of the publication is on option (IV). Within its scope, the author contributed to the development from first principles and the theoretical proof-of-concept, providing all helium-related aspects in an iterative design process. These contributions are supplemented by further information provided in the subsequent Section 3.2.

3.1 Cryogenic payloads for the Einstein Telescope: Baseline design with heat extraction, suspension thermal noise modeling, and sensitivity analyses

Reprinted journal article with permission from Xhesika Koroveshi, Lennard Busch, Ettore Majorana, Paola Puppo, Piero Rapagnani, Fulvio Ricci, Paolo Ruggi and Steffen Grohmann, *Phys. Rev. D*, **108**, 123009 (2023).

DOI: 10.1103/PhysRevD.108.123009.

The notation of the original journal article has been synchronized with this thesis. All corresponding changes are listed below[*].

Abstract

The Einstein Telescope (ET) is a third-generation gravitational wave detector that includes a room-temperature high-frequency (ET-HF) and a cryogenic low-frequency laser interferometer (ET-LF). The cryogenic ET-LF is crucial for exploiting the full scientific potential of ET. We present a new baseline design for the cryogenic payload that is thermally and mechanically consistent and compatible with the design sensitivity curve of ET. The design includes two options for the heat extraction from the marionette, based on a monocrystalline high-conductivity marionette suspension fiber and a thin-wall titanium tube filled with static He II, respectively. Following a detailed description of the design options and the suspension thermal noise (STN) modeling, we present the sensitivity curves of the two baseline designs, discuss the influence of various design parameters on the sensitivity of ET-LF and conclude with an outlook to future R&D activities.

3.1.1 Introduction

The Einstein Telescope (ET) is a third generation gravitational wave (GW) detector with a xylophone design, combining a low-frequency (LF) and a high-frequency (HF) laser interferometer. Sensitivities lie in the range of 3 to 30 Hz (ET-LF) and 30 Hz to 10 kHz (ET-HF), respectively. The low-frequency sensitivity is crucial for exploiting the full scientific potential of ET, in particular with regard to:

(1) the observation of binary neutron stars (BNSs), staying long time in the bandwidth,

(2) pre-merger detection to probe the central engine of gamma-ray bursts (GRBs), particularly to understand the jet composition, the particle acceleration mechanism, the radiation and energy dissipation mechanisms,

(3) detecting a large number of kilonovae counterparts,

---

[*]

original	c_p	d_i	d_o	g	mi	MI	Q	$\dot{Q}$	s_i	s_o	S	y	α
this thesis	c	$d_{ST,i}$	$d_{ST,o}$	g_0	tm	TM	Q_m	$\dot{Q}_c$	$s_{ST,i}$	$s_{ST,o}$	A_{cross}	z	α_{HT}

original (continued)	α	σ	σ_{max}
this thesis (continued)	α_{TE}	σ_m	$\sigma_{m,max}$

(4) detecting primordial black holes (PBHs) at redshifts $z > 30$, and

(5) detecting intermediate massive back holes (IMBHs) in the range of $10^2 - 10^4\,M_\odot$ [72].

Figure 3.1 shows the noise contributions to the sensitivity curve ET-D [2], based on payload design parameters listed in Table 3.1. Cryogenic operation of the payload is indispensable to suppress the suspension thermal noise (STN) to the level of gravity gradients—i.e. Newtonian noise (NN). Both STN and NN are the fundamental noises that dominate the ET-LF noise budget at frequencies below 10 Hz.

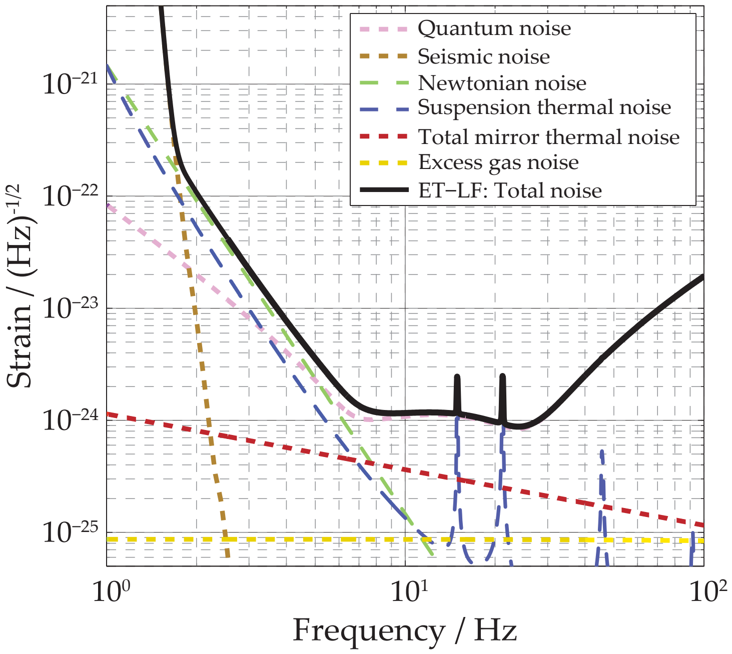

Figure 3.1: ET-LF noise contributions in the ET-D sensitivity curve [2].

Table 3.1: ET-LF payload design parameters from [2], using a branched pendulum model as in Virgo.

	Marionette	Recoil mass	Test mass
Mass / kg	422	211	211
Suspension length / m	2	2	2
Suspension diameter / mm	3	3	3
Suspension material / –	Ti6Al4V	Silicon	Silicon
Loss angle / –	$1 \cdot 10^{-5}$	$1 \cdot 10^{-8}$	$1 \cdot 10^{-8}$
Temperature / K	2	10	10

The technical implementation of the parameters in Table 3.1 is not straightforward [140, 141]. Therefore, in this paper we develop a baseline design of a cryogenic payload for ET-LF, which is consistent in terms of mechanical and thermal design as well as STN modeling. It shall serve as a stepping stone for the cryostat design and for future payload design optimization, rather than assuming it to be “final”. The focus of this paper is purely on the payload, not yet including the impact of cooling interfaces, which is a subject of future R&D.

Section 3.1.2 introduces the baseline cryogenic payload design for ET-LF with two heat extraction concepts, which are further explained in Sections 3.1.3 and 3.1.4. This is followed in Section 3.1.5 by a detailed description of the STN modeling. Section 3.1.6 then presents the sensitivity curves of the baseline designs. The influence of various design parameters on the sensitivity of ET-LF is analyzed in Section 3.1.7, before main conclusions and an outlook to future R&D activities are presented in Section 3.1.8.

3.1.2 Baseline design of a cryogenic payload for ET-LF

3.1.2.1 Overall operating conditions

ET-LF shall be operated with a 1550 nm wavelength laser at an arm power of 18 kW. The baseline material for the mirror and its suspension fibers is monocrystalline silicon. An alternative material for the mirror and its suspensions is sapphire. The operating temperature of the mirror is between 10 K and 20 K. While a 0.1 W heat load has been estimated in [2, 71], we re-define an engineering design target of

$$\dot{Q}_\mathrm{c} = 0.5\,\mathrm{W} \tag{3.1}$$

total heat load on the ET-LF payload, considering the size and complexity of the cryostat and including the need for optical access. This value entails a thermal safety margin and compares to a range of 0.5–1.0 W that KAGRA, the first cryogenic gravitational wave detector, assumes on its cryogenic test masses of 23 kg, partially caused by a higher absorption in its sapphire mirrors [142].

3.1.2.2 Conceptual design of the payload

The baseline design of the ET-LF cryogenic payload is derived from the double pendulum layout of the AdVirgo payload [49]. It is depicted in Fig. 3.2 and includes the following main components:

(1) *Platform (PF)*, from which the marionette and the cage are suspended separately, using a single suspension for the marionette and three suspensions for the cage, respectively. The platform is the first stage inside the ET-LF cryostat volume, being suspended from a warm super-attenuator system.

(2) *Marionette (MA)*, which coordinates the position of the mirror via four monocrystalline silicon suspension fibers. These suspensions are connected to so-called mirror ears that are attached via hydroxide catalysis bonding (HCB) onto the sides of the mirror.

(3) *Actuation cage (CA)*, which serves as a reaction mass for both the mirror and the marionette. In addition, various sensory devices are installed on this robust structure to avoid a direct contact with the sensitive optics. In AdVirgo, the cage is rigidly attached to the PF, whereas a suspended cage is proposed here.

(4) *Mirror/Test mass (TM)*, which constitutes the core optical element of the interferometer.

The design of the cryogenic payload must consider thermal and mechanical feasibility, while fulfilling a low STN contribution compatible with the ET-D sensitivity curve [2]. The correct implementation of interfaces, temperature gradients, and mechanical safety factors is essential. Further design aspects include the cryostat dimensions and space requirements for installation and auxiliary systems, the fabrication of long and

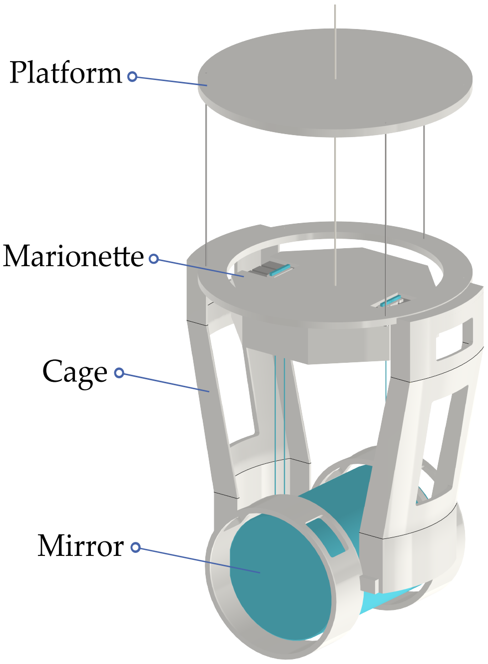

Figure 3.2: Baseline design of the ET-LF cryogenic payload based on the AdVirgo double pendulum design.

high-quality monocrystalline suspension fibers, and the achievable marionette temperature based on the cooling concept.

The AdVirgo payload operating at room temperature has a MA made of 316L stainless steel [49]. In the ET-LF cryogenic payload, the material for the MA remains to be decided. In addition to mechanical functionality, the choice is influenced by thermal aspects—i.e. the transient cooldown behavior and the achievable temperatures in steady-state operation. Therefore, aluminum alloys offer an alternative material choice for the MA.

The combination of various constraints yields the baseline design parameters listed in Table 3.2. While the mirror suspensions are generally made of monocrystalline silicon or sapphire fibers, we propose two alternative concepts for the heat extraction and the marionette suspension, respectively. The first concept presented in Section 3.1.3 relies on a cooling interface on the CA and the PF, requiring a monocrystalline high-conductivity marionette suspension made of silicon or sapphire as well. The second concept uses a thin-wall titanium tube as marionette suspension that is filled with superfluid He II. This concept provides cooling at 2 K down to the marionette and is explained in Section 3.1.4. In both heat extraction concepts, the cooling interface design will affect the sensitivity. Defining the interface deteriorative impact on sensitivity and thermal resistivity requires a refined and experimental-based analysis. The designs will result from experimental investigation and optimization, which are not yet advanced enough to be included in the scope of this paper.

Table 3.2: Baseline design parameters of the ET-LF payload, including two marionette cooling concepts.

		Marionette		Mirror	
Cooling concept	Monolithic	Monolithic	He II-filled	Silicon	Sapphire
Mass / kg	200	220	200	200	220
Suspension length / m	1.0	1.0	1.0	1.2	1.2
Suspension diameter / mm	8.1	6.5	8.3	3.0	2.3
Suspension material / –	Silicon	Sapphire	Ti, He II	Silicon	Sapphire
Bulk loss angle / –	$1 \cdot 10^{-9}$	$3 \cdot 10^{-9}$	$1 \cdot 10^{-6}$	$1 \cdot 10^{-9}$	$3 \cdot 10^{-9}$
Temperature / K	15	17	2	15 . . . 20	20 . . . 23

3.1.3 Concept with monocrystalline marionette suspension

3.1.3.1 Motivation

The initial conceptual payload design with the parameters in Table 3.1 is based on a heat extraction interface on the marionette, which is thermally insulated from the platform via a low-conductivity Ti6Al4V suspension [2]. STN computations [143, 144] reveal that the cooling interface must be implemented on the CA and passed to the PF, as the direct connection of any high-dissipation cooling path on the marionette would critically affect the thermal noise. Hence, the suspension material must induce low STN and provide high thermal conductivity and mechanical strength. Al6N can be used to connect the payload to the cryogenic system, but is not an option to suspend the marionette due to a very low yield strength [145], which is more than one order of magnitude smaller compared to crystalline silicon or sapphire. The low STN requirement is achieved for crystalline sapphire and silicon at low temperatures thanks to their high mechanical quality factor Q_m [146], where Q_m is the inverse of the loss angle ϕ at resonance [147, 148], cf. Section 3.1.5.

The overall results from the computations converge in the assessment that the marionette suspension mechanics must assure low thermal noise—i.e. mechanical dissipation—in order to preserve ET-LF sensitivity goals. The most advanced toy model takes into account the presence of soft Al6N thermal links, similar to those implemented in KAGRA [98, 149], connecting the CA to the thermal shield, combined with a heat extraction through the PF via a crystalline marionette suspension fiber with high Q_m and high thermal conductivity. The payload and cryostat dimensions, as well as the sensitivity goal in ET-LF, differ from KAGRA, implying differences in the thermal and mechanical design requirements [71, 142], which are not straightforward to define.

Figure 3.3 depicts the examined thermal heat link interface possibilities on the cryogenic payload. A simple double-stage payload with sapphire marionette and mirror suspensions is used as a reference. In the simplest case (left), the thermal link (TL) to the cryogenic system is modelled by a connection to the MA, showing a critical impact on the predicted sensitivity. A more realistic case (right) adopts a connection onto the CA and PF, ensuring sustainable mechanics of the thermal link connection. Figure 3.4 shows the effect of the soft thermal link on the STN for the cases depicted in Figure 3.3. Imposing a nominal assumption for the STN roughly comparable with that of ET-LF, it can be realized that the TL should be connected far from the TM. Figure 3.4 demonstrates that the thermal links must be connected to the CA, being the minimum distance from the mirror in order not to compromise the STN. The criticality

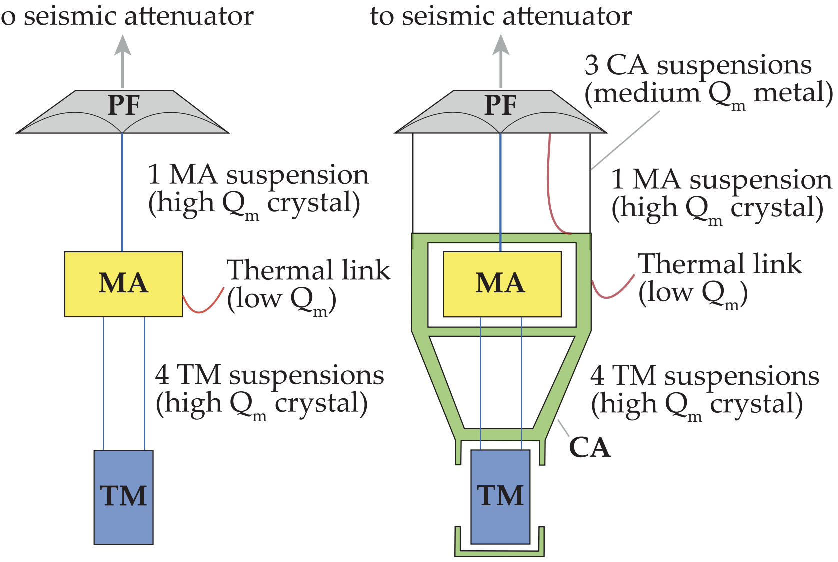

Figure 3.3: Schemes of thermal link connection possibilities onto the cryogenic payload.

is reached with the parameters mentioned in the caption of Figure 3.4. The computation is analytic, but FEA modeling provides similar results [141, 150]. A secondary but yet significant issue is the noise injection and the drag through the thermal link, which has been estimated with a similar schematic as in Figure 3.4 [143].

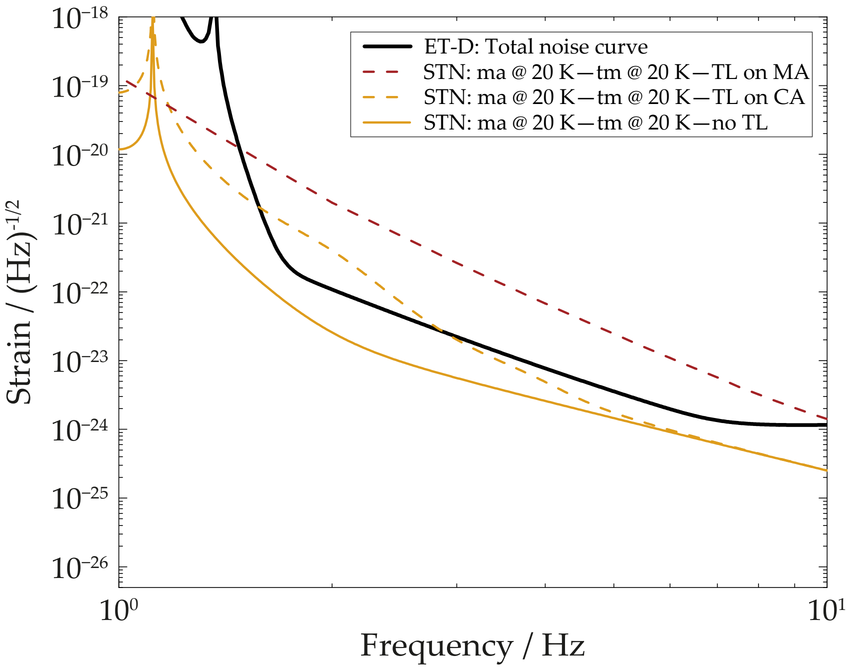

Figure 3.4: Impact on the STN due to a direct connection of a 1 m thermal link (made of 28 braids, each composed by 49 Al6N wires with $d = 150\,\mu\mathrm{m}$ [98] and assuming $\phi_{\mathrm{TL}} = 0.5$) on the MA and CA, respectively.

The outline of the solid conduction cooling through thermal links is that in order to reduce the thermal noise (cf. Section 3.1.5) induced from the link, it must be connected to the CA and cannot reach the MA. The implementation is feasible through a careful mechanical and thermal design of the payload in order to operate at $T_{\mathrm{TM}} \approx 20\,\mathrm{K}$. The monocrystalline-based concept in this paper assumes using the same material (silicon or sapphire) for the mirror, the mirror suspensions and the marionette suspension. Nonetheless, also a hybrid monocrystalline suspension application is being analyzed [151, 152].

3.1.3.2 Mechanical dimensioning

The marionette suspension is dimensioned for the total mechanical load of the MA and the TM, considering a safety factor $\mathrm{SF} = 3$ with regard to the ultimate strength $\sigma_{\mathrm{m,max}}$. The material properties listed in Table 3.3 for sapphire and silicon yield the dimensions in Table 3.2, which are used in the STN modeling in this paper. For sapphire, a very conservative value of 400 MPa is assumed, based upon [159]. Significantly higher values of breaking strength at low temperatures, spread in the range of 1000 to 2600 MPa, have been recently measured [178] and certified using samples produced in Japan by Shinkosha [179] and machined from a single ingot.

3.1.3.3 Thermal behavior

The thermal behavior depends on the thermal conductivity in the range of 10 to 30 K. In thin suspension fibers, the phonon boundary scattering may significantly reduce the bulk conductivity [180]. Thermal conductivity data for high-purity monocrystals and monocrystalline fibers of silicon and sapphire are therefore compared in Figure 3.5. In silicon fibers, a marginal reduction of thermal conductivity is visible [182], whereas a significant reduction is reported for sapphire fibers [161]. Further thermal conductivity measurements of silicon and sapphire fiber samples are planned within future R&D activities.

The nominal heat load from Equation (3.1) together with the dimensions in Table 3.2 and the thermal conductivity data of monocrystalline fibers according Figure 3.5 yield temperature gradients along the marionette suspension of $\Delta T_{\mathrm{ma}} = 3\,\mathrm{K}$ for silicon and $\Delta T_{\mathrm{ma}} = 5\,\mathrm{K}$ for sapphire, respectively.

Table 3.3: Physical properties of silicon and sapphire at 20 K and metals at 2 K. Some of the indicated references comprise temperature dependencies, which are included in the STN model presented in Sections 3.1.6 and 3.1.7.

	Silicon	Sapphire	Ti6Al4V	Titanium	Al5056[a]
T/K	20	20	2.0	2.0	2.0
ϕ_{bulk} / –	$1\cdot10^{-9}$ [153][b]	$3\cdot10^{-9}$ [154]	$1\cdot10^{-4}$ [155][c]	$1\cdot10^{-6}$ [156]	$2.5\cdot10^{-8}$ [157]
σ_{y} / MPa	230 [158][d]	400 [159][d]	1600 [160]	1200 [160]	280 [160]
$\lambda(T)$ / $\mathrm{W\,m^{-1}\,K^{-1}}$	4940 [92]	6000 [161]	0.22 [162]	2.5 [162]	2.0 [163]
$c(T)$ / $\mathrm{J\,kg^{-1}\,K^{-1}}$	3.40 [164]	0.69 [165]	0.01 [162]	0.12 [162]	0.10 [166]
$\alpha_{\mathrm{TE}}(T)$ / $\mathrm{K^{-1}}$	$-2.9\cdot10^{-9}$ [167]	$1.3\cdot10^{-8}$ [89]	$6.0\cdot10^{-6}$ [168]	$5.5\cdot10^{-8}$ [168]	$14\cdot10^{-6}$ [160]
β / $\mathrm{K^{-1}}$	$-7.9\cdot10^{-6}$ [169][e]	$-4.4\cdot10^{-6}$ [170][e]	$-4.6\cdot10^{-4}$ [171][e]	$-4.6\cdot10^{-4}$ [171][e]	$1.2\cdot10^{-4}$ [172]
E / GPa	130 [173][f]	360 [174][f]	127 [175][f]	130 [160]	81 [172]
ρ / $\mathrm{kg\,m^{-3}}$	2330 [176]	3980 [176]	4540 [162]	4540 [162]	2660 [162]
α_{surf} / m	$5\cdot10^{-13}$ [177]	$5\cdot10^{-13}$[g]	0.0	0.0	0.0

[a] Physical properties, except for ϕ_{bulk}, λ and c, are taken from Al5083 due to the lack of data at cryogenic temperatures for Al5056.

[b] Value given at $T = 10\,\mathrm{K}$ and applied in accordance with the silicon surface loss parameter reported in [177].

[c] Value given at $T = 80\,\mathrm{K}$ due to lack of data at lower temperatures.

[d] For brittle materials, the yield strength σ_{y} and the ultimate strength $\sigma_{\mathrm{m,max}}$ are nearly equivalent. The data given for 300 K tend to increase by about 10 % at cryogenic temperatures.

[e] Values in the range of 80 to 300 K; expected to decrease further at cryogenic temperatures.

[f] Data given for 300 K tend to increase by about 30 % at cryogenic temperatures.

[g] For sapphire the same surface loss parameter as silicon is assumed due to the lack of experimental data.

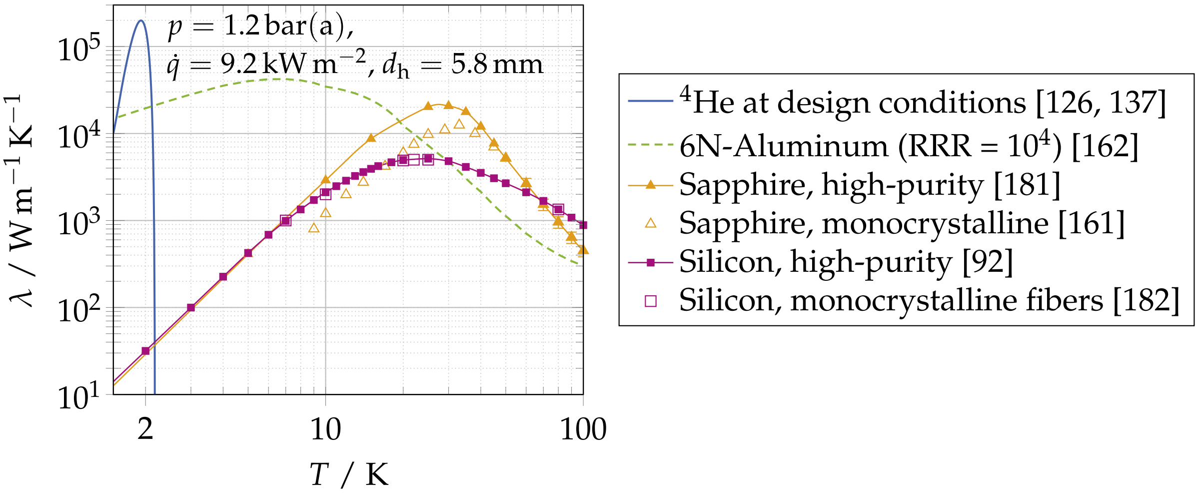

Figure 3.5: Thermal conductivity of helium compared to several high-purity solids.

3.1.4 Concept with He II-filled marionette suspension tube

3.1.4.1 Motivation for using He II

Cryogenic fluids have been extensively used to operate the second generation of resonant GW detectors [183] and later proposed for cooling the test masses of the GW interferometers [184]. The use of He II is motivated by the exceptional properties of superfluid helium, rather than its temperature around 2 K. The abundant ^{4}He isotope can exist in two liquid forms, separated by the λ-line depicted in Figure 3.6. While liquid helium at $T > T_\lambda$ (called He I) exhibits normal fluid behavior, it becomes a quantum fluid (called He II) at $T < T_\lambda$ when fractions of the atoms condense in the ground-state as a Bose-Einstein condensate [132, 185]. The He II is composed of a normal and a superfluid component, as described by the two-fluid model [130, 131]. The second-order phase transition from He I to He II is associated with dramatic property changes. Particularly relevant is the exceptional increase in thermal conductivity, yielding a thermal reservoir to absorb and conduct heat in the quietest possible manner. This property enables the concept of heat extraction from the ET-LF payload via a static He II column inside a thin-wall marionette suspension tube. For the conditions given in Figure 3.5, He II can exceed the thermal conductivity of high-purity sapphire or silicon by at least one order of magnitude. This concept provides a temperature of 2 K at the marionette, which is an essential parameter to reduce the STN as discussed in Section 3.1.6.

Related to the thermal conductivity, the quantum fluid properties may imply that thermal and mechanical dissipation in the static He II column is very low, and that momen-

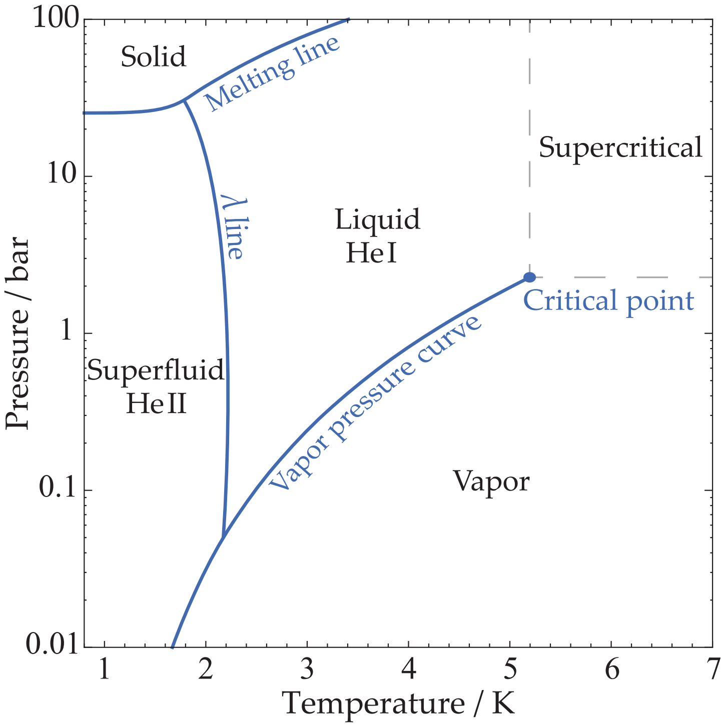

Figure 3.6: Phase diagram of ^{4}He.

tum transfer to/from the suspension tube may not take place due to superfluidity. These hypotheses, however, require experimental validation, as the integration of a quantum fluid in suspensions of GW detectors has never been analyzed and presents a new field of research.

3.1.4.2 Conceptual layout

The conceptual layout of the He II marionette suspension is depicted in Figure 3.7. In addition to the thin-wall marionette suspension tube, an internal guiding tube enables cooldown of the payload in counterflow with supercritical helium ($p > 2.3$ bar) at adjustable supply temperatures. The helium supply can be implemented at a cooling interface on the PF, using multiple thin-wall and 'soft' capillaries attached to vibration isolation systems, similar to the heat link concept in KAGRA [96, 149]. The capillaries connect the cooling interface to a cryogenic supply unit in the vicinity of the cryostat, cf. [186, 187]. Exemplary capillary dimensions are given in [188]. For steady-state operation, the normal He I is transformed in a static He II column [186]. The internal guiding tube has no function in this case—i.e. heat conduction takes place via the entire He II cross section. By contact with the He II suspension, the marionette reaches a temperature of 2 K. The silicon mirror temperature is around 15 K due to the heat load and the temperature gradient in the monocrystalline mirror suspensions.

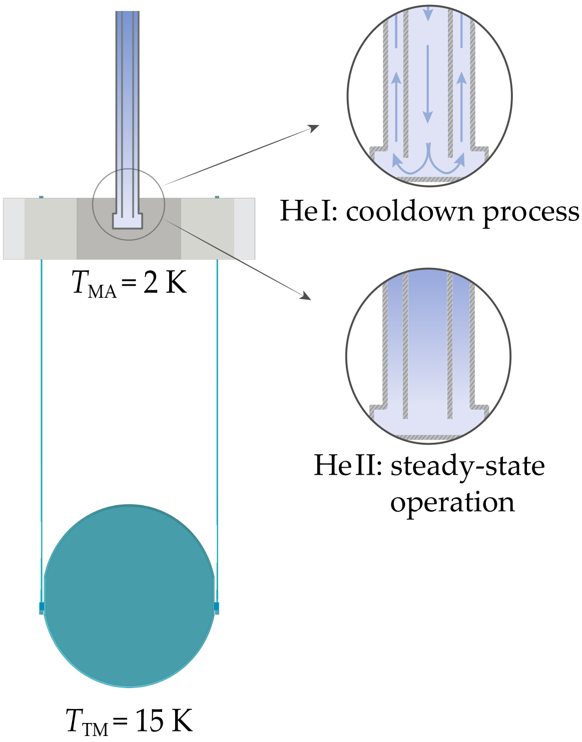

Figure 3.7: Conceptual layout of the He II marionette suspension.

3.1.4.3 Mechanical dimensioning

The marionette suspension tube carries the mechanical load of the MA and the TM. The dimensioning includes a mechanical safety factor $\mathrm{SF} = 3$ with regard to the yield strength σ_{y} of the tube material (c.f. Table 3.3 for material options). Beside low-temperature ductility and mechanical strength, a decisive constraint in the material choice is related to suspension losses. This yields a preference for titanium, as discussed in Section 3.1.6.

3.1.4.4 Thermal dimensioning

In this marionette suspension concept, the thermal dimensioning (i.e. the He II cross section) is independent from the mechanical dimensioning (i.e the suspension tube wall cross section). The two-fluid model [130, 131] describes the heat transport in static He II by a counter-flow between the normal and the superfluid components on a molecular level — i.e. there is no macroscopic movement of the bulk liquid. The most efficient laminar regime is achieved only in narrow channels of $d < 10\,\mu\mathrm{m}$, where the normal and superfluid components do not interact. In channels of $d > 1\,\mathrm{mm}$, an additional turbulent term starts dominating the temperature gradient by the excitation of rotons and a resulting mutual friction among the two components. The mutual friction signifies a dissipative process that limits the heat transport [185], but the thermal conductivity remains nonetheless higher than in pure solids as shown in Figure 3.5.

The temperature gradient along the He II column in the marionette suspension is given by

$$\Delta T_{\mathrm{ma}} = \frac{32\,\eta\,L_{\mathrm{ma}}}{(d_{\mathrm{h}}\,\rho\,s)^2\;T}\dot{q} + \frac{L_{\mathrm{ma}}}{h\left(\frac{T}{T_\lambda}\right)\,g_{\mathrm{peak}}(p)}\dot{q}^{3.4} \tag{3.2}$$

where the left term signifies the analytic description of the laminar regime [132] and the right term uses the model from Sato et al. [137] for the turbulent regime. L_{ma} denotes the marionette suspension length, η the dynamic viscosity, ρ the density and s the entropy of the He II, d_{h} refers to the hydraulic diameters of the circular and the annular cross sections shown in Fig. 3.8, $\dot{q}$ is the heat flux, and $h(T)$ and $g_{\mathrm{peak}}(p)$ are empirical functions from Sato et al. [137]. For the baseline design under nominal operating conditions, the contribution from the laminar term is negligibly small.

Defining a temperature gradient of $\Delta T_{\mathrm{ma}} = 50\,\mathrm{mK}$ with regard to the overall He II operating concept explained in [186], the suspension tube design parameters are summarized in Table 3.4. The suspension tube lower end temperature is the highest temperature in the He II system set to 1.9 K, where the thermal conductivity peak is located. The suspension tube outer diameter $d_{\mathrm{ST,o}}$ results from the required He II cross

Table 3.4: Suspension tube design parameters.

Parameter	Value
L_{ma}	1.0 m
M_{MA}	200 kg
M_{TM}	200 kg
Constraints:	
Mechanical SF	3.0
$T(z = L_{\mathrm{ma}})$	1.9 K
$p_{\mathrm{He\,II,in}}$	1.2 bar(a)
ΔT_{ma}	50 mK
$\dot{Q}_{\mathrm{c}}$	0.5 W
Design results:	
$d_{\mathrm{ST,o}}$	8.30 mm
$s_{\mathrm{ST,o}}$	0.36 mm
$d_{\mathrm{ST,i}}$	5.80 mm
$s_{\mathrm{ST,i}}$	0.05 mm

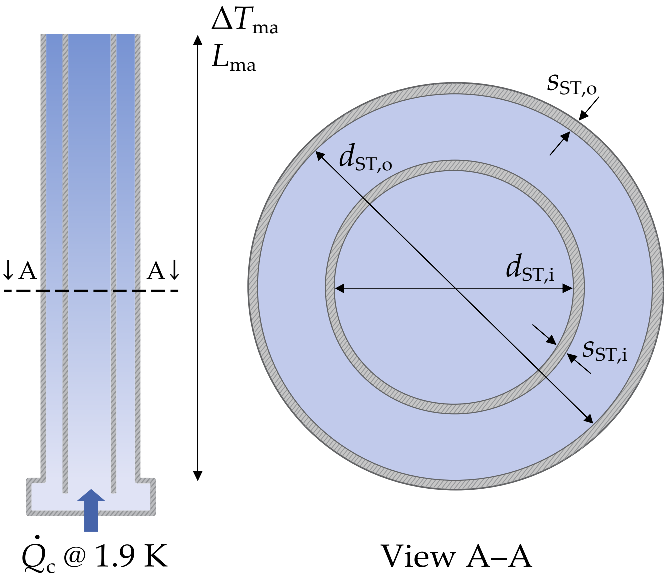

Figure 3.8: Suspension tube design.

section, whereas the wall thickness $s_\mathrm{ST,o}$ from the mechanical design. The inner guiding tube dimensions are chosen such that equal cross sections of the inner tube and the annular gap yield similar flow velocities during cooldown. Figure 3.9 shows the relation between the required suspension tube diameter $d_\mathrm{ST,o}$ and the heat load that can be extracted at $\Delta T_\mathrm{ma} = 50\,\mathrm{mK}$ and $L_\mathrm{ma} = 1\,\mathrm{m}$.

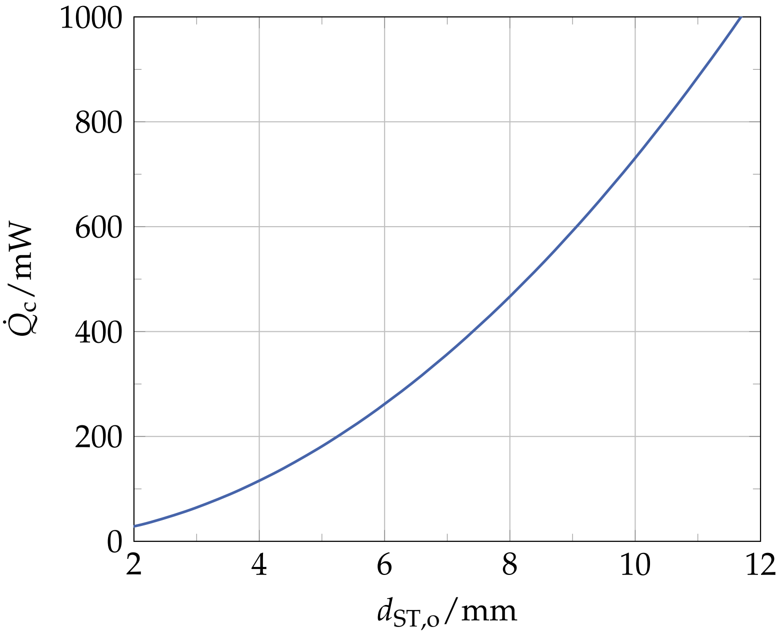

Figure 3.9: Cooling capacity of the He II suspension as function of the outer tube diameter.

3.1.4.5 Cooldown with normal He I flow

One main advantage of this concept is the ability for convective cooldown of the ET-LF payload. This is enabled by normal He I flow through the double-walled marionette suspension tube as indicated in Figure 3.7. The heat flux $\dot{q}$ from the marionette to the helium flow is correlated by

$$\dot{q} = \alpha_{\mathrm{HT}} \left(T_{\mathrm{wall}} - T_{\mathrm{He}} \right), \tag{3.3}$$

where α_{HT} denotes the heat transfer coefficient, T_{wall} the wall temperature and T_{He} the fluid temperature. Using aluminum alloy 1200 as marionette material, the marionette temperature change is given by

$$\frac{\mathrm{d}T_{\mathrm{MA}}(t)}{\mathrm{d}t} = \frac{-\dot{q} A_{\mathrm{HT}}}{c_{\mathrm{Al}}(T_{\mathrm{MA}}(t)) M_{\mathrm{MA}}} \tag{3.4}$$

where A_{HT} is the heat transfer area, $c_{\mathrm{Al}}(T)$ the specific heat capacity and M_{MA} the marionette mass. This equation simplifies the marionette as a block capacitance, neglecting the influences of finite heat conductivity. The cooldown process is therefore analyzed numerically by CFD simulation. In the model development process, simulations were set up in ANSYS Fluent® (finite volume method) and in COMSOL Multiphysics® (finite element method), allowing validation of the numerical model independence.

Simulations are carried out for the marionette and suspension design parameters in Tables 3.2 and 3.4. The suspension tube length is 1.105 m in total, of which 105 mm are centrally connected to the bottom half of the marionette, passing through a slightly wider bore in the upper half. This insertion yields a heat transfer area of $A_{\mathrm{HT}} \approx 2750\,\mathrm{mm}^2$. Table 3.5 lists additional simulation parameters and material properties in the relevant temperature range of 3.0 to 293.15 K. The 3.0 K denote the convective pre-cooling limit before the transformation to He II operation.

In the numerical model, the geometry is simplified by axial symmetry, yielding a cylindrical marionette instead of the octagonal prism shape displayed in Figure 3.2. The helium properties are implemented via REFPROP [3] in ANSYS Fluent®, and by the Peng-Robinson (Twu) equation of state [190] in COMSOL Multiphysics®, respectively. The operating conditions in Table 3.5 yield exclusively turbulent flow regimes. In order to solve the flow problems, the standard turbulence eddy viscosity k - ϵ model with renormalization group (RNG) methods developed by Yakhot et al. [191] is applied for its accuracy regarding heat transfer [192]. Scalable wall functions are implemented for the generated spatial discretization, since they enable an adequate resolution of thermally and fluid-dynamically induced effects close to the walls within the fluid domain.

Table 3.5: CFD simulation parameters and material properties of the marionette convective cooling model.

Parameter/property	Value/expression
$\dot{M}_{\mathrm{He}}$	$1.0\,\mathrm{g\,s^{-1}}$
$p_{\mathrm{He,out}}$	$2.5\,\mathrm{bar(a)}$
$T_{\mathrm{He,in}}(t)$	$\max\{\overline{T}_{\mathrm{MA}}(t) - \Delta T_{\mathrm{MA-He,in}}, 3.0\,\mathrm{K}\}$
$\Delta T_{\mathrm{MA-He,in}}$	$100\,\mathrm{K}$
$T_{\mathrm{MA}}(t = 0)$	$293.15\,\mathrm{K}$
$\overline{T}_{\mathrm{MA}}(t_{\mathrm{end}})$	$3.01\,\mathrm{K}$
d_{MA}	$700\,\mathrm{mm}$
H_{MA}	$210\,\mathrm{mm}$
A_{HT}	$2750\,\mathrm{mm^2}$
$\lambda_{\mathrm{Al}}(T)$	$59.4 \ldots 502\,\mathrm{W\,m^{-1}\,K^{-1}}$ [189]
$c_{\mathrm{Al}}(T)$	$0.29 \ldots 942\,\mathrm{J\,kg^{-1}\,K^{-1}}$ [162]
$\lambda_{\mathrm{Ti}}(T)$	$4.03 \ldots 36.0\,\mathrm{W\,m^{-1}\,K^{-1}}$ [162]
$c_{\mathrm{Ti}}(T)$	$0.20 \ldots 520\,\mathrm{J\,kg^{-1}\,K^{-1}}$ [162]

The helium supply temperature $T_{\mathrm{He,in}}$ is set as function of the average marionette temperature for controlled cooldown. A constant $\Delta T = 100\,\mathrm{K} = \overline{T}_{\mathrm{MA}}(t) - \Delta T_{\mathrm{MA-He,in}}$ is defined until the lowest helium supply temperature of 3 K is reached and held constant subsequently. The low-pressure limit of $p_{\mathrm{He,out}} = 2.5\,\mathrm{bar(a)}$ ensures supercritical single-phase flow during the entire cooldown process. The marionette and suspension tube surfaces are considered adiabatic, while the internal guiding tube is diabatic.

Figure 3.10 shows exemplary results of the CFD simulation at an intermediate time step with $\overline{T}_{\mathrm{MA}} = 103\,\mathrm{K}$ and $T_{\mathrm{He,in}} = 3\,\mathrm{K}$. At the bottom end, the helium flow is returned from the inner guiding tube to the outer annular gap. Due to internal heat exchange in the suspension, the helium supply flow is heated up by $\Delta T \approx 57\,\mathrm{K}$ before entering the marionette heat transfer area A_{HT} at $T_{\mathrm{He}} \approx 60\,\mathrm{K}$. Yet, the temperature difference between marionette and helium is still around 40 K, driving the heat extraction from the marionette. In comparison, the temperature gradients within the marionette are small due to the high thermal conductivity of aluminum alloy 1200, especially at $T < 100\,\mathrm{K}$ [189].

Results of the numerical simulation in terms of cooldown time and pressure loss are presented in Figure 3.11. The pressure loss $\Delta p_{\mathrm{He}} = p_{\mathrm{He,in}} - p_{\mathrm{He,out}}$ decreases with

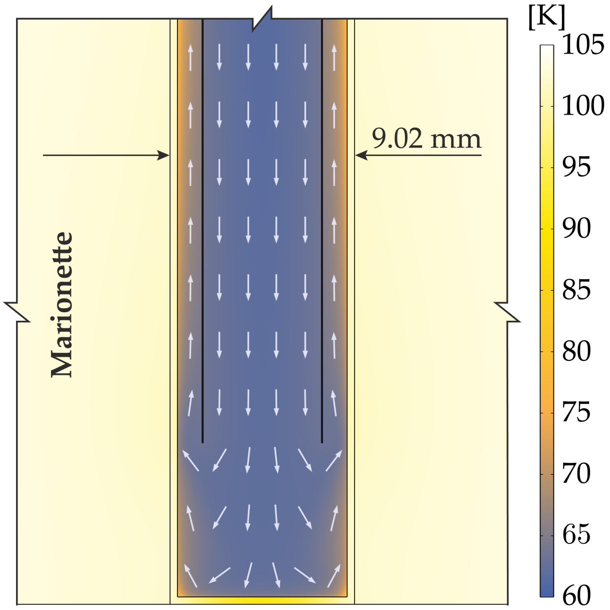

Figure 3.10: Temperature contours and velocity field in the bottom section of the marionette; intermediate results at $\overline{T}_{\mathrm{MA}} \approx 103\,\mathrm{K}$.

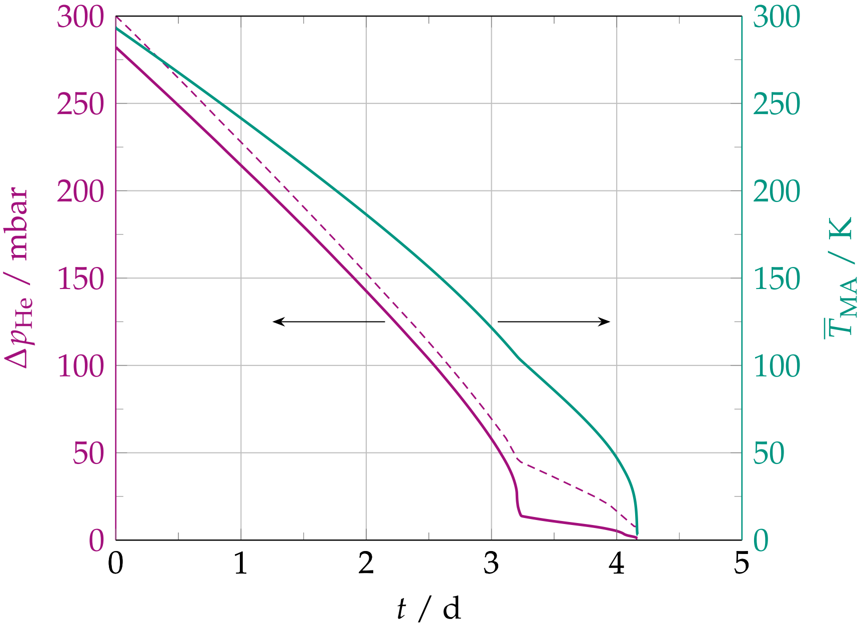

Figure 3.11: Helium pressure loss in the suspension tube and marionette temperature during cooldown for the conditions listed in Table 3.5.

temperature due to decreasing flow velocities at increasing densities. A distinct point in the cooldown curve is found at $t \approx 3.2\,\mathrm{d}$, where $T_{\mathrm{He,in}}$ reaches the low temperature limit of 3 K. Towards the end of the cooldown at $t \geq 4\,\mathrm{d}$ and $T \leq 50\,\mathrm{K}$, the marionette temperature decreases rapidly due to the T^3 dependence of specific heat capacity. The results in Figure 3.11 indicate that the marionette can be cooled from ambient to operating temperature in about 4.2 d. With a helium mass flow rate of $1\,\mathrm{g\,s^{-1}}$, the pressure drop in the suspension is $\Delta p_{\mathrm{He}} < 300\,\mathrm{mbar}$, which is compatible with the helium supply system presented in [186]. In addition to the numerical approach, the results are verified by implementing heat transfer and pressure drop correlations in a set of differential equations, yielding the dashed line for the pressure drop in Figure 3.11. A more detailed discussion of this model exceeds the scope of this paper.

In a next step, the cooldown of a silicon test mass is investigated, using the data of the marionette cooldown model to define the temperatures of the mirror suspensions at their upper ends. Radiative heat transfer is included in this model, as former studies have shown the need of combined convective and radiative cooling to achieve sufficient cooldown rates [187]. The simulation data are summarized in Table 3.6. Conservative assumptions are made for the emissivity of silicon with $\epsilon_{\mathrm{TM,Si}} = 0$ at $T < 120\,\mathrm{K}$ and $\epsilon_{\mathrm{TM,Si}} = 0.75$ at $T > 260\,\mathrm{K}$, respectively, due to the lack of data. Thermal radiation is implemented from the test mass to a surrounding black body at $T = 5\,\mathrm{K}$ starting at $t = 0$, representing the thermal shield operation around the payload [186]. Figure 3.12 contains the simulation results, showing that the silicon test mass can be cooled from ambient to operating temperature in about 12.8 d. The first phase at $t < 5.2\,\mathrm{d}$ is driven by thermal radiation, where temperature differences between the test mass and the shield are large, and the marionette cooldown is yet in progress. In the second phase, thermal radiation is effectively disabled with $\epsilon_{\mathrm{TM,Si}} = 0$. The heat extraction from the test mass occurs exclusively via the test mass suspension fibers to the helium-cooled marionette. Towards the cooldown end, this mechanism is amplified by increasing thermal conductivity values of silicon and the strongly decreasing heat capacity.

Table 3.6: Simulation parameters used in the test mass cooldown model.

Parameter	Value
M_{TM}	200 kg
d_{TM}	450 mm
H_{TM}	570 mm
d_{tm}	3.0 mm
L_{tm}	1.2 m
T_{Shield}	5.0 K
$\epsilon_{\mathrm{TM,Si}}(T)$	0.41 . . . 0.75 [193][a]
$\lambda_{\mathrm{Si}}(T)$	2330 . . . 5130 $\mathrm{W\,m^{-1}\,K^{-1}}$ [92]
$c_{\mathrm{Si}}(T)$	0.28 . . . 707 $\mathrm{J\,kg^{-1}\,K^{-1}}$ [194]

[a] Range represents values from 120 to 260 K for a sample with dimensions 70 mm × 30 mm × 103.5 mm

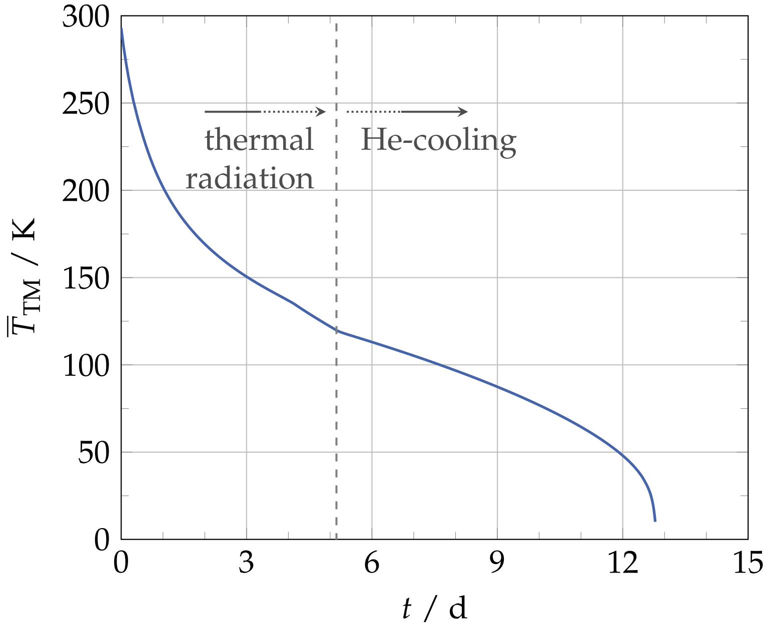

Figure 3.12: Cooldown of an ET-LF silicon test mass installed within a thermal shield at $T = 5\,\mathrm{K}$ for the conditions listed in Tables 3.5 and 3.6.

3.1.5 Modelling of suspension thermal noise

3.1.5.1 Theoretical foundations

Thermal noise is a thermally driven motion, which is directly related to the mechanical dissipative behavior of a system. Since thermal noise is a generalized type of Brownian motion with a random displacement of particles, it can be described using the fluctuation-dissipation theorem (FDT) [195]. It states that the dissipations in the system are the driving force for thermal fluctuations, which are presented in form of a displacement spectral density. The FDT is able to include the contributions of various dissipative sources, using an equivalent macroscopic mechanical model that describes the total impedance of the system in the frequency domain [196]. The theoretical foundations and further details of thermal noise modeling in mechanical systems, especially for suspensions used in gravitational wave detectors, are explained in [147, 196–200]. The general approach can be summarized by the following steps:

(1) Choice of the representative mechanical model and the dissipation mechanisms affecting the system.

(2) Definition of the one-dimensional equation of motion for the mechanical displacement $x(t)$ and its Fourier transform $X(\omega)$.

(3) Definition of the mechanical impedance $Z(\omega)$ and its inverse, the admittance $Y(\omega)$. $Z(\omega)$ is the ratio between the Fourier transforms of the applied force and system velocity and is calculated by applying an external force on the system and inspecting its reaction based on its equation of motion:

$$Z(\omega) \equiv \frac{F}{i\omega X(\omega)} \quad \text{and} \quad Y(\omega) \equiv [Z(\omega)]^{-1} . \tag{3.5}$$

(4) Calculation of the thermal noise spectral density based on the FDT:

$$S_{\mathrm{xx}}(\omega) = \frac{4k_{\mathrm{B}}T}{\omega^2} \cdot \mathrm{Re}\left([Z(\omega)]^{-1}\right) , \tag{3.6}$$

where k_{B} is the Boltzmann constant, T the suspension temperature and ω the angular frequency.

3.1.5.2 Dissipation in a pendulum system

Energy dissipation in a mechanical system can arise from various sources, contributing directly to the generation of thermal noise [147]. The dissipation is quantified by the loss angle ϕ, representing the ratio between the imaginary and the real restoring force in the system [201].

The suspension thermal noise model in this paper considers the ET-LF payload as a double pendulum, with MA and TM as point-masses and suspensions with homogeneous mechanical losses. The loss angle of a suspension includes the summation of different dissipation mechanisms as

$$\phi_{\mathrm{susp}}(\omega) = \phi_{\mathrm{bulk}} + \phi_{\mathrm{therm}}(\omega) + \phi_{\mathrm{surf}} + \phi_{\mathrm{join}} . \tag{3.7}$$

Bulk losses, ϕ_{bulk}, designate intrinsic dissipations in the bulk material. These losses arise from the structural composition and from defects in the material, depending on temperature and frequency [148]. The frequency dependence is usually considered negligible and the temperature-dependence is determined experimentally [202]. For the ET-LF marionette suspension, several materials are proposed as depicted in Tables 3.2 and 3.3. Their bulk losses at cryogenic temperatures are summarized in Table 3.7. For the mirror suspensions, the proposed materials include monocrystalline silicon or sapphire. The bulk loss angles applied in this STN model are summarized in Table 3.3.

Table 3.7: Bulk loss angles ϕ_{bulk} of various materials at cryogenic temperatures.

Material	Type/treatment	T / K	ϕ_{bulk} / –
Silicon	Single crystal (100) [153]	3.5	$5 \cdot 10^{-10}$
		10	$1 \cdot 10^{-9}$
		20	$3 \cdot 10^{-9}$
Silicon	Single crystal (100) [146]	10	$5 \cdot 10^{-9}$
		20	$8 \cdot 10^{-9}$
Silicon	Single crystal (100) [203]	18	$5 \cdot 10^{-9}$
Silicon	Single crystal (111) [146]	10	$1.1 \cdot 10^{-8}$
		20	$1.2 \cdot 10^{-8}$
Sapphire	Single crystal, annealed [154]	10	$2 \cdot 10^{-9}$
		20	$3 \cdot 10^{-9}$
Sapphire	Single crystal, annealed [204]	4.0	$2 \cdot 10^{-10}$
		10	$1 \cdot 10^{-9}$
		20	$3 \cdot 10^{-9}$
Sapphire	Hemlite Grade [205]	4.2	$4 \cdot 10^{-9}$
		10	$5 \cdot 10^{-9}$
		20	$5.6 \cdot 10^{-9}$
Titanium	Grade 1, annealed [156]	1...20	$6 \cdot 10^{-7}$
Titanium	Grade 1, stress-relieved [156]	1...20	$1 \cdot 10^{-6}$
Titanium	Grade 1, untreated [156]	1...20	$1 \cdot 10^{-6}$
Titanium	Grade 2 [206]	4.2	$5 \cdot 10^{-7}$
		20	$1 \cdot 10^{-6}$
Ti6Al4V	Grade 5 [155]	80	$1 \cdot 10^{-4}$
Al5056	untreated [207]	2.0	$6 \cdot 10^{-8}$
Al5056	annealed [207, 208]	2.0	$2.5 \cdot 10^{-8}$
Al5056	··· [34]	2.0	$1.6 \cdot 10^{-7}$

Thermoelastic losses, ϕ_{therm}, are frequency-dependent losses occurring in a suspension under tension, characterized by a broad maximum at a characteristic frequency [147, 209]. These losses originate from local temperature gradients generated by the compression and expansion at the suspension bending point. These gradients induce a heat flux that is accompanied with entropy generation (i.e. energy dissipation) [90, 177]. For modeling, [90] proposes to consider both a contribution from the linear expansion coefficient α_{TE}, and a non-linear contribution from the temperature dependence of the Young's modulus E via the thermal elastic coefficient $\beta = {}^{\mathrm{d}\ln E}/_{\mathrm{d}T}$

$$\phi_{\mathrm{therm}}(\omega) = \frac{ET}{\rho c}\left(\alpha_{\mathrm{TE}} - \sigma_{\mathrm{m}}\frac{\beta}{E}\right)^2 \left(\frac{\omega\tau}{1+(\omega\tau)^2}\right) , \tag{3.8}$$

with σ_{m} as the suspension tension and τ as the thermal diffusion time, for a circular suspension given as [210]

$$\tau = \frac{d^2\rho c}{13.55\lambda} , \tag{3.9}$$

with d as the suspension diameter and λ as the thermal conductivity of the suspension material. This type of losses depends on geometry and tension (cf. Equation (3.8)). Thus, a reduction or nullification via an optimized suspension profile design, as applied in silica suspensions in current detectors, could be possible [158].

Surface losses, ϕ_{surf}, are mechanical losses in a thin surface layer h_{s}, the dissipation depth, which differ from the bulk losses [177, 211]. These depend on the surface quality and on treatment techniques (e.g. polishing, dry or wet chemical etching), but are generally not yet fully understood [204]. ϕ_{surf} are determined from experimental data, using the surface loss parameter $\alpha_{\mathrm{surf}} = h_{\mathrm{s}}\phi_{\mathrm{bulk}}$. The relation between ϕ_{surf}, α_{surf}, the geometry factor μ, the surface area A_{surf} and the volume V is given by [211] and simplified for thin circular fibers with $\mu = 2$ to

$$\phi_{\mathrm{surf}} = \alpha_{\mathrm{surf}}\frac{\mu A_{\mathrm{surf}}}{V} = h_{\mathrm{s}}\phi_{\mathrm{bulk}}\frac{8}{d} \tag{3.10}$$

This equation shows that surface losses become increasingly relevant with higher surface-to-volume ratio.

Jointing losses, ϕ_{join}, are additional mechanical losses resulting from the clamping between the suspensions and their anchors. The minimization of these losses requires dedicated numerical simulations including the real payload geometry alongside experimental validation [212]. Equivalently to the ET conceptual design study [2] and the design report update [71], this type of loss requires a more advanced design and is hence not yet considered in the model.

3.1.5.3 Dynamic behavior of the pendulum system

The suspension thermal noise modeling requires the mechanical impedance $Z(\omega)$ of the payload derived from the equations of motion as given in Equation (3.6). The double pendulum system representing the ET-LF payload is depicted in Figure 3.13. It is modeled as a double mode oscillator with a stiffness constant for each pendulum stage [147, 200]. The equations of motion in the frequency domain are given as

$$\begin{aligned} 0 &= -M_{\mathrm{MA}}\omega^2 X_{\mathrm{ma}} + k_{\mathrm{ma}} X_{\mathrm{ma}} + k_{\mathrm{tm}}(X_{\mathrm{ma}} - X_{\mathrm{tm}})\,, \qquad (3.11)\\ F &= -M_{\mathrm{TM}}\omega^2 X_{\mathrm{tm}} + k_{\mathrm{tm}}(X_{\mathrm{tm}} - X_{\mathrm{ma}})\,, \qquad (3.12)\end{aligned}$$

where F is an external force applied onto the mirror stage. The spring constants k_{ma} and k_{tm} of the marionette and the mirror stages, respectively, are calculated via the representative mechanical system of each pendulum stage. González [199] provides a detailed summary of mechanical models applicable to suspensions used in gravitational wave detectors.

The *marionette stage* is modeled using a simple pendulum with a suspended point mass, considering a lossless gravitational potential and a lossy elastic potential as the only energy sources. The latter is a simplified treatment to introduce dissipation, given that the violin modes of the marionette suspension have been shown to have a negligible impact compared to the dominating ones of the mirror suspensions. Hence, the marionette violin modes do not need to be considered in the dynamics of the representative system. The marionette spring constant k_{ma} is obtained from the lossless

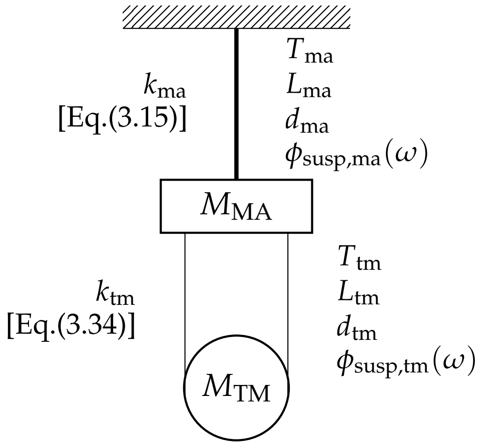

Figure 3.13: Scheme of the representative mechanical system used to model the STN of the ET-LF payload (ma = marionette suspension, MA = marionette, tm = test mass suspension, TM = test mass).

gravitational spring constant k_g and the lossy elastic spring constant k_el via

$$k_\mathrm{ma} = k_\mathrm{g} + k_\mathrm{el}(1 + i\phi_\mathrm{susp}(\omega)) \ . \tag{3.13}$$

Introducing the dilution factor D, which depicts the ratio between the system's elastic and gravitational potential energies [147, 201], as

$$D = \frac{k_\mathrm{el}}{k_\mathrm{g}} = \frac{n\sqrt{EI\sigma_\mathrm{m}}}{2L^2}\frac{L}{Mg_0} = \frac{1}{2L}\sqrt{\frac{nEI}{Mg_0}} \ , \tag{3.14}$$

with M as the total mass suspended by n wires, σ_m as the tension in each wire, I as the area moment of inertia, g_0 as the gravitational acceleration, and L as the suspension length, k_ma yields [213]

$$k_\mathrm{ma} = k_\mathrm{g}(1 + D + i\phi_\mathrm{pend}(\omega)) \ . \tag{3.15}$$

The definition of the pendulum loss angle $\phi_\mathrm{pend}(\omega)$ in Equation (3.16) shows that the pendulum losses are lower than the suspension losses ϕ_susp according Equation (3.7) due to dilution via D

$$\phi_\mathrm{pend}(\omega) = \phi_\mathrm{susp}(\omega)D \ . \tag{3.16}$$

The equation of motion for the marionette stage includes only a complex spring potential

$$-k_\mathrm{ma}x(t) = M_\mathrm{MA}\frac{\partial^2 x(t)}{\partial t^2} \ , \tag{3.17}$$

yielding in the frequency domain $[x(t) \rightarrow X(\omega) \cdot e^{i\omega t}]$

$$k_\mathrm{ma}X(\omega) - M_\mathrm{MA}\omega^2 X(\omega) = 0 \ . \tag{3.18}$$

The *mirror stage* is modeled using a pendulum consisting of four anelastic suspension fibers suspending a point mass. Thus, in addition to the pendulum's degree of freedom (d.o.f.), from which the pendulum mode is extracted, also the degrees of freedom related to the transverse motion along the suspension are included in order to obtain the infinite series of violin modes associated to its bending [198, 199, 213].

The effective mirror spring constant k_tm associated to the suspension elasticity and gravitational restoring force is derived by solving the elastic equation for a slightly deflected suspension stretched by a tension σ_m [199, 213]

$$-E_\mathrm{cx}I\frac{\partial^4 x(z,t)}{\partial z^4} + \sigma_\mathrm{m}\frac{\partial^2 x(z,t)}{\partial z^2} = \rho S\frac{\partial^2 x(z,t)}{\partial t^2} \ . \tag{3.19}$$

The introduction of the Fourier transform of the displacement $X(z, \omega)$ yields

$$E_{\mathrm{cx}} I \frac{\partial^4 X(z,\omega)}{\partial z^4} - \sigma_{\mathrm{m}} \frac{\partial^2 X(z,\omega)}{\partial z^2} - \rho A_{\mathrm{cross}} \omega^2 X(z,\omega) = 0 \,, \tag{3.20}$$

with A_{cross} as the cross-sectional area of the suspension. The complex Young's modulus E_{cx} introduces the dissipation into the system as

$$E_{\mathrm{cx}} = E(1 + i\phi_{\mathrm{susp}}(\omega)) \,. \tag{3.21}$$

The general solution of Equation (3.20) yields the displacement of the suspension $X(z, \omega)$ along the suspension axis z

$$X(z,\omega) = C_1 \sin(k_{\mathrm{s}} z) + C_2 \cos(k_{\mathrm{s}} z) + C_3 e^{k_{\mathrm{e}} z} + C_4 e^{-k_{\mathrm{e}} z} \tag{3.22}$$

with k_{s} as the wave number associated to the flexural stiffness of the suspension [198, 214]

$$k_{\mathrm{s}} = \sqrt{\frac{\sigma_{\mathrm{m}} + \sqrt{{\sigma_{\mathrm{m}}}^2 + 4 E_{\mathrm{cx}} I \rho A_{\mathrm{cross}} \omega^2}}{2 E_{\mathrm{cx}} I}} \,, \tag{3.23}$$

and k_{e} as the wave number of an elastic fiber

$$k_{\mathrm{e}} = \sqrt{\frac{-\sigma_{\mathrm{m}} + \sqrt{{\sigma_{\mathrm{m}}}^2 + 4 E_{\mathrm{cx}} I \rho A_{\mathrm{cross}} \omega^2}}{2 E_{\mathrm{cx}} I}} \,, \tag{3.24}$$

where the constants C_1 to C_4 are defined from the system boundary conditions. For simplicity, henceforth the frequency dependency of $X(z, \omega)$ is dropped.

The first two boundary conditions result from the upper part of the suspension at $z = 0$, where the fixed clamping on the marionette yields

$$X(0) = 0 \quad \text{and} \quad \frac{\partial X}{\partial z}(0) = 0 \,. \tag{3.25}$$

The third and the fourth boundary conditions are associated with the bottom part at $z = L_{\mathrm{tm}}$, where the mirror is attached and foregoes a displacement of X_0

$$\begin{aligned} X(L_{\mathrm{tm}}) &= X_0 \,, && (3.26) \\ \frac{\partial X}{\partial z}(L_{\mathrm{tm}}) &= 0 \quad \text{or} \quad \frac{\partial^2 X}{\partial z^2}(L_{\mathrm{tm}}) = 0 \,. && (3.27) \end{aligned}$$

Assuming the mirror as a lumped mass causes the suspension slope at the bottom to be a free parameter [199]. Somiya [214] reports how this boundary condition can be defined for different mirror positioning approaches. In the case of the mirror facing in the beam direction, the suspension bends at the attachment point yielding $\frac{\partial X}{\partial z}(L_{\mathrm{tm}}) = 0$

[213]. This condition is applied in this paper, equivalently to the ET-LF design in [71]. After defining the suspension displacement function $X(z)$ according Equation (3.22), the effective mirror spring constant k_{tm} can be derived by applying an external force F on the suspended mass at $z = L_{\mathrm{tm}}$ [198, 213]. From the equation of motion of a lumped mass

$$E_{\mathrm{cx}} I \frac{\partial^3 X}{\partial z^3}(L_{\mathrm{tm}}) - \sigma_{\mathrm{m}} \frac{\partial X}{\partial z}(L_{\mathrm{tm}}) - M_{\mathrm{TM}} \omega^2 X(L_{\mathrm{tm}}) = F \,, \tag{3.28}$$

and $\frac{\partial X}{\partial z}(L_{\mathrm{tm}}) = 0$ as boundary condition, the mirror spring constant k_{tm} for four suspensions is given by Equation (3.34).

The mechanical impedance $Z_{\mathrm{horz}}(\omega)$, needed for the STN calculation in Equation (3.6), is defined by the equations of motion for the double pendulum system, presented in matrix form in Equation (3.35). Through this motion matrix, the mechanical impedance $Z_{\mathrm{horz}}(\omega)$ is obtained from Equation (3.36). The spring constants k_{ma} and k_{tm} implemented in our STN model are taken from Equations (3.15) and (3.34).

The system dynamics described above refer to the horizontal d.o.f., representing the dominant source for the STN. Nonetheless, the vertical d.o.f. delivers also a non-negligible contribution to the STN and is included in the model. The approach for modeling the vertical impedance $Z_{\mathrm{vert}}(\omega)$ is analogous to the algorithm above, whereby both the marionette and mirror stages are represented via simple pendulum systems, whose vertical spring constants are given by [213]

$$k_{\mathrm{tm,vert}} = \frac{4 E_{\mathrm{tm}} A_{\mathrm{cross,tm}}}{L_{\mathrm{tm}}}(1 + i\phi_{\mathrm{susp,tm}}) \,, \tag{3.29}$$

$$k_{\mathrm{ma,vert}} = (2\pi \cdot 0.4\,\mathrm{Hz})^2 M_{\mathrm{MA+TM}}(1 + i\phi_{\mathrm{susp,ma}}) \tag{3.30}$$

The vertical spring constant for the marionette suspension can be evaluated as a set of two springs connected in series, namely the marionette suspension itself and the spring blades at its upper part. The resulting vertical spring constant is dominated by the soft magnetic spring blades of the superattenuator system. The value 0.4 Hz in Equation (3.30) refers to the natural frequency measured for the magnetic anti-spring blades in AdVirgo [213]. Similar spring blades are assumed in this model for ET-LF.

Finally, the overall STN spectral density is

$$S_{\mathrm{xx,total}}(\omega) = S_{\mathrm{xx,horz}}(\omega) + {\theta_{\mathrm{vh}}}^2 S_{\mathrm{xx,vert}}(\omega) \,, \tag{3.31}$$

where θ_{vh} is the vertical-to-horizontal coupling factor. Weak coupling of vertical motion into horizontal motion results from the non-parallel alignment of the test masses at the ends of the interferometer arms due to the Earth's curvature. For a 10 km ET-LF arm, θ_{vh} yields

$$\theta_{\mathrm{vh}} = \frac{L_{\mathrm{arm}}}{d_{\mathrm{Earth}}} = 7.8 \cdot 10^{-4} \,. \tag{3.32}$$

3.1.5.4 Implementation of temperature distribution

For systems including nonuniform temperatures, the STN is usually modeled using the normal modal approach [2, 71, 213], as the standard FDT assumes a single homogeneous temperature level in the whole system, as seen in Equation (3.6). The modal approach can be a heavy computational task [215] and includes only homogeneous dissipation. To include inhomogeneuos losses, Levin [197] introduces an extended formulation of the standard FDT. Komori et al. [216] propose a discrete version of this extended FDT, which can be applied for STN modeling of systems with inhomogeneous temperature, such as cryogenic payloads. This approach foresees the discretization of the system into elements, where each element is associated with a homogeneous temperature and an individual mechanical impedance, where the thermal noise spectral density sensed by the element j of the system is given by [216]

$$S_{\mathrm{xx}}(\omega) = \frac{2k_{\mathrm{B}}}{\omega^2} \sum_j T_j Z^{-1}(Z_{\mathrm{j}} + Z_{\mathrm{j}}{}^{\dagger}) Z^{-1\dagger} \,. \tag{3.33}$$

The STN model in this paper uses the discrete FDT approach for modeling the cryogenic payload consisting of two elements (i.e., mirror stage and marionette stage). Here homogeneous losses and a constant temperature along the suspensions, namely the highest temperatures at the lower ends, are assumed.

$$\begin{aligned} k_{\mathrm{tm}} &= \frac{-E_{\mathrm{cx}} I \frac{\partial^3 X}{\partial z^3}(L_{\mathrm{tm}})}{X(L_{\mathrm{tm}})} \\ &= \frac{4E_{\mathrm{cx}} I k_{\mathrm{s}} k_{\mathrm{e}} (k_{\mathrm{s}}{}^3 \cos(k_{\mathrm{e}} L_{\mathrm{tm}}) + k_{\mathrm{s}}{}^2 k_{\mathrm{e}} \sin(k_{\mathrm{e}} L_{\mathrm{tm}}) + k_{\mathrm{e}}{}^3 \sin(k_{\mathrm{e}} L_{\mathrm{tm}}))}{(k_{\mathrm{s}}{}^2 - k_{\mathrm{e}}{}^2) \sin(k_{\mathrm{e}} L_{\mathrm{tm}}) - 2k_{\mathrm{s}} k_{\mathrm{e}} \cos(k_{\mathrm{e}} L_{\mathrm{tm}})} \end{aligned} \tag{3.34}$$

$$\begin{bmatrix} k_{\mathrm{ma}} + k_{\mathrm{tm}} - M_{\mathrm{MA}}\omega^2 & -k_{\mathrm{tm}} \\ -k_{\mathrm{tm}} & k_{\mathrm{tm}} - M_{\mathrm{TM}}\omega^2 \end{bmatrix} \begin{bmatrix} X_{\mathrm{ma}} \\ X_{\mathrm{tm}} \end{bmatrix} = \begin{bmatrix} 0 \\ F \end{bmatrix} \tag{3.35}$$

$$Z_{\mathrm{horz}}(\omega) = \frac{1}{i\omega} \begin{bmatrix} k_{\mathrm{ma}} + k_{\mathrm{tm}} - M_{\mathrm{MA}}\omega^2 & -k_{\mathrm{tm}} \\ -k_{\mathrm{tm}} & k_{\mathrm{tm}} - M_{\mathrm{TM}}\omega^2 \end{bmatrix} \tag{3.36}$$

Figure 3.13 illustrates the main modeling parameters implemented for the marionette and mirror suspensions. This conservative approach reduces computational effort, as

---

[†] Complex conjugate and transposed matrices

results from KAGRA [216] show that including the temperature gradients along the suspensions in the STN model has a negligible impact.

3.1.6 Sensitivity of the baseline design

Using the STN model of Section 3.1.5 with the parameters in Tables 3.2 and 3.3, the STN curves of the baseline design options are depicted in Figure 3.14. Both the monocrystalline and the He II-filled marionette suspension concepts fulfill the sensitivity requirements of the ET-D curve [2]. The combination of a He II-filled marionette suspension with a sapphire mirror yields STN values similar to the monolithic sapphire marionette concept and is therefore not displayed.

When comparing the three STN curves of the baseline design in Figure 3.14 with the suspension losses from Equation (3.7), plotted for various materials in Figure 3.15, two major conclusions can be drawn:

(1) The suspension loss angle ϕ_{susp}, especially of the mirror suspensions, has a crucial impact on the STN, yielding the difference between silicon and sapphire in the monocrystalline concepts.

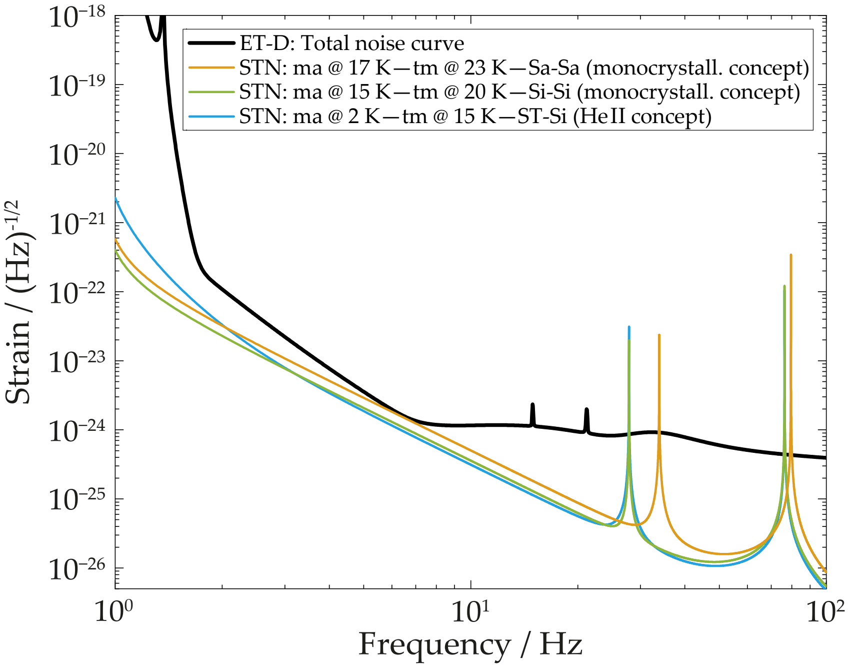

Figure 3.14: STN of the baseline design for the monocrystalline and He II–based marionette cooling concepts (Sa = sapphire, Si = silicon, ST = He II suspension tube).

(2) The lower marionette suspension temperature T_{ma} compensates higher marionette suspension losses ϕ_{susp} in the He II filled titanium suspension tube, yielding results similar to the monocrystalline silicon suspension concept in the range of 3 to 30 Hz.

The latter effect can be deduced from the thermal noise of a simple harmonic oscillator far from its resonance (pendulum mode) at $\omega \gg \omega_0$ [147] as

$$S_{\mathrm{xx}}(\omega) \propto T\phi_{\mathrm{susp}} \, . \tag{3.37}$$

When approaching the pendulum peak $\omega \approx \omega_0$, however, the impact of ϕ_{susp} dominantes the STN, which is visible at 1 Hz in Figure 3.14.

Various values for the bulk loss angle ϕ_{bulk} of monocrystalline silicon and sapphire have been reported at cryogenic temperatures, see Table 3.7. This implies the necessity for R&D to refine the confidence interval of the data, which are immensely affected from the experimental setup. In this work, ϕ_{bulk} values of $1{\cdot}10^{-9}$ and $3{\cdot}10^{-9}$ have been applied for silicon and sapphire, respectively. Given the crucial influence of this parameter, as also presented in Section 3.1.7, these values should be revised accordingly based on future R&D.

The thermoelastic losses of silicon and sapphire at $T \leqslant 25\,\mathrm{K}$ are negligible compared to the dominant bulk losses in ϕ_{susp}, as depicted for 20 K in Figure 3.15. Further investigations on surface losses of treated, strength-improved monolithic silicon and sapphire crystals are crucial, in order to use reliable values in the model, because especially in small-scale structures such as suspensions, these losses can be a significant source [158, 177]. For thin silicon flexures, Nawrodt et al. [177] report a surface loss parameter α_{surf} of $5 \cdot 10^{-13}\,\mathrm{m}$ at $T = 10\,\mathrm{K}$, yielding a dissipation depth of $h_{\mathrm{s}} = 5 \cdot 10^{-4}\,\mathrm{m}$. For sapphire, currently the surface loss parameter has not been investigated; hence, it is assumed to be equal to that of silicon. In this model, for both silicon and sapphire suspensions a value of $\alpha_{\mathrm{surf}} = 5 \cdot 10^{-13}\,\mathrm{m}$ is applied.

In the He II concept, only losses in the titanium suspension tube are being considered so far. An additional contribution may originate from the static superfluid. Though the He II dissipation is expected to be minor, this may change when the relative velocity between the two fluid components exceeds a critical value [134, 217]. Above this critical velocity, a tangle of quantized vortices arises. Then an extra term, due to the interaction of the quantum vortices with the normal fluid should appear in addition to that of the viscous normal component. Since the ratio between the superfluid and the normal component is a function of temperature, the whole He II contribution to the

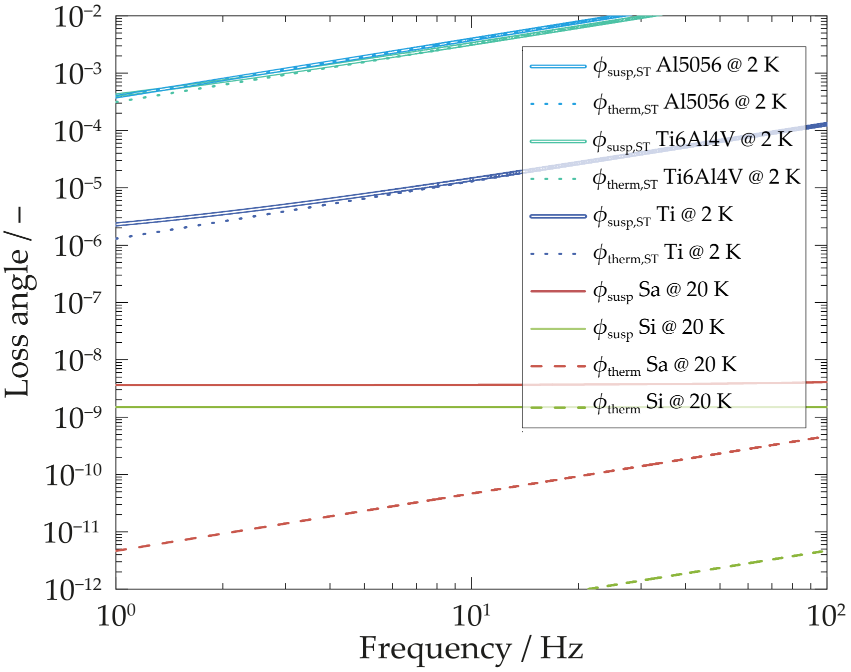

Figure 3.15: ϕ_{susp} (Equation (3.7)) and ϕ_{therm} (Eq. (3.8)) of the marionette suspension for metallic suspension tubes (ST) and for monolithic silicon and sapphire suspensions, with design parameters from Table 3.2.

dissipation has to be investigated in future experiments, both in terms of frequency and temperature [218].

In metals, ϕ_{therm} represents the dominant loss contribution to ϕ_{susp}, cf. Figure 3.15. Here, especially the parameters α_{TE} and β are decisive. Compared to the other metals, titanium induces the lowest suspension losses, hence it is the proposed material for the suspension tube design. In this model, β_{Ti} is conservatively set equal to $\beta_{\mathrm{Ti6Al4V}} = -4.6 \cdot 10^{-4}$, instead of $-1.9 \cdot 10^{-5}$ as reported in [219]. For the bulk losses, the conservative value of $\phi_{\mathrm{bulk}} = 1 \cdot 10^{-6}$ at 2 K is used for the titanium suspension tube. A contribution from ϕ_{surf} is neglected, because the surface treatment and finishing technologies in metals are usually expected to provide a high-quality surface and hence a minor ϕ_{surf}. The cross-sectional area of the marionette suspension tube,

$$A_{\mathrm{cross,ST}} = \pi \left(\frac{d_{\mathrm{ST,o}}}{2} + s_{\mathrm{ST,o}} \right)^2 - \pi \left(\frac{d_{\mathrm{ST,o}}}{2} \right)^2 , \tag{3.38}$$

is implemented in the evaluation of the tension in Equation (3.8)

$$\sigma_{\mathrm{m}} = \frac{M_{\mathrm{MA+TM}}\, g_0}{A_{\mathrm{cross,ST}}} , \tag{3.39}$$

and converted to an equivalent diameter

$$d_{\mathrm{ST}} = \sqrt{\frac{4A_{\mathrm{cross,ST}}}{\pi}}\,, \tag{3.40}$$

to be applied in Equation (3.9). The suspension tube area moment of inertia used in Equation (3.14) is

$$I_{\mathrm{ST}} = \frac{\pi}{4}\left[\left(\frac{d_{\mathrm{ST,o}}}{2} + s_{\mathrm{ST,o}}\right)^4 - \left(\frac{d_{\mathrm{ST,o}}}{2}\right)^4\right]. \tag{3.41}$$

3.1.7 Parameter study

3.1.7.1 General

This section presents a study of various payload design parameters that influence the STN in the ET-LF frequency range. We use the He II-filled marionette suspension concept with a silicon mirror as a reference, because variations of other design parameters do not affect the temperature $T_{\mathrm{ma}} = T_{\mathrm{MA}} = 2\,\mathrm{K}$ in this case. Therefore, effects of different mirror suspension designs can be better discriminated. The applied physical property data are summarized in Table 3.3. For a consistent comparison, the analysis considers the resulting mirror temperatures $T_{\mathrm{tm}} = T_{\mathrm{TM}}$ due to the parameter variations—i.e., a mechanical dimensioning and a thermal modeling is applied prior to each STN modeling. The results of the parameter study are visualized in Figures 3.16 and 3.17 in the frequency range of 0.3 to 100 Hz in order to include the impact on the pendulum modes below 1 Hz.

3.1.7.2 Influence of the mirror suspension design

The mirror suspension design determines the STN in the frequency range above 10 Hz, especially due to the violin and the vertical modes, but it also impacts the sensitivity at lower frequencies. Variations of the mirror suspension temperature, length, diameter and bulk losses are investigated.

With $T_{\mathrm{ma}} = T_{\mathrm{MA}} = 2\,\mathrm{K}$, the temperature $T_{\mathrm{tm}} = T_{\mathrm{TM}}$ is a function of the heat load. Around the design target from Eq. (3.1), heat loads of 0.1 W, 0.5 W and 1.0 W yield silicon mirror temperatures of 9 K, 15 K and 20 K, respectively. The corresponding STN curves in Figure 3.16a indicate a minor effect of the heat load on the STN. It must be noted, however, that the achievable mirror temperature strongly depends on the marionette temperature.

The length of the mirror suspensions is an essential design parameter, influencing both the STN and the cryostat design. Figure 3.16b shows the STN for mirror suspensions of 2.0 m, 1.2 m and 0.8 m length, yielding mirror temperatures of 18 K, 15 K and 13 K at 0.5 W heat load. A decreasing length L_{tm} yields a shift of all the modes to higher frequencies. This is beneficial for the sensitivity regrading the violin and vertical modes, but it also implies a shift of the pendulum modes below 1 Hz to higher frequencies. The latter results in an STN increase from 1 Hz to 20 Hz. Therefore, L_{tm} is a design parameter to be optimized, considering constraints imposed by the ET-LF sensitivity, ongoing R&D on high-quality fiber manufacturing [182] and the ET-LF cryostat and tower dimensions.

The impact of the mirror suspension diameter d_{tm} is presented in Figure 3.16c, considering different ultimate strength values and mechanical safety factors. Measured ultimate strength values of silicon at cryogenic temperatures lie between 230 MPa [158] and 120 MPa [220]. In order to consider mechanical strength uncertainties related to silicon jointing methods, the application of a safety factor of 3 or 6 is foreseen in the parameter study. This yields $d_{\mathrm{tm}_{\mathrm{a}}\mathrm{cr}} = 3\,\mathrm{mm}$ for $\sigma_{\mathrm{m,max}} = 230\,\mathrm{MPa}$ with $\mathrm{SF} = 3$, $d_{\mathrm{tm}} = 4\,\mathrm{mm}$ for $\sigma_{\mathrm{m,max}} = 120\,\mathrm{MPa}$ with $\mathrm{SF} = 3$ and $d_{\mathrm{tm}} = 5.6\,\mathrm{mm}$ for $\sigma_{\mathrm{m,max}} = 120\,\mathrm{MPa}$ with $\mathrm{SF} = 6$. Increasing suspension diameters d_{tm} result in higher STN values, despite a better heat extraction with lower temperatures T_{tm}. This is mainly caused by the shifting of the vertical and first violin modes towards each other. Furthermore, d_{tm} determines the position of the mirror suspension bending points via $\lambda_{\mathrm{bp}} = \sqrt{EI/\sigma_{\mathrm{m}}}$, which due to payload-control-related constrains must be aligned with the center of mass of the suspended mirror and marionette. As a consequence, the overall length of the mirror suspensions must include these additional lengths in the upper and lower parts. For the baseline design parameters in Table 3.2, both sapphire and silicon yield a total additional length of 6 cm. This additional length has a negligible impact on the STN modeling, but is an important aspect to be considered in the suspension manufacturing and payload design, such as the calculation of the suspension system frequencies and temperature gradients.

The mirror suspension bulk loss angle $\phi_{\mathrm{bulk,tm}}$ has a strong impact on the STN, given that it directly affects the overall mechanical dissipation of the suspensions, cf. Equation (3.7). Figure 3.16d shows the STN for silicon mirror suspensions with $\phi_{\mathrm{bulk,tm}}$ of $1{\cdot}10^{-9}$, $3{\cdot}10^{-9}$ and $5{\cdot}10^{-9}$. The surface losses are calculated under the assumption of a constant dissipation depth of $h_s = 5 \cdot 10^{-4}\,\mathrm{m}$ according to Equation (3.10), yielding total suspension losses $\phi_{\mathrm{susp,tm}}$ of $2.3{\cdot}10^{-9}$, $7{\cdot}10^{-9}$ and $1.2{\cdot}10^{-8}$, respectively. Increasing $\phi_{\mathrm{bulk,tm}}$ induces a higher STN over the complete frequency range.

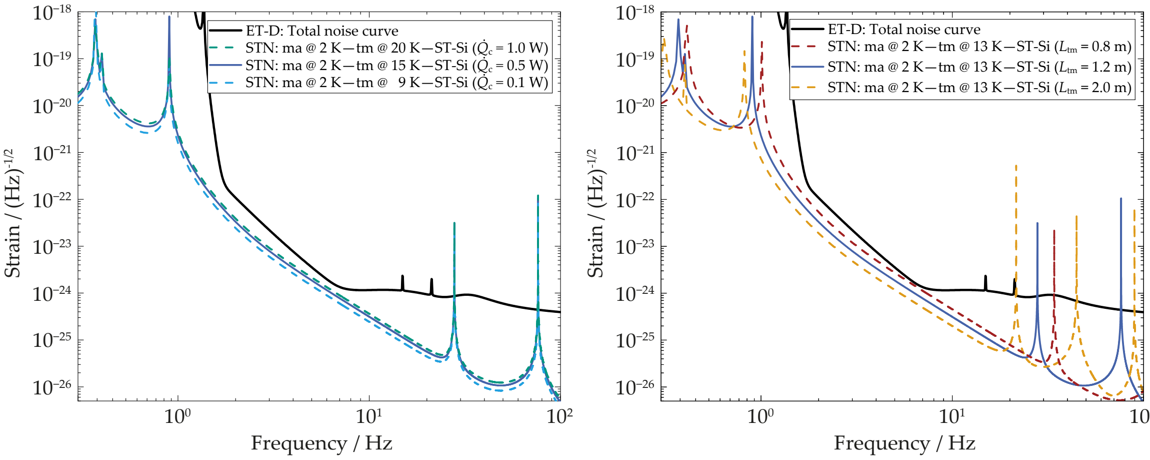

(a) Impact of heat load/mirror temperature T_{tm}

(b) Impact of mirror suspension length L_{tm}

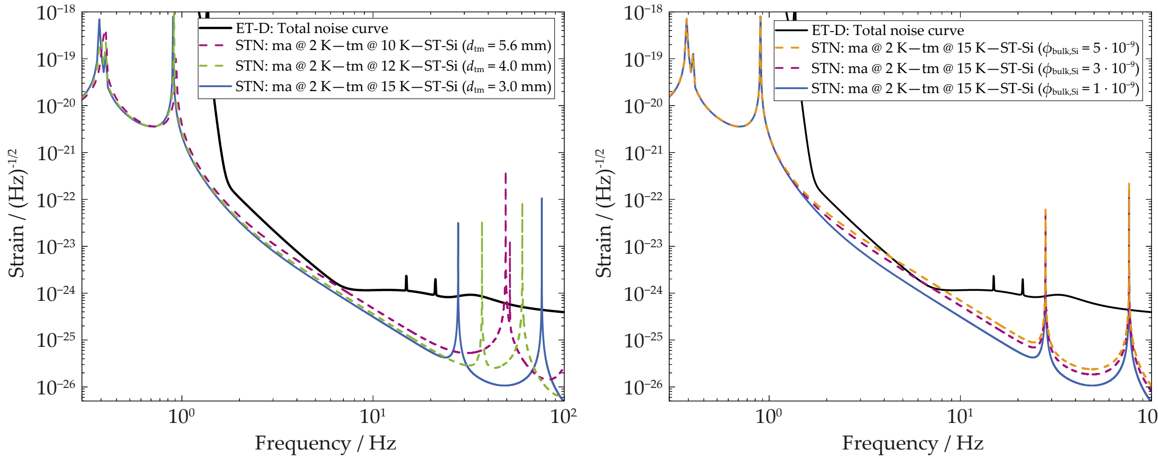

(c) Impact of mirror suspension diameter d_{tm}

(d) Impact of mirror suspension bulk loss angle $\phi_{\mathrm{bulk,tm}}$

Figure 3.16: Sensitivity analyses of the mirror suspension parameters T_{tm}, L_{tm}, d_{tm} and $\phi_{\mathrm{bulk,tm}}$ on the STN.

3.1.7.3 Influence of the marionette suspension design

The marionette suspension has a dominant impact on the STN at frequencies below 10 Hz. Again, we use the He II filled marionette suspension concept for reference, where $T_{\mathrm{ma}} = T_{\mathrm{MA}} = 2\,\mathrm{K}$ is fixed on principle, and we investigate the influence of the suspension length, the marionette mass, and the suspension material. The resulting trends may apply to monolithic marionette suspensions as well, but more detailed design studies including the cooling interface will be necessary in order to determine appropriate temperature values.

Figure 3.17a presents the STN modeled with marionette suspension lengths of $L_{\mathrm{ma}} = 0.8\,\mathrm{m}$, $1.0\,\mathrm{m}$, and $2.0\,\mathrm{m}$. A decrease in L_{ma} yields a shift of the pendulum modes to higher frequencies. Increasing STN values, however, are only observed at

$f < 3\,\text{Hz}$. The violin and the vertical modes remain unchanged, as they are defined solely by the mirror suspensions.

The variation of STN with marionettes of 100 kg, 200 kg and 400 kg is analyzed in Figure 3.17b. A reduction of the marionette mass results in a shift of the pendulum and the vertical modes to higher frequencies, resulting in slightly higher STN values in the frequency range of 3 to 5 Hz. The benefit of a lighter marionette, however, is a reduced cooldown time. Additional restrictions may come from the payload control system, whereby the marionette should not weigh less than the mirror.

The marionette suspension tube material influences the STN via the suspension losses ϕ_{susp} (cf. Figure 3.15) and the wall thickness resulting from the mechanical dimensioning. Figure 3.17c depicts the impact of different materials on the STN, showing that the ET-D sensitivity curve can only be reached with a titanium suspension tube.

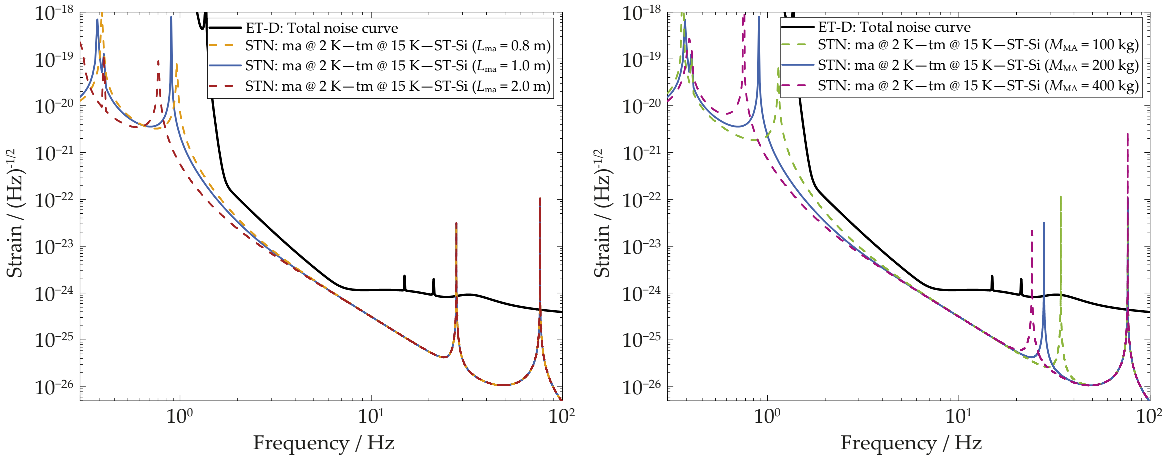

(a) Impact of marionette suspension length L_{ma} (b) Impact of marionette mass M_{MA}

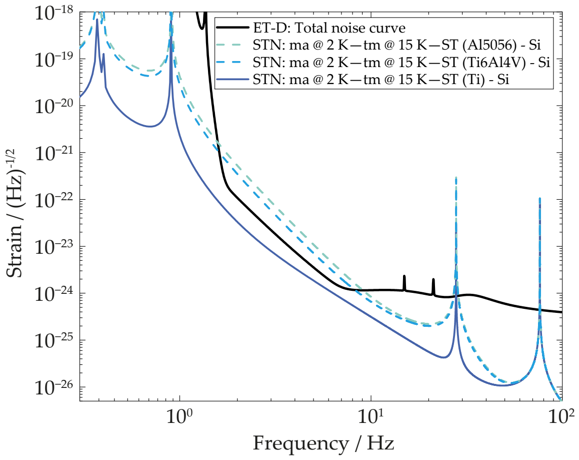

(c) Impact of marionette suspension tube material

Figure 3.17: Parameter analysis of the marionette design parameters: L_{ma}, M_{MA}, $\phi_{\text{susp,ma}}$ on the STN.

3.1.8 Conclusions and outlook

We presented a baseline design for the ET-LF cryogenic payload, which is thermally and mechanically consistent and fulfills the STN requirements given by the ET-D sensitivity curve. Analytic and finite element analysis (FEA) simulations indicate that soft thermal links cannot be connected to the marionette. Therefore, two possible heat extraction concepts are proposed, including a high-Q_m and high-conductivity monocrystalline marionette suspension made of silicon or sapphire, and a He II-filled marionette suspension tube made of titanium, respectively. In the latter case, the lower operating temperature of 2 K compensates for the lower Q_m of titanium. The theoretical fundamentals of STN modeling applied to cryogenic payloads are described in detail, and available sources for material data are compiled. A parameter study is performed in order to identify the impact of various design parameters on the ET-LF sensitivity, illustrating the parameter space for future payload design optimizations. The suspension losses are shown to have a decisive impact, highlighting the need for dedicated R&D on bulk and surface losses under ET-LF operating conditions. A reduction of the mirror suspension length is shown to deteriorate the STN in the ET-LF frequency range, whereas the marionette suspension length has a less important impact. Hence, a combined variation of these two parameters may be beneficial in future design studies. The actual value of the heat load on the mirror is shown to have a marginal impact on the STN, assuming that the necessary cooling capacity is available.

Future R&D on cryogenic payloads will be embedded in a wide context of activities outlined, e.g., in [221]. For the monocrystalline concept foreseeing a silicon or sapphire marionette suspension, the cooldown behavior and vibration transmission will be investigated in upcoming R&D in the ET-Cryo facility of the Amaldi Research Center (ARC), devoted on testing and developing the main features of an ET-LF payload using a solid conductive cooling cryostat. Thermal shielding and soft thermal links, as well as high-Q_m and high-conductivity monocrystalline suspensions for the marionette and mirror will be tested. Also, key relevant features concerning the cryostat design versus payload will be tested in order to envisage the actual impact of connecting the payload to the cryogenic system. The ARC ET-Cryo Lab is ready and the design of the test cryostat is underway. The alternative He II concept is shown to fulfill the STN requirements as well, cooling the marionette to 2 K and conducting the heat load through a static He II column inside the marionette suspension tube. This concept enables convective cooldown of the ET-LF payload by controlled He I flow in about two weeks. Open questions related to the integration of a quantum fluid in a gravitational wave detector suspension—in particular, the effect of He II on mechanical dissipation and vibration transmission—will be addressed in future experiments by the authors at KIT. A new facility for Q_m-measurements down to 2 K is presently being planned, allowing investigations of both solid and He II-filled suspensions. The scope of this facility includes R&D on the mechanical integration of the cooling interface on the platform, the supply capillaries, and their vibration attenuation system in order to investigate the noise propagation from the cooling system into the payload.

Acknowledgements

The authors would like to acknowledge the support from the German Ministry for Education and Research (BMBF, Gr 05A20VK4), and from the Karlsruhe School of Elementary Particle and Astroparticle Physics: Science and Technology (KSETA). The study in this paper has been developed within the frameworks of Italian PRIN2020, cod. 2020BSYXCB LoVeC-ET (Low-frequency Versus Cryogenics for ET), the EC exchange programme NEWS - H2020-MSCA-RISE-2016 GA no. 734303, and the ETIC – Einstein Telescope Infrastructure Consortium (IR0000004) - MUR call n. 3264 PNRR, Miss.4 - Comp. 2, Line 3.1. We are indebted to KAGRA colleagues for the precious discussions concerning solid conduction cooling down of payloads.

3.2 Thermal modeling supplements

The principle of implementing the cooling system interface within the payload by means of a tube filled with a static He II column is introduced in Section 3.1. This technique and its impact on the thermal characteristics of cryogenic payloads in ET-LF are investigated in further detail in this section. Both, steady-state operation and transient cooldown are addressed.

3.2.1 Steady-state operation

As described in Section 3.1.4.4, the marionette suspension tube as part of the payload cooling approach with He II is designed such that in steady-state, the interface with the marionette bulk is at $T \approx 2\,\mathrm{K}$. In order to approximate the resulting test mass temperatures, the thermal gradient along the TM suspension fibers has to be taken into account. This can be achieved by integrating the one-dimensional Fourier's law along the suspension fiber length, which yields

$$\int_{T_{\mathrm{MA}}}^{T_{\mathrm{TM,min}}} \lambda_{\mathrm{tm}}(T)\,\mathrm{d}T = \dot{Q}_{\mathrm{c}} \cdot \frac{L_{\mathrm{tm}}}{A_{\mathrm{cross,tm}}}\,, \tag{3.42}$$

with

$$A_{\text{cross,tm}} = n_{\text{fibers}} \cdot \frac{\pi d_{\text{tm}}^2}{4} \,. \tag{3.43}$$

Here, $\dot{Q}_\text{c}$ is the design heat load defined in Equation (3.1). The total fiber amount per TM, $n_{\text{fibers}} = 4$, as well as the solid fiber diameter d_{tm} are reflected in the thermally conducting cross-sectional area $A_{\text{cross,tm}}$. Considering a given, temperature-dependent thermal conductivity of sapphire or silicon, an increased marionette temperature T_{MA} leads to a raised suspension fiber warm end temperature. The latter corresponds to the minimum achievable TM temperature $T_{\text{TM,min}}$. Figure 3.18 shows its dependence on T_{MA} in the interval between 2 K and 20 K. Exemplary fiber geometries from Section 3.1.7 and Table 3.2 are considered. In every fiber, an excess length is added to the given values of L_{tm} in order to account for the approximate bending point position as addressed in Section 3.1.7.2. Analogous studies for the remaining fiber configurations specified therein are found in Appendix A.3.

The figure highlights that there is little margin with respect to the marionette temperature to achieve the desired TM operating temperature range of 10 K to 20 K (cf. Table 1.1). The lower limits for $T_{\text{TM,min}}$ ($T_{\text{MA}} \to 0$) are between ∼18.7 K (silicon, $L_{\text{tm}} = 1.2\,\text{m}$, $d_{\text{tm,Si}} = 3.0\,\text{mm}$) and ∼23.7 K (sapphire, $L_{\text{tm}} = 2.0\,\text{m}$, $d_{\text{tm,Sa}} = 2.3\,\text{mm}$). The displayed fiber configurations with $L_{\text{tm}} = 1.2\,\text{m}$ allow marionette temperatures of up to ∼10.5 K (silicon) for $T_{\text{TM,min}} \leq 20\,\text{K}$. For higher values of T_{MA}, achievable TM temperatures increase strongly. Using sapphire, desired TM operating temperatures are approached only towards the low-temperature limit for $L_{\text{tm}} = 1.2\,\text{m}$.

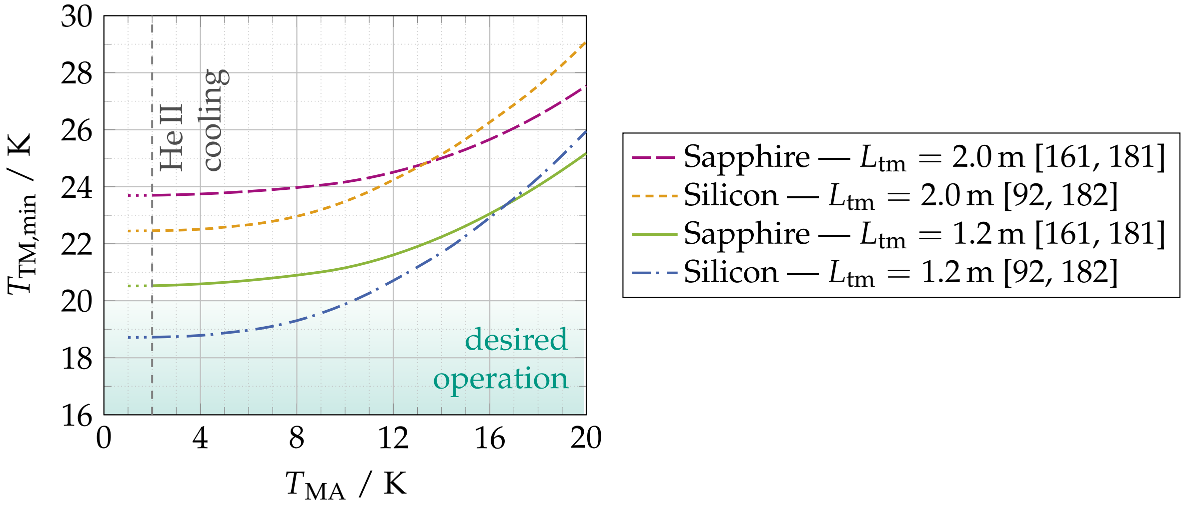

Figure 3.18: Minimum reachable test mass temperature dependence on marionette interface temperature using different TM suspension fiber materials and -lengths ($d_{\text{tm,Si}} = 3.0\,\text{mm}$, $d_{\text{tm,Sa}} = 2.3\,\text{mm}$).

Overall, the slopes of all depicted curves visualize that the benefit of marionette cooling to lower temperatures gradually declines for both considered materials for $T_{\mathrm{MA}} \lesssim 15\,\mathrm{K}$. This is due to the considerable drop in the thermal conductivity of both materials in that region (cf. Figure 3.5). However, marionette cooling to $T \approx 2\,\mathrm{K}$ via superfluid helium, as presented in Section 3.1.4, may enable the use of sapphire fibers with $L_{\mathrm{tm}} = 2.0\,\mathrm{m}$ $T_{\mathrm{TM,min}} \rightarrow 20\,\mathrm{K}$), provided that slight concessions on T_{TM} are acceptable. Under the same marionette cooling conditions, silicon fibers with $L_{\mathrm{tm}} = 1.2\,\mathrm{m}$ provide some margin on $T_{\mathrm{TM,min}}$. Regardless, the approach of utilizing static He II for heat extraction from the payload is not only motivated by the low fluid operation temperature, but predominantly by the ultra-low noise cooling potential of its implementation, as introduced in Sections 2.4 and 3.1.4.1.

The above presented analytic approximations do not provide information about thermal gradients within marionette and test mass. Figures 3.2 and 3.7 show that the interfaces between TM suspension fibers and marionette are located close to its outer edges, while the suspension tube is inserted in its center. Similarly, at their lower ends, the fibers are attached to the test mass in the vicinity of its longitudinal axis midpoint, while the majority of the heat load is expected on the TM faces due to laser power absorption and thermal radiation from the beam pipes. In both instances, thermal gradients will occur due to the conducted $\dot{Q}$ towards the payload heat sink constituted by the static superfluid helium within the suspension tube. These are investigated in the following.

Numerical models are set up in COMSOL Multiphysics® [222] for this purpose, under consideration of the mirror and marionette spatial extents. The test mass and suspension fiber geometrical parameters listed in Table 3.6 are used. The marionette is modelled as a regular octagonal prism as displayed in Figures 3.2 and 3.7 with $M_{\mathrm{MA}} = 200\,\mathrm{kg}$. The spatial discretization is presented in Appendix A.4.1.

The interface with the He II-filled suspension tube is considered via a Dirichlet boundary condition ($T = 2.0\,\mathrm{K}$) applied at the surface of the centrally located marionette bore. The assumption of a uniform temperature on this suspension tube interface is reasonable due to the diminishing temperature gradients inside the static He II column (cf. Section 3.1.4.4). The complete expected heat load of $\dot{Q} = 0.5\,\mathrm{W}$ is applied to just one of the TM faces, inducing increased thermal gradients with respect to a more homogeneous application, which implies a conservative approach to the issue. Below, the modelled domains and their considered material options are listed in the order that they appear along the heat conduction path.

- Test mass bulk — silicon
- Suspension fiber anchor supports (‘ears’) — silicon
- Suspension fibers (including anchors) — silicon
- Marionette suspension fiber platforms — 316L stainless steel / Al alloy 1200
- Marionette bulk — 316L stainless steel / Al alloy 1200

A detailed description of these parts in the scope of AdVirgo can be found in [223]. Thermal contact resistances across the interfaces between these domains $R_{ij} = {}^{\Delta T}/_{\dot{q}}$ are neglected due to several reasons. Firstly, the silicon parts will be jointed via welding and bonding techniques such as hydroxide catalysis bonding (HCB), which is expected to yield vanishing values of R when compared to the thermal conduction resistance represented by the thin suspension fibers (cf. Figure 3.18).

Similarly, expected thermal contact resistances of the Al/Al or steel/steel interfaces on the order of some $\mathrm{mK\,m^2\,W^{-1}}$ [224] suggest that the temperature difference across the contacts under consideration with $\dot{q} \approx 80\,\mathrm{W\,m^{-2}}$ remains well below 1 K. Established thermal contact conductance correlations [225, 226] yield that the comparatively low values of R are a consequence of the high contact pressure ($p \approx 300\,\mathrm{kPa}$) induced by the test mass weight being supported by the marionette suspension fiber platforms.

With the boundary conditions described above applied, numerical models were solved utilizing the key solver settings listed in Appendix A.4.1, yielding steady-state temperature profiles of the listed domains. Figure 3.19 depicts the temperature distribution within a test mass for a He II-cooled marionette composed of Al alloy 1200. The visualization provides two main outcomes. First, thermal gradients to be expected within the TM bulk are vanishingly small. The displayed temperature contours encompass both the test mass itself and the ears for suspension fiber anchoring. Yet, the total thermal gradient across both of these domains is $\Delta T \approx 1\,\mathrm{mK}$. At this small scale, merely a general sense of the gradient along the longitudinal test mass axis, as induced by the one-sided heat load application, can be given.

The second main outcome is that analytical approximations can, in fact, provide a good estimate of $T_{\mathrm{TM,min}}$ (cf. Figure 3.18). In the scope of the different considered marionette materials, this is only the case for Al 1200, however. As Figure 3.20a shows, this material choice yields a small thermal gradient of $\Delta T < 250\,\mathrm{mK}$ within the marionette bulk. Therefore, the resulting fiber cold end temperatures are only slightly elevated with respect to the assumption of a homogeneous marionette temperature distribution in Equation (3.42). For a stainless steel marionette, the situation is sub-

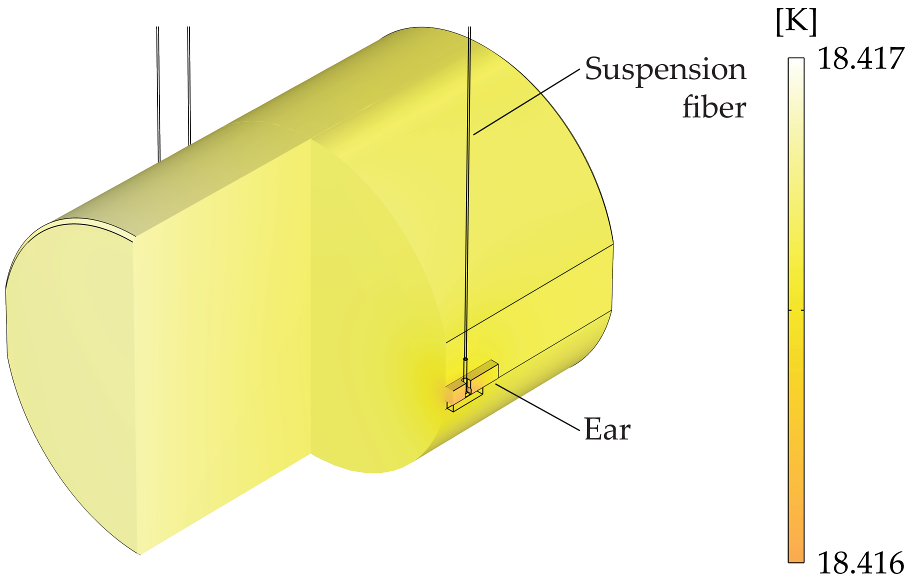

Figure 3.19: Exemplary temperature distribution in a silicon ET-LF test mass with $d_{\mathrm{TM}} = 450\,\mathrm{mm}$.

stantially different. Figure 3.20b makes this evident. The thermal gradient within the marionette, between the suspension fiber platforms and the suspension tube contact surface is nearly two orders of magnitude higher ($\Delta T \approx 13\,\mathrm{K}$). The extent of this difference arises from two factors. Firstly, Al 1200 exhibits a considerably higher thermal conductivity, especially in the low temperature range at hand. Secondly, its density [227] is significantly lower as compared to 316L stainless steel [228]. Thus, given the required $M_{\mathrm{MA}} = 200\,\mathrm{kg}$ (cf. Table 3.2), the resulting volume for an aluminum marionette is larger. Consequently, the mean cross-sectional area of thermal conduction within the marionette bulk is increased. An application of Equation (3.42) illustrates the reducing effect of these circumstances on the thermal gradient.

3.2.2 Transient cooldown modeling supplement

Two decoupled numerical models for transient marionette- and subsequent test mass cooldown are briefly outlined in Section 3.1.4.5. In turn, the following paragraphs lay out a correlation-based calculation for an approximate verification of model integrity as well as key cooldown operation parameter studies utilizing a single, fully-coupled model.

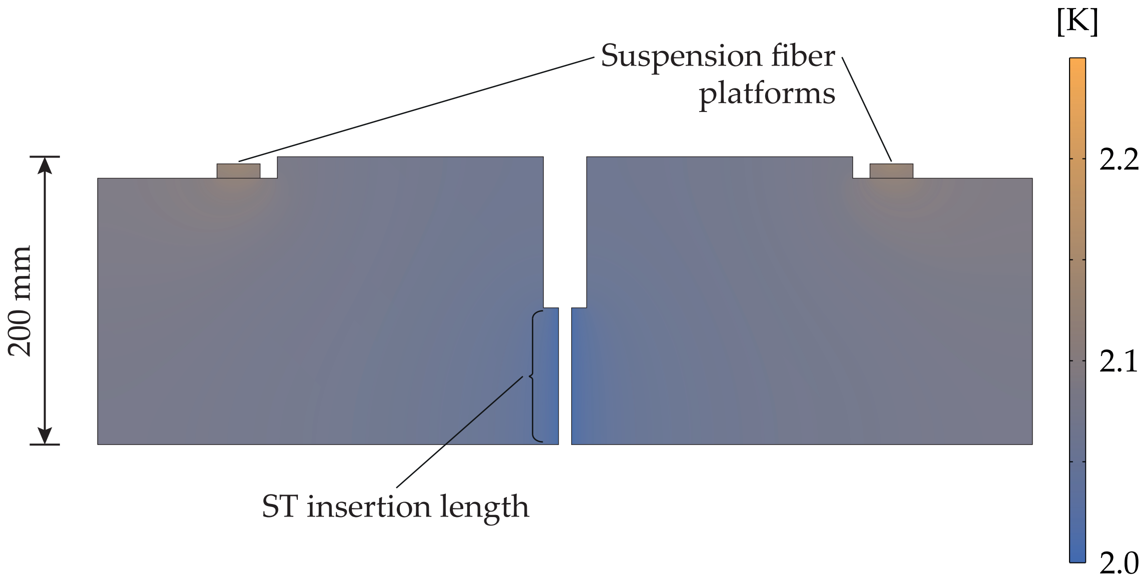

(a) Aluminum alloy 1200 marionette.

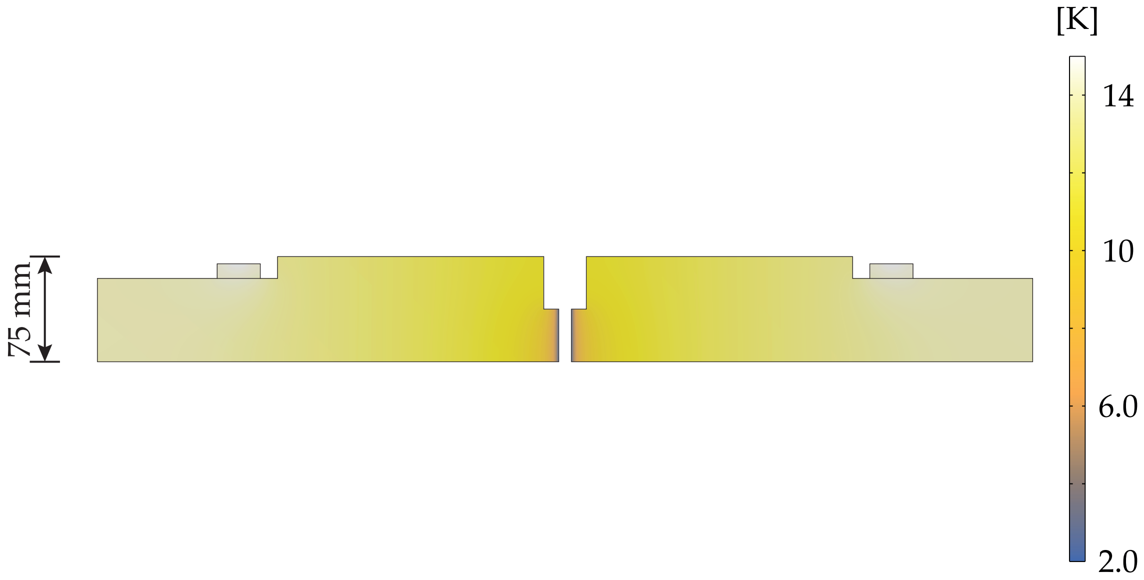

(b) 316L stainless steel marionette.

Figure 3.20: Exemplary temperature distributions in ET-LF cryogenic marionettes of different materials (slice through center axis).

Correlation-based determination of scale

In Section 3.1.4.5, the value of $\Delta t_{\text{cooldown}} \approx 4.2\,\text{d}$ is presented as an approximation of the time required to cool the marionette from T_{amb} to $\sim$3 K via forced convection with exemplary operating parameters. This time interval can be used as a starting point for a subsequent correlation-based verification of the numerical model validity. Solving Equation (3.4) for $\dot{q}$ and substituting the upper and lower time integration limits with

$t = \Delta t_{\mathrm{cooldown}}$ and $t = 0$, respectively, yields the expression

$$\bar{\dot{q}} = \frac{-M_{\mathrm{MA}} \cdot \int_{T_{\mathrm{MA}}(t=0)}^{\overline{T}_{\mathrm{MA}}(\Delta t_{\mathrm{cooldown}})} c_{\mathrm{Al}}(T)\,\mathrm{d}T}{\Delta t_{\mathrm{cooldown}} \cdot A_{\mathrm{HT}}} \tag{3.44}$$

for a mean heat flux $\bar{\dot{q}}$ covering the complete cooldown duration. The definite integral in Equation (3.44) is solved using dedicated software [229], yielding $\bar{\dot{q}} \approx 33\,\mathrm{kW\,m^{-2}}$. This value corresponds to a mean cooling power $\overline{\dot{Q}}_{\mathrm{c}} \approx 91\,\mathrm{W}$. According to Equation (3.3), with the assumption of $T_{\mathrm{wall}} - T_{\mathrm{fluid}} = \Delta T_{\mathrm{MA-He,in}} = 100\,\mathrm{K}$, this implies a mean heat transfer coefficient $\bar{\alpha}_{\mathrm{HT}} \approx 330\,\mathrm{W\,m^{-2}\,K^{-1}}$. This value can be compared to an established Nusselt number correlation for convective heat transfer to supercritical helium [230]:

$$Nu = 0.0259 \cdot Re^{0.8} Pr^{0.4} \left(\frac{T_{\mathrm{fluid}}}{T_{\mathrm{wall}}}\right)^{0.716} \tag{3.45}$$

The ranges of Reynolds and Prandtl numbers in the suspension tube return annulus during cooldown are $4.6 \cdot 10^3 \leq \mathrm{Re} \leq 3.1 \cdot 10^4$ and $0.56 \leq \mathrm{Pr} \leq 1.28$. They allow the calculation of an expected heat transfer coefficient interval of $35\,\mathrm{W\,m^{-2}\,K^{-1}}$ to $840\,\mathrm{W\,m^{-2}\,K^{-1}}$ via (3.45). $\bar{\alpha}_{\mathrm{HT}}$ lies well in the lower half of this range. In a calculation of scale, this is to be expected since the temperature difference $T_{\mathrm{wall}} - T_{\mathrm{fluid}}$ must be fairly lower than the assumed 100 K due to the heat transfer from return- to supply flow in the suspension tube through the thin inner guiding tube wall.

The numerical model's validity regarding pressure loss is analyzed compared to correlations as well. For a single-phase compressible plug flow in steady-state, continuum-, momentum- and energy equation yield a system of two ordinary differential equations [132]:

$$\frac{\mathrm{d}p}{\mathrm{d}z} = \frac{\frac{4\dot{q}\dot{m}\gamma}{\rho d\left(c_p - w^2\gamma\right)} - \frac{\xi \dot{m}^2}{2\rho d}}{1 - \frac{\dot{m}^2}{\rho}\left(\psi + \gamma \frac{\mu_{\mathrm{JT}} c_p + w^2\psi}{c_p - w^2\gamma}\right)} \tag{3.46}$$

$$\frac{\mathrm{d}T}{\mathrm{d}z} = \frac{\frac{4\dot{q}}{\dot{m} d\left(c_p - w^2\gamma\right)} - \frac{\xi \dot{m}^2 \mu_{\mathrm{JT}} c_p + w^2\psi}{2\rho d\left(c_p - w^2\gamma\right)}}{1 - \frac{\dot{m}^2}{\rho}\left(\psi + \gamma \frac{\mu_{\mathrm{JT}} c_p + w^2\psi}{c_p - w^2\gamma}\right)} \tag{3.47}$$

All helium property data (temperature- and pressure-dependent) [231] is accessed via CoolProp [232]. Modelling of the friction coefficient $\xi = f(Re)$ is presented in Appendix A.6. The differential equation system ((3.46), (3.47)) is used to determine the pressure loss in the suspension tube considering the different cross-sections of supply- and return flow. The suspension tube is simplified as to be a straight sequence of two horizontal pipes of length L_{ST} each, the first one with a circular flow cross-section and the second with an annular one. It must be acknowledged that therefore, this simplification considers neither the helium flow reversal at the bottom of the suspension tube, nor the direct heat transfer coupling between supply- and return flow along the tube length. For the estimation of $\dot{q}$, it is assumed that the helium mass flow $\dot{M}_{\mathrm{He}}$ exits the suspension tube return annulus at $\overline{T}_{\mathrm{MA}}$. The heat flow required to raise the flow temperature is subsequently assigned to the respective outer wall surface areas of supply and return. Thus, by additionally considering the unequivocal relation between $\overline{T}_{\mathrm{MA}}$ and $T_{\mathrm{He,in}}$ (see Section 3.1.4.5 in Table 3.5), it is possible to calculate the scale of Δp_{ST} for all values of $\overline{T}_{\mathrm{MA}}$ in the cooldown process (see Figure 3.11).

When comparing the numerical with the correlation-based pressure loss results, there are two major conclusions of importance within the scope of this work. Firstly, a continuous overestimation of the pressure loss along the suspension tube by the correlation-based approach is observed. This is deduced by considering the calculation of $\dot{q}$, as explained above. The assumption of $T_{\mathrm{He,out}} = \overline{T}_{\mathrm{MA}}$ leads to excessively high values for both $\dot{q}$ and Δp_{ST}. An exemplary value for this is $\Delta p_{\mathrm{ST}} \approx 300\,\mathrm{mbar}$ at $\overline{T}_{\mathrm{MA}} = T_{\mathrm{amb}}$. For comparison, if the helium flow is considered to warm up to half the extent ($T_{\mathrm{He,out}} = T_{\mathrm{He,in}} + 0.5 \cdot \Delta T_{\mathrm{MA-He,in}}$), the evaluation of (3.46) and (3.47) yields $\Delta p_{\mathrm{ST}} \approx 270\,\mathrm{mbar}$, matching the numerically determined value of $\Delta p_{\mathrm{ST}} \approx 280\,\mathrm{mbar}$ with remarkable precision. In any case, the correlation-based calculated values for Δp_{ST} shown in Figure 3.11 exceed the numerical ones by $\leq 16\,\%$ throughout the first, major part of the cooldown, until $t \approx 3.2\,\mathrm{d}$.

Secondly, from $t \approx 3.2\,\mathrm{d}$ on, the decline of the correlation-based Δp_{ST} decelerates, analogously to the numerical simulation results. This is due to the fact that the helium in the suspension tube successively approaches critical conditions, with rapidly increasing density and thus, notably lower flow velocities. The magnitude of analytically determined values of Δp_{ST}, however, remains on a significantly higher level, approximately between 25 mbar and 50 mbar. The underlying reason for this overestimation is the same as in the first part of the cooldown process, described above. The assumption of $T_{\mathrm{He,out}} = \overline{T}_{\mathrm{MA}}$, on the other hand, is significantly more impactful in this region due to the sharp increase of $c_{p,\mathrm{He}}$ in the vicinity of the critical point. This increases the overestimation of the correlation-based $\dot{q}$ and Δp_{ST}. In the end of the cooldown process, when $\overline{T}_{\mathrm{MA}}$ gradually approaches $T_{\mathrm{He,in}}$, this overestimation shrinks due to diminishing values of $\dot{q}$.

To conclude, the presented correlation-based methods show good agreement with the numerical model, underlining the validity of the latter. With regard to the pressure drop in the suspension tube, relatively small deviations prevail. However, these are attributed to an indicated systematic error in the correlation-based calculation method. Concerning the cooldown duration determinations for the marionette, the described approximations confirm the order of magnitude of the obtained results via the numerical simulation model.

Coupled model: parameter studies

Concluding the thermal simulation efforts for TM cooldown presented in Section 3.1.4.5, a coupled numerical model has been developed. The model encompasses the suspension tube including the enclosed helium sections, as well as all solid domains listed in Section 3.2.1, allowing for comprehensive conjugate heat transfer investigations along the primary segments of the heat extraction path from the test mass [233]. Appendix A.4.2 addresses the geometry, its spatial discretization and numerical solver details.

Utilizing the model, a range of parameter studies is conducted, assessing the influence of cooldown operation parameter variation. The foremost parameter depending on the final sizing of the helium supply infrastructure is $\dot{M}_{\mathrm{He}}$. Figure 3.21 hence reports the impact of changed helium mass flows through the suspension tube on $\Delta t_{\mathrm{cooldown}}$. The ineffectiveness of a mass flow increase exceeding $1.0\,\mathrm{g\,s^{-1}}$ is evident. This is due to the fact that the thin TM suspension fibers represent the dominating heat extraction

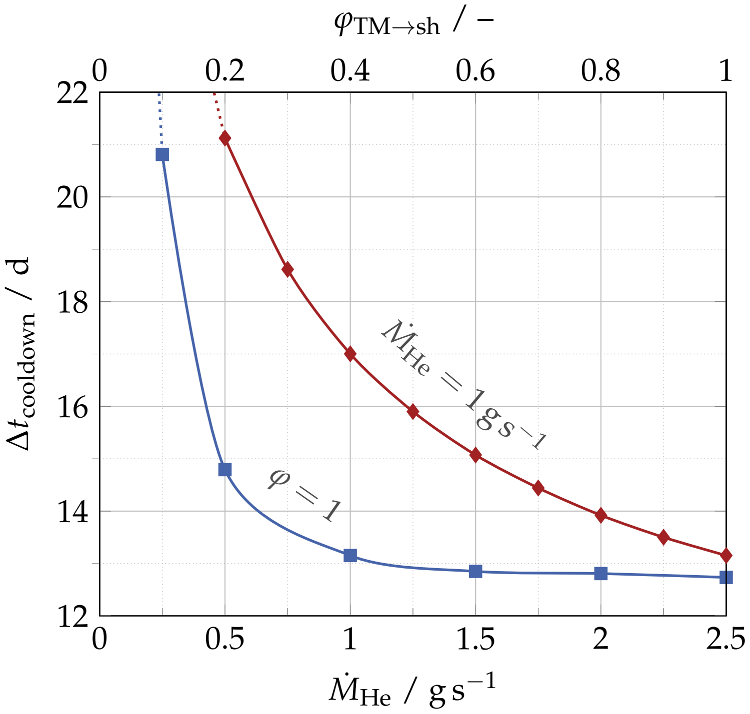

Figure 3.21: Simulated cooldown times of an ET-LF silicon test mass from T_{amb} to 10 K installed for the conditions listed in Tables 3.5 and 3.6 at varied values of $\dot{M}_{\mathrm{He}}$ (■) and $\varphi_{\mathrm{TM}\rightarrow\mathrm{sh}}$ (◆). Subset of points evaluated by Sindermann [233].

limitation. In the beginning of the cooldown process, heat extraction is governed by thermal radiation to the surrounding thermal shield at 5 K (cf. Figure 3.12). In this phase, conduction of heat out of the test mass through the suspension fibers plays a subordinate role so that even high relative marionette cooldown rate accelerations yield diminishing merits. Decreasing values of $\dot{M}_{\mathrm{He}}$ below $1.0\,\mathrm{g\,s^{-1}}$, however, lead to progressively elevated TM cooldown times. This is attributable to increasing delays in the onset of thermal conduction-controlled heat extraction from the TM after extraction by thermal radiation to the surrounding shield is halted for $\overline{T}_{\mathrm{TM}} < 120\,\mathrm{K}$ in the numerical model (cf. Section 3.1.4.5). These process characteristics are well visible in the test mass cooldown curves presented in Appendix A.5, which also lists key numerical solver settings.

Further, the effect of variation of the geometrical view factor from the test mass to the thermal shield $\varphi_{\mathrm{TM}\rightarrow\mathrm{sh}}$ is displayed by Figure 3.21. This is an important parameter predominantly influenced by the design choices regarding the actuation cage (CA), which partly surrounds the test mass (cf. Figure 3.2). The corresponding curve portrays the significant impact of $\varphi_{\mathrm{TM}\rightarrow\mathrm{sh}}$ on $\Delta t_{\mathrm{cooldown}}$. In comparison to the idealized case of $\varphi_{\mathrm{TM}\rightarrow\mathrm{sh}} = 1$, covering approximately one half of the field of view between TM and thermal shield leads to a 20 %-increase of $\Delta t_{\mathrm{cooldown}}$ to ca. 16 days. Further obstructing the view to the thermal shield by the test mass results in cooldown times of more than 3 weeks, underlining simultaneously the general importance of thermal radiation for the transient process. Hitherto, no sufficiently advanced design of the actuation cage exists. Thus, the conducted numerical simulations neglect the fact that it undergoes a transient cooldown process itself by thermal radiation to the surrounding shield. The decrease rate of $T_{\mathrm{CA}}(t)$, however, can be accelerated by means of soft connections with high thermal conductivity between actuation cage and platform (PF), following the payload heat extraction schemes addressed in Sections 2.1 and 2.2.

The design concept of the considered innermost thermal shield is explained in detail in Chapter 5. Aspects of low-noise helium supply to consumers in the ET-LF payload cryostats are presented in Chapter 6. In turn, the following chapter outlines the cryogenic infrastructure, part of which is required particularly for operating the ET-LF payloads.

4 Cryogenic infrastructure for the Einstein Telescope

As presented in Chapter 1, cryogenic operation of ET-LF is indispensable to achieve the full scientific potential of the Einstein Telescope. On a large-scale perspective, this implies the incorporation of cooling system facilities into the collective ET infrastructure. The general purpose of the former is to supply cooling power at low temperatures to a variety of consumers while avoiding the introduction of inadmissible additional noise to the detector, which would result in reduced sensitivities with respect to the design values (cf. Figure 1.6).

4.1 Cryogenic consumers

The core consumers of cooling power are the ITMs and ETMs of ET-LF (cf. Section 1.3 and Chapter 3). These optics will be hosted within cryostats, located at the bottom ends of the vacuum super-attenuator (SA) towers. In contrast, other optics such as the beam splitter (BS) (cf. Figure 1.2) can be operated at room temperature. This is because the optical power transmitted through the beam splitter is low compared to the optical power circulating in the Fabry-Pérot cavities of the interferometer arms. Thus, the noise potential of the BS is substantially lower than that of the TMs [234].

In order to provide a suitable environment for the optics at $T_{\mathrm{TM}} = 10...20\,\mathrm{K}$, thermal shields at intermediate temperatures between T_{TM} and T_{amb} need to be installed inside the cryostats, surrounding the payloads. Figure 4.1 shows the schematics of such a setup. In the center of the cryostat, the payload is indicated. It is encompassed by multiple thermal shields at different intermediate temperatures, allowing for an adequately efficient cryostat operation. All thermal shields, as well as the surrounding vacuum vessel, require sizable apertures on opposite sides to allow the laser beam passage.

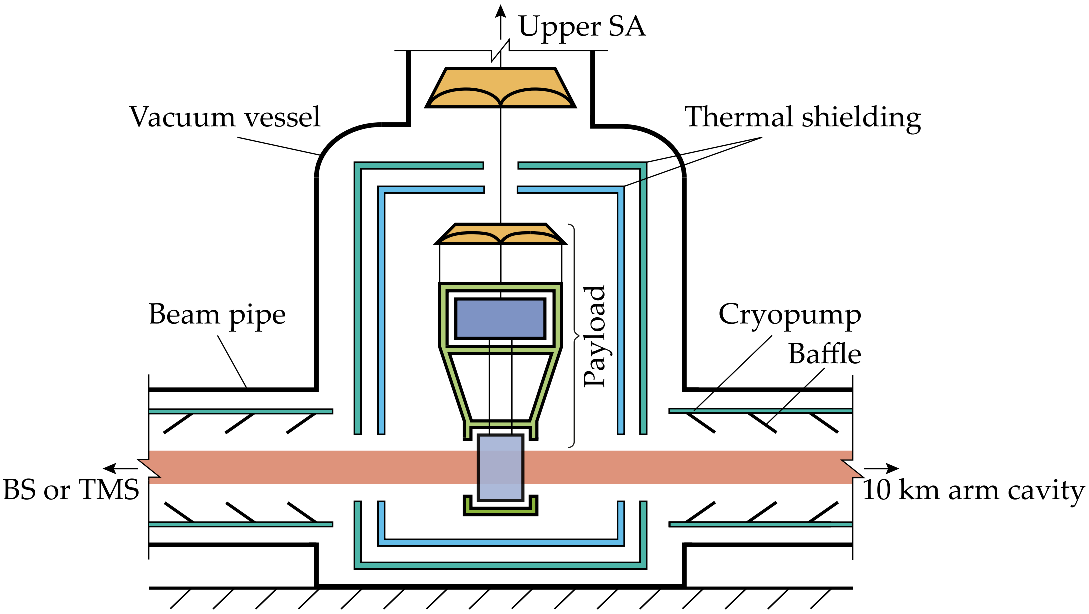

Figure 4.1: Schematic representation of an ET-LF test mass cryostat constituting the base of an SA vacuum tower (not to scale).

Furthermore, in the attached beam pipes, cryopumps (elsewhere called 'cryotraps') including angled baffles are shown. Depending on the particular beam pipe direction (either into a 10 km long Fabry-Pérot cavity or towards an adjacent tower at T_{amb}), the cryopumps extend between 10 m and 20 m into the beam pipes [108]. The pumps are required for two key reasons. First, they allow extreme high vacuum (XHV) levels inside the TM cryostat with respect to the adjacent beam pipes by cryosorption of outgassing molecules. Second, they act as an extension of the payload thermal shields into the beam pipes, limiting the solid angle of thermal radiation heat load on the cold TMs from the warm beam tubes [2, 71].

Moreover, along the inside of the cylindrical cryopumps in the vacuum tubes, Figure 4.1 indicates the attachment of angled baffles. These cold baffles limit detector noise contribution due to light backscattering by absorbing stray light, which otherwise couples with the interferometer's main mode. This is further addressed in Section 5.2. The baffles are operated at lower temperatures compared to the cryopumps, allowing further radiative heat load reduction to the test mass cryostat core.

Cryopumps will not only be required adjacent to the ET-LF TM-towers, but also in ET-HF [235], similar to the case of the room-temperature towers in AdVirgo [43]. In total, this results in a variety of cryogenic consumers in ET, as listed in Table 4.1. In the table, there is no distinction between the different sub-types of the thermal shielding or the cryopumps. The consumers are evenly distributed among the three vertices in the triangular xylophone configuration of ET (cf. Figure 1.7). Figure 4.2 provides

Table 4.1: Types and numbers of key cryogenic consumers in ET in the triangular xylophone configuration.

Cryogenic consumer	Payload	Thermal shielding	Cryopumps (pairs)	
Detector assignment	ET-LF	ET-LF	ET-LF	ET-HF
Optics assignment	each ITM & ETM			
Total amount in ET	12	12	12	12

a schematic view of the approximate foreseen arrangement of the stated cryogenic consumers within the underground caverns of an ET vertex.

The ET-LF beam splitters (BSs) are located centrally in the vertex caverns. Located within the same cavern in a distance of ca. 60 m to 70 m along the ET triangle sides, the ET-LF ITMs are positioned. The ET-HF BSs are situated in ancillary caverns, separated from the large vertex caverns mainly reserved for ET-LF components.

This allows to separate the vertex optics and associated vacuum tanks of ET-LF and ET-HF. Further, Figure 4.2 indicates that the ancillary ET-HF cavern is linked to the two branches of the large vertex cavern. In addition, the ancillary cavern carries a third connection tunnel to satellite caverns hosting the ETMs of the opposing LF- and HF detectors, ca. 500 m from the closest ET-LF BS [71]. These satellite caverns are

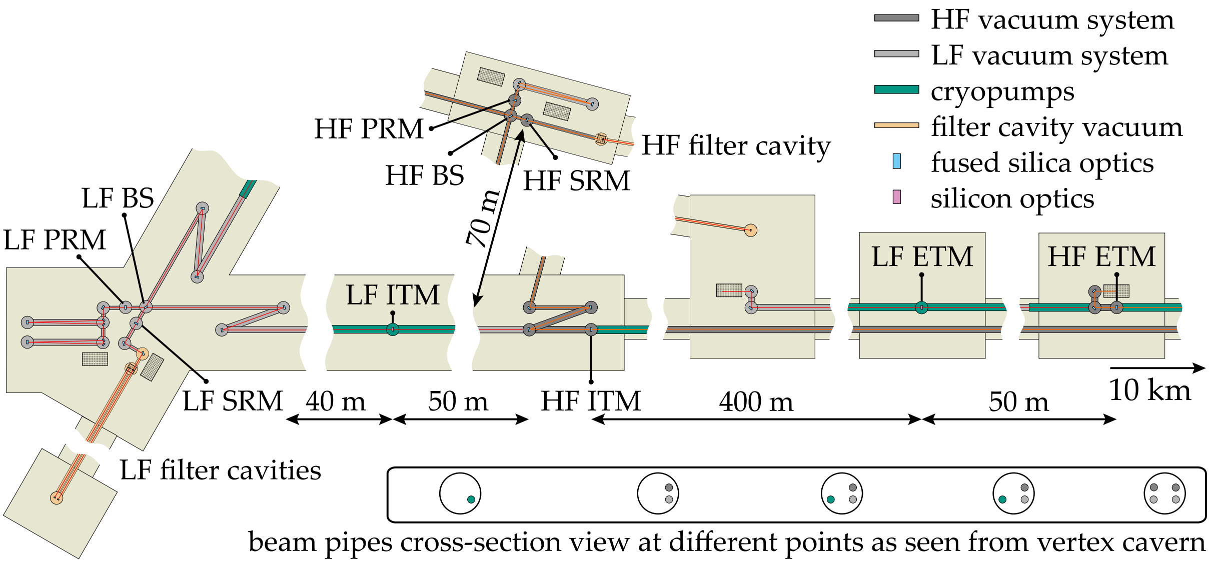

Figure 4.2: Sketch of the top view of one of the corners in the triangular xylophone configuration for ET, showing an exemplary implementation of the optical layout, the vacuum system for the main optics and the corresponding cavern layout (adapted from [236], licensed under CC BY 4.0).

shown on the right-hand side of Figure 4.2. Both ETM towers in the satellite caverns are encased by cryopumps. The ET-HF ITMs including their corresponding cryopump attachments, in turn, are located at the ends of the vertex cavern branches.

Moreover, Figure 4.2 points out that the beam pipes of ET-LF and ET-HF are foreseen to be arranged on top of one another as shown in the legend on the bottom right-hand side. This is planned so as to be as spatially efficient as possible in sight of the 10 km long tunnels for the optical cavities. Consequently, beams of one interferometer have to pass towers of another. The order of superposition has been selected such that the LF beams pass beneath the HF optics. This configuration ensures that no high-power laser beams of ET-HF come close to any cryogenic suspension fibers and only the low-power beams of ET-LF have to pass below the comparatively uncritical optics of ET-HF operated at T_{amb}, which further avoids placing additional demands on the delicate ET-LF payload design (cf. Chapter 3).

To conclude the above description of cryogenic consumers, each of the three ET vertices incorporates a total of four TMs with respective thermal shielding and eight cryopumps on either side of all ITMs and ETMs. All of these components require cooling power at differing temperature levels. The following section provides an in-depth description of an approach to provide these powers in ET. It was presented by the author at the Cryogenic Engineering Conference 2021 and subsequently included in its proceedings published in the IOP Conference Series: Materials Science and Engineering.

The optical layouts of ET in two configurations, a single triangular setup and two widely separated 'L'-shaped detectors, are currently under revision [72]. Although this will affect some detailed engineering, the conceptual cryogenic infrastructure design presented in this thesis remains valid.

4.2 Conceptual layout of a helium cooling system for the Einstein Telescope

Lennard Busch and Steffen Grohmann

2022 *IOP Conf. Ser.: Mater. Sci. Eng.* **1240** 012095.
DOI: 10.1088/1757-899X/1240/1/012095.

Abstract

The ET is a 3^{rd} generation gravitational-wave detector planned in triangular shape with 10 km arm lengths in an underground installation at a depth of 200…300 m. While 2^{nd} generation detectors and the ET-HF interferometer are operated at room-temperature, the ET-LF interferometer shall be operated at cryogenic mirror temperatures of 10…20 K in order to reduce the thermal noise. Considering thermal dissipation limits in the heat extraction path from the mirror to the heat sink, He II provides ultra-low-noise cooling to allow for an interferometer sensitivity at levels below $1 \cdot 10^{-20}\,\mathrm{m}/\sqrt{\mathrm{Hz}}$ in the detection band. In order to limit particle adsorption on the cold mirror surface, the total pressure in the cryostat must be reduced to $p \leq 10^{-10}$ mbar, i.e. partial pressures of water and heavier components $p_i \leq 10^{-14}$ mbar, respectively, using a cryopump/shield around the mirror that is cooled with supercritical helium to $T \approx 5$ K.

We present the conceptual layout of a helium cooling system that can provide cooling power for several ET-LF cryostats and their corresponding cryotraps, including mirror cooling at 2 K as well as thermal shielding at 5 K and at 50…80 K. A process flow diagram focuses on the cooling system's key components with their locations and their interconnections. On the diagram's basis, we explain the cooldown process and steady-state operation, ranging from outer shield and cryotrap cooling to the formation of He II in the mirror heat extraction path.

4.2.1 Introduction

The thermal noise goals of the ET-LF detector are ambitious. They have been declared in the ET conceptual design study in 2011 [2] and in the design report update in 2020 [71]. In order to achieve these goals, a TM temperature between 10 and 20 K is anticipated in [2, 71]. The heat extraction from the TMs is restricted by thin suspension fibers in the last mirror suspension stage ("payload"). At expected total heat loads on a TM in the order of $\dot{Q} = 10^2$ mW [2, 71], the temperature at the payload heat sink is required to be kept at 10 K or below to extract sufficient heat via conduction to maintain TM temperatures of $T \leq 20$ K [188]. In order to reach a TM temperature of 10 K, where thermal noise benefits are expected to increase [71], the heat sink is required to be at 2 K with a heat load of $\dot{Q} \leq 100$ mW. The difference between the 2 K and higher-temperature heat sink cooling options and the corresponding TM temperatures is largest at heat loads of $\dot{Q} \leq 100$ mW and becomes less significant at higher heat loads.

The decrease of the payload heat sink temperature to 2 K, however, is not only motivated by the lower resulting TM temperature, but rather by the properties of superfluid helium. Its steady-state thermal conductivity is typically one order of magnitude larger compared to the peak values of the best solids, and hence there is no need for macroscopic He II flow for payload cooling. He II is generated by pumping on a normal ^{4}He bath (He I), which is supplied by a cryoplant. The second order phase transition from liquid He Ito superfluid He II can be described by Bose-Einstein condensation, whereby ^{4}He atoms successively condense into their ground state. This implies that thermal noise is switched off in the condensed phase, presumably yielding very low or even negligible thermal dissipation among the condensed and the excited states in He II. Moreover, there is no cooling power limit with regard to ET requirements and state-of-the-art helium technology. One helium cryoplant can provide sufficient cooling capacity for all cryostats located in an ET detector vertex, including thermal shielding.

4.2.2 System layout

Our conceptual layout of the ET-LF helium cooling system is guided by the design principle of the Large Hadron Collider (LHC) refrigeration system [237], where the coldbox is split in two parts. At CERN, the main coldbox supplying supercritical helium at 4.6 K/3 bar(a) is located above ground and satellite coldboxes for liquefaction and final refrigeration are placed underground [238]. This concept is limited by the hydrostatic pressure head in the vertical helium return line, which increases the saturation pressure and temperature in the underground installations. The return gas in the LHC cooling system is therefore heated to 20 K by mixing with warm return streams, which reduces the pressure head by lowering the gas density [237]. This necessity, however, impairs the cryoplant efficiency [239].

Since ET is planned to be installed at −200. . . −300 m depth compared to the −100 m of the LHC, we propose to install the coldbox in an underground auxiliary cavern. This requires only warm helium transfer lines to the compressor system, which must be installed remotely above ground due to noise emission. This configuration considerably reduces the return line pressure head as well as the thermodynamic losses in the vertical transfer lines, both having a positive impact on the cooling system efficiency. Smaller 1.8 K units for liquefaction and final refrigeration are placed in the main underground caverns of ET close to the TM cryostats and cryotraps. In our conceptual design, one helium refrigerator at each of the 3 detector vertices of ET provides refrigeration capacity to all cryostats and the adjacent arm pipe cryotraps. There are 2 input test masses and 2 end test masses, i.e. 4 cryostats in total per vertex. Each cryostat comprises the payload and 2 separately cooled thermal shields. Due to the temperature gradient in the suspension fibers, the inner thermal shield surrounding the payload can be operated at a lower temperature compared to the test mass, which is a strategy to avoid or limit frost formation on the cold mirror surface. The helium cooling system hence provides cooling power at 3 different temperature levels as indicated in Table 4.2. The temperature level of the cryotraps and outer thermal shield in the range of 50. . . 80 K depends on the final cryoplant design. The cooling capacities are present estimates, not including transfer line losses and additional capacity required for the cool-down process. In any case, commercial helium refrigerator technology is available to cover the requirements of this concept.

The ET-LF helium cooling system consists of the following 5 main components that are connected by helium transfer lines:

Table 4.2: Temperature levels and estimated cooling capacities (orders of magnitude) required for each of the 4 TM cryostats and adjacent cryotraps in one of the 3 ET detector vertices during steady-state operation.

Component	Temperature level (K)	Cooling power (W)
Arm pipe cryotraps	50...80	x . . . 10^4
Outer thermal shield	50...80	x . . . 10^3
Inner thermal shield	5	x . . . 10^2
Payload heat sink	2	x . . . 10^0

1. the compressor system,
2. the coldbox,
3. the interconnection box,
4. the 1.8 K units and
5. the test mass cryostats.

The interconnection box is placed close to the coldbox in an underground auxiliary cavern, distributing helium supply and merging helium return flows. Horizontal transfer lines link the interconnection box with the individual 1.8 K units. A subcooler in the 1.8 K units enables the reconditioning of the 5 K helium flow after passing the up to c. 500 m long transfer lines to the ET-LF cryostat locations.

4.2.3 System working principle

Figure 4.3 shows our conceptual process flow diagram of the cooling system in order to visualize the working principle of both, the cool-down process and the steady-state operation. It highlights the same 5 main components stated in Section 4.2.2. The coldbox, which is shown as a black box, is separated from the warm compressor system by means of warm helium transfer lines. The supply line provides the coldbox with helium at pressures around 12 bar(a). The return line operated above atmospheric pressure joins the warm helium header in valve V08[a].

Further, the coldbox incorporates 2 supply outlets to and 2 return connections from the interconnection box. The first coldbox outlet used for outer shield and cryotrap cooling is drawn from a stage of the implemented Collins process in which the helium reaches temperatures between 50 K and 80 K at pressures between 6 bar(a) and 12 bar(a). A corresponding return at slightly higher temperature is fed back into the coldbox, passing through an internal heat exchanger before entering the warm return line to the compressor system. The second outlet used both for the inner shield and the detector cooling comes from the cold end of the Collins process that supplies supercritical helium, typically at 5 K/5 bar(a). The particular operating parameters of the helium cryoplant will be fine-tuned later in a detailed process optimization.

---

[a] General remark: Valves on the low-pressure side of the process may be executed as check valves rather than control valves, depending on the final safety concept.

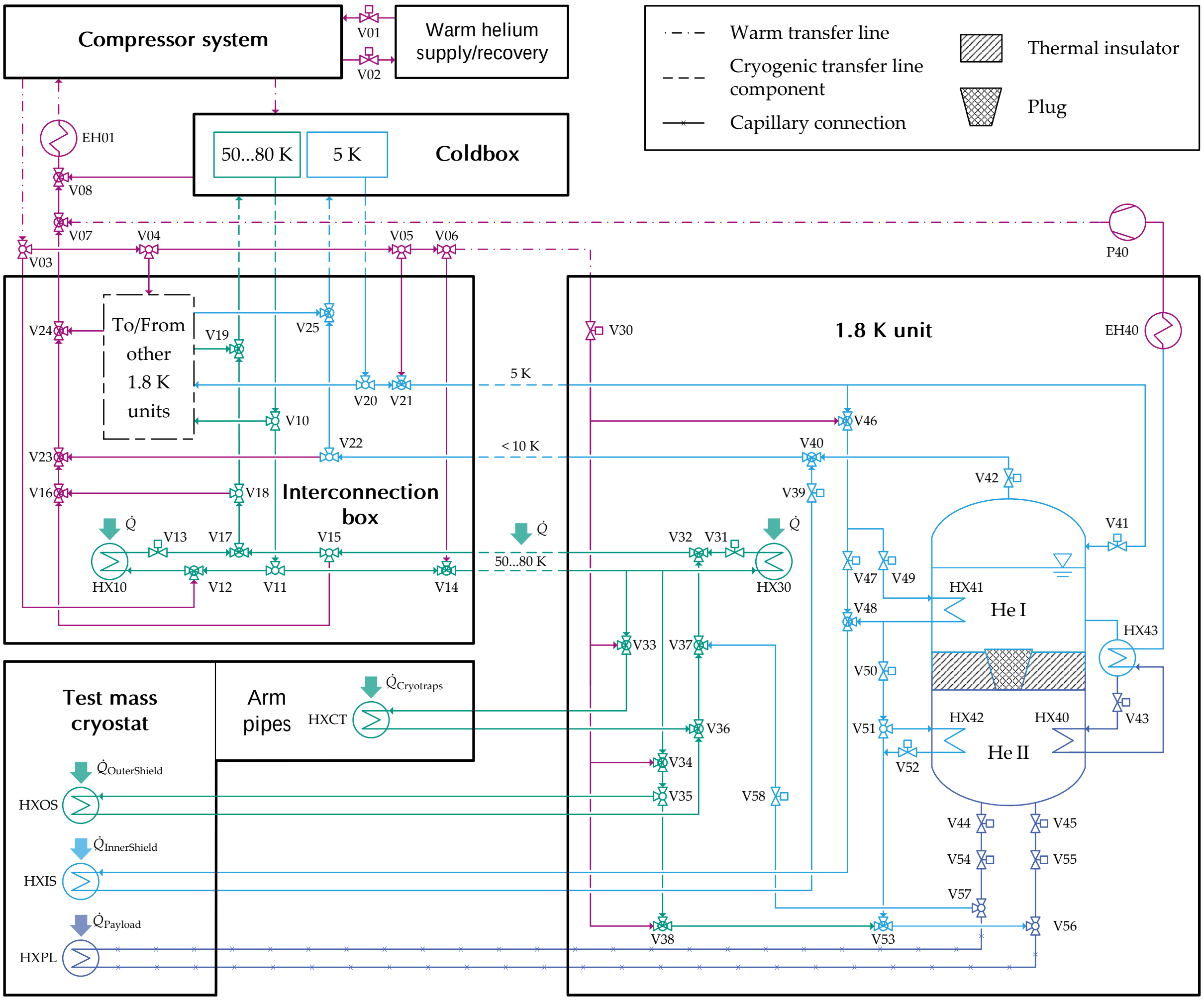

Figure 4.3: Process flow diagram of a helium cooling system for ET-LF with valves ("V"), heat exchangers ("HX"), electric heaters ("EH") and vacuum pumps ("P"). The $\dot{Q}_i$ represent heat loads absorbed by the cooling system at different temperature levels. Colors indicate different helium temperature levels, ranging from **blue** ($T \approx 2\,\mathrm{K}$) over **cyan** ($T \approx 5\,\mathrm{K}$) and **green** ($T = 50$ to $80\,\mathrm{K}$) to **purple** ($T = 80$ to $300\,\mathrm{K}$). For interpretation of the references to color in this figure, the reader is referred to the web version of this paper.

After commissioning, the entire helium circuit is evacuated, purged and filled with pure ^{4}He, ensuring an over-pressure during warm standby, while connecting the system to the warm He supply/recovery system via valves V01, V02 and V03. The functional principle of the transient cool-down procedure and the steady-state operation is explained in the following subsections on the basis of Figure 4.3.

4.2.3.1 Outer thermal shield and cryotrap cooling

The green circuit in Figure 4.3 shows the cooling process of the outer thermal shields installed in the cryogenic transfer lines, the interconnection box, the 1.8 K units and the TM cryostats, as well as the cryotraps in the arm pipes next to the cryostats. To start the cool-down process, warm helium is supplied from the reservoir to the compressor system via valve V01, providing sufficient helium to pressurize the system. During transient cool-down of the entire cryogenic system or of individual cryostats, supercritical helium is supplied at $p = 6...12\,\mathrm{bar(a)}$ and $T = 50...80\,\mathrm{K}$ (depending on the final cryoplant design) through the first coldbox outlet. In order to control the cool-down speed, the cold 50 to 80 K streams are mixed with room-temperature helium. The return flows from the individual components have higher temperatures compared to steady-state operation and cannot be used for heat recovery in the coldbox. Therefore, these helium returns are warmed up to room-temperature and fed back in the return line to the compressor, bypassing the coldbox. When transient cool-down is completed, the 50 to 80 K supercritical helium flow is supplied continuously at constant temperature and pressure, while the flow rate can be reduced compared to the cool-down mode.

Valve V10 allows flow distribution among the 1.8 K units (only one 1.8 K unit and test mass cryostat is shown in Figure 4.3). Valve V11 serves to split the flow into two parts. One part is used to cool the thermal shield of the interconnection box by means of HX10. The other part is directed towards the 1.8 K unit, passing the horizontal transfer line in the cavern. Inside the 1.8 K unit, the 50 to 80 K header distributes helium towards 3 HXs. One flow cools the 1.8 K unit thermal shield via HX30. The two others are directed towards the cryotrap heat exchanger (HXCT) in the arm pipes and the outer thermal shield heat exchanger (HXOS) in the TM cryostat. Valves V33 and V34 allow mixing the supply streams to HXOS and HXCT with warm helium from the header via V30 for controlled, independent cool-down of the TM outer shield and the cryotraps. The return flows are joined with the HX30 return in V32, passing the cryogenic transfer line to the interconnection box and being mixed with the HX10 return in V17. Downstream of V17, the return flow is either diverted to the warm header during cool-down via V18 and V16, or led to the cold return line towards V19 during steady-state operation. Valve V15 serves as a separate return bypass for independent cool-down of the depicted 1.8 K unit from the interconnection box. While valves V13, V31, V33 and V35 serve for flow control in HX10, HX30, HXCT and HXOS, valves V36, V37, V32, V17 and V19 may be executed as check valves or simple piping joints[a].

The return flow passing V32 towards the interconnection box and V19 towards the coldbox is used to thermally shield the colder supply and return lines to/from the 1.8 K units and from/to the coldbox in the corresponding cryogenic transfer lines.

In the warm helium recovery line, warm returns from outer shield cooling are mixed in V23 with the warm return from the depicted 1.8 K unit operation, and with the corresponding flows from the other 1.8 K units in V24 (simplified illustration). Before being returned to the compressor system, the merged streams are warmed up to room-temperature in EH01 to avoid temperatures below the dew point in the warm vertical transfer line. Once the return flows have reached sufficiently low temperatures during the cool-down process, the cold streams are redirected in V18 to be used in the coldbox. Downstream, V19 allows the addition of cold returns from the other 1.8 K units (simplified).

4.2.3.2 1.8 K unit operation

After completion of the outer shield cool-down process described in Section 4.2.3.1, the refrigerator provides a stream of supercritical helium at 5 K/5 bar(a) via the second coldbox outlet. V20 allows flow distribution among the four 1.8 K units. The cold streams may be mixed with warm helium again to enable gradual cool-down of this circuit via V05 and V21.

Downstream of the transfer line connecting the interconnection box with the depicted 1.8 K unit, the 5 K/5 bar(a) helium flow is expanded through the Joule-Thomson valve V41 into a vessel, with valves V43, V44 and V45 being closed. Valve V42 controls the vessel pressure to $p \approx 1.2\,\mathrm{bar(a)}$ corresponding to a saturated He I bath temperature of $T \approx 4.4\,\mathrm{K}$. The vessel is divided into two sections by means of a so-called λ-plate which thermally separates the liquid He I from the superfluid He II phase in the lower part of the vessel. In steady-state operation, the λ-plate's central orifice is closed by a plug. This plug can be lifted externally, enabling the initial filling of the complete vessel with liquid He I. Additionally, the plug serves as an exhaust valve for the He II section in case of incidents, opening into the upper vessel which incorporates a pressure relief device to the atmosphere.

During the cool-down phase, the helium exhaust from V42 returns to the warm recovery header via V23. Once this return flow reaches a sufficiently low temperature, it is fed back into the coldbox by means of V22. As soon as the liquid level in the vessel is sufficiently high, the plug in the λ-plate is closed.

Subsequently, the vacuum pumping system 40 and the electric heater EH40 are started. The Joule-Thomson valve V43 is opened, expanding a liquid flow drawn from the He I bath to $p \approx 11\,\mathrm{mbar(a)}$, corresponding to a saturation temperature of 1.7 K. The low-pressure two-phase flow passes HX40, cooling the lower bath section in the vessel. At a temperature $T_\lambda \approx 2.17\,\mathrm{K}$, the liquid in the lower section is transformed into the superfluid He II by second-order phase transition. With further cooling until steady-state operation, the temperature of the He II phase is controlled to $T \approx 1.8\,\mathrm{K}$. The λ-plate separating the two liquid phases includes minimal leaks in order to allow for pressure compensation. Exposed to the vessel pressure of $1.2\,\mathrm{bar(a)}$, the He II phase is in a sub-cooled state.

The low-pressure exhaust flow from HX40 pre-cools the He I in HX43, increasing the liquid phase yield downstream of V43. It is warmed up in EH40 in order to enable room-temperature compression to the return line pressure by means of roots or rotary-vane pumps used for P40[b] [241]. The warm exhaust flow from P40 is directly returned into the warm helium header via V07.

4.2.3.3 Inner shield cooling

The inner thermal shield of the TM cryostat is operated at $T \approx 5\,\mathrm{K}$ and is cooled prior to the payload in order to provide cold surfaces for cryopumping close to the mirrors, avoiding or limiting frost build-up on the optics. The respective cooling power is provided by a supercritical helium flow through HXIS, which represents the inner shield heat exchanger as shown in Figure 4.3. The corresponding flow at 5 K/5 bar(a) is drawn from the header inside the 1.8 K unit. A separate warm helium supply is implemented for mixing in order to control gradual cool-down via V46.

In steady-state operation, the supercritical helium supply passes V49 for further cooling in HX41 by means of the He I bath, enabling inner shield temperatures for cryopumping as low as possible. Valve V39 is used to expand the yet supercritical return flow to the lower pressure of the He I bath return line, which it joins in V40. This configuration is implemented to ensure single-phase flow through HXIS, substantially reducing vibrational noise in the inner shield as compared to two-phase flow [242]. Noise damping in the inner shield is necessary, as Shapiro et al. [243] report on noise coupling between the inner thermal shield and the interferometer optics due to scattered laser light.

---

[b] The usage of *cold* or *mixed* compression as suggested in [240] to pump on the helium at 11 mbar(a) is not an option, due to the low expected flow rates and the lack of commercial equipment in this capacity range.

4.2.3.4 Pre-cooling of the payload

The cooling system is designed such that the cool-down speed of the payload can be controlled across the whole temperature range between 300 and 2 K. This is foreseen to ensure minimal thermal stress in the sensitive last suspension stage. The pipework connections indicated in Figure 4.3 between the payload heat exchanger (HXPL) and valves V56 and V57 are implemented in form of multiple parallel thin-wall capillaries. This improves the performance of the He II cooling as well as the seismic vibration attenuation compared to rigid pipes or solid thermal links[c].

In the cool-down phase, helium streams of different temperatures are mixed so that the helium temperature through V56, the supply capillaries, the payload heat sink HXPL, the return capillaries and V57 are controllable at supercritical pressure. Hence, the helium flow through this circuit is single-phase, limiting the vibrational noise induced in the payload interface during cool-down, analogously to the inner thermal shield cooling. In the beginning of cool-down, V38 is the defining mixing valve. A flow of room-temperature helium from V30 joins a flow at 50 to 80 K from V35. The resulting stream passes V53 and is fed into the capillary loop via V56. The warm exhaust is directed back to the compressor system via V37, where it joins the HXOS/HXCT return.

Once HXPL reaches temperatures of 50 to 80 K, a colder flow drawn from the 5 K header via V46 can be added by opening the second inlet of V53. Upstream, this flow is further cooled in HX41 and the flow rate towards V53 is adjusted by V50. The other part of the flow is used for the inner shield cooling (cf. Section 4.2.3.3). While supply temperatures of $T \geq 5\,\mathrm{K}$ are desired, HX42 is bypassed using V51.

Below 5 K, all the helium flowing through HXPL is precooled by the He II bath to $T \approx 3\,\mathrm{K}$ via HX42, with V52 controlling the flow rate, while keeping the upstream pressure supercritical. With a closed inlet from V38 into V53, valves V50, V52 and V58 allow for pressure control inside the capillary pipework and HXPL. At temperatures $T < 4.4\,\mathrm{K}$, these valves are used to match the capillary pressure with the He II bath pressure. Hence, at this point of the cool-down, there is subcooled He I located between valves V52 and V58. In-between valves V54 and V44 as well as V55 and V45, there is an insulating vacuum that serves to limit the parasitic heat leak into the He II bath during capillary cool-down.

---

[c] Solid thermal links have proved to be a limiting factor for the interferometer sensitivity in the past [96], requiring substantial efforts for noise attenuation.

4.2.3.5 Steady-state payload cooling

The prerequisite for initiating the last cool-down step is the presence of subcooled He I at $T \approx 3\,\mathrm{K}$ and $p \approx 1.2\,\mathrm{bar(a)}$ between V56 and V57. The subsequent formation of He II inside the entire capillary connection length between the 1.8 K unit and the payload marks the end of the TM cryostat cool-down process. The superfluid transition temperature at the capillary steady-state operational pressure of $p = 1.2\,\mathrm{bar(a)}$ is $T_\lambda \approx 2.17\,\mathrm{K}$. Thus, due to the preceding capillary cool-down to $T \approx 3\,\mathrm{K}$, only a small temperature reduction of $\Delta T \approx -0.83\,\mathrm{K}$ needs to be achieved. Therefore, the inlet into valve V56 from V53 and the outlet from V57 to V58 are first closed, stopping the flow of sub-cooled He I through the capillaries and HXPL. Next, valves V54 and V44 as well as V55 and V45 are opened, so that the superfluid He II phase extends down to V56 and V57. Finally, V56 and V57 are opened, connecting the capillaries directly to the He II bath in the vessel. Hence, a He II condensation front forms, gradually progressing from the vessel through the stationary liquid in the capillaries towards HXPL, with HX40 being the heat sink of the He II process. This requires sufficient thermal insulation of the capillaries, which is provided by thermal shields cooled with the returns from HXIS and HXOS.

At the end of the cool-down process, the supply and return capillaries to/from HXPL are both filled with stationary He II connected to the bath, enabling efficient low-noise heat extraction from the payload. This represents the steady-state system operation for the 2 K-cooling of the payload interface.

4.2.4 Summary and prospects

Our conceptual helium cooling system design for ET-LF covers all cooling requirements with one cooling system in each of the three ET detector vertices. It enables full flexibility in terms of cool-down and warm-up of the arm pipe cryotraps, the TM cryostat's outer shields, the inner shields and the payload. This is typically required to provide experimental flexibility and to limit the installed cooling capacity for a subsequent cool-down of components, as compared to synchronous cool-down and warm-up of the entire cryogenic system. In steady-state operation, minimum noise input is guaranteed by stationary subcooled He II heat extraction through thin capillaries from the payload to the 1.8 K units, and by single-phase supercritical flow through the inner shield heat exchangers. The temperature of the inner shield can be as low as 5 K, enabling efficient cryopumping closely around the somewhat warmer optics.

The general concept proposed in this document leaves room for further system development and optimization. For a more detailed engineering of the cryoplant and the underground cryogenic infrastructure, estimates of the heat loads in steady-state operation and during cool-down need to be refined, depending on advancements in the ET system design.

As a next step, our investigations will focus on the design of the capillary connections between the 1.8 K units and the payload heat exchangers. In this context, we will develop a thermally consistent capillary configuration and transfer line design, which at the same time offers minimal noise introduction into the payload via the cooling system interface.

4.3 Advances and outlook

This section is a supplement to Section 4.2, providing insights to aspects of further ET cooling system development. Specifically, on the basis of evolved cooling system design parameters, its input power consumption is approximated in a first approach. Moreover, foundational insights are given regarding the future cryoplant incorporation in the cryogenic infrastructure of ET as well as the design of the required cryogenic helium transfer lines.

4.3.1 Consumer specifications refinement

During the course of this work, the ET project progress allowed refining the temperature levels and heat load estimations of Table 4.2. The respective values are listed in Table 4.3. Firstly, it reveals the advancement in the cryopump design for ET-LF which considers the necessity of different cryopump/cryotrap (CP) designs based on their position. In fact, the pumps towards an adjacent tower at T_{amb} require a low-temperature section at 3.7 K for hydrogen pumping and have an overall length of 20 m. In contrast, the CPs towards the Fabry-Pérot arm cavities are merely 10 m long and their complete cryopumping section is operated at 80 K. These design differences arise from the higher residual gas pressures inside the adjacent towers at T_{amb} with respect to the 10 km long optical cavities [108, 235, 244].

Further, the CPs in ET-LF will be equipped with angled optical baffles (cf. Figure 4.1) at 10 K, which completely mask the TM view on the 80 K cryopumping surfaces. This

Table 4.3: Refined temperature levels and estimated cooling capacities required for every cryogenic consumer in ET during steady-state operation. Of all listed consumers, twelve equal units will be installed ET-wide (cf. Table 4.1).

Consumer	GWD	Temperature level / K	Cooling power / W
Cryopumps around TM cryostat[a]	ET-LF	3.7 80	1.65 4300
Optical baffles[a]	ET-LF	10	42
Cryopumps around TM tower[a]	ET-HF	3.7 80	4.10 1900
3rd (outer) thermal shield	ET-LF	80	2700
2nd (elsewhere[b]: 'inner') thermal shield	ET-LF	5.0	25
1st (innermost) thermal shield[c]	ET-LF	1.9	2.00
Payload heat sink[d]	ET-LF	1.9	1.00

[a] Conceptual design of these pumps and baffles is under development [108, 235].
[b] Cf. Section 4.2.
[c] Cf. Chapter 5.
[d] Comprises expected heat load on payload (cf. Section 3.1) and cooling power for instrumentation thermalization.

configuration significantly contributes to the efforts of limiting thermal radiation heat loads on the cryogenic TMs of ET-LF [2, 71].

The design concept of the ET-HF cryopumps has yet to be developed. It is anticipated, however, that in comparison to the pumps in ET-LF, longer pumping sections at 3.7 K and shorter ones at 80 K are needed to provide the required vacuum qualities. The lower necessary vacuum levels around the ET-HF test masses result from the fact that, unlike in ET-LF, the TMs will be operated at T_{amb} and hence are not susceptible to residual gas molecule adsorption [106].

Within the thermal shielding concept of ET-LF cryostats, a 1st shield is considered at 2 K operating temperature and an engineering design value of $\dot{Q}_{\text{c}} = 2\,\text{W}$. A study of this design choice is provided in Chapter 5. Similarly, for the payload heat sink supplying cooling power to the TMs, a total target design value of $\dot{Q}_{\text{c}} = 1\,\text{W}$ has been defined within the ET project. This includes 0.5 W for payload instrumentation cabling thermalization and further 0.5 W for heat extraction from the mirrors, as is presented in Section 3.1.

Besides, the 2$^{\text{nd}}$ thermal shield's operating temperature persists at 5 K, while for the outer thermal shield, the temperature level is specified to 80 K, harmonizing with the adjacent CPs in ET-LF. The cooling power required for both the 2$^{\text{nd}}$ and 3$^{\text{rd}}$ thermal shield has been determined by scaling the approximated heat loads on the 3.7 K- and 80 K cryopump sections in ET-LF with the shields' outer surface areas. This reflects the fact that the dominating cause of heat load on the cryopumps and thermal shields is thermal radiation. State-of-the art MLI commonly used in low-temperature applications to limit radiative heat loads is incompatible with the ultra-high vacuum (UHV) and XHV requirements of ET [71]. While the outgassing water can be effectively pumped on the surfaces of the inner shields, microscopic dust particles stemming from the MLI blankets may propagate to and settle on the TM surfaces. This results in the creation of significant hotspots during interferometric laser operation, ultimately degrading the detector performance. The development of a suitable replacement of MLI for ET is therefore the subject of current R&D efforts [102].

The conceptual cooling system design presented in Section 4.2 allows a straightforward consideration of the ET-HF cryopumps as well as the introduction of an innermost thermal shield at $T = 2\,\text{K}$. As Figure 4.2 shows, the ET-HF cryopumps are located 50 m to 60 m away from the closest ET-LF TM cryostat. Thus, they can be provided with cold helium from the respective cryogenic supply unit (CSU) (elsewhere called '1.8 K unit') via short transfer lines linked to the V33/V36 connection (cf. Figure 4.3). The optical baffles at 10 K can be similarly supplied by means of either a helium flow mixed from additional connections to V46 and V33 or using the 5 K circuit by branching off the flow downstream of V48. The latter case results in a temperature gradient $\Delta T \approx 5\,\text{K}$ between the baffles and their respective cooling interfaces. For both of these supplements, it proves advantageous that, from the perspective of an ET vertex center, near which the central coldbox will be placed, the ET-HF cryopumps are positioned farther away than their LF counterparts. Specifically, final refrigeration and flow conditioning for both the cryogenic consumers attributed to the ET-LF TMs and the cryopumps on either side of the ET-HF TMs can be achieved in the CSUs situated close to the ET-LF TMs. Figure 4.4 visualizes this. The arrangement allows for fewer transfer lines running in parallel through the caverns and avoids the need for additional CSUs or valve boxes next to the HF cryopumps.

The innermost thermal shield in an ET-LF cryostat may be connected to the same He II bath as the payload heat exchanger via independent links (cf. Chapter 6). For a gradual shield cooldown, an interconnection similar to the V38/V53/V56/V57/V58/V37 configuration is required. An adaptation of the process flow diagram shown in Fig-

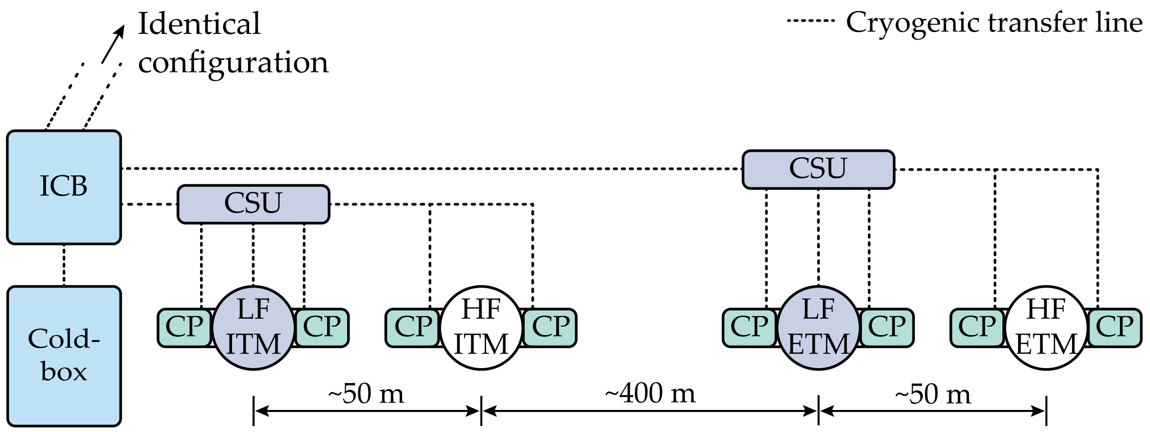

Figure 4.4: Basic illustration of the underground helium infrastructure layout in an ET vertex of the triangular xylophone configuration. Schematic top view based on Figure 4.2.

ure 4.3 considering the refined cryogenic consumers mentioned above is provided in Appendix A.1.

4.3.2 Cryogenic transfer lines

The cryogenic infrastructure concept presented in Section 4.2 relies on helium distribution via cold transfer lines. Depending on the type of cryostats they connect to, different configurations are required. Relatively short lines couple the decentralized cryogenic supply units with the consumers. In contrast, significantly longer lines link the former with centrally positioned interconnection boxes (cf. Figure 4.3). Figure 4.5a shows an indicative cross-section of this transfer line type, which includes supply- and return piping at different temperature levels.

The helium-carrying process pipes are surrounded by a supporting structure made of glass-fiber reinforced plastic (GFRP) to position the pipes, while further providing thermal insulation against the ambiance. Protection from room-temperature thermal radiation is granted by a thin shield that is thermally anchored to the $\sim$80 K return line (anchors not depicted in cross-section). The shown GFRP supports are integrated at discrete intervals along the transfer line length. Figure 4.5b presents an exemplary layout.

The short support sections are depicted, which must not rigidly link the thermal shield and vacuum envelope to accommodate the thermal contractions of the cryogenic parts with respect to their dimensions at T_{amb}. Contractions of the cryogenic pipes themselves, which need to be rigidly connected at their ends, are enabled by the integra-

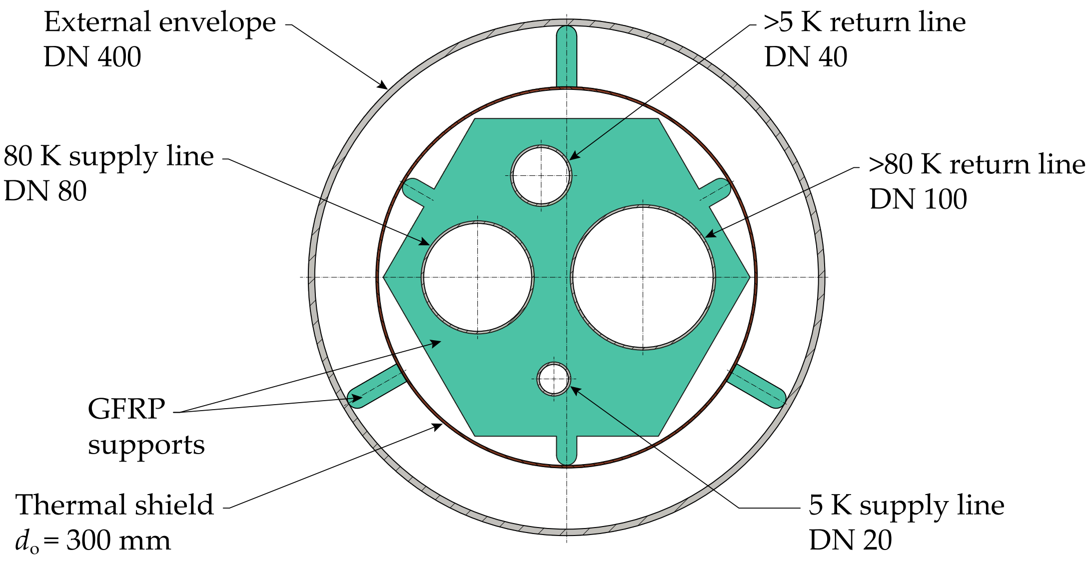

(a) Cross-section view.

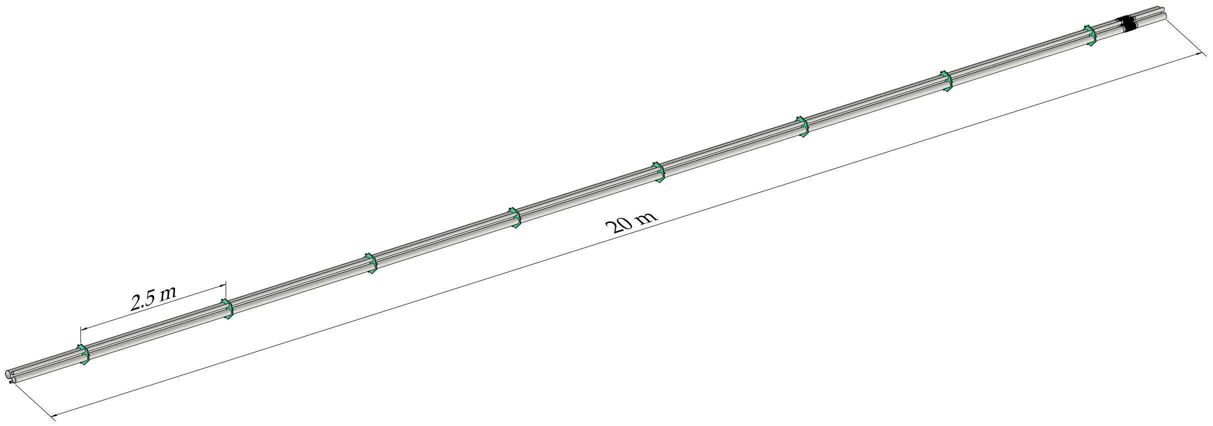

(b) 3D view of a module interior including support structures and bellows.

Figure 4.5: Schematic visualization of a 20 m long cryogenic transfer line section between an interconnection box and a cryogenic supply unit (cf. Figures (4.3) and (4.4)). Inner pipe diameters are chosen to allow for estimated pressure drops of $\Delta p \leq 100$ mbar between end connections which are ∼500 m apart.

tion of bellows (right hand side of Figure 4.5b) that compensate the respective length changes. Conventionally, long cryogenic transfer line pipes are built from prefabricated sections of 10 to 20 m length due to transport limitations. Figure 4.4 indicates the approximate distances these lines must span in order to distribute helium from a centrally located (i.e. close to the ET triangle vertices) coldbox with adjacent interconnection box (ICB) to the CSUs positioned in proximity of most consumers. The ET-wide total length of these main transfer lines is around 5 km.

Along their entire distance, the cold helium lines are subject to heat loads, predominantly by thermal radiation and -conduction through the solid support structure. For the transfer line configuration presented in Figure 4.5, the approximated total length-specific heat load on the return line at $T_{\mathrm{He}} > 80\,\mathrm{K}$ is $\dot{Q}_{\mathrm{c}} = 3.0\,\mathrm{W\,m^{-1}}$ [245]. On both the supply- and return line at $T_{\mathrm{He}} \approx 5\,\mathrm{K}$, these loads are estimated to amount to $\dot{Q}_{\mathrm{c}} = 0.15\,\mathrm{W\,m^{-1}}$, based on comparison to similar lines [246]. Consequently, the sum of the heat load on all return lines at $T_{\mathrm{He}} > 80\,\mathrm{K}$ in ET is $\dot{Q} \approx 15\,\mathrm{kW}$, while the supply- and return lines carrying helium at $T_{\mathrm{He}} \approx 5\,\mathrm{K}$ are subjected to $\dot{Q} \approx 1.5\,\mathrm{kW}$ combined.

With respect to the long transfer lines addressed above, the connections between cryogenic supply units and ET-LF cryostats will be much shorter ($L \approx 10\ldots20\,\mathrm{m}$) but also more complex due to the incorporation of a third supply/return connection at $T \approx 2\,\mathrm{K}$ (cf. Figure 4.3). As is addressed in Section 4.2, these connections will be comprised of thin capillaries or tubes. This is due to the fact that they will be linked to the sensitive cryogenic payloads in ET-LF, which places extreme constraints on the design. The increased variety of interfaces with different ET subsystems in close proximity to the payloads implies to develop the supply lines to the ET-LF cryostats from within the project. This is made evident in Chapters 5 and 6.

4.3.3 Cryoplant input power

As Section 4.2 shows, purely helium-based cryoplants are able to supply cooling power at all required temperature levels in ET. Due to the fact that final refrigeration to temperatures below 5 K is done in satellite cryogenic supply units close to the respective consumers, the coldboxes located centrally in the ET vertices may follow a state-of-the-art design of expert companies in this field. Exemplary references are the industry-supplied established coldboxes for the LHC [247, 248]. They are integrated into the corresponding overall cryogenic architecture [238], where the consumers are located underground, while the warm compressor stations are situated on the surface, as is envisaged in Section 4.2. Each of the eight cryoplants for the LHC has an installed input power of $P_{\mathrm{input}} \approx 5\,\mathrm{MW}$ [249, 250]. The following paragraphs show that the estimated required input power for the ET cryoplants is significantly lower.

The refined cooling power ranges presented in Section 4.3.1 permit a first scale determination of the input power consumption of the required cryogenic plants in ET. An extensive survey of Strobridge [251] includes an indication of typical Carnot efficiency fractions COP/COP_{C} of cryogenic refrigerators depending on their cooling capacity. This allows input power consumption estimations of cryoplants used to generate the approximated cooling capacities for ET via

$$P_{\mathrm{input}}(T_{\mathrm{c}}, \dot{Q}_{\mathrm{c}}) = \frac{\dot{Q}_{\mathrm{c}}(T_{\mathrm{c}})}{COP_{\mathrm{C}}(T_{\mathrm{c}}, T_{\mathrm{amb}})} \cdot \left(\frac{COP}{COP_{\mathrm{C}}}\right)^{-1}_{\dot{Q}_{\mathrm{c}}(T_{\mathrm{c}})} . \tag{4.1}$$

The approximated cooling power provided by a cryogenic refrigerator is denoted by $\dot{Q}_c$ and the coefficient of performance of the Carnot process by COP_C. Thus, the total cryoplant power consumptions in ET for the provision of cooling capacities at all required cryogenic temperature levels can be estimated.

In order to gain reliable calculation results, a consideration of the cryogenic helium infrastructure presented in Section 4.2 is imperative. Provision of consumers with cooling power at $T < T_{\mathrm{sat,He}}(p = 1\,\mathrm{atm})$ entails a subsequent warmup of the corresponding helium flow in order to enable recompression. Thus, these return flows cannot be used for precooling helium supply and as a consequence, regarding these cooling powers, the ET cryoplants act as helium *liquefiers* instead of refrigerators. This process distinction is effectively illustrated in [252].

Equivalent refrigerator cooling capacity

In order to apply Equation (4.1), liquefaction cooling power provided by the cryogenic infrastructure at $T < 4.2\,\mathrm{K}$ is converted to *equivalent refrigerator cooling capacity* following Wagner [252]. Accordingly, comparing a refrigeration cycle to a liquefaction cycle at equal input power leads to

$$\dot{M}_{\mathrm{eq,refr}} = \frac{l_{\mathrm{liq}}}{l_{\mathrm{refr}}} \cdot \dot{M}_{\mathrm{liq}} \,. \tag{4.2}$$

The terms l_{liq} and l_{refr} refer to the specific *minimum liquefaction and -refrigeration work* (elsewhere also called 'ideal' or 'reversible' work), respectively (e.g. [253–255]). They represent the specific energy required by the thermodynamic cycles illustrated in Figure 4.6 to re-cool helium from states ② to state ①.

$$l_{1\text{-}2} = (h_1 - h_2) - T_{\mathrm{amb}}\,(s_1 - s_2) \ , \tag{4.3}$$

with h denoting specific enthalpy and s specific entropy. State ① is the helium supplied to the consumer and state ② constitutes the He return conditions to the cryoplant. A sample of relevant points in the scope of the helium cooling system presented in Section 4.2 is visualized in Figure 4.6.

In order to provide cooling power at $T_c = 1.9\,\mathrm{K}$ at the interfaces with the ET-LF cryostats (cf. Table 4.3), the lowest temperature in the helium infrastructure is chosen as $T_c = 1.65\,\mathrm{K}$ to account for thermal gradients along the heat extraction path to the cold side of HX40 (cf. Figure 4.3). Due to the sub-atmospheric saturation pressure of helium at $T_c = 1.65\,\mathrm{K}$, the corresponding flow is warmed up to T_{amb} by electrical heater EH40 before it is returned to the cryoplant. Consequently, with respect to the

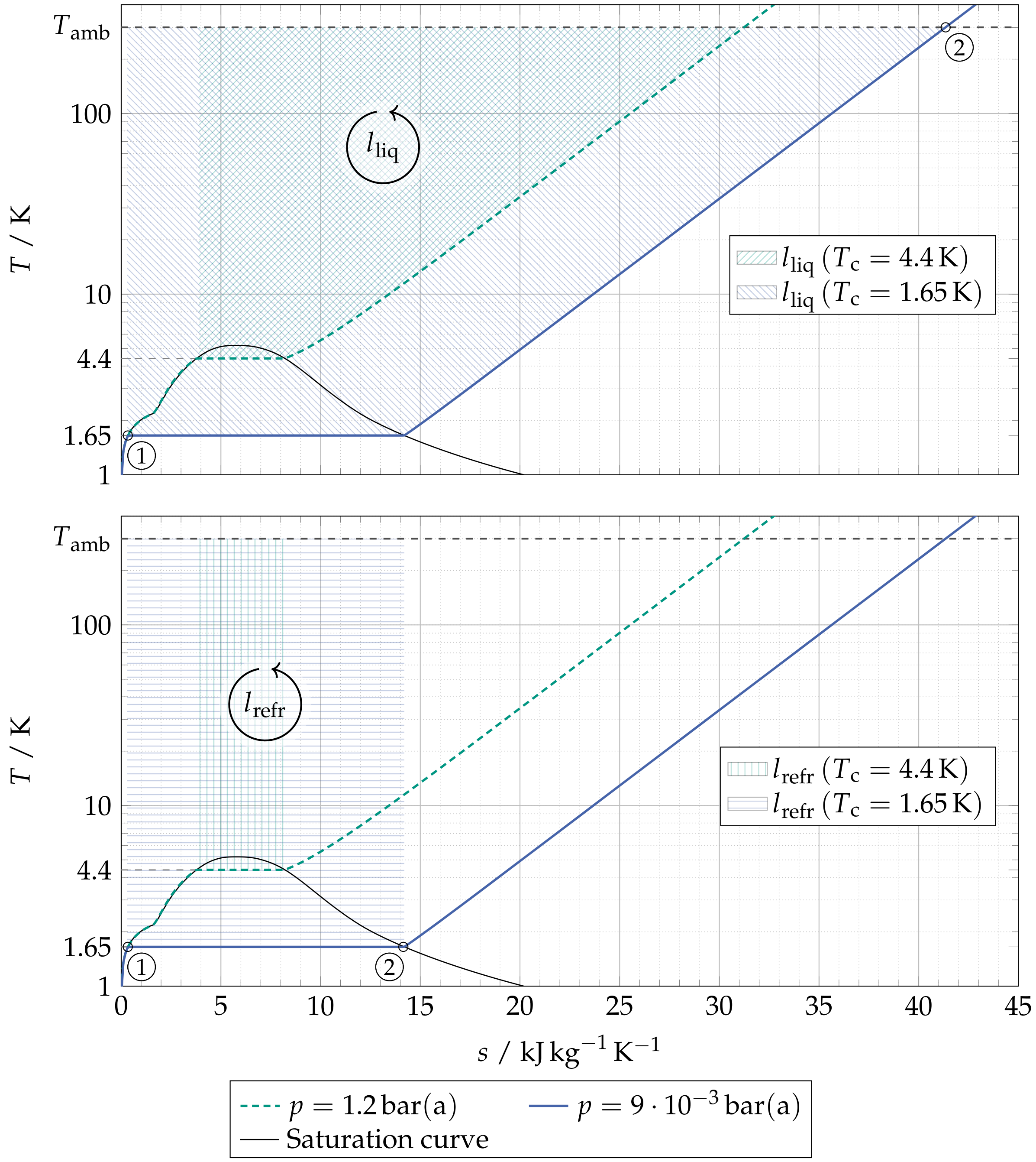

Figure 4.6: Visualization of minimum liquefaction- (*top*) and equivalent refrigeration (*bottom*) specific energy demands for cooling at subatmospheric pressure in ET consumers. Fluid property data from [126].

provision of cooling power at 1.65 K, the ET cryoplants operate as liquefiers. Thus, state ② is at saturated vapor conditions in refrigerator mode and at $T = T_{\mathrm{amb}}$ in liquefaction mode. The hatched area (▨) within the graph is an effective visualization of the resulting l_{liq}. The analogous case (□) applies to l_{refr}.

The above holds analogously for all cycles with $T_{\mathrm{c}} = 3.7\,\mathrm{K}$, which cool parts of the cryopumps (cf. Table 4.3). Design details of the associated heat extraction paths are yet unavailable, and therefore, no thermal gradients are considered in this work.

Ultimately, equivalent refrigeration capacities are obtained via

$$\dot{Q}_{\mathrm{c,eq,refr}}(T_{\mathrm{c}}) = \dot{M}_{\mathrm{eq,refr}} \cdot \Delta h_{\mathrm{vap}}\left(T_{\mathrm{c}}\right), \tag{4.4}$$

with the specific enthalpy of vaporization Δh_{vap}. Calculated values required in this context are listed in Table 4.4. In turn, Appendix A.2 gives the corresponding state variable values at ① and ②, along with Δh_{vap}.

Equivalent refrigeration capacities and input power results

Finally, the above-addressed refined cryogenic consumer specifications, helium transfer line conceptual structure and equivalent refrigeration capacity calculation method allow for a cryoplant cooling capacity- and input power sizing for ET. Table 4.5 presents an overview of cooling capacities needed in ET as well as approximated equivalent refrigeration powers and the resulting efficiencies of each of the three ET cryoplants for cooling power provision at all required values of T_{c}.

With the given values, Equation (4.1) yields a preliminary cryoplant input power determination for ET. Figure 4.7 puts these into proportion. The total estimated electric input power for ET cryogenics is around 2.5 MW. All cryopumps including actively cooled optical baffles in ET-LF cause $\sim$ 45 % of this total consumption. The other $\sim$1.4 MW predominantly originate in transfer losses of the helium at $T \approx 5.0\,\mathrm{K}$ and ET-LF cryostat thermal shielding at $T \approx 80\,\mathrm{K}$. The lowest-temperature cryogenic con-

Table 4.4: Parameter values for equivalent refrigeration capacity calculation via Equation (4.4). Given mass flows are based on the total ET cooling power consumption.

T_{c} / K	$\dot{M}_{\mathrm{liq}}$ / g s^{-1}	l_{liq} / kJ kg^{-1}	l_{refr} / kJ kg^{-1}	$\frac{l_{\mathrm{liq}}}{l_{\mathrm{refr}}}$ / –
1.65	0.53	10 550	4140	2.55
3.70	1.01	7128	1777	4.01

Table 4.5: Approximated cooling capacities required in ET during steady-state operation depending on their expected temperature levels and consequent estimated cryoplant efficiencies.

Parameter	T_c 80 K	 10 K	 5 K	 3.7 K	 1.7 K
			ET total		
$\dot{Q}_c$ / W	$1.1 \cdot 10^5$	500	300	70	36
$\dot{Q}_{c,eq,refr}$ / W	"	"	"	280	92
			per cryoplant		
$\dot{Q}_{c,eq,refr}$ / W	$3.5 \cdot 10^4$	170	100	94	31
$\dot{Q}_{CTL,total}$ / W	$5.0 \cdot 10^3$	n/a	500	n/a	n/a
$\dot{Q}_{c,eq,refr,total}$ / W	$4.1 \cdot 10^4$	170	600	94	31
$\frac{COP}{COP_C}$ / – [251]	0.26	0.11	0.15	0.10	0.08

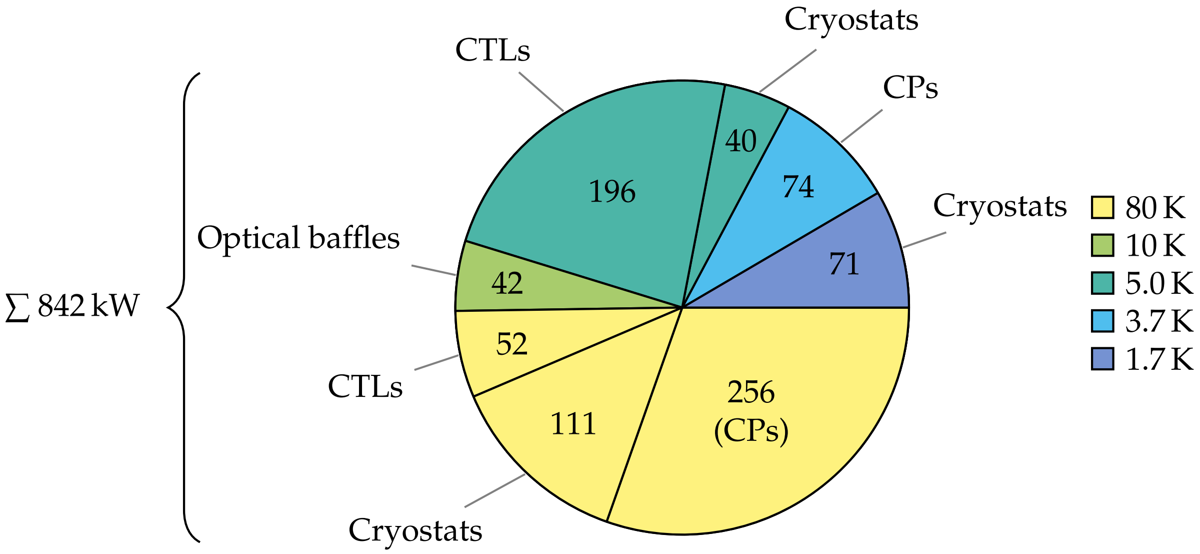

Figure 4.7: First electric power consumption estimations for each of the three cryoplants in ET (triangular xylophone configuration) with distinction between temperature levels at which cooling capacities are supplied (cf. Table 4.3).

sumers at $T \approx 1.7\,\mathrm{K}$ are responsible for merely $\sim 8\,\%$ of the total electric power consumption. Per cryoplant in each of the three ET vertices, the sum of cooling power consumption results in $P_{\mathrm{input}} \approx 850\,\mathrm{kW}$, which is to be supplied virtually exclusively to the surface compressor system (cf. Figure 4.3).

It is emphasized again that the cooling power calculations above hold for steady-state operation. Some additional power will be needed for cooldown, depending on a more detailed design and operating strategy.

5 Thermal shielding in the ET-LF cryostats

Existing applications of thermal shields around cryogenic optics for interferometric GWDs have proven to be a considerable design challenge due to the extreme implementation demands in the immediate vicinity of the test masses. This chapter is therefore dedicated to the developments carried out in the scope of this thesis regarding the shield design as well as first constraints for the overall cryostat geometries in ET-LF.

5.1 Conceptual cryostat design

The basic scheme of an ET-LF test mass cryostat is presented in Section 4.1. Multiple thermal shields encompass the cryogenic payload, preventing excessive heat load due to thermal radiation and substantially enhancing the TM cooldown performance (cf. Sections 3.1.4.5 and 3.2.2). The implementation of three thermal shields is suggested, allowing configurations such as two actively cooled inner shields and a passive outer one or three actively cooled shields with the innermost being operated at $T \approx 2\,\mathrm{K}$. The latter approach is described in detail in Section 5.3. Either of the mentioned configurations is supported by the fact that MLI is unsuitable for the implementation in the environment of cryogenic test masses (cf. Section 4.3.1).

Examination of the general composition of an ET-LF test mass cryostat, which accordingly hosts three thermal shields and a payload with the baseline parameters listed in Table 3.2 allows for the derivation of its overall proportions. Figure 5.1 presents the conceptual layout. Further fundamental considerations regarding the cryostat layout include an assembly- and integration access from below, as implemented in Virgo [39], as well as a singular cryostat vacuum. This streamlines the cryostat design and enables established procedures for payload incorporation. The latter can be ensured via the bottom aperture of inner diameter $d_\mathrm{i} = 1.6\,\mathrm{m}$. Access can be enabled by a basement level underneath the large ET tower caverns [71]. Some clearance to the 1st (innermost) thermal shield is provided around the payload, for its installation and additional instrumentation close to the mirror. Within this clearance, heat link vibration isolation systems (HLVISs) are indicated, attached to the top of this shield. These are

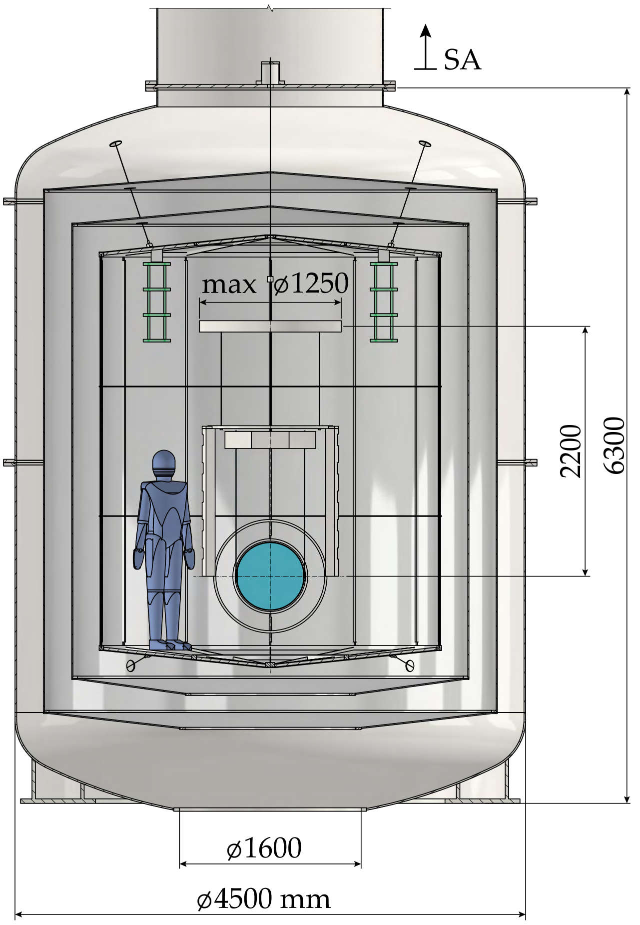

Figure 5.1: Conceptual layout of the ET-LF test mass cryostats with outer dimensions (for isometric view, cf. Figure 5.5).

further addressed in Sections 5.3 and 6.2. The shields themselves are implemented as thin metal panels connected by intermediate struts as elaborated in Section 5.3. The cryostat structure concept envisages gaps of 250 mm between all shields in longitudinal and radial direction. The same clearance is applied between the outer (3^{rd}) shield and the vacuum vessel. This accounts for required space for shield reinforcement structures as well as interface geometries to the cooling system and possible thermal insulation alternatives to MLI. Further, the spacing suggestion enables a determination of the scale of the total cryostat dimensions. It amounts to an outer diameter $d_o = 4.5\,\text{m}$ and height $H_o = 6.3\,\text{m}$ from floor level to the flange connection to the upper SA vacuum vessel.

These spatial extents are well compatible with the ET beam pipe arrangement possibilities in the long tunnels hosting the majority of the Fabry-Perót cavities, as Figure 5.2 visualizes. Four beam pipes are arranged inside the tunnel (cf. Figure 4.2). The exemplary layout envisages beam pipes with a diameter of 1.0 m. The inner tunnel diameter is assumed to be 6.5 m [71]. A minimum clearance of 0.5 m is foreseen between the beam pipes and the concrete tunnel lining in order to account for ancil-

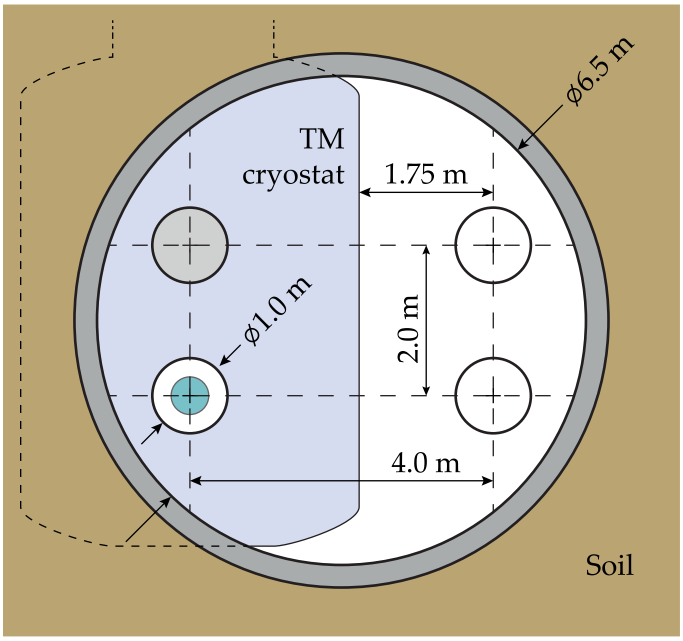

Figure 5.2: Exemplary cross section configuration through a cavity tunnel in ET with indicated ET-LF test mass cryostat in an adjacent cavern.

lary geometries such as tube reinforcements or flanges. This maintains a separation of the pipe center axes of 2.0 m in vertical and 4.0 m in horizontal direction, providing a maximum free path of 3.0 m in the tunnel center for installation- and maintenance purposes. Put in relation to the overall ET-LF test mass cryostat dimensions, this yields a clearance of 1.75 m between the cryostat wall and the beam pipe center axes of the opposing HF and LF interferometers. The ET interferometric layout does not require the placement of two TM towers directly adjacent to one another. Thus, substantial space remains around all cryostats for expected structural reinforcements of the vacuum vessel, which are likely required to prevent low resonant frequencies of the latter. Among others, this issue is approached for the case of the innermost thermal shield in the following sections.

5.2 Detector noise contributions

A vital design aspect of the test mass surroundings is the consideration of their noise introduction into the GWD. In this thesis, which follows a cryostat design procedure from inside outwards, the focus is on the architecture of the innermost thermal shield. It must account for three key noise sources:

(I) Phase- and amplitude noise due to light backscattering

(II) Seismic noise due to mechanical vibration coupling to the payload

(III) Newtonian noise due to residual mass redistributions, such as microscopic transient fluctuations in the coolant flow

The latter one is considered in the fundamental working principle of the steady-state He II shield cooling which does not involve a fluid flow in the TM vicinity (cf. Section 5.3). The former two are addressed in the following.

Light backscattering

Figure 5.3 visualizes the process of light scattering in an interferometric GWD on a macroscopic level. A small portion of photons hitting a test mass scatter from the primary beam due to imperfections in substrate or coating. This scattered light can re-enter the main beam after undergoing reflection, scattering, or diffraction from any surface with a viewing angle on the mirror, which ultimately causes a slight phase shift in the main beam's light [256]. Vibrations of these surfaces cause this phase shift to oscillate, mimicking the effect of a gravitational wave [257]. Further, back-scattered light causes fluctuations of the radiation pressure on the test mass [258].

These effects lead to the introduction of phase- and amplitude noise to the detector. The former dominates at higher detection frequencies, and the latter at lower ones [258]. For intermediate values of the scattering angle θ_s, this issue has been accounted for in current GWDs by implementing ground-connected baffles in the beam pipe. Small-angle scatter from the far test mass and large angles are covered by suspended baffles [39, 44]. Foreseeing similar measures in ET is imperative for achieving its sensitivity goals [256].

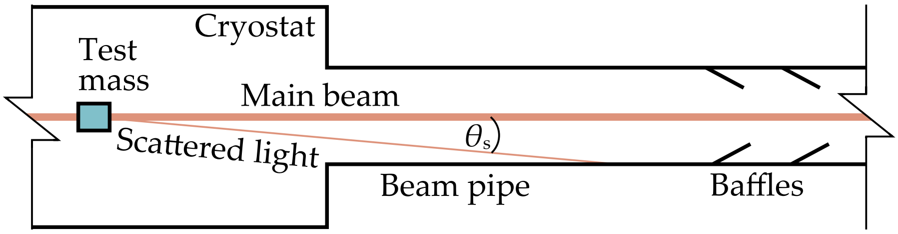

Figure 5.3: Schematic visualization of light scattering at a test mass face at an angle θ_s from the main beam axis.

In KAGRA, where thermal shields are rigidly connected to the cryostat via supports composed of thermally insulating material, wide-angle baffles are introduced between test masses and innermost thermal shields. The baffles are implemented as hollow cylinders of length $L = 570\,\mathrm{mm}$ separated by a $10\,\mathrm{mm}$ gap from each test mass face towards the arm cavity [109], diminishing the viewing angle between thermal shields and mirrors [259]. The inside baffle surfaces are finished with a low-reflectance coating, mitigating light backscattering. Further, the baffles are suspended from the shield itself as a single pendulum with vertical springs in order to attenuate excessive shield vibrations attributed to structural resonances and cryocooler operation [97, 109]. Additionally connected flexible heat links (cf. Section 2.1) provide sufficient thermal contact for cooling the baffles [93].

Mechanical vibration coupling

For the cryogenic operation of payloads in interferometric GWDs, within the scope of the cooling concepts presented in Sections 2.1, 2.2 and 2.4, mechanical links will be required connecting the cooling system to a payload interface.

An approach to mitigate seismic noise transmission via these links into the bottom of the TM suspension chain is to intercept them with heat link vibration isolation systems (HLVISs) [96]. Such systems are implemented in KAGRA as visualized in Figure 5.4. They consist of a chain of three stages, each connected to the previous one by four ten-

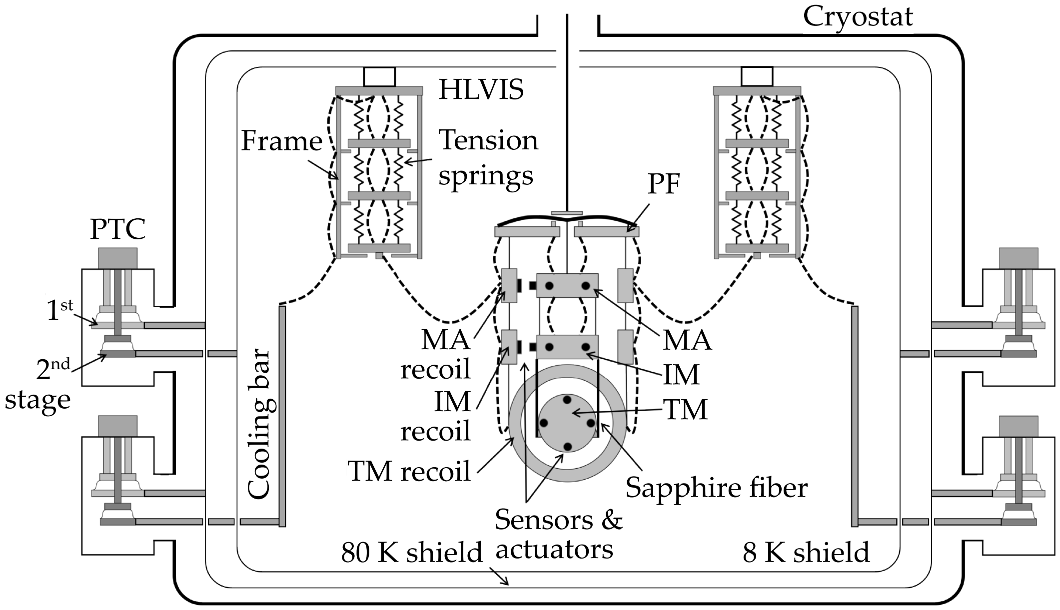

Figure 5.4: KAGRA payload cryostat heat extraction path scheme including heat link vibration isolation systems (HLVISs) (adapted from [96], licensed under CC BY 3.0).

sion springs. The flexible heat links originating from the cooling bar are successively anchored to these stages. This results in a drastically declining vibrational transfer function for $f > 10\,\mathrm{Hz}$ of the heat extraction path in KAGRA. Carrying a part of the low-temperature heat extraction path, these systems are hosted inside the innermost thermal shield. However, attaching the HLVISs to the shield ultimately couple the shield vibrations to the test mass.

It is estimated within the KAGRA project that this mechanical coupling introduces significant noise to the detector, especially at low frequencies, which is attributed to internal resonance of the cooling system and cryocooler operation [97]. The displacement spectral density of the vibrations coupled from the shield to the KAGRA test masses at around 10 Hz is on the order of $10^{-19}\,\mathrm{m\,Hz^{-0.5}}$. In the case of ET, this would correlate to a strain noise contribution on the order of $10^{-23}\,\mathrm{Hz^{-0.5}}$ considering the 10 km arm length. Comparing this magnitude to the ET design sensitivity (cf. Figure 1.6) reveals that a similar vibration coupling level as in KAGRA may limit the sensitivity of ET-LF in the particularly important lower end of the detection band.

The noise originating from the sources explained above must be reduced within the Einstein Telescope to achieve the substantially advanced target sensitivity. The arising requirements imply a tailor-made thermal shield architecture for ET-LF. Consequently, in this thesis, a He II-cooled shield design concept is developed that considers such noise mitigation efforts and is consistent with the overall cryogenic infrastructure concept for ET presented in Chapter 4.

5.3 Low-noise thermal shielding around the cryogenic payloads in the Einstein Telescope

Lennard Busch, Gregory Iaquaniello, Philippe Rosier, Michael Stamm,
Steffen Grohmann

2024 *IOP Conf. Ser.: Mater. Sci. Eng.* **1301** 012013.
DOI: 10.1088/1757-899X/1301/1/012013.

Abstract

The Einstein Telescope (ET) is a planned third-generation gravitational-wave detector that includes a low-frequency (LF) and a high-frequency (HF) laser interferometer. Cryogenic operation of ET-LF is imperative for exploiting the full scientific potential of ET, with mirrors operated at temperatures of 10 to 20 K in order to reduce the thermal noise. Thermal shielding around the optics is essential to support the cooldown process and to decrease the heat load. Additionally in steady-state operation, mechanical vibrations must be kept to an absolute minimum in order to limit noise contributions from scattered light.

We present a cooling concept for a thermal shield surrounding the cryogenic optics of ET-LF, which considers rapid cooldown and low vibration in steady-state operation. During cooldown, cooling tubes enable the flow of supercritical helium, driving the shield temperature decrease by forced convection. For steady-state operation, the shield cooling mechanism is converted to static heat conduction in He II within the same tubes. A first mechanical model is presented that fulfills the thermal and vibrational requirements. Thermal characteristics of the shield are demonstrated by means of analytical and numerical modeling results. Modal and dynamic analyses are performed to obtain natural frequencies and transfer functions.

5.3.1 Introduction

The Einstein Telescope (ET) is a European third-generation gravitational-wave (GW) detector currently under development. It combines a cryogenic low-frequency (LF) and a room-temperature high-frequency (HF) laser interferometer. GW detection frequencies of ET lie in the range of 3 Hz to 30 Hz (ET-LF) and 30 Hz to 10 kHz (ET-HF). The sensitivity goals of ET require extremely low noise budgets as stated in [71, 74].

A comprehensive study shows that the cryogenic ET-LF is imperative for exploiting the full scientific potential of ET [72]. Its strain target is on the order of 10^{-22} to 10^{-24} $\mathrm{Hz}^{-0.5}$. In order to achieve these demanding goals, a test mass operating temperature between 10 K and 20 K is required. Cryogenic test masses are part of the ET-LF payload, which comprises the lower end of the suspension chain attenuating ambient vibrations. A baseline design for the cryogenic payloads is published in [260]. One of the cooling concepts uses static He II heat conduction inside a suspension tube. He II operation is enabled by the cryogenic infrastructure concept described in [186]. ET-LF cryogenic payloads are installed in cryostats, requiring thermal shielding that must be optimized regarding the support of the test mass cooldown via thermal radiation [260], the reduction of heat load on the payload during detector operation as well as low vibrations, particularly in the detection frequency band of $f = 3 \ldots 30\,\mathrm{Hz}$.

Multiple actively-cooled thermal shields are considered in the ET-LF cryostats [186], whilst moving masses close to the core optics, such as the flow of helium, are potentially problematic. Hence, the concept for the innermost shield relies on static He II heat extraction, equivalently to the payload cooling concept, providing the quietest possible environment for the payload. The focus of this contribution is on a suitable design for this shield.

5.3.2 Thermal shielding structure

Figure 5.5 shows a conceptual ET-LF cryostat design including thermal shielding, following the payload baseline in [260]. The cryostat is able to host interferometer mirrors (test masses) with a diameter of up to 600 mm. A maximum payload diameter of 1.25 m is anticipated, fitting through a bottom access with 1.3 m minimum diameter. Considering the required assembly space based on experience from the Virgo GW detector, the inner shield dimensions are 3.0 m in diameter and 3.8 m in height. Figure 5.5 schematically depicts two additional thermal shields inside the cryostat, which has a large top flange to connect the upper tower containing the room-temperature suspension chain [71].

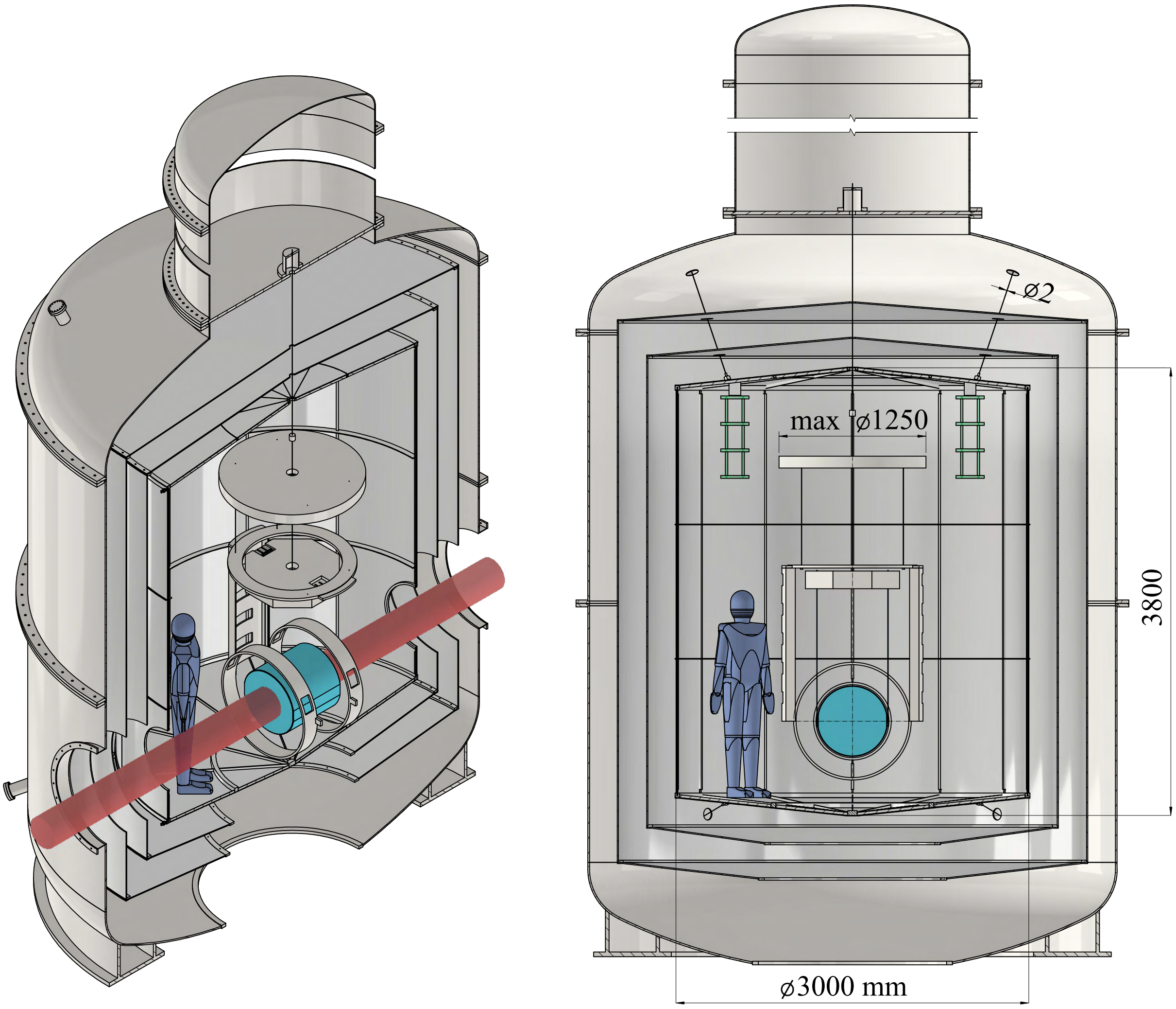

Figure 5.5: Conceptual layout of thermal shields for cryogenic ET-LF payloads within a dummy cryostat including indicated interferometer laser beam.

The helium cooling system concept for ET-LF foresees active cooling of the two outer thermal shields with supercritical helium flow at 80 K to 50 K and 5 K, respectively. The third shield as innermost screen around the payload is cooled at 2 K via thermal conduction through static He II, avoiding macroscopic fluid flow. Figure 5.6 presents the conceptual geometry of this shield. The He II cooling concept offers sufficient cooling capacity for both the payload and the inner shield. The potentially quietest form of cooling relates to the unique properties of superfluid helium rather than the 2 K temperature level. Particularly relevant is the exceptionally high thermal conductivity [132], yielding a thermal reservoir to absorb and conduct heat in the quietest (i.e. least dissipative) possible manner.

The basic support structure of the shield in Figure 5.6 consists of straight (vertical) as well as circular (circumferential) extruded hollow metal profiles, forming an interconnected channel system. Helium supply to the shield can be implemented using

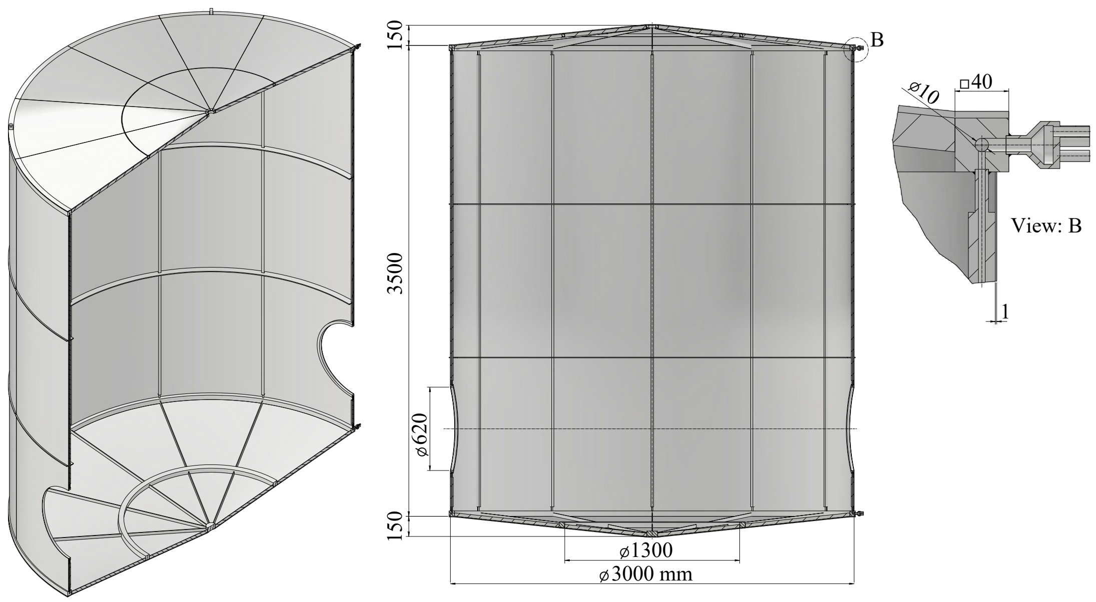

Figure 5.6: Conceptual design of the inner thermal shield in an ET-LF test mass cryostat, cooled with static He II.

thin-wall tubes in combination with bellows attached to vibration isolation systems, similar to the heat link concept in the KAGRA GW detector [96]. Two heat link vibration isolation systems are schematically indicated in Figure 5.5, connected to the shield top, facing inwards (see also Section 5.3.4). The thin-wall helium supply tubes connect the shield cooling interface to a cryogenic supply unit in the vicinity of the cryostat [186]. Figure 5.6 (View B) shows a schematic interface geometry between such tubes and the inner shield. One interface is placed on each circular header at the bottom and top of the shield frame, constituting the supply and return path during cooldown. Between the header profiles with 10 mm inner diameter, vertical profiles with 5 mm inner diameter are installed. The shield frame is covered with 1 mm thick metal panels, providing good thermal contact. A shield material allowing for small thermal gradients as well as a lightweight design is favorable. Therefore, commercially pure aluminum (Al 1000 series) is foreseen for both the welded frame profiles and the panels. The resulting total shield mass is ca. 450 kg.

5.3.3 Thermal modelling

The ET-LF inner thermal shield as displayed in Figure 5.6 has three operating modes: (I) pre-cooling from 300 K to 3 K or 4 K via forced convection heat transfer with a supercritical helium flow, (II) He II condensation into the pre-cooled shield, and (III) steady-state operation with static He II heat conduction. While pre-cooling with helium at adjustable temperatures is rather straightforward [186], the latter two modes are explained in the following.

5.3.3.1 Steady-state operation

Based on first estimations, we define an engineering design target of $\dot{Q}_{\text{total}} = 2.0\,\text{W}$ total heat load on the ET-LF inner thermal shield at the steady-state operating temperature $T_{\text{sh}} \approx 2\,\text{K}$. Contributions are expected to originate from multiple optical view ports for local payload control [82], from thermal radiation from the beam pipe, from scattered laser light, and from the shield suspensions. Other sources are mitigated by means of the additional active shielding (cf. Figure 5.5). Based on $\dot{Q}_{\text{total}}$, FEM simulations have been conducted. Assuming the shield frame profiles at a uniform temperature of $T = 1.9\,\text{K}$ and a homogeneous distribution of $\dot{Q}_{\text{total}}$ on the shield surfaces yields temperature gradients of $\Delta T_{\text{sh}} < 100\,\text{mK}$. About 5/8 of $\dot{Q}_{\text{total}}$ is absorbed by the vertical and 3/8 by the header frame profiles. The results again can be used to approximate the static 1D temperature profiles within the He II channels via the differential equation

$$\frac{\mathrm{d}T}{\mathrm{d}x} = \frac{-\dot{q}_{\text{He II}}(x)^m}{\lambda_{\text{eff}}(T(x), p_{\text{r}})}, \tag{5.1}$$

where λ_{eff} is the empirical thermal conductivity function by Sato et al. [137] with the Gorter-Mellink exponent [217] $m = 3.4$, while the channel pressure is denoted by p_{r}. The heat flux $\dot{q}_{\text{He II}}$ towards the heat sink at $x = 0$ is approximated to increase linearly. The He II channels and their interconnections are treated as a fluid column grid, which allows consecutive solving of Equation (5.1). In each grid segment, the temperature increase in the previous channel section is considered by the value of $T(x = 0)$. Exemplary results yield He II temperatures from 1.85 K at the supply connections to 1.87 K at the farthest point from the He-supply.

5.3.3.2 He II condensation into the pre-cooled shield

Subsequent to pre-cooling with supercritical helium flow, the pressure in the shield is reduced to the He II reservoir pressure $p_{\text{r}} \approx 1.2\,\text{bar}$ by means of the infrastructure explained in [186] and flow is halted. With a temperature of 3 to 4 K, the helium is in a sub-cooled liquid state. The last cooldown step then includes the conversion of the normal He I to the superfluid He II within the hollow frame profiles. This is achieved by connecting the supply and return lines of the shield *in parallel* to the He II reservoir, causing the He II phase front to propagate into the shield by absorbing the sensible heat[a] from both the He I and the shield, and conducting it to the reservoir via static He II heat conduction. At T_λ, the superfluid phase forms with dramatic property changes [130, 131].

The following model describes the superfluid phase front propagation, starting from a He II reservoir at the coordinate $x = 0$. Figure 5.7 visualizes the calculation principles of the one-dimensional model at an intermediate time t. At the start of the conversion process at $t = 0\,\mathrm{s}$, the fluid connection to the He II reservoir at $T_\mathrm{r} < T_\lambda$ is opened with the cross-sectional area A_He. All He I in the channel is at the uniform pre-cooling temperature $T_\mathrm{start} > T_\lambda$ and at the reservoir pressure p_r. The reservoir temperature T_r is held constant by the cooling system. In the transient process, the temperature of the He I next to the phase front is decreased via thermal conduction first to and then below T_λ. Thereby the phase front, characterized by the fixed temperature $T_\lambda(p_\mathrm{r})$, successively progresses along the length of the channel that is modeled with an adiabatic end. To consider the synchronous cooldown of the shield, the respective cross-sectional areas A_He and A_sh are included in the model, assuming ideal solid-to-liquid heat transfer.

The He II condensation model is divided into two parts. The first part describes the movement of the phase front position $x_\lambda(t)$ along the channel length by differential equations, while the second part introduces a numerical approximation of the He I

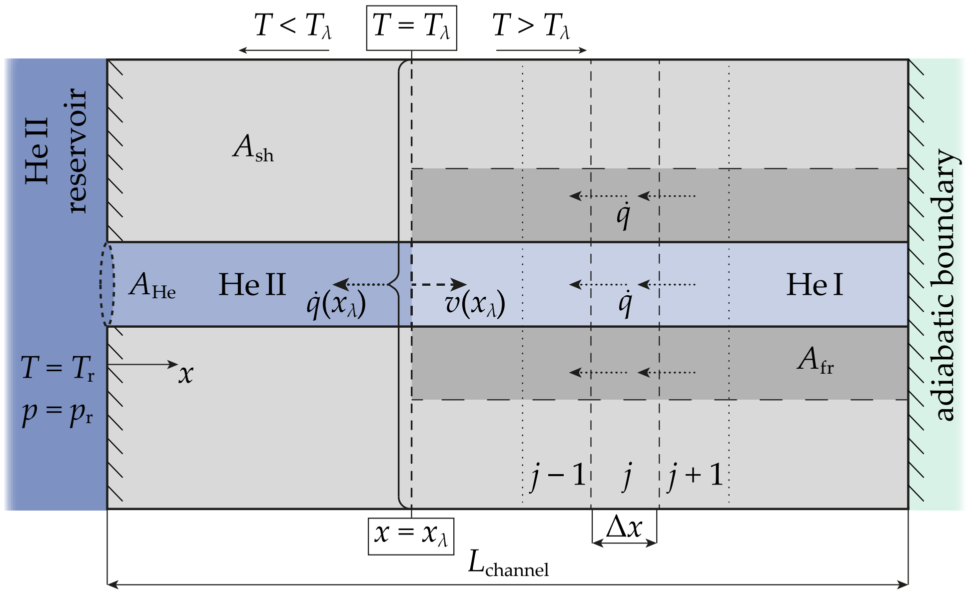

Figure 5.7: Scheme of the 1D semi-analytical superfluid phase front movement model for a circular helium channel surrounded by the thermal mass of the shield and the shield frame, respectively.

---

[a] The He I/He II phase transition is of second order, thus no latent heat is evolved [128]. However, there is a strong increase of heat capacity near the transition temperature T_λ [129].

region to obtain complete temperature profiles of the cooldown process. In the region $T < T_\lambda$ left of the phase front in Figure 5.7, static He II heat conduction dominates the heat transport from the He I phase and the surrounding thermal mass due to the extremely high thermal conductivity of He II. Therefore, the heat flux $\dot{q}$ from the phase front at (T_λ, x_λ) to the reservoir at $(T_\mathrm{r}, 0)$ is given by

$$\dot{q}(x_\lambda) = \left[\frac{1}{x_\lambda} \int_{T_\lambda}^{T_\mathrm{r}} \lambda_\mathrm{eff}(T, p_\mathrm{r})\, \mathrm{d}T \right]^{\frac{1}{m}} . \tag{5.2}$$

The enthalpy change of an infinitesimally short element $\mathrm{d}x$ to the right of the phase front due to the temperature change from T_start to T_λ is

$$\mathrm{d}H_{\mathrm{start}-\lambda} = \mathrm{d}x \int_{T_\mathrm{start}}^{T_\lambda} \Big[A_\mathrm{He}\, \rho_\mathrm{He\,I}\,(T, p_\mathrm{r})\ c_{p,\mathrm{He\,I}}\,(T, p_\mathrm{r}) + A_\mathrm{sh}\, \rho_\mathrm{sh}\, c_\mathrm{sh}\,(T) \Big] \mathrm{d}T\,, \tag{5.3}$$

where ρ and c denote density and specific heat capacity, and A_sh is the cross-sectional area of the adjacent shield mass homogeneously distributed along the channel length L_channel. The time derivative of the enthalpy change in the element equals the heat flow through the He II region

$$\frac{\mathrm{d}H_{\mathrm{start}-\lambda}}{\mathrm{d}t} = \dot{q}(x_\lambda)\, A_\mathrm{He}\,. \tag{5.4}$$

The combination of Equations (5.3) and (5.4) yields the velocity of the phase front propagating from the reservoir into the He I region

$$v(x_\lambda) = \frac{\mathrm{d}x_\lambda}{\mathrm{d}t} = \frac{A_\mathrm{He}\, \dot{q}(x_\lambda)}{\int_{T_\mathrm{start}}^{T_\lambda} \Big[A_\mathrm{He}\, \rho_\mathrm{He\,I}\,(T, p_\mathrm{r})\ c_{p,\mathrm{He\,I}}\,(T, p_\mathrm{r}) + A_\mathrm{sh}\, \rho_\mathrm{sh}\, c_\mathrm{sh}\,(T) \Big] \mathrm{d}T}\,, \tag{5.5}$$

with $\dot{q}(x_\lambda)$ from Equation (5.2). Hence, the time relation for the He II phase front position is

$$t(x_\lambda) = \int_0^{x_\lambda} \frac{1}{v(x)}\, \mathrm{d}x \quad \text{with} \quad t(0) = 0\,. \tag{5.6}$$

Figure 5.8 shows the phase front positions calculated with the system parameters and material properties listed in Table 5.1.

Table 5.1: Parameters and material property references used in the He II condensation model.

Parameter/ property	Value/reference
T_{start}	$3.0 \ldots 4.0\,\text{K}$
T_{r}	$1.85\,\text{K}$
p_{r}	1.2 bar(a) [186]
L_{channel}	10 m
A_{He} A_{sh}	$78.5\,\text{mm}^2$ $6830\,\text{mm}^2$
$(\rho, c_p)_{\text{He I}}$	HEPAK [126, 261]
$\lambda_{\text{He I}}$	REFPROP [231]
$T_\lambda(p_{\text{r}})$	2.166 K [126, 261]
λ_{eff}	Sato et al. [137]
c_{Al}[a]	Kittel [262] Hartmann et al. [263]
λ_{Al1000}[b]	Woodcraft et al. [264]
A_{fr}	$1520\,\text{mm}^2$
Δx	1 mm
Δt	1 ms

[a] Including phonon [262] and electron [263] contributions.

[b] Al 1000 series – lower limit [264].

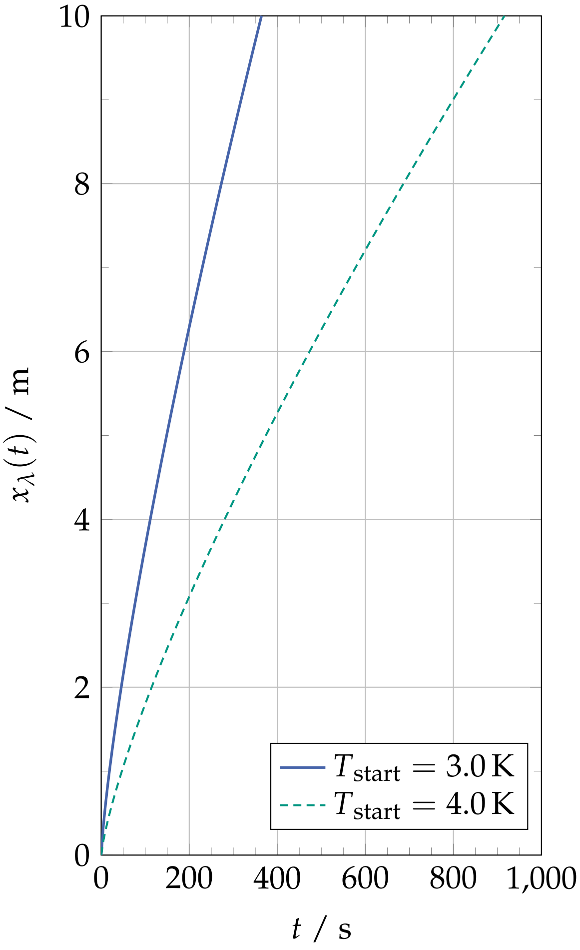

Figure 5.8: Superfluid phase front position in an aluminum channel as a function of time.

A_{He} and A_{sh} are chosen considering the internal diameter of the hollow frame profiles as well as the approximate shield mass distribution comprising both frame and panels (cf. Figure 5.6). At the pre-cooling temperature of 3.0 K as planned in [186], the phase front reaches a 10 m far end of the channel after $t \approx 360\,\text{s}$. In this period of time, an amount of heat of around 260 J is removed from the shield section, including the helium column. Simultaneously, around 180 J are deposited due to $\dot{Q}_{\text{total}}$. This allows a rough estimation of $t > 600\,\text{s}$ for the completion of the He II condensation process along L_{channel}. If pre-cooling is provided only at 4.0 K, the mean phase front velocity is about 2.5 times lower. Compared to the cryogenic payload cooldown taking several days [260], the He II phase front propagation is fast and not a limiting parameter. The propagation results are in good agreement with Bielert et al. [265], using the parameters $A_{\mathrm{sh}} = 0\,\mathrm{m}^2$, $T_{\mathrm{r}} = 1.9\,\mathrm{K}$ and $T_{\mathrm{start}} = 4.5\,\mathrm{K}$ at saturation pressure $p_{\mathrm{r}} \approx 1.3\,\mathrm{bar}$ in the model. Relative deviations $< 5\,\%$ originate from the updated λ_{eff} model as well as the Gorter-Mellink coefficient.

In order to calculate the temperature profile along the He II region for every value of x_λ, Equation (5.1) is solved in the interval $x = 0 \ldots x_\lambda$ with $T(x = 0) = T_{\mathrm{r}}$. To determine the temperature profile to the right of the phase front at $T > T_\lambda$, thermal conduction through the cross-section of the channel frame A_{fr} cannot be neglected, because $\lambda_{\mathrm{He\,I}} < \lambda_{\mathrm{Al1000}} \ll \lambda_{\mathrm{eff}}$ and $A_{\mathrm{He}} < A_{\mathrm{fr}}$. Modelling of heat transfer in this region is implemented by means of a Crank-Nicolson implicit numerical scheme [266]. The region is discretized into elements of length Δx, yielding a total number of $N = {}^{L_{\mathrm{channel}}}/_{\Delta x}$ elements at $t = 0\,\mathrm{s}$. The Crank-Nicolson scheme comprises a three-point stencil. Thus, heat flows to/from an element j are considered from/to its adjacent cells $j - 1$ and $j + 1$ as indicated in Figure 5.7. The governing equation of energy change and 1D Fourier heat conduction is

$$\begin{aligned}\Big[A_{\mathrm{He}}\,\rho_{\mathrm{He\,I}}(T, p_{\mathrm{r}})\,c_{p,\mathrm{He\,I}}(T, p_{\mathrm{r}}) + A_{\mathrm{sh}}\,\rho_{\mathrm{sh}}\,c_{\mathrm{sh}}(T)\Big]\frac{\partial T}{\partial t}& \\ = \frac{\partial}{\partial x}\left[\left[A_{\mathrm{fr}}\,\lambda_{\mathrm{fr}}(T) + A_{\mathrm{He}}\,\lambda_{\mathrm{He\,I}}(T, p_{\mathrm{r}})\right]\frac{\partial T}{\partial x}\right]&, \qquad (5.7)\end{aligned}$$

which is evaluated numerically. The superfluid phase front propagation is implemented by means of a moving boundary condition via the results for $x_\lambda(t)$ presented above. This yields a progressive decrease of N over time with a temperature of $T_{j=0} = T_\lambda$ in the first cell.

The complete temperature profiles $T_{\mathrm{He}}(x, t)$ along the channel are obtained by combining the results for the He II and He I regions calculated at discrete time steps $t = i \cdot \Delta t$ with $i \in [1..\lfloor t(L_{\mathrm{channel}})/\Delta t \rfloor]$. Figure 5.9 shows the evolution of such temperature profiles. The complete temperature gradient in the He I region, $T_{\mathrm{start}} - T_\lambda \approx 0.83\,\mathrm{K}$, occurs within around 10 mm next to the phase front. Temperature gradients in the He II phase are small and decrease continuously as the phase front propagates. Increased gradients are only observed close to the phase front, where λ_{eff} decreases strongly towards T_λ starting from the peak value around 1.9 K. Following the steep temperature gradients of the displayed curves, a slight reduction of the phase front velocity over time can be recognized (shorter distances at equivalent time intervals).

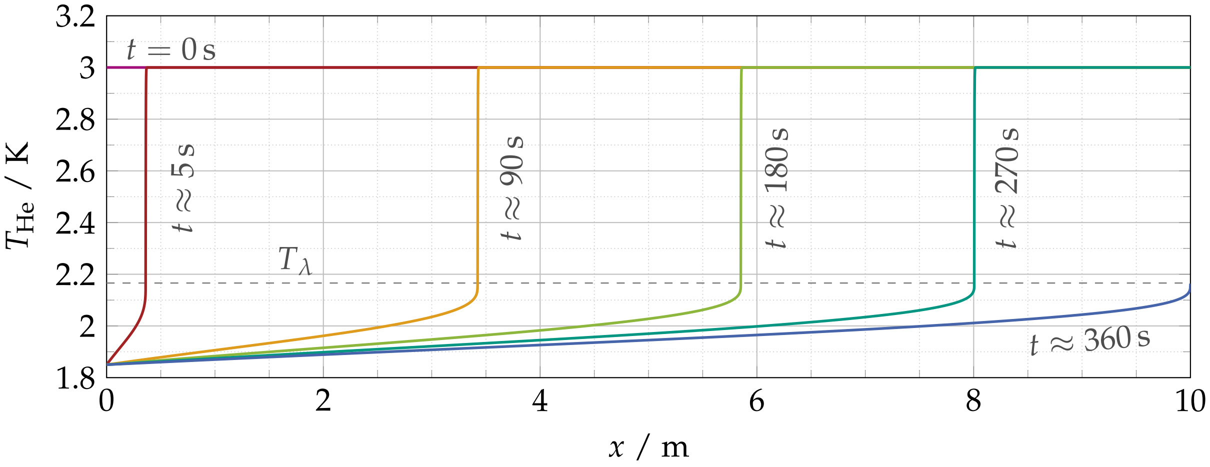

Figure 5.9: Temperature gradients along a 1D helium channel for the parameters in Table 5.1 at $T_{\mathrm{start}} = 3.0\,\mathrm{K}$.

5.3.4 Modal analyses

Given low-noise cooling as described in the previous sections, an adequate mechanical shield design must reduce otherwise significant detector noise contributions. One of the two main contributions is caused by back-scattering of light from all surfaces with a viewing angle to the mirror [258]. The other is induced by mechanical coupling between the attachment point of a payload heat link vibration isolation system and the payload itself [97]. In order to account for these contributions, two major shield vibration mitigation aspects are considered from the early stages of the shield design on: (I) reduction of the vibrational transfer function from the ambiance to the shield and (II) elevation of the structural resonant frequencies of the shield (i.e. box modes).

The former aspect, yet in prospect, is indicated in Figure 5.5. The approach is to suspend the shield via maraging steel wires through magnetic damping systems located within attachments to the cryostat lid. Additional wires at the bottom side of the shield enable reducing displacement of this extremity in order to constrain the pendulum mode frequencies.

Regarding aspect (II), the shield needs to comprise sufficient structural reinforcements (cf. Figure 5.6) at limited total weight so as not to spoil the suspension- and cooldown performances. In a first phase, the design of the shield has been evaluated in terms of structural, modal and dynamical characteristics, with iterative improvements on decisive geometrical parameters such as panel and frame thickness, structural shape and additional ribs. For a finite element analysis, mechanical material properties were taken from [267]. In terms of vibration and sensitivity to seismic activities as well as ambient instrumentation and equipment noise, first, the natural frequencies in free modal analysis were investigated and increased to avoid low frequency resonance in the range below 30 Hz, i.e. within the ET-LF detection frequency band. As Figure 5.10a shows, preliminary results yield improved natural frequencies of ca. 45 Hz for the shield faces at ca. 51.5 Hz for the shell. This opposes to ca. 4 Hz for an unreinforced structure.

Subsequently, transfer functions in frequency harmonic response were calculated to estimate the resulting shield deformation amplitudes at these specific resonant frequencies. The spatially resolved vibrational amplitude results further allow locating favorable, low-noise attachment positions of the payload heat link vibration isolation system (cf. Figure 5.5) and estimating the respective vibration source constraints.

The frequency response analysis was conducted in the frequency range $f = 0...53$ Hz using the spatial shield discretisation indicated in Figure 5.10a with a conservative structural damping ratio of 2 %. Figure 5.10b shows respective results at the nodes exhibiting the maximum displacement values in longitudinal and transversal directions, with magnitudes of ca. 31 near the center of the shield faces at $f \approx 45$ Hz, and ca. 16 in the center of the shell panels at $f \approx 51.5$ Hz. Furthermore, it is indicated that the dynamic response of the pursued shield structure minimizes the risk of vibration within the ET-LF detection frequency band. Below 30 Hz, the amplification magnitudes stay at a low level, to be compared with the interferometer noise budget requirements.

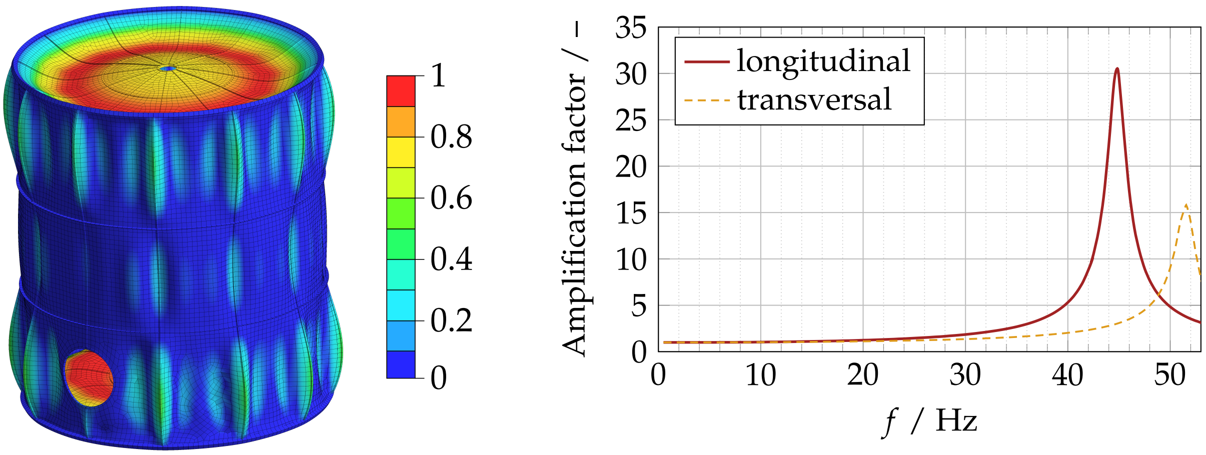

(a) Relative vibrational deformation for the first resonant mode at $f \approx 45$ Hz.

(b) Frequency response functions at shield nodes of maximum displacement due to box modes.

Figure 5.10: Modal and harmonic response analysis results.

5.3.5 Conclusions and prospects

A low-noise inner thermal shielding for the ET-LF cryostats based on static He II cooling is presented. The shield frame comprises extruded aluminum profiles for cool-down with supercritical helium flow, and for steady-state operation with static He II heat conduction. The condensation of He II into the pre-cooled shield is modeled by differential equations, demonstrating the overall feasibility and showing that the phase front propagation driven only by the He II heat conduction is sufficiently fast. The modeling of the steady-state thermal behavior shows temperature gradients in the shield below 100 mK.

Further, the results of an iterative process of shield structure alteration show significantly improved shield resonant frequency modes and quantify the vibration amplitudes with transfer functions in frequency harmonic response. These results are required to understand and conduct a noise evaluation due to light back-scattering into the mirror. This structural shield concept paves the way to investigate in further detail the support of the shield through magnetically damped wire suspensions.

Finally, this development will serve as decisive input for the study of payload heat link vibration isolation systems. Within the He II cooling concept for ET-LF, the heat links are foreseen to be thin tubes with bellows enabling helium supply. Similar tubes are envisaged to supply the presented ET-LF inner shield. Tangible plans for future experimental work on the detailed design and implementation of these interfaces in the Einstein Telescope exist.

Acknowledgments

The authors would like to acknowledge the support from the German Ministry for Education and Research (BMBF, Gr 05A20VK4), and from the Karlsruhe School of Elementary Particle and Astroparticle Physics: Science and Technology (KSETA).

5.4 Addendum and outlook

This section first investigates the initial phase of the innermost thermal shield cooldown process, complementing the He II condensation into the pre-cooled shield described in Section 5.3.3.2. Subsequently, prospects of the shield suspension development are outlined.

5.4.1 Shield cooldown approximation

The numerical calculations detailed in Section 5.3.3.2 present the modelling of the last cooldown step, which includes the conversion of normal He I to superfluid He II. For this modelling, it is assumed that the previous part of the cooldown process is completed and static He I at $T = 3.0\,\mathrm{K}$ is present in the frame channels. This previous part is based on transient heat extraction from the shield to a flow of supercritical helium, analogous to the process described in detail in Sections 3.1.4.5 and 3.2.2.

The time scale required to decrease the shield temperature via this mechanism is determined by applying Equations (3.3), (3.4) and (3.45) to the case of shield cooldown. Table 5.2 lists boundary conditions of an exemplary operating mode configuration and resulting ranges for Reynolds, Prandtl and Nusselt numbers during the transient process. Helium fluid properties are taken from [231]. Values of the specific heat capacity of aluminum are retrieved from [268], which allow a calculation of the enthalpy difference corresponding to a cooldown of the entire shield via

$$\Delta H_{\mathrm{shield}} = M_{\mathrm{shield}} \int_{T_{\mathrm{shield}}(t_{\mathrm{end}})}^{T_{\mathrm{shield}}(t=0)} c_{\mathrm{Al}}(T)\,\mathrm{d}T\,. \tag{5.8}$$

For the parameters in Table 5.2, this yields $\Delta H_{\mathrm{shield}} \approx 74\,\mathrm{MJ}$.

Further, the resulting Nusselt number range allows the derivation of the scale of the mean heat transfer coefficient $\overline{\alpha}_{\mathrm{HT}} \approx 100\,\mathrm{W\,m^{-2}\,K^{-1}}$. Consequently, the order of magnitude of the duration of the preliminary shield cooldown is calculated by

$$\Delta t = \frac{\Delta H_{\mathrm{shield}}}{\overline{\alpha}_{\mathrm{HT}} A_{\mathrm{HT,total}} \left(T_{\mathrm{wall}} - T_{\mathrm{He}}\right)}\,. \tag{5.9}$$

For the considered exemplary operating mode, this yields $\Delta t \approx 3\,\mathrm{h}$. This value is dependent on the exact operating parameters. However, it confirms that cryogenic shield operation can be achieved on the timescale of a few hours.

Table 5.2: Exemplary convective shield cooldown operating parameters and resulting ranges of the dimensionless numbers in Equation (3.45).

Parameter	Value/expression
$\dot{M}_{\mathrm{He}}$	$1.0\,\mathrm{g\,s^{-1}}$
p_{He}	$2.5\,\mathrm{bar(a)}$
$T_{\mathrm{wall}} - T_{\mathrm{He}}$	$50\,\mathrm{K}$
$T_{\mathrm{shield}}(t = 0)$	T_{amb}
$\overline{T}_{\mathrm{shield}}(t_{\mathrm{end}})$	$3.0\,\mathrm{K}$
M_{shield}	$450\,\mathrm{kg}$
$d_{\mathrm{i,header}}$	$10\,\mathrm{mm}$
$d_{\mathrm{i,vertical}}$	$5\,\mathrm{mm}$
$A_{\mathrm{HT,total}}$	$1.31\,\mathrm{m^2}$
Re	$\sim 1.2{\cdot}10^3 ... 2.2{\cdot}10^4$
Pr	$\sim 0.57 ... 1.26$
Nu	$\sim 2.6 ... 43$

5.4.2 Shield suspension approach

Figure 5.5, showing the ET-LF cryostat concept, indicates the approach to suspend the innermost thermal shield from the cryostat walls by means of thin maraging steel wires in order to reduce the vibrational transfer function from the ambiance to the shield. The envisaged underlying damping principle comprises two key aspects. Lateral displacements are attenuated through the introduction of the pendulum itself via shield supporting suspension wires. Vertical displacements are attenuated by means of geometric anti-spring (GAS) filters, which are mechanical attenuators based on triangular cantilever blades coupled to inclined links [269]. Figure 5.11 visualizes this concept.

The pendulum structure is composed of three annular geometries connected by suspension wires. A bottom ring is rigidly attached to the lower end of the shield. It is suspended by maraging steel wires which are intercepted at half length by a rigid ring in order to remove their transverse eigenmodes. At their top end, they are fixed at another annulus which in turn is stabilized by cantilever springs of the GAS system (shown in unloaded, straight state). The other ends of the springs are clamped to a rigid structure, an exemplary configuration of which is shown by Stochino et al. [270]. This structure can be linked firmly to the cryostat vacuum vessel.

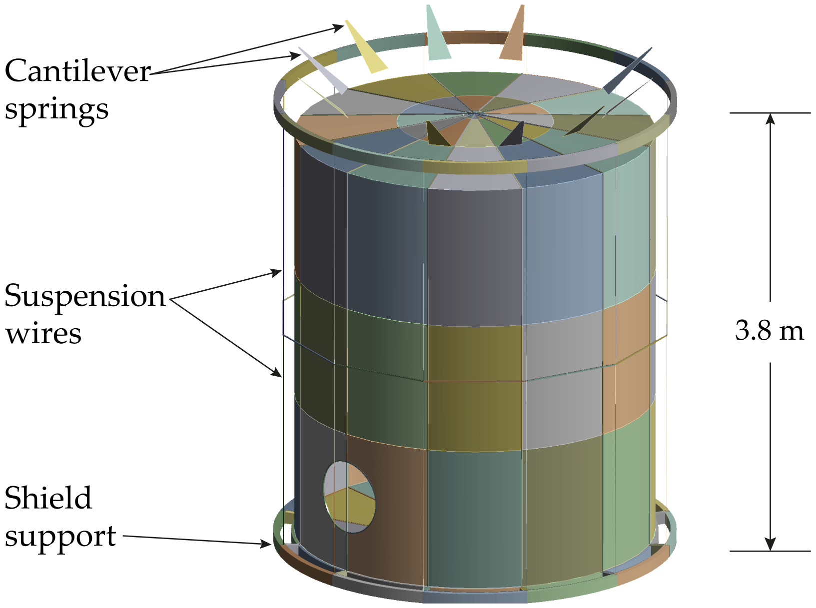

Figure 5.11: Conceived approach for the innermost thermal shield in the ET-LF test mass cryostats. Image: courtesy of G. Iaquaniello, Laboratoire de Physique des 2 Infinis Irène Joliot-Curie.

Suspending the shield in this manner exhibits great potential in achieving low-frequency pendulum modes due to the extended wire length reaching down to the bottom of the shield as well as high vertical attenuation performance within the ET-LF detection frequency band through GAS filter implementation. Further, the length of the maraging steel wires provides a noteworthy thermal insulation from the ambiance. An analytical calculation of a comparable heat load by solid conduction through 304 stainless steel yields $\dot{Q} \leq 1\,\text{mW}$ for an exemplary suspension configuration of 10 wires with $d = 4\,\text{mm}$ and $L \geq 3.8\,\text{m}$.

6 Heat extraction from the cryostats to the infrastructure

The preceding chapters discuss the macroscopic cryogenic infrastructure approach for ET and cryogenic features of the ET-LF payloads and innermost thermal shields as cooling power consumers. The shared characteristic of these consumers is the reliance on supply with supercritical helium flow for transient cooldown as well as static He II for steady state operation, both of which are provided by the presented helium cooling system architecture. The focus of this chapter is on the subsystem constituting the link between these consumers within the ET-LF test mass cryostats and the adjacent cryogenic supply units (CSUs), the latter being major constituents of the cryogenic infrastructure.

6.1 Thermal and hydraulic dimensioning

As introduced in Chapters 3, 4 and 5, helium supply to the payloads and innermost thermal shields is envisaged by means of multiple thin-wall and ‘soft’ tubes (elsewhere called ‘capillaries’). This is due to the fact that rigid lines would imply an undamped connection to the ambiance, giving way to the induction of excessive noise into the detector. The following section presents potential dimensioning ranges for these tubes, derived from their function of withdrawing sufficiently large heat flow rates from the consumers, and aligned with the pressure loss constraints of the proposed helium infrastructure concept.

6.1.1 Helium supply tube configurations

Table 4.3 lists the refrigeration capacity design values for each ET-LF cryogenic payload ($\dot{Q}_\mathrm{c} = 1\,\mathrm{W}$) and the corresponding innermost thermal shield ($\dot{Q}_\mathrm{c} = 2\,\mathrm{W}$). These values allow the calculation of the number of helium supply tubes required for steady-state heat extraction via the differential form of Equation (3.2) reflecting the direction of heat flow,

$$\frac{\mathrm{d}T_{\mathrm{He\,II}}(z)}{\mathrm{d}z} = -\underbrace{\frac{32\,\eta}{\left(d_{\mathrm{i,tubes}}\,\rho\,s\right)^2 \cdot T_{\mathrm{He\,II}}(z)}}_{\text{laminar term}} \cdot \dot{q} - \underbrace{\frac{1}{h\left(\frac{T_{\mathrm{He\,II}}(z)}{T_\lambda(p_\mathrm{r})}\right) \cdot g_{\mathrm{peak}}(p_\mathrm{r})} \cdot \dot{q}^{3.4}}_{\text{turbulent term}} , \tag{6.1}$$

with the heat flux through static He II within the tubes defined as

$$\dot{q} = \frac{4 \cdot \dot{Q}_\mathrm{c}}{n_{\mathrm{tubes}} \cdot d_{\mathrm{i,tubes}}^2 \cdot \pi} . \tag{6.2}$$

The fluid properties of He II are a function of $T_{\mathrm{He\,II}}(z)$, while the steady-state condition $p = p_\mathrm{r}$ (cf. Figure 5.7) applies to the pressure along the complete length of all tubes. The cold- and warm-end temperatures $T_{\mathrm{He\,II}}(z = 0)$ and $T_{\mathrm{He\,II}}(z = L_{\mathrm{tubes}})$ constituting the global temperature difference $\Delta T_{\mathrm{He\,II}}$ along the supply tube length L_{tubes} are decisive parameters for these calculations. Considering a thermal gradient of $\Delta T_{\mathrm{ma}} = 50\,\mathrm{mK}$ along the suspension tube (cf. Section 3.1.4.4), $T_{\mathrm{He\,II}}(z = L_{\mathrm{tubes}}) = 1.85\,\mathrm{K}$ is obtained for the design parameter $T = 1.9\,\mathrm{K}$ at the suspension tube bottom end as stated in Table 3.4.

At their cold ends, the helium supply tubes enter into a reservoir located within the CSUs in the vicinity of the ET-LF test mass cryostats (cf. Figure 4.3). Consequently, $T_{\mathrm{He\,II}}(z = 0)$ is a design parameter of the cryogenic infrastructure. It is limited by the necessity to provide $p_{\mathrm{sat,He}}$ at the cold side of HX40, which serves as the heat sink for the entire heat extraction path from both payload and innermost thermal shield.

A reasonable exemplary value is $T\mathrm{He\,II}(z = 0) = 1.75\,\mathrm{K}$, corresponding to a temperature gradient of $\Delta T_{\mathrm{He\,II}} = 100\,\mathrm{mK}$ over a tube length of $L_{\mathrm{tubes}} = 10\,\mathrm{m}$. Assuming again a temperature difference of 100 mK across HX40 yields $p_{\mathrm{sat,He}}(T = 1.65\,\mathrm{K}) \approx 9.2\,\mathrm{mbar}$. At this pressure, the total required helium mass flow through HX40 for payload- and innermost thermal shield cooling implies a volume flow $\dot{V}_{\mathrm{He}} \approx 400\,\mathrm{m}^3\,\mathrm{h}^{-1}$ at the suction side of vacuum pump P40 at T_{amb}. Suitable vacuum booster models for this purpose can be found in [271–273], to be connected in series with a backing pump. An exemplary eligible vacuum pumping station consists of an *Okta 1000 M* roots booster pump from Pfeiffer Vacuum+Fab Solutions and a *COBRA NS 0160 C* screw backing pump [274] from Busch Vacuum Solutions.

Table 6.1 summarizes the parameters driving the helium supply tube design. The helium supply tubes for the innermost thermal shield will span across a similar distance and enter into the same reservoir as the payload supply tubes. Therefore, apart from the differing cooling power, the same constraints and design parameters are adopted.

Table 6.1: Overview of principal design parameters guiding the helium supply tube design.

	Constraints			Exemplary design parameters		
Parameter	$\dot{Q}_{\mathrm{c,payload}}$	$\dot{Q}_{\mathrm{c,shield}}$	$T_{\mathrm{He\,II}}(z = L_{\mathrm{tubes}})$	$T_{\mathrm{He\,II}}(z = 0)$	p_{r}	L_{tubes}
Value	1.0 W	2.0 W	1.85 K	1.75 K	1.2 bar(a)	10 m

The listed parameters enable the determination of suitable helium supply tube configurations, i.e. combinations of n_{tubes} and $d_{\mathrm{i,tubes}}$ matching the design constraints. Figure 6.1 illustrates possible configurations for both payload- and innermost thermal shield supply tube connections. The strong increase of n_{tubes} towards lower values of $d_{\mathrm{i,tubes}}$ is evident. Exemplary configurations consist of $n_{\mathrm{tubes}} = 20$ tubes each for the payload and the innermost thermal shield at $d_{\mathrm{i,tubes}} \approx 3.5\,\mathrm{mm}$ and $d_{\mathrm{i,tubes}} \approx 5\,\mathrm{mm}$, respectively. In steady-state operation, all helium supply tubes leading to a consumer contain static He II columns connected to a common reservoir (see Figure A.1). During transient cooldown, half of these tubes function as feed lines carrying supercritical/He I flow, while the other half serve as return lines.

A further approach to dimension the supply tube configurations is to avoid the development of a turbulent heat transfer regime in the static He II, in accordance with the two-fluid-model and correspondingly observed heat transport phenomena (cf. Sec-

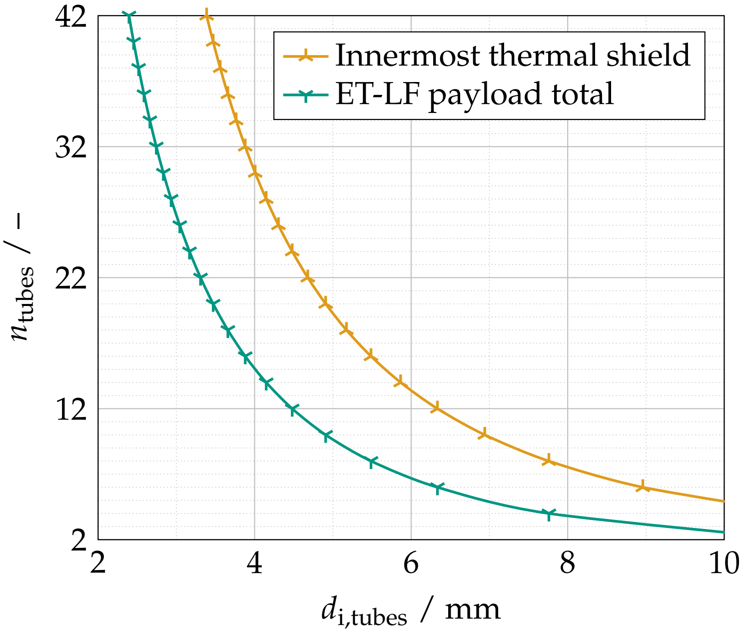

Figure 6.1: Helium supply tube array configuration options for steady-state heat extraction from a cryogenic payload in ET-LF and the surrounding thermal shield for the conditions listed in Table 6.1.

tion 2.4, complemented by [275]). This suppresses the turbulent contribution to the temperature gradient in the static He II phase, represented by the turbulent term on the right-hand side of Equation (6.1). The prerequisite is that the heat flux through the static He II-column does not exceed a critical value $\dot{q}_{\mathrm{crit}}$ for neither the normalfluid nor the superfluid component [132, 275]. The values for $\dot{q}_{\mathrm{crit}}$ are calculated via

$$\dot{q}_{\mathrm{crit,nc}} = s_{\mathrm{He\,II}} \cdot T_{\mathrm{He\,II}} \cdot \frac{\eta_{\mathrm{nc}}}{d_{\mathrm{i,tubes}}} \cdot Re(v_{\mathrm{crit,nc}}) \tag{6.3}$$

for the normal fluid component as well as

$$\dot{q}_{\mathrm{crit,sc}} = s_{\mathrm{He\,II}} \cdot T_{\mathrm{He\,II}} \cdot \frac{\rho_{\mathrm{sc}}\rho_{\mathrm{He\,II}}}{\rho_{\mathrm{nc}}} \cdot v_{\mathrm{crit,sc}} \tag{6.4}$$

for the superfluid component. The normal fluid critical velocity is understood by classical turbulent onset so that $Re(v_{\mathrm{crit,nc}}) \approx 1200$ (cf. Equation (2.4)). In turn, $v_{\mathrm{crit,sc}}$ is an empirically determined quantity, approximately following a $d_{\mathrm{i}}^{-1/4}$ law [132]

$$v_{\mathrm{crit,sc}} \simeq d_{\mathrm{i}}^{-1/4} \ \text{in}\ \mathrm{cm\,s^{-1}}, \tag{6.5}$$

with d_{i} given in cm. Figure 6.2 shows the calculated flux $\dot{q}_{\mathrm{crit,sc},i}$ for $\dot{Q}_{\mathrm{c}} = 1.0\,\mathrm{W}$ and the resulting minimum amount of helium supply tubes $n_{\mathrm{tubes,min}}$ determined via Equation (6.2). The He II conditions are $p = p_{\mathrm{r}}$ and $T_{\mathrm{He\,II}} = T_{\mathrm{He\,II}}(z = L_{\mathrm{tubes}}) = 1.85\,\mathrm{K}$. The supply tube warm end temperature is selected here in order to ensure preven-

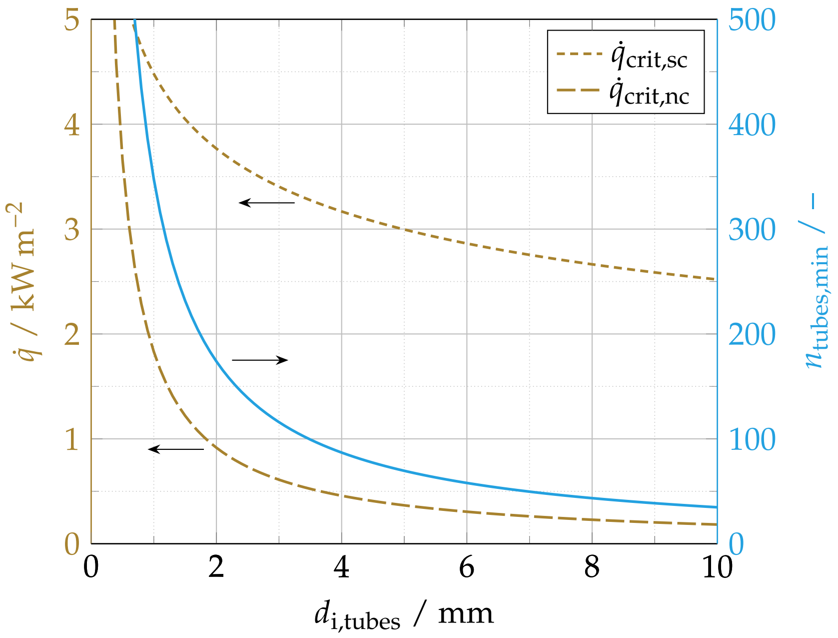

Figure 6.2: Critical heat fluxes for the introduction of superfluid- and normalfluid turbulence as well as resulting minimum amount of supply tubes containing static He II.

tion of turbulence generation along L_{tubes} since $\dot{q}_{\mathrm{crit,sc}}(d_{\mathrm{i}})$ slightly decreases with rising temperature.

The curve for $\dot{q}_{\mathrm{crit,nc}}$ captures the inverse dependence on $d_{\mathrm{i,tubes}}$, with values rising from $\dot{q}_{\mathrm{crit,nc}}(d_{\mathrm{i,tubes}} \geq 4\,\mathrm{mm}) \lesssim 0.5\,\mathrm{kW\,m^{-2}}$ to $\dot{q}_{\mathrm{crit,nc}}(d_{\mathrm{i,tubes}} \leq 1\,\mathrm{mm}) \gtrsim 3.5\,\mathrm{kW\,m^{-2}}$. A similar trend is shown for $\dot{q}_{\mathrm{crit,sc}}$, although damped by the exponent in Equation (6.5). Feynman [134] provides a detailed reasoning for the dependence of $v_{\mathrm{crit,sc}}$ on the tube diameter.

As a result, the plot of $n_{\mathrm{tubes,min}}$ follows the same pattern as $\dot{q}_{\mathrm{crit,nc}}$ due to the presence of $d^2_{\mathrm{i,tubes}}$ in the laminar term of Equation (6.2). Further, the magnitude of values for $n_{\mathrm{tubes,min}}$ becomes evident. Even for $d_{\mathrm{i,tubes}} = 7\,\mathrm{mm}$, ca. 50 supply tubes are required to prevent turbulence. For diameters below 2 mm, this number rises to some hundreds of tubes. Although this way, conduction of $\dot{Q} = 1.0\,\mathrm{W}$ could be achieved with $\Delta T_{\mathrm{He\,II}}$ on the order of merely a few µK, the large quantity of tubes required makes this an unsuitable design approach for the helium supply tubes in ET. Segmenting fewer larger tubes into smaller ones by introducing thin inner walls to achieve the same thermal effect inadvertently counteracts vibration attenuation efforts (cf. Section 6.2). This is due to the increased mechanical connection rigidity to the cryogenic supply unit.

Accordingly, a reasonable approach for the design of the helium supply tubes involves a lower amount of tubes, tolerating a turbulent heat transfer regime in the static He II. Figure 6.3 illustrates a schematic configuration hosted within a connecting line between a cryogenic supply unit and the adjacent ET-LF test mass cryostat (cf. Figure 4.3). Analogous to the concept for the long cryogenic transfer lines shown in Figure 4.5a, GFRP supports are used for pipe positioning within the vacuum envelope. Supports and pipes are arranged in a nested manner to allow the use of two thermal shields anchored to the return lines at $T > 80\,\mathrm{K}$ (outer shield) and $T > 5\,\mathrm{K}$ (inner shield). Hence, parasitic heat loads to the centrally located channel containing the He II supply tubes are minimized. Designated tube supports (not shown) are required to offer minimal vibration transmission from the ambiance to the tubes (cf. Section 6.2).

6.1.2 Pressure losses

During payload- and innermost thermal shield cooldown, supercritical helium flows provide the required refrigeration power, as discussed in Sections 3.1.4.5 and 5.4.1. The envisaged supply pressure at the cryogenic supply unit is $p \approx 5\,\mathrm{bar(a)}$ (cf. Section 4.2.3). Considering the pressure level of $p \approx 1.2\,\mathrm{bar(a)}$ in the underground return

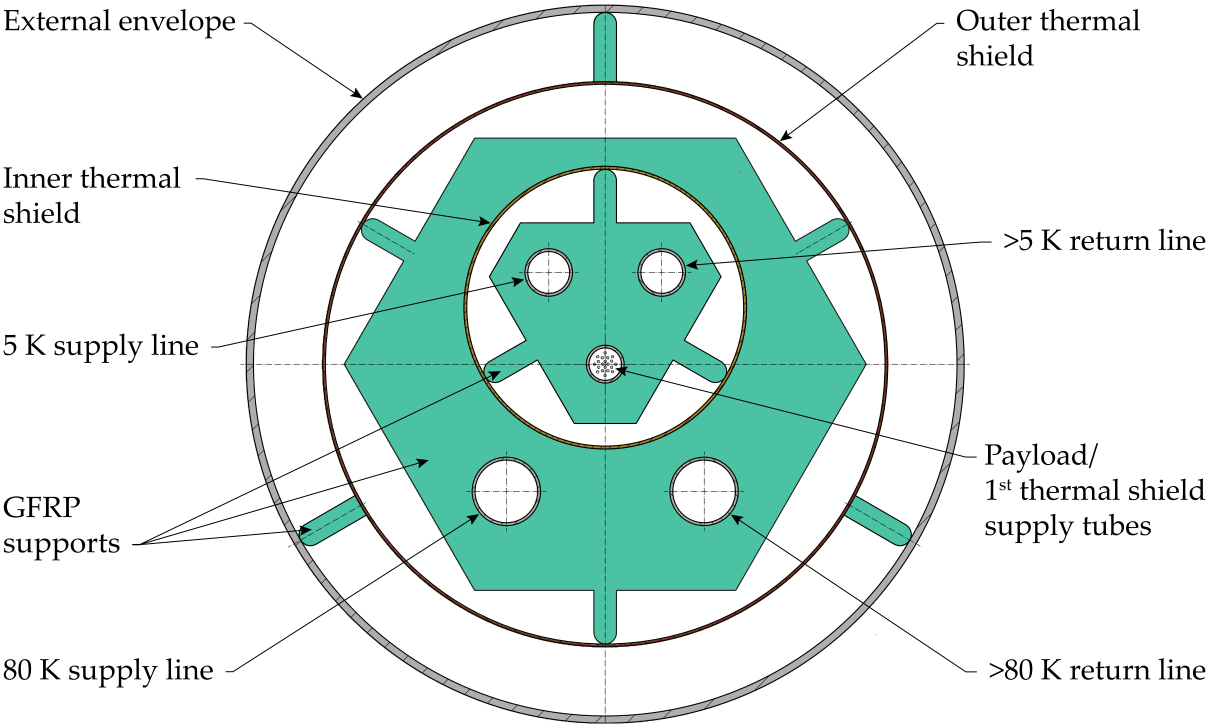

Figure 6.3: Cross-section view of a schematic architecture for the line connecting an ET-LF test mass cryostat with the adjacent cryogenic supply unit (cf. Figure 4.3).

lines, this allows for a pressure drop of $\Delta p < 3.8\,\mathrm{bar}$ in the helium flow section consisting of the feed tubes, the suspension tube or the innermost thermal shield, and the return tubes to the cryogenic supply unit. Due to the more restrictive design constraints on the suspension tube dimensions and its helium supply tubes, pressure drop calculations in this section are focused on these parts.

The pressure drop along the marionette suspension tube is discussed in Sections 3.1.4.5 and 3.2.2, which report $\Delta p_{\mathrm{ST}} < 300\,\mathrm{mbar}$ for $\dot{M}_{\mathrm{He}} = 1.0\,\mathrm{g\,s^{-1}}$. The scale of the pressure drop along the supply- and return tubes can be determined using the combination of differential equations 3.46 and 3.47 with the friction coefficient $\xi = f(Re)$ as presented in Appendix A.6. Consequently, Figure 6.4 shows Δp over $L_{\mathrm{tubes}} = 10\,\mathrm{m}$ with $p_{\mathrm{sup}} = 5.0\,\mathrm{bar(a)}$ depending on the helium inlet temperature $T_{\mathrm{He,sup}}$. The heat flux $\dot{q}$ to the fluid is negligible due to the extensive thermal shielding around the tubes (cf. Figure 6.3), the cooldown of which is to be conducted in parallel or prior to the helium tubes.

Expected Reynolds number values lie in the range of $Re \approx 10^3 ... 5 \cdot 10^4$ for the displayed supply tube configurations and mass flows $\dot{M}_{\mathrm{He}}$. The calculations of the pressure drop over L_{tubes} for $\dot{M}_{\mathrm{He}} = 1.0\,\mathrm{g\,s^{-1}}$ yield $\Delta p \leq 130\,\mathrm{mbar}$ across the complete range of $T_{\mathrm{He,supply}} = 3.0...300\,\mathrm{K}$. Further, the curve profiles portray the traversal of different flow regimes with varying temperature. In the case of $\dot{M}_{\mathrm{He}} = 1.0\,\mathrm{g\,s^{-1}}$

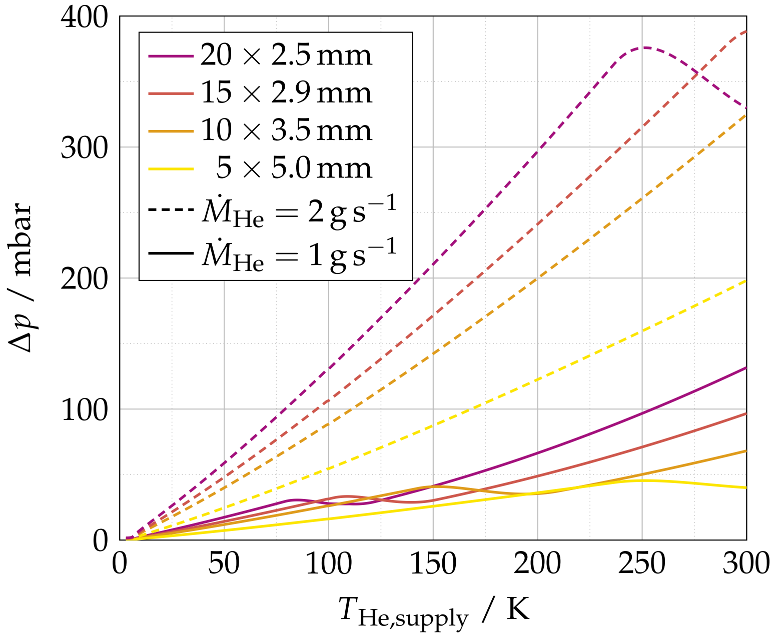

Figure 6.4: Approximated pressure losses in various helium feed tube configurations for payload cooling along $L_{\mathrm{tubes}} = 10\,\mathrm{m}$ at $T_{\mathrm{He,supply}} = 3...300\,\mathrm{K}$.

and $n_{\mathrm{tubes}} = 20$ with an inner diameter $d_{\mathrm{i,tubes}} = 2.5\,\mathrm{mm}$ each, at temperatures $T \to 300\,\mathrm{K}$, the helium flow exhibits a fully laminar regime. Towards lower temperatures, however, first, the transitional regime is reached around $T_{\mathrm{He,supply}} = 115\,\mathrm{K}$ before an increasingly turbulent regime establishes with a local maximum of Δp at $T_{\mathrm{He,supply}} \approx 85\,\mathrm{K}$ due to the increased value of $\xi(Re = 3000)$. This trend also shows for the other supply tube configurations, with the onset of turbulence shifted to increasingly high temperatures for smaller amounts of tubes due to the correspondingly larger diameters. At elevated mass flow $\dot{M}_{\mathrm{He}} = 2.0\,\mathrm{g\,s^{-1}}$, flow regimes remain turbulent throughout virtually the complete investigated range of $T_{\mathrm{He,supply}}$. The corresponding calculations yield pressure drops of $\Delta p \leq 390\,\mathrm{mbar}$.

For pressure losses in the helium return tubes with the same length L_{tubes} from the payload interface to the CSU reservoir, similar values are expected due to the relatively weak dependence of the involved fluid properties on the absolute pressure in the relevant range. Considering pressure drops of $\Delta p < 300\,\mathrm{mbar}$ over the suspension tube connected to the feed tube ends, the return tubes are supplied with pressures of $p_{\mathrm{He}} > 4.5\,\mathrm{bar(a)}$ in the case of $\dot{M}_{\mathrm{He}} = 1.0\,\mathrm{g\,s^{-1}}$. Setting aside in this conceptual calculation the pressure-reducing influence of upstream installations, this yields return pressures on the order of $p_{\mathrm{He}} > 4.3\,\mathrm{bar(a)}$ to the cryogenic supply unit over the complete payload cooldown process.

In comparison, lower pressure losses are expected over the innermost thermal shield helium supply- and return loop since the higher required cooling power during steady-state operation (cf. Table 6.1) implies larger total flow cross-sections in the tube connections during cooldown (cf. Figure 6.1). Consequently, the presented helium supply tube configurations exhibit the potential for mass flows $\dot{M}_{\mathrm{He}} > 1.0\,\mathrm{g\,s^{-1}}$ and significant margins regarding additional pressure losses in the infrastructure, such as for increased cryogenic transfer line lengths, decreased diameters, pipe fittings, heat exchangers, and, notably, flow control valves.

6.2 Attenuation possibilities

The heat extraction path from an ET-LF test mass cryostat to the heat sink within a CSU represents a mechanical link between extremely sensitive detector parts and the environment, susceptible to transmission of excessive seismic or technical noise. Experience from KAGRA demonstrates the importance of vibration isolation measures into this link for a detector operation that meets the noise level demands [96, 97]. Unlike KAGRA, the helium cooling system for ET does not rely on the use of cryocoolers entailing pressure oscillators for provision of cooling power to the test mass cryostats. Therefore, the system is inherently less prone to the introduction of technical noise into the optics. Nevertheless, potentially noisy equipment such as valves including actuators and vacuum pumps connected to the CSUs is required for system operation (cf. Section 4.2.3). Considering the ambitiously low noise level envisaged for the Einstein Telescope, it is anticipated that vibration isolation measures are required along the TM cryostat heat extraction paths. It is the purpose of this section to provide an overview of potential measures that generally limit the transfer of vibrations from ambient systems and the ground into the TM cryostat, and to address their implementation possibilities in the cryogenic system presented in this work.

Figure 6.5 shows the connection scheme of the heat extraction path between the platform (PF) within an ET-LF test mass payload and the He II bath inside a CSU, in accordance with Figure 4.3. In order to contain the static He II columns for steady-state heat extraction from the marionette suspension tube, which terminates in the PF, a continuous mechanical structure is required. The majority of its length is made up of the helium tubes with small diameter discussed above. Towards the He II bath inside the cryogenic supply unit, they merge into pipes of larger diameter, which allow the implementation of few valves (not shown) to control the operating modes via regulation of helium supply and -return. The bath itself should be positioned in a geodetically elevated position compared to the entirety of the connected tubing in order to facilitate a gravity-supported He II condensation towards the payload interface and provide a positive hydrostatic head during nominal operation. The pipe sections directly at-

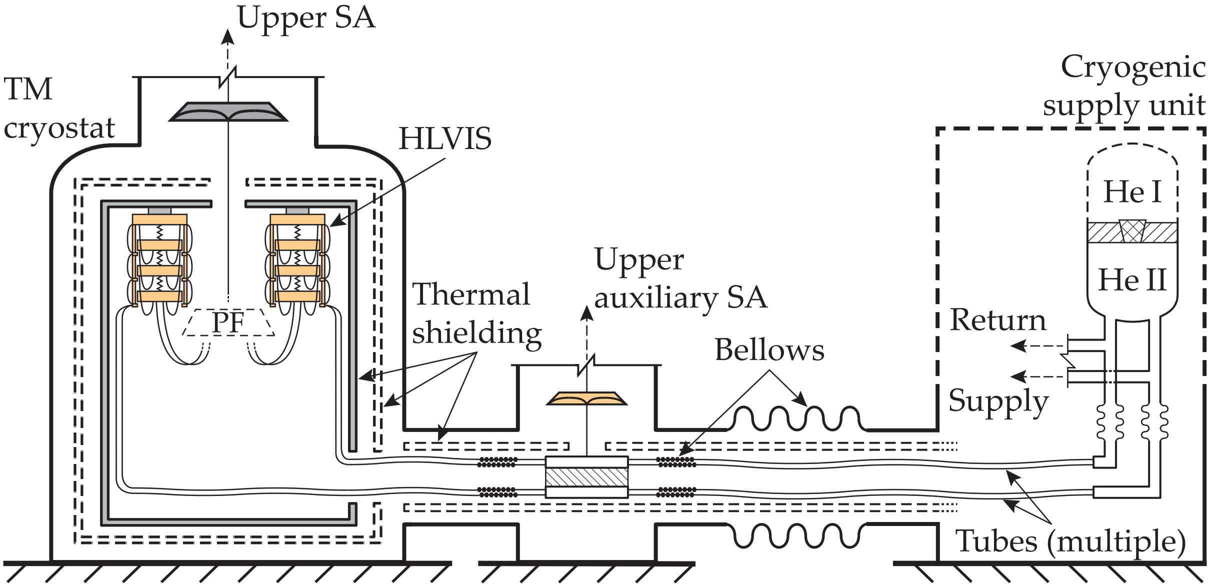

Figure 6.5: Schematic illustration of potential vibration isolation measures along the payload heat extraction path based on static superfluid helium.

tached to the bath vessel can be equipped with soft bellows in order to isolate the thin helium tubes from the He I/He II tank.

Further, large bellows in the envelope of the vacuum-insulated connecting line (cf. Figure 6.3) offer mechanical decoupling for the TM cryostat from the CSU wall, which can be installed on a damped mount. Thermal shields inside the line may be supported by the vacuum envelope on the TM cryostat-facing side in order to avoid a rigid mechanical bypass of these bellows. Cooling of the thermal shielding along the connection line can be provided via soft metal links to the helium return lines from the outer shield in the TM cryostat. The design of highly thermally conductive links for this purpose may follow the flexible connections addressed in Section 2.1.

While the thin-walled helium tubes inherently offer vibration damping potential, they can additionally be intercepted by small-scale bellows or hoses. State-of-the-art manufacturing techniques allow the fabrication of bellows with sufficiently small diameters, examples of which are depicted in Figure 6.6.

Such bellows, granting increased tube flexibility, can be positioned close to an auxiliary super-attenuator (SA) hosted in an intermediate cryostat along the heat extraction path outside the TM cryostat. Its purpose is to provide support for the thin helium tubes in combination with sufficient mechanical attenuation as compared to the thermal shielding or vacuum envelope. The utilization of an auxiliary SA along the TM cryostat heat extraction path is conceived in [71]. While the concept of attenuating a mechanical connection to a remote heat sink is implemented in KAGRA (cf. Fig-

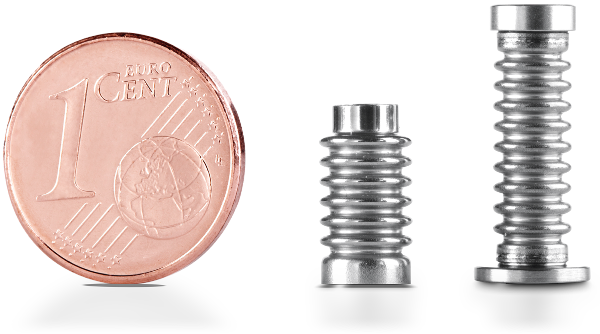

Figure 6.6: Photo of exemplary state-of-the-art bellows with flow diameters sufficiently small for implementation in the TM cryostat helium supply- and return tubes. Image: courtesy of Witzenmann GmbH [276].

ure 2.2), the principle of incorporating an auxiliary SA is being explored in the Amaldi Research Center (ARC).

Collectively attaching the helium tube arrays to the bottom end of the auxiliary SA is accomplished by introducing two pipe sections with increased diameter to merge all helium feed and -return tubes, respectively. The separated helium domains allow for fluid flow provision during transient operation. Both pipe segment walls, however, can be joined together in order to facilitate their suspension as a single coupled mass.

Within the test mass cryostat, the helium tubes must be guided through heat link vibration isolation system (HLVIS) attached to the innermost thermal shield, following the concept applied in KAGRA (cf. Figure 5.4). Further compliant elements may be implemented in this subsystem environment in order to maximize the tube flexibility before and after the payload interface integrated in the platform. Connecting three bellows orthogonally to each other in series exhibits desired attenuation potential, as each vibrational degree of freedom is aligned parallel to the axial direction of one of the bellows. Attenuation of the helium tubes for the innermost thermal shield can be implemented analogously to the presented measures above.

7 Conclusions and prospects

This work provides a comprehensive concept for the provision of cooling power to the various cryogenic consumers in the Einstein Telescope (ET). Four pivotal aspects of such a concept are examined. These include heat extraction from the ET-LF payloads via an integrated interface design, a large-scale helium infrastructure, an initial architecture for the innermost thermal shield within the test mass cryostats and a first approach to viable configurations of low-noise heat extraction paths from the latter.

The investigated marionette suspension tube represents the least-invasive geometry to implement an interface with the helium cooling system inside ET-LF payloads as compared to established layouts in existing gravitational-wave detectors (GWDs) operated at room temperature. From detailed thermodynamic investigations of the suspension tube operation, two major points can be concluded from this work. First, the tube facilitates achieving the desired steady-state test mass (TM) operating temperatures ranging from 10 K to 20 K. Second, it enables sufficiently fast TM cooldown in approximately two weeks by allowing supercritical helium flow across a marionette interface. In comparison to the cooldown duration of almost four weeks for the existing test masses in KAGRA, helium-cooling demonstrates significant potential for accelerated startups of a cryogenic GWD, particularly considering that the TMs in the Einstein Telescope are increased in mass by roughly an order of magnitude.

In accordance with the helium-based payload cooling approach, a concept for the required helium infrastructure that addresses ET-wide provision of refrigeration capacity is presented. This concept considers all cryogenic consumers in the underground caverns, while envisaging compressors at surface level. Every required temperature level in the consumers is covered by the centralized cooling system approach foreseeing a coldbox in each ET vertex with helium outlets at $T_{\mathrm{He}} = 5\,\mathrm{K}$ and $p_{\mathrm{He}} = 5\,\mathrm{bar(a)}$ as well as $T_{\mathrm{He}} \approx 80\,\mathrm{K}$ and $p_{\mathrm{He}} = 12\,\mathrm{bar(a)}$. Notably, apart from the vacuum pumps required for He II generation, no noisy system components are present underground, allowing the provision of He II for low-vibration payload- and thermal shield cooling. Further, the exclusive use of helium as coolant provides a safer infrastructure architecture compared to systems involving liquid nitrogen due to decreased oxygen deficiency hazard in underground caverns. In addition, the helium-based cooling system dissipates negligibly low amounts of heat in the subsurface facilities. This proves beneficial for the required detector infrastructure setup, as it significantly reduces demands on both the tunnel ventilation- and cooling water supply systems. Residual heat dissipation originates predominantly from vacuum pumps for cryogenic supply units (CSUs), cold- and interconnection boxes as well as insulated helium transfer lines. In comparison to the extensive pumping systems required to maintain vacuum quality in the large tower- and beam line volumes of ET, nevertheless, the heat dissipation from these components is expected to be relatively minor. Reviewing the cooling system efficiency, however, insulated helium transfer lines show unfavorably high increases in required compressor input power when supplying remote cryogenic consumers with low cooling capacity needs. A potential solution for these particular consumers is to implement a local, decentralized refrigeration power supply by means of cryocoolers, saving on long transfer lines and avoiding the associated losses.

In the context of developing the innermost thermal shield of the TM cryostat, this thesis shows that the He II phase front propagation into the shield frame channels, approximated to complete within a few minutes, does not limit the overall cooldown duration. The full shield cooldown from room temperature to $T \approx 2\,\mathrm{K}$ is predicted to require a few hours. This conclusion further holds for the He II condensation along the payload- and thermal shield supply tubes, which extend from the He II bath inside the adjacent CSU. Similar distances must be covered, and less residual heat is stored in the thin-walled tubes compared to the shield frame profiles interconnecting the complete shield mass. The presented shield design in this work demonstrates the feasibility of a reasonably lightweight design allowing short cooldown times for supercritical flow conditions down to $T \approx 3\,\mathrm{K}$ and small thermal gradients $\Delta T < 100\,\mathrm{mK}$ across the shield structure during steady-state operation. In combination, dedicated shield reinforcements and an adapted suspension approach promise structural resonant frequencies outside the ET-LF detection band as well as low vibrational transfer function values, yielding a design potential that aligns with the detector noise constraints.

Both the payload and the innermost thermal shield can be supplied with cooling power through interfaces with static He II. The presented studies of helium supply to these consumers via thin tubes identify a range of tube array configurations that satisfy both the thermal steady-state requirements and the transient hydraulic constraints. A suitable design approach for the helium supply tubes employs a limited number of separate channels operating in a turbulent heat transfer regime in static He II during steady-state. Viable supply tube array configurations enable the implementation of multiple vibration attenuation measures along the heat extraction path to a CSU. Conceivable damping means include the established technology of heat link vibration isolation system (HLVIS) from KAGRA, small-scale state-of-the-art bellows supplied by industry as well as the utilization of an auxiliary super-attenuator.

Looking ahead, and depending on the chosen transient operation parameters, it is recommended to determine the exact starting points of the cooldown phases for both the marionette and the innermost thermal shield. This ensures that the required XHV conditions are met that prevent frost buildup on the TMs. Detailed design studies are necessary in the future on integrating the cooling interface at the top end of the suspension tube, and on the marionette interface at the bottom end. Furthermore, it is anticipated that, analogous to existing GWD payloads, geometric anti-spring filters will be implemented in the platform, with their ends providing the mechanical support of the marionette suspension tube. Beyond this, via contact to the platform, thermal anchoring must be provided for all payload instrumentation cabling, which is fixed to the descending super-attenuator suspension chain. This results in an supplementary heat load to be extracted via the helium supply- and return tubes during steady-state operation. In the context of this thesis, an additional $\dot{Q} = 0.5\,\mathrm{W}$ is assumed. However, this value must be refined once all cabling requirements are established in order to determine a thermally adequate helium tube array confguration. Independent on the choice of connecting geometry, leak-tightness of the suspension tube couplings against superfluid helium must be given. Finally, the fundamental question as to which extent the presence of static He II inside the tube effects mechanical dissipation and vibration transmission has to be addressed experimentally. The construction of a new test facility for Q_m-measurements of helium-filled suspension tubes down to 2 K is imminent [139], with the author having made significant contributions to its planning in the course of the work for this thesis.

In parallel to these technical developments, infrastructure design prospects must also be advanced. Future investigations require a refined optical- and corresponding cavern layout involving possible locations for the vertex coldboxes of the helium cooling system as well as the placement of all cryogenic consumers. Moreover, an imminent task is to determine the constraints on the temperature levels in non-isothermally cooled components, i.e. large sections of the cryopumps as well as the outer thermal shielding in the ET-LF test mass cryostats and shields within CSUs, interconnection boxes and transfer lines. This allows deducing required helium mass flows and corresponding engineering designs of the transfer lines, yielding sufficient specifications to tender each cryoplant, consisting of an underground coldbox, room-temperature vertical helium lines and a surface compressor station. Further, future design efforts will be advantageous in diminishing pressure losses in the critical heat exchangers and electric heaters along the subatmospheric-pressure helium suction lines which enable cooling power generation to maintain the He II supply baths inside the CSUs.

Alongside the cryogenic infrastructure, the innermost thermal shield also presents specific future design needs. A detailed engineering design that fully exploits the potential of the concept requires thorough consideration of the implications for the suspension system of the shield. In particular, the shield suspension design must take into account constraints on the tolerable level of detector noise, i.e. phase- and amplitude noise via light backscattering, Newtonian noise induced by residual shield motion, and seismic noise due to mechanical coupling of the payload and shield via the HLVISs. Additional Newtonian noise is caused by displacements of the outer thermal shields in the TM cryostats. An approach to minimize such residual motion during their steady-state operation is to restrict the helium flow providing cooling power to an exclusively laminar regime, mitigating microscopic transient density fluctuations in the coolant flow as well as excessive shield motions provoked by turbulent local pressure oscillations. A double-walled shield design with helium flowing through a long yet narrow gap offers a promising design strategy in this regard.

Furthermore, the low-noise helium provision systems to both the payload and the innermost thermal shield require further development to advance toward detailed engineering. A suitable next step in this context is to explore in detail the vibration isolation requirements introduced by the helium supply tube layout. The design of the latter requires extensive investigations of constraints on the vibrational transfer function along the helium tubes to both the innermost thermal shield and payload. Corresponding results moreover permit the determination of a comprehensive helium loop layout including the choice of a specific supply- and return tube array configuration, an HLVIS design as well as a bellow combination choice.

Finally, these prospective developments must be complemented with corresponding safety considerations. Therefore, safety concepts for the helium cooling system must be developed. As per EN 17527, its design must consider potential scenarios such as loss of insulating vacuum, helium entrapment, and -leakage, and ensure that protection measures are in place, including suitable pressure relief devices [277]. In particular, the innermost thermal shield and the marionette suspension tube require a thorough and systematic risk assessment, which involves critical considerations driven by the imperative to preserve the detector noise budget. Future work has to include developing hermetic designs with appropriate pressure ratings and determining eligible locations for pressure relief devices. These developments must further respect constraints imposed by numerous relevant interfaces with other subsystems of the detector assembly. Accordingly, they should be pursued in the framework of a carefully coordinated safety study within the Einstein Telescope project.

References

[1] A. Sato, M. Maeda, and Y. Kamioka, “Chapter 201 - Normalized representation for steady state heat transport in a channel containing He IIcovering pressure range up to 1.5 MPa,” in *Proceedings of the Twentieth International Cryogenic Engineering Conference (ICEC20)*, L. Zhang, L. Lin, and G. Chen, Eds., Oxford: Elsevier Science, 2005, pp. 849–852. DOI: 10.1016/B978-008044559-5/50204-0.

[2] The ET Science Team, “Einstein gravitational wave Telescope conceptual design study,” ET-0106C-10, Tech. Rep., 2011. [Online]. Available: https://apps.et-gw.eu/tds/ql/?c=7954 (visited on 06/29/2024).

[3] E. Lemmon, M. Huber, and M. McLinden, *NIST Standard Reference Database 23: Reference Fluid Thermodynamic and Transport Properties-REFPROP, Version 9.1*, Natl Std. Ref. Data Series (NIST NSRDS), National Institute of Standards and Technology, Gaithersburg, MD, 2013.

[4] A. Einstein, “Näherungsweise Integration der Feldgleichungen der Gravitation,” *Sitzungsberichte der Königlich Preussischen Akademie der Wissenschaften*, pp. 688–696, Jan. 1916, English translation in [278].

[5] B. F. Schutz, “Gravitational-wave sources,” *Classical and Quantum Gravity*, vol. 13, no. 11A, A219–A238, 1996. DOI: 10.1088/0264-9381/13/11A/031.

[6] C. Bambi, S. Katsanevas, and K. D. Kokkotas, Eds., *Handbook of Gravitational Wave Astronomy*, en. Singapore: Springer Nature Singapore, 2022. DOI: 10.1007/978-981-16-4306-4.

[7] S. Barke, Y. Wang, J. J. E. Delgado, M. Tröbs, G. Heinzel, and K. Danzmann, “Towards a gravitational wave observatory designer: Sensitivity limits of spaceborne detectors,” *Classical and Quantum Gravity*, vol. 32, no. 9, p. 095 004, Apr. 2015. DOI: 10.1088/0264-9381/32/9/095004.

[8] J. D. Romano and N. J. Cornish, “Detection methods for stochastic gravitational-wave backgrounds: A unified treatment,” *Living Reviews in Relativity*, vol. 20, no. 1, p. 2, Apr. 2017, ISSN: 1433-8351. DOI: 10.1007/s41114-017-0004-1.

[9] K. S. Thorne, “Gravitational radiation.,” in *Three Hundred Years of Gravitation*, Cambridge University Press, 1987, pp. 330–458, ISBN: 0-521-34312-7.

[10] C. Cutler and K. S. Thorne, "An overview of gravitational-wave sources," in *General Relativity and Gravitation*. 2002, pp. 72–111. DOI: 10.1142/978981277655 6_0004.

[11] B. S. Sathyaprakash and B. F. Schutz, "Physics, Astrophysics and Cosmology with Gravitational Waves," *Living Reviews in Relativity*, vol. 12, no. 1, p. 2, Dec. 2009. DOI: 10.12942/lrr-2009-2.

[12] B. Allen, "The stochastic gravity-wave background: Sources and detection," in *Relativistic gravitation and gravititional radiation*, J. Marck and J. Lasota, Eds., ser. Cambridge contemporary astrophysics, Cambridge University Press, 1997, pp. 373–417, ISBN: 978-0-521-59065-5.

[13] M. Maggiore, "Gravitational wave experiments and early universe cosmology," *Physics Reports*, vol. 331, no. 6, pp. 283–367, 2000. DOI: 10.1016/S0370-1573(99)0 0102-7.

[14] M. Bailes *et al.*, "Gravitational-wave physics and astronomy in the 2020s and 2030s," *Nature Reviews Physics*, vol. 3, no. 5, pp. 344–366, Apr. 2021. DOI: 10.103 8/s42254-021-00303-8.

[15] A. Burrows, "Colloquium: Perspectives on core-collapse supernova theory," *Rev. Mod. Phys.*, vol. 85, pp. 245–261, 1 2013. DOI: 10.1103/RevModPhys.85.245.

[16] B. Müller, "The core-collapse supernova explosion mechanism," *Proceedings of the International Astronomical Union*, vol. 12, no. S329, pp. 17–24, 2016. DOI: 10.1 017/S1743921317002575.

[17] J. M. Lattimer, "The nuclear equation of state and neutron star masses," *Annual Review of Nuclear and Particle Science*, vol. 62, no. 1, pp. 485–515, 2012. DOI: 10.1 146/annurev-nucl-102711-095018.

[18] L. Baiotti, "Gravitational waves from neutron star mergers and their relation to the nuclear equation of state," *Progress in Particle and Nuclear Physics*, vol. 109, p. 103 714, 2019, ISSN: 0146-6410. DOI: 10.1016/j.ppnp.2019.103714.

[19] B. D. Metzger, "Kilonovae," *Living Reviews in Relativity*, vol. 20, no. 1, p. 3, Dec. 2017. DOI: 10.1007/s41114-017-0006-z. (visited on 11/30/2023).

[20] K. Belczynski *et al.*, "Evolutionary roads leading to low effective spins, high black hole masses, and o1/o2 rates for ligo/virgo binary black holes," *A&A*, vol. 636, A104, 2020. DOI: 10.1051/0004-6361/201936528.

[21] M. Morscher, B. Pattabiraman, C. Rodriguez, F. A. Rasio, and S. Umbreit, "The dynamical evolution of stellar black holes in globular clusters," *The Astrophysical Journal*, vol. 800, no. 1, p. 9, 2015. DOI: 10.1088/0004-637X/800/1/9.

[22] M. Vogel, "Formation of the first black holes," *Contemporary Physics*, vol. 60, no. 4, pp. 331–332, 2019. DOI: 10.1080/00107514.2019.1684381.

[23] A. Askar *et al.*, “Black holes, gravitational waves and fundamental physics: A roadmap,” *Classical and Quantum Gravity*, vol. 36, no. 14, p. 143 001, Jun. 2019. DOI: 10.1088/1361-6382/ab0587.

[24] A. Maselli, P. Pani, V. Cardoso, T. Abdelsalhin, L. Gualtieri, and V. Ferrari, “From micro to macro and back: Probing near-horizon quantum structures with gravitational waves,” *Classical and Quantum Gravity*, vol. 36, no. 16, p. 167 001, Jul. 2019. DOI: 10.1088/1361-6382/ab30ff.

[25] S. Alexander, E. McDonough, R. Sims, and N. Yunes, “Hidden-sector modifications to gravitational waves from binary inspirals,” *Classical and Quantum Gravity*, vol. 35, no. 23, p. 235 012, Nov. 2018, ISSN: 1361-6382. DOI: 10.1088/1361-6382/aaeb5c.

[26] A. A. Starobinsky, “Spectrum of relict gravitational radiation and the early state of the universe,” *JETP Lett.*, vol. 30, I. M. Khalatnikov and V. P. Mineev, Eds., pp. 682–685, 1979.

[27] L. P. Grishchuk, “Amplification of gravitational waves in an isotropic universe,” *Soviet Journal of Experimental and Theoretical Physics*, vol. 40, p. 409, Sep. 1975.

[28] C. M. Will, “The Confrontation between General Relativity and Experiment,” *Living Reviews in Relativity*, vol. 17, no. 1, Jun. 2014. DOI: 10.12942/lrr-2014-4.

[29] J. R. Gair, M. Vallisneri, S. L. Larson, and J. G. Baker, “Testing general relativity with low-frequency, space-based gravitational-wave detectors,” *Living Reviews in Relativity*, vol. 16, no. 1, Sep. 2013. DOI: 10.12942/lrr-2013-7.

[30] N. Yunes and X. Siemens, “Gravitational-wave tests of general relativity with ground-based detectors and pulsar-timing arrays,” *Living Reviews in Relativity*, vol. 16, no. 1, Nov. 2013. DOI: 10.12942/lrr-2013-9.

[31] E. Berti *et al.*, “Testing general relativity with present and future astrophysical observations,” *Classical and Quantum Gravity*, vol. 32, no. 24, p. 243 001, Dec. 2015. DOI: 10.1088/0264-9381/32/24/243001.

[32] K. Pardo, M. Fishbach, D. E. Holz, and D. N. Spergel, “Limits on the number of spacetime dimensions from gw170817,” *Journal of Cosmology and Astroparticle Physics*, vol. 2018, no. 07, pp. 048–048, Jul. 2018. DOI: 10.1088/1475-7516/2018/07/048.

[33] V. Cardoso and P. Pani, “Testing the nature of dark compact objects: A status report,” *Living Reviews in Relativity*, vol. 22, no. 1, Jul. 2019. DOI: 10.1007/s41114-019-0020-4.

[34] P. Astone *et al.*, “Long-term operation of the Rome "Explorer" cryogenic gravitational wave detector,” *Phys. Rev. D*, vol. 47, pp. 362–375, 2 Jan. 1993. DOI: 10.1103/PhysRevD.47.362.

[35] P. Astone *et al.*, "The gravitational wave detector NAUTILUS operating at T = 0.1 K," *Astroparticle Physics*, vol. 7, no. 3, pp. 231–243, 1997. DOI: 10.1016/S0927-6505(97)00023-6.

[36] G. A. Prodi *et al.*, "Initial operation of the gravitational wave detector AURIGA," in *2nd Edoardo Amaldi Conference on Gravitational Waves*, World Scientfic, Jul. 1997, pp. 148–158.

[37] B. Willke *et al.*, "The GEO 600 gravitational wave detector," *Classical and Quantum Gravity*, vol. 19, no. 7, p. 1377, Mar. 2002. DOI: 10.1088/0264-9381/19/7/321.

[38] A. Abramovici *et al.*, "LIGO: The Laser Interferometer Gravitational-Wave Observatory," *Science*, vol. 256, no. 5055, pp. 325–333, 1992. DOI: 10.1126/science.256.5055.325.

[39] T. Accadia *et al.*, "Virgo: A laser interferometer to detect gravitational waves," *Journal of Instrumentation*, vol. 7, no. 03, P03012, 2012. DOI: 10.1088/1748-0221/7/03/P03012.

[40] K. Tsubono and the TAMA collaboration, "TAMA PROJECT," in *Gravitational Wave Detection*, ser. Frontiers science series, vol. 20, Saitama, Japan: Universal Academy Press, Inc., 1997, pp. 183–191, ISBN: 4-946443-38-X.

[41] B. P. Abbott *et al.*, "Observation of gravitational waves from a binary black hole merger," *Phys. Rev. Lett.*, vol. 116, p. 061102, 6 Feb. 2016. DOI: 10.1103/PhysRevLett.116.061102.

[42] The Royal Swedish Academy of Sciences, *NobelPrize.org*, Oct. 2017, Press release. [Online]. Available: https://www.nobelprize.org/prizes/physics/2017/press-release/ (visited on 11/16/2023).

[43] F. Acernese *et al.*, "Advanced Virgo: a second-generation interferometric gravitational wave detector," *Classical and Quantum Gravity*, vol. 32, no. 2, p. 024001, Dec. 2014. DOI: 10.1088/0264-9381/32/2/024001.

[44] The LIGO Scientific Collaboration *et al.*, "Advanced LIGO," *Classical and Quantum Gravity*, vol. 32, no. 7, p. 074001, Mar. 2015. DOI: 10.1088/0264-9381/32/7/074001.

[45] J. Casanueva Diaz, *Control of the Gravitational Wave Interferometric Detector Advanced Virgo* (Springer Theses). Cham: Springer International Publishing, 2018. DOI: 10.1007/978-3-319-96014-2.

[46] Y. Aso *et al.*, "Interferometer design of the KAGRA gravitational wave detector," *Phys. Rev. D*, vol. 88, p. 043007, 4 Aug. 2013. DOI: 10.1103/PhysRevD.88.043007.

[47] KAGRA collaboration *et al.*, "KAGRA: 2.5 generation interferometric gravitational wave detector," *Nature Astronomy*, vol. 3, no. 1, pp. 35–40, Jan. 2019, ISSN: 2397-3366. DOI: 10.1038/s41550-018-0658-y.

[48] F. Matichard *et al.*, "Seismic isolation of Advanced LIGO: Review of strategy, instrumentation and performance," *Classical and Quantum Gravity*, vol. 32, no. 18, p. 185 003, Aug. 2015. DOI: 10.1088/0264-9381/32/18/185003.

[49] L. Naticchioni on behalf of the Virgo Collaboration, "The payloads of Advanced Virgo: current status and upgrades," *Journal of Physics: Conference Series*, vol. 957, p. 012 002, Feb. 2018. DOI: 10.1088/1742-6596/957/1/012002.

[50] S. Braccini *et al.*, "Measurement of the seismic attenuation performance of the virgo superattenuator," *Astroparticle Physics*, vol. 23, no. 6, pp. 557–565, 2005. DOI: 10.1016/j.astropartphys.2005.04.002.

[51] G. M. Harry, T. P. Bodiya, and R. DeSalvo, Eds., *Optical coatings and thermal noise in precision measurement*. Cambridge, New York, 2012, ISBN: 978-1-107-00338-5.

[52] M. G. Beker *et al.*, "Improving the sensitivity of future GW observatories in the 1–10 Hz band: Newtonian and seismic noise," *General Relativity and Gravitation*, vol. 43, no. 2, pp. 623–656, Feb. 2011. DOI: 10.1007/s10714-010-1011-7.

[53] S. A. Hughes and K. S. Thorne, "Seismic gravity-gradient noise in interferometric gravitational-wave detectors," *Phys. Rev. D*, vol. 58, p. 122 002, 12 Nov. 1998. DOI: 10.1103/PhysRevD.58.122002.

[54] M. Tse *et al.*, "Quantum-enhanced advanced ligo detectors in the era of gravitational-wave astronomy," *Phys. Rev. Lett.*, vol. 123, p. 231 107, 23 Dec. 2019. DOI: 10.1103/PhysRevLett.123.231107.

[55] G. M. Harry *et al.*, "Thermal noise from optical coatings in gravitational wave detectors," *Appl. Opt.*, vol. 45, no. 7, pp. 1569–1574, Mar. 2006. DOI: 10.1364/AO.45.001569.

[56] B. P. Abbott *et al.*, "LIGO: the Laser Interferometer Gravitational-Wave Observatory," *Reports on Progress in Physics*, vol. 72, no. 7, p. 076 901, Jun. 2009. DOI: 10.1088/0034-4885/72/7/076901.

[57] G. Hammond, S. Hild, and M. Pitkin, "Advanced technologies for future ground-based, laser-interferometric gravitational wave detectors," *Journal of Modern Optics*, vol. 61, no. sup1, S10–S45, 2014. DOI: 10.1080/09500340.2014.920934.

[58] LIGO Scientic Collaboration and Virgo Collaboration, *LIGO Document G2001862-v4: LIGO-Virgo Cumulative Event Rate Plot O1-O3b*, 2023. [Online]. Available: https://dcc.ligo.org/LIGO-G2001862/public (visited on 05/11/2025).

[59] R. Abbott *et al.*, "GWTC-2: Compact Binary Coalescences Observed by LIGO and Virgo during the First Half of the Third Observing Run," *Phys. Rev. X*, vol. 11, p. 021 053, 2 Jun. 2021. DOI: 10.1103/PhysRevX.11.021053.

[60] A. Buikema *et al.*, "Sensitivity and performance of the advanced ligo detectors in the third observing run," *Phys. Rev. D*, vol. 102, p. 062 003, 6 Sep. 2020. DOI: 10.1103/PhysRevD.102.062003.

[61] F. Acernese *et al.*, *Virgo Detector Characterization and Data Quality during the O3 run*, 2022. DOI: 10.48550/arXiv.2205.01555. eprint: 2205.01555.

[62] LIGO Scientic Collaboration, Virgo Collaboration and KAGRA Collaboration, *GWTC-3 Data Release Documentation*, 2021. DOI: 10.7935/pr1e-j706.

[63] J. D. E. Creighton and W. G. Anderson, *Gravitational-wave physics and astronomy: an introduction to theory, experiment and data analysis* (Wiley series in cosmology). Weinheim, Germany: Wiley-VCH, 2011, ISBN: 978-3-527-40886-3.

[64] E. Capocasa, "Optical and noise studies for Advanced Virgo and filter cavities for quantum noise reduction in gravitational-wave interferometric detectors," Theses, Unversité Paris VII (Denis Diderot), Nov. 2017. [Online]. Available: https://theses.hal.science/tel-03141038 (visited on 12/06/2023).

[65] P. Brady, G. Losurdo, and H. Shinkai, "LIGO, VIRGO, and KAGRA as the International Gravitational Wave Network," in *Handbook of Gravitational Wave Astronomy*, C. Bambi, S. Katsanevas, and K. D. Kokkotas, Eds. Singapore: Springer Singapore, 2020, pp. 1–21. DOI: 10.1007/978-981-15-4702-7_51-1.

[66] C. S. Unnikrishnan, "IndIGO and LIGO-India: Scope and Plans for Gravitational Wave Research and Precision Metrology in India," *International Journal of Modern Physics D*, vol. 22, no. 01, p. 1 341 010, 2013. DOI: 10.1142/S0218271813410101.

[67] S. Fairhurst, "Localization of transient gravitational wave sources: Beyond triangulation," *Classical and Quantum Gravity*, vol. 35, no. 10, p. 105 002, Apr. 2018. DOI: 10.1088/1361-6382/aab675.

[68] P. Raffai *et al.*, "Optimal networks of future gravitational-wave telescopes," *Classical and Quantum Gravity*, vol. 30, no. 15, p. 155 004, Jun. 2013. DOI: 10.1088/0264-9381/30/15/155004.

[69] M. Punturo *et al.*, "The Einstein Telescope: a third-generation gravitational wave observatory," *Classical and Quantum Gravity*, vol. 27, no. 19, p. 194 002, Sep. 2010. DOI: 10.1088/0264-9381/27/19/194002.

[70] Publication Office of the European Union, *CORDIS - EU research results*, 2007. [Online]. Available: https://cordis.europa.eu/project/id/211743 (visited on 05/28/2024).

[71] ET Steering Committee Editorial Team, “Design Report Update for the Einstein Telescope,” Tech. Rep., 2020. [Online]. Available: https://apps.et-gw.eu/tds/ql/?c=15418 (visited on 10/15/2023).

[72] M. Branchesi *et al.*, “Science with the Einstein Telescope: A comparison of different designs,” *Journal of Cosmology and Astroparticle Physics*, vol. 2023, no. 07, p. 068, Jul. 2023. DOI: 10.1088/1475-7516/2023/07/068.

[73] S. Hild *et al.*, “A xylophone configuration for a third-generation gravitational wave detector,” *Classical and Quantum Gravity*, vol. 27, no. 1, p. 015 003, Dec. 2009. DOI: 10.1088/0264-9381/27/1/015003.

[74] S. Hild *et al.*, “Sensitivity studies for third-generation gravitational wave observatories,” *Class Quantum Gravity*, vol. 28, no. 9, p. 094 013, Apr. 2011. DOI: 10.1088/0264-9381/28/9/094013.

[75] M. Di Giovanni *et al.*, “A Seismological Study of the Sos Enattos Area—the Sardinia Candidate Site for the Einstein Telescope,” *Seismological Research Letters*, vol. 92, no. 1, pp. 352–364, Nov. 2020. DOI: 10.1785/0220200186.

[76] S. Koley *et al.*, “Surface and underground seismic characterization at terziet in limburg—the euregio meuse–rhine candidate site for einstein telescope,” *Classical and Quantum Gravity*, vol. 39, no. 2, p. 025 008, Jan. 2022. DOI: 10.1088/1361-6382/ac2b08.

[77] M. Kraan, *Einstein Telescope 2020*. [Online]. Available: https://www.nikhef.nl/pub/departments/mt/projects/EinsteinTelescoop/Artistic/2020/ (visited on 05/28/2024).

[78] S. Miyoki, (Clio, and L. Collaborators), “Underground cryogenic laser interferometer clio,” *Journal of Physics: Conference Series*, vol. 203, no. 1, p. 012 075, Jan. 2010. DOI: 10.1088/1742-6596/203/1/012075.

[79] H. Abe *et al.*, “The Current Status and Future Prospects of KAGRA, the Large-Scale Cryogenic Gravitational Wave Telescope Built in the Kamioka Underground,” *Galaxies*, vol. 10, no. 3, 2022. DOI: 10.3390/galaxies10030063.

[80] S. Chelkowski, S. Hild, and A. Freise, “Prospects of higher-order Laguerre-Gauss modes in future gravitational wave detectors,” *Phys. Rev. D*, vol. 79, p. 122 002, 12 Jun. 2009. DOI: 10.1103/PhysRevD.79.122002.

[81] J. Miller, P. Willems, H. Yamamoto, J. Agresti, and R. DeSalvo, “Thermal distortions of non-gaussian beams in fabry–perot cavities,” *Classical and Quantum Gravity*, vol. 25, no. 23, p. 235 016, Nov. 2008. DOI: 10.1088/0264-9381/25/23/235016.

[82] The Virgo Collaboration, "Advanced Virgo Technical Design Report," European Gravitational Observatory (EGO), Tech. Rep. VIR-0128A-12, Apr. 2012. [Online]. Available: https://tds.virgo-gw.eu/ql/?c=8940 (visited on 07/16/2024).

[83] T. Akutsu *et al.*, "The status of KAGRA underground cryogenic gravitational wave telescope," *Journal of Physics: Conference Series*, vol. 1342, no. 1, p. 012 014, Jan. 2020. DOI: 10.1088/1742-6596/1342/1/012014.

[84] LIGO Scientific Collaboration, "Instrument Science White Paper 2018," Laser Interferometer Gravitational Wave Observatory (LIGO), Tech. Rep. LIGO-T1800133-v4, 2018. [Online]. Available: https://dcc.ligo.org/LIGO-T1800133/public (visited on 07/16/2024).

[85] T. Akutsu *et al.*, "Overview of KAGRA: Detector design and construction history," *Progress of Theoretical and Experimental Physics*, vol. 2021, no. 5, 05A101, Aug. 2020, ISSN: 2050-3911. DOI: 10.1093/ptep/ptaa125.

[86] O. L. Anderson and H. E. Bömmel, "Ultrasonic absorption in fused silica at low temperatures and high frequencies," *Journal of the American Ceramic Society*, vol. 38, no. 4, pp. 125–131, 1955. DOI: 10.1111/j.1151-2916.1955.tb14914.x.

[87] J. Wiedersich, S. V. Adichtchev, and E. Rössler, "Spectral shape of relaxations in silica glass," *Phys. Rev. Lett.*, vol. 84, pp. 2718–2721, 12 Mar. 2000. DOI: 10.1103/PhysRevLett.84.2718.

[88] K. G. Lyon, G. L. Salinger, C. A. Swenson, and G. K. White, "Linear thermal expansion measurements on silicon from 6 to 340 K," *Journal of Applied Physics*, vol. 48, no. 3, pp. 865–868, Aug. 2008, ISSN: 0021-8979. DOI: 10.1063/1.323747.

[89] C. Taylor, M. Notcutt, E. Wong, A. Mann, and D. Blair, "Measurement of the coefficient of thermal expansion of a cryogenic, all-sapphire, fabry-perot optical cavity," *Optics Communications*, vol. 131, no. 4, pp. 311–314, 1996, ISSN: 0030-4018. DOI: 10.1016/0030-4018(96)00293-3.

[90] G. Cagnoli and P. A. Willems, "Effects of nonlinear thermoelastic damping in highly stressed fibers," *Phys. Rev. B*, vol. 65, p. 174 111, 17 Apr. 2002. DOI: 10.1103/PhysRevB.65.174111.

[91] A. Bernardini, E. Majorana, P. Puppo, P. Rapagnani, F. Ricci, and G. Testi, "Suspension last stages for the mirrors of the Virgo interferometric gravitational wave antenna," *Review of Scientific Instruments*, vol. 70, no. 8, pp. 3463–3472, Aug. 1999. DOI: 10.1063/1.1149938.

[92] Y. S. Touloukian, R. W. Powell, C. Y. Ho, and P. G. Klemens, *Thermophysical properties of matter - the TPRC data series. Volume 1. Thermal conductivity - metallic elements and alloys*, Data book, Thermophysical and Electronic Properties Information Analysis Center, Lafayette, IN, 1970.

[93] T. Ushiba *et al.*, "Cryogenic suspension design for a kilometer-scale gravitational-wave detector," *Classical and Quantum Gravity*, vol. 38, no. 8, p. 085 013, Mar. 2021. DOI: 10.1088/1361-6382/abe9f3.

[94] C. Tokoku *et al.*, "Cryogenic system for the interferometric cryogenic gravitationalwave telescope, KAGRA - design, fabrication, and performance test -," *AIP Conference Proceedings*, vol. 1573, no. 1, pp. 1254–1261, Jan. 2014. DOI: 10.1063/1.4860850.

[95] Y. Sakakibara, N. Kimura, T. Akutsu, T. Suzuki, and K. Kuroda, "Performance test of pipe-shaped radiation shields for cryogenic interferometric gravitational wave detectors," *Classical and Quantum Gravity*, vol. 32, no. 15, p. 155 011, Jul. 2015. DOI: 10.1088/0264-9381/32/15/155011.

[96] T. Yamada, "KAGRA cryogenic suspension control toward the observation run 3," *Journal of Physics: Conference Series*, vol. 1468, no. 1, p. 012 217, Feb. 2020. DOI: 10.1088/1742-6596/1468/1/012217.

[97] R. Bajpai *et al.*, "Vibration analysis of KAGRA cryostat at cryogenic temperature," *Classical and Quantum Gravity*, vol. 39, no. 16, p. 165 004, Jul. 2022. DOI: 10.1088/1361-6382/ac7cb5.

[98] T. Yamada *et al.*, "High performance thermal link with small spring constant for cryogenic applications," *Cryogenics*, vol. 116, p. 103 280, 2021. DOI: 10.1016/j.cryogenics.2021.103280.

[99] T. Akutsu *et al.*, "First cryogenic test operation of underground km-scale gravitational-wave observatory kagra," *Classical and Quantum Gravity*, vol. 36, no. 16, p. 165 008, Jul. 2019. DOI: 10.1088/1361-6382/ab28a9.

[100] T. Akutsu *et al.*, "Radiative cooling of the thermally isolated system in kagra gravitational wave telescope," *Journal of Physics: Conference Series*, vol. 1857, no. 1, p. 012 002, Apr. 2021. DOI: 10.1088/1742-6596/1857/1/012002.

[101] E. Majorana, "ARC and CAOS, two experimental facilities dedicated to Einstein Telescope cryogenics and suspensions," in *Proceedings of 38th International Cosmic Ray Conference — PoS(ICRC2023)*, vol. 444, 2023, p. 1578. DOI: 10.22323/1.444.1578.

[102] M. Ricci *et al.*, "Cryogenic Facility for Prototyping ET-LF Payloads Using Conductive Cooling," *Galaxies*, vol. 13, no. 1, 2025, ISSN: 2075-4434. DOI: 10.3390/galaxies13010012.

[103] K. Hasegawa *et al.*, "Molecular adsorbed layer formation on cooled mirrors and its impacts on cryogenic gravitational wave telescopes," *Phys. Rev. D*, vol. 99, p. 022 003, 2 Jan. 2019. DOI: 10.1103/PhysRevD.99.022003.

[104] S. Miyoki *et al.*, “Cryogenic contamination speed for cryogenic laser interferometric gravitational wave detector,” *Cryogenics*, vol. 41, no. 5, pp. 415–420, 2001. DOI: 10.1016/S0011-2275(01)00084-4.

[105] S. Tanioka, K. Hasegawa, and Y. Aso, “Optical loss study of molecular layer for a cryogenic interferometric gravitational-wave detector,” *Phys. Rev. D*, vol. 102, p. 022 009, 2 Jul. 2020. DOI: 10.1103/PhysRevD.102.022009.

[106] J. Steinlechner and I. W. Martin, “Thermal noise from icy mirrors in gravitational wave detectors,” *Phys. Rev. Res.*, vol. 1, p. 013 008, 1 Aug. 2019. DOI: 10.1103/PhysRevResearch.1.013008.

[107] N. Kimura, *Cooling Process to avoid frosting on the surface of the KAGRA Test Mass*, Talk held at Gravitational Wave Advanced Detector Workshop (GWADW), Online, 17–21 May 2021, Slideshow. [Online]. Available: https://gwdoc.icrr.u-tokyo.ac.jp/cgi-bin/DocDB/ShowDocument?docid=12930 (visited on 01/18/2024).

[108] S. Hanke, X. Luo, K. Battes, and C. Day, “Cryopump concept development for the cryogenic mirror region of the Einstein Telescope – the future gravitational wave observatory,” *IOP Conference Series: Materials Science and Engineering*, vol. 1301, no. 1, p. 012 043, May 2024. DOI: 10.1088/1757-899X/1301/1/012043.

[109] R. Bajpai, T. Tomaru, T. Suzuki, K. Yamamoto, T. Ushiba, and T. Honda, “Estimation of newtonian noise from the kagra cooling system,” *Phys. Rev. D*, vol. 107, p. 042 001, 4 Feb. 2023. DOI: 10.1103/PhysRevD.107.042001.

[110] C. Wang, “A 4 K Pulse Tube Cryocooler with Large Cooling Capacity,” in *Proceedings of the 19th International Cryocooler Conference*, San Diego, California: International Cryocooler Conference, Inc., Jun. 2016, pp. 299–305, ISBN: 978-1-934021-05-7.

[111] Cryomech Inc., *PT420 Pulse Tube Cryocooler*, Technical Specifications, Bluefors Oy, Helsinki, Finland, 2024. [Online]. Available: https://bluefors.com/products/pulse-tube-cryocoolers/pt420-pulse-tube-cryocooler/ (visited on 07/20/2024).

[112] I. Fiori, A. Effler, P. Nguyen, F. Paoletti, R. M. S. Schofield, and M. C. Tringali, “Environmental noise in gravitational-wave interferometers,” in *Handbook of Gravitational Wave Astronomy*, C. Bambi, S. Katsanevas, and K. D. Kokkotas, Eds. Springer Singapore, 2020, pp. 1–72. DOI: 10.1007/978-981-15-4702-7_10-1.

[113] The ETpathfinder Team, “ETpathfinder Design Report,” Tech. Rep., Jan. 2020. [Online]. Available: https://www.etpathfinder.eu/wp-content/uploads/2020/03/ETpathfinder-Design-Report.pdf (visited on 01/26/2024).

[114] A. Xhahi, H. Holland, H. Bulten, and H. ter Brake, “Conceptual design of a sorption-based cryochain for the ETpathfinder,” *Cryogenics*, vol. 134, p. 103 717, 2023. DOI: 10.1016/j.cryogenics.2023.103717.

[115] A. Utina *et al.*, "ETpathfinder: a cryogenic testbed for interferometric gravitational-wave detectors," *Classical and Quantum Gravity*, vol. 39, no. 21, p. 215 008, Sep. 2022. DOI: 10.1088/1361-6382/ac8fdb.

[116] Y. Wu, C. H. Vermeer, H. J. Holland, B. Benthem, and H. J. M. ter Brake, "Development of a sorption-based Joule-Thomson cooler for the METIS instrument on E-ELT," *IOP Conference Series: Materials Science and Engineering*, vol. 101, no. 1, p. 012 170, Nov. 2015. DOI: 10.1088/1757-899X/101/1/012170.

[117] J. F. Burger *et al.*, "Long-life vibration-free 4.5 K sorption cooler for space applications," *Review of Scientific Instruments*, vol. 78, no. 6, p. 065 102, Jun. 2007. DOI: 10.1063/1.2745245.

[118] H. J. Bulten for the ETpathfinder collaboration, *Cryogenics and Water Migration in ETpathfinder*, Talk held at Gravitational Wave Advanced Detector Workshop (GWADW), Online, 17–21 May 2021, Slideshow. [Online]. Available: https://agenda.infn.it/event/26121/contributions/136331/ (visited on 01/18/2024).

[119] R. X. Adhikari *et al.*, "A cryogenic silicon interferometer for gravitational-wave detection," *Classical and Quantum Gravity*, vol. 37, no. 16, p. 165 003, Jul. 2020. DOI: 10.1088/1361-6382/ab9143.

[120] M. Evans *et al.*, *A Horizon Study for Cosmic Explorer: Science, Observatories, and Community*, 2021. arXiv: 2109.09882 `[astro-ph.IM]`.

[121] A. Sider *et al.*, *E-TEST prototype design report*, 2022. arXiv: 2212.10083 `[astro-ph.IM]`.

[122] A. Sider *et al.*, "E-TEST: a compact low-frequency isolator for a large cryogenic mirror," *Classical and Quantum Gravity*, vol. 40, no. 16, p. 165 002, Jul. 2023. DOI: 10.1088/1361-6382/ace230.

[123] J. van Heijningen, "A fifty-fold improvement of thermal noise limited inertial sensitivity by operating at cryogenic temperatures," *Journal of Instrumentation*, vol. 15, no. 06, P06034, Jun. 2020. DOI: 10.1088/1748-0221/15/06/P06034.

[124] E. Ferreira, F. Bocchese, F. Badaracco, J. van Heijningen, S. Lucas, and A. Perali, "Superconducting thin film spiral coils as low-noise cryogenic actuators," *Journal of Physics: Conference Series*, vol. 2156, no. 1, p. 012 080, Dec. 2021. DOI: 10.1088/1742-6596/2156/1/012080.

[125] W. F. Vinen, "Fifty years of superfluid helium," in *Advances in Cryogenic Engineering*, R. Fast, Ed., New York: Plenum Press, 1990, pp. 1–14. DOI: 10.1007/978-1-4613-0639-9.

[126] Horizon Technologies, CryoData Inc., *HEPAK^{TM} Version 3.4.* Littleton, CO, 1998. [Online]. Available: https://htess.com/hepak/ (visited on 07/16/2024).

[127] F. London, "On the bose-einstein condensation," *Phys. Rev.*, vol. 54, pp. 947–954, 11 Dec. 1938. DOI: 10.1103/PhysRev.54.947.

[128] P. Ehrenfest, “Phasenumwandlungen im ueblichen und erweiterten sinn, classifiziert nach den entsprechenden singularitaeten des thermodynamischen potentiales.,” en, in *Proc. Royal Acad. Amsterdam*, vol. 36, N.V. Noord-Hollandsche Uitgevers-Mij, 1933, 153–157 (Commun. Kamerlingh Onnes Inst. Leiden, Suppl. 75b).

[129] W. Keesom and K. Clusius, en, in *Proc. Royal Acad. Amsterdam*, vol. 35, 1932, 307 (Commun. Kamerlingh Onnes Inst. Leiden, Suppl. 219e).

[130] L. Tisza, “Transport phenomena in Helium II,” *Nature*, vol. 141, p. 913, 1938. DOI: 10.1038/141913a0.

[131] L. Landau, “Theory of the superfluidity of Helium II,” *Phys. Rev.*, vol. 60, pp. 356–358, 4 Aug. 1941. DOI: 10.1103/PhysRev.60.356.

[132] S. W. Van Sciver, *Helium Cryogenics* (International Cryogenics Monograph Series), 2nd ed. Springer New York, 2012. DOI: 10.1007/978-1-4419-9979-5.

[133] J. F. Allen, R. Peierls, and M. Z. Uddin, “Heat Conduction in Liquid Helium,” *Nature*, vol. 140, no. 3532, pp. 62–63, Jul. 1937, ISSN: 0028-0836, 1476-4687. DOI: 10.1038/140062a0. (visited on 12/04/2024).

[134] R. Feynman, “Chapter II Application of Quantum Mechanics to Liquid Helium,” in ser. Progress in Low Temperature Physics, C. Gorter, Ed., vol. 1, Elsevier, 1955, pp. 17–53. DOI: 10.1016/S0079-6417(08)60077-3.

[135] H. E. Hall and W. F. Vinen, “The rotation of liquid helium II II. The theory of mutual friction in uniformly rotating helium II,” en, *Proceedings of the Royal Society of London. Series A. Mathematical and Physical Sciences*, vol. 238, no. 1213, pp. 215–234, Dec. 1956, ISSN: 0080-4630, 2053-9169. DOI: 10.1098/rspa.1956.0215. (visited on 12/06/2024).

[136] G. A. Williams and R. E. Packard, “Photographs of Quantized Vortex Lines in Rotating He II,” *Phys. Rev. Lett.*, vol. 33, pp. 280–283, 5 Jul. 1974. DOI: 10.1103/PhysRevLett.33.280.

[137] A. Sato, M. Maeda, T. Dantsuka, M. Yuyama, and Y. Kamioka, “Temperature Dependence of the Gorter-Mellink Exponent m Measured in a Channel Containing He II,” *AIP Conference Proceedings*, vol. 823, pp. 387–392, 2006. DOI: 10.1063/1.2202439.

[138] G. Bon Mardion, G. Claudet, P. Seyfert, and J. Verdier, “Helium ii in low-temperature and superconductive magnet engineering,” in *Advances in Cryogenic Engineering*, K. D. Timmerhaus, Ed. Boston, MA: Springer US, 1978, pp. 358–362. DOI: 10.1007/978-1-4613-4039-3_44.

[139] S. Grohmann, "Cryogenic Developments for the Einstein Telescope," International Cryogenic Engineering Conference, Geneva, Switzerland, 2024. [Online]. Available: https://indico.cern.ch/event/1296489/contributions/5881373/ (visited on 01/19/2025).

[140] F. Basti *et al.*, "A cryogenic payload for the 3rd generation of gravitational wave interferometers," *Astroparticle Physics*, vol. 35, no. 2, pp. 67–75, 2011. DOI: 10.1016/j.astropartphys.2011.05.004.

[141] P. Puppo, X. Koroveshi, E. Majorana, P. Rapagnani, and S. Grohmann, *Update on the suspension thermal noise modelling of the ET-LF cryogenic payload*, Talk held at ECLOUD and GWDVac'22 Workshops, Portoferraio, Italy, 2022. [Online]. Available: https://agenda.infn.it/event/28336/contributions/177984/ (visited on 07/16/2024).

[142] K. Yamamoto, *Payload design at KAGRA and its impact to vacuum and cryogenics*, Talk held at ECLOUD and GWDVac'22 Workshops, Portoferraio, Italy, 2022. [Online]. Available: https://agenda.infn.it/event/28336/contributions/179456/ (visited on 07/16/2024).

[143] E. Majorana, *Outline of cryogenic payload compliance with Einstein Telescope LF*, Talk held at GWADW, 2021. [Online]. Available: https://agenda.infn.it/event/26121/contributions/136321/ (visited on 07/16/2024).

[144] P. Puppo, *FEA models for the ET payload: status and preliminary results*, Talk held at GWADW, 2022. [Online]. Available: https://apps.et-gw.eu/tds/ql/?c=16309 (visited on 07/16/2024).

[145] T. Sumomogi, M. N. Masashi Yoshida, H. Osono, and T. Kino, "Mechanical properties of ultra high-purity aluminum," *Journal of The Japan Institute of Metals*, vol. 68, pp. 958–964, 2004. DOI: 10.2320/jinstmet.68.958.

[146] R. Nawrodt *et al.*, "High mechanical Q-factor measurements on silicon bulk samples," *Journal of Physics: Conference Series*, vol. 122, p. 012 008, Jul. 2008. DOI: 10.1088/1742-6596/122/1/012008.

[147] P. R. Saulson, "Thermal noise in mechanical experiments," *Phys. Rev. D*, vol. 42, pp. 2437–2445, 8 Oct. 1990. DOI: 10.1103/PhysRevD.42.2437.

[148] A. S. Nowick and B. S. Berry, Eds., *Anelastic Relaxation in Crystalline Solids*. Academic Press, 1972. DOI: 10.1016/B978-0-12-522650-9.X5001-0.

[149] T. Yamada, *Reduction of vibration transfer via heat links in KAGRA cryogenic mirror suspension system*, Talk held at GWADW, 2021. [Online]. Available: https://agenda.infn.it/event/26121/contributions/136324/ (visited on 07/16/2024).

[150] P. Ruggi, *Mechanical noise in gravitational wave detectors*, Talk held at Amaldi Research Center Summer School, Paestum, Italy, 2022. [Online]. Available: https://agenda.infn.it/event/28968/contributions/176786/.

[151] A. Dari, F. Travasso, H. Vocca, and L. Gammaitoni, "Breaking strength tests on silicon and sapphire bondings for gravitational wave detectors," *Classical and Quantum Gravity*, vol. 27, no. 4, p. 045 010, Jan. 2010. DOI: 10.1088/0264-9381/27/4/045010.

[152] M. Phelps *et al.*, "Strength of hydroxide catalysis bonds between sapphire, silicon, and fused silica as a function of time," *Phys. Rev. D*, vol. 98, p. 122 003, 12 Dec. 2018. DOI: 10.1103/PhysRevD.98.122003.

[153] D. F. McGuigan, C. C. Lam, R. Q. Gram, A. W. Hoffman, D. H. Douglass, and H. W. Gutche, "Measurements of the mechanical Q of single-crystal silicon at low temperatures," *Journal of Low Temperature Physics*, vol. 30, pp. 621–629, 1978. DOI: 10.1007/BF00116202.

[154] C. R. Locke, M. E. Tobar, and E. N. Ivanov, "Properties of a monolithic sapphire parametric transducer: Prospects of measuring the standard quantum limit," *Classical and Quantum Gravity*, vol. 19, no. 7, pp. 1877–1888, 2002. DOI: 10.1088/0264-9381/19/7/388.

[155] S. Amadori *et al.*, "Low temperature anelasticity in Ti6Al4V alloy and Ti6Al4V-SiCf composite," *Materials Science and Engineering: A*, vol. 521-522, pp. 340–342, 2009. DOI: 10.1016/j.msea.2008.09.156.

[156] W. Duffy, "Acoustic quality factor of titanium from 50 mK to 300 K," *Cryogenics*, vol. 40, no. 6, pp. 417–420, 2000. DOI: 10.1016/S0011-2275(00)00053-9.

[157] W. Duffy, "Acoustic quality factor of aluminium and selected aluminium alloys from 50 mK to 300 K," *Cryogenics*, vol. 42, pp. 245–251, Mar. 2002. DOI: 10.1016/S0011-2275(02)00021-8.

[158] A. V. Cumming *et al.*, "Silicon mirror suspensions for gravitational wave detectors," *Classical and Quantum Gravity*, vol. 31, no. 2, p. 025 017, Dec. 2013. DOI: 10.1088/0264-9381/31/2/025017.

[159] E. R. Dobrovinskaya, L. A. Lytvynov, and V. Pishchik, "Properties of sapphire," in *Sapphire: Material, Manufacturing, Applications*. Boston: Springer US, 2009, pp. 55–176. DOI: 10.1007/978-0-387-85695-7_2.

[160] J. W. Ekin, *Experimental Techniques for Low-Temperature Measurements*. Oxford University Press, Oxford, UK, 2006. DOI: 10.1093/acprof:oso/9780198570547.001.0001.

[161] A. Khalaidovski *et al.*, "Evaluation of heat extraction through sapphire fibers for the GW observatory KAGRA," *Classical and Quantum Gravity*, vol. 31, no. 10, p. 105 004, Apr. 2014. DOI: 10.1088/0264-9381/31/10/105004.

[162] CryoData Inc., *CryoComp*, Data from: NIST - Properties of solid materials from cryogenic- to room-temperatures, 1999. [Online]. Available: https://trc.nist.gov/cryogenics/materials/materialproperties.htm (visited on 07/16/2024).

[163] B. Baudouy and A. Four, "Low temperature thermal conductivity of aluminum alloy 5056," *Cryogenics*, vol. 60, pp. 1–4, 2014. DOI: 10.1016/j.cryogenics.2013.12.008.

[164] Y. S. Touloukian and E. H. Buyco, *Thermophysical properties of matter - the TPRC data series. Volume 4. Specific heat - metallic elements and alloys*, Data book, Thermophysical and Electronic Properties Information Analysis Center, Lafayette, IN, 1971.

[165] G. K. White and M. L. Minges, "Thermophysical properties of some key solids: An update," *International Journal of Thermophysics*, vol. 18, pp. 1269–1327, 1997. DOI: 10.1007/BF02575261.

[166] M. Barucci *et al.*, "Very low temperature specific heat of Al 5056," *Physica B: Condensed Matter*, vol. 405, no. 6, pp. 1452–1454, 2010. DOI: 10.1016/j.physb.2009.11.013.

[167] C. A. Swenson, "Recommended Values for the Thermal Expansivity of Silicon from 0 to 1000 K," *Journal of Physical and Chemical Reference Data*, vol. 12, no. 2, pp. 179–182, 1983. DOI: 10.1063/1.555681.

[168] Y. S. Touloukian, R. K. Kirby, R. E. Taylor, and P. D. Desai, *Thermophysical properties of matter - the TPRC data series. Volume 12. Thermal expansion metallic elements and alloys*, Data book, Thermophysical and Electronic Properties Information Analysis Center, Lafayette, IN, 1975.

[169] U. Gysin *et al.*, "Temperature dependence of the force sensitivity of silicon cantilevers," *Phys. Rev. B*, vol. 69, p. 045 403, 4 Jan. 2004. DOI: 10.1103/PhysRevB.69.045403.

[170] J. B. Wachtman Jr., W. E. Tefft, D. G. Lam Jr., and C. S. Apstein, "Exponential Temperature Dependence of Young's Modulus for Several Oxides," *Phys. Rev.*, vol. 122, pp. 1754–1759, 6 Jun. 1961. DOI: 10.1103/PhysRev.122.1754.

[171] M. Fukuhara and A. Sanpei, "Elastic moduli and internal frictions of Inconel 718 and Ti-6Al-4V as a function of temperature," *Journal of Materials Science Letters*, vol. 12, pp. 1122–1124, 1993. DOI: 10.1007/BF00420541.

[172] National Institute of Standards and Technology (NIST), *Properties of solid materials from cryogenic- to room-temperatures*, 2021. [Online]. Available: https://trc.nist.gov/cryogenics/materials/materialproperties.htm (visited on 07/16/2024).

[173] M. A. Hopcroft, W. D. Nix, and T. W. Kenny, "What is the Young's Modulus of Silicon?" *Journal of Microelectromechanical Systems*, vol. 19, no. 2, pp. 229–238, 2010. DOI: 10.1109/JMEMS.2009.2039697.

[174] J. B. Wachtman Jr. and D. G. Lam Jr., "Young's modulus of various refractory materials as a function of temperature," *Journal of the American Ceramic Society*, vol. 42, no. 5, pp. 254–260, 1959. DOI: 10.1111/j.1151-2916.1959.tb15462.x.

[175] R. R. Boyer, G. Welsch, and E. W. Collings, *Materials properties handbook: Titanium Alloys*. Materials Park, Ohio: ASM International, 1994, ISBN: 978-0-87170-481-8.

[176] R. Nawrodt *et al.*, *Mirror thermal noise calculation for ET*, Scientific note, 2009. [Online]. Available: https://apps.et-gw.eu/tds/ql/?c=7556 (visited on 07/16/2024).

[177] R. Nawrodt *et al.*, "Investigation of mechanical losses of thin silicon flexures at low temperatures," *Fraunhofer IOF*, vol. 30, p. 115 008, Jun. 2013. DOI: 10.1088/0264-9381/30/11/115008.

[178] T. Yamada, *Sapphire bending tests*, Public and Internal note database at Institute for Cosmic Ray Research (ICRR) University of Tokyo, 2023. [Online]. Available: https://gwdoc.icrr.u-tokyo.ac.jp/cgi-bin/DocDB/ShowDocument?docid=14883 (visited on 07/16/2024).

[179] Shinkosha Co., Ltd. 2-4-1 Kosugaya, Sakae-ku, Yokohama, Kanagawa 247-0007 Japan.

[180] R. G. Scurlock, *Low Temperature Behaviour of Solids*. Routledge and Kegan Paul PLC, 1966, ISBN: 9780710043832.

[181] Y. S. Touloukian, R. W. Powell, C. Y. Ho, and P. G. Klemens, *Thermophysical properties of matter - the TPRC data series. Volume 2. Thermal conductivity - nonmetallic solids*, Data book, Thermophysical and Electronic Properties Information Analysis Center, Lafayette, IN, 1971.

[182] F. Travasso *et al.*, "Towards a silicon monolithic suspension," *Proceedings of the 2nd gravitational-waves science & technology symposium (GRASS)*, 2019, Padova, Italy. DOI: 10.5281/zenodo.3820523.

[183] P. Astone *et al.*, "Noise behaviour of the explorer gravitational wave antenna during λ transition to the superfluid phase," *Cryogenics*, vol. 32, no. 7, pp. 668–670, 1992. DOI: 10.1016/0011-2275(92)90300-Y.

[184] P. Puppo and F. Ricci, "Cryogenics and Einstein Telescope," *General Relativity and Gravitation volume*, vol. 43, no. February, pp. 657–669, 2011. DOI: 10.1007/s10714-010-1037-x.

[185] W. F. Vinen, "The physics of superfluid helium," in *CAS - CERN Accelerator School: Superconductivity and Cryogenics for Accelerators and Detectors*, 2004. DOI: 10.5170/CERN-2004-008.363.

[186] L. Busch and S. Grohmann, "Conceptual layout of a helium cooling system for the Einstein Telescope," *IOP Conference Series: Materials Science and Engineering*, vol. 1240, no. 1, p. 012 095, May 2022. DOI: 10.1088/1757-899x/1240/1/012095.

[187] L. Busch and S. Grohmann, *Thermal design of the He-II suspension tube for ET-LF: Status and outlook*, Talk held at ECLOUD and GWDVac Workshops, Portoferraio, Italy, 2022. DOI: 10.5445/IR/1000153741.

[188] L. Busch, X. Koroveshi, and S. Grohmann, *Helium-based cooling concept of the ET-LF interferometer*, Talk at Gravitational Wave Advanced Detector Workshop (GWADW), Online, 17–21 May 2021, 2021. [Online]. Available: https://agenda.infn.it/event/26121/contributions/136476/ (visited on 07/16/2024).

[189] B. Baudouy, "Low temperature thermal conductivity of aluminum alloy 1200," *Cryogenics*, vol. 51, pp. 617–620, Nov. 2011. DOI: 10.1016/j.cryogenics.2011.09.002.

[190] C. H. Twu, J. E. Coon, and J. R. Cunningham, "A new generalized alpha function for a cubic equation of state Part 1. Peng-Robinson equation," *Fluid Phase Equilibria*, vol. 105, no. 1, pp. 49–59, 1995. DOI: 10.1016/0378-3812(94)02601-V.

[191] V. Yakhot and S. A. Orszag, "Renormalization group analysis of turbulence. I. Basic theory," *Journal of scientific computing*, vol. 1, no. 1, pp. 3–51, 1986. DOI: 10.1007/BF01061452.

[192] ANSYS, Inc., *Ansys Fluent Theory Guide*. Canonsburg, PA, 2022, Release 2022 R1.

[193] M. Constancio Jr *et al.*, "Silicon emissivity as a function of temperature," *International Journal of Heat and Mass Transfer*, vol. 157, p. 119 863, 2020. DOI: 10.1016/j.ijheatmasstransfer.2020.119863.

[194] P. D. Desai, "Thermodynamic properties of iron and silicon," *Journal of Physical and Chemical Reference Data*, vol. 15, no. 3, pp. 967–983, 1986. DOI: 10.1063/1.555761.

[195] H. B. Callen and T. A. Welton, "Irreversibility and generalized noise," *Phys. Rev.*, vol. 83, pp. 34–40, 1 Jul. 1951. DOI: 10.1103/PhysRev.83.34.

[196] P. R. Saulson, *Fundamentals of Interferometric Gravitational Wave Detectors*. World Scientific, 1994. DOI: 10.1142/2410.

[197] Y. Levin, "Internal thermal noise in the LIGO test masses: A direct approach," *Phys. Rev. D*, vol. 57, pp. 659–663, 2 Jan. 1998. DOI: 10.1103/PhysRevD.57.659.

[198] G. I. González and P. R. Saulson, "Brownian motion of a mass suspended by an anelastic wire," *The Journal of the Acoustical Society of America*, vol. 96, no. 1, pp. 207–212, 1994. DOI: 10.1121/1.410467.

[199] G. González, "Suspensions thermal noise in the LIGO gravitational wave detector," *Classical and Quantum Gravity*, vol. 17, no. 21, pp. 4409–4435, Oct. 2000. DOI: 10.1088/0264-9381/17/21/305.

[200] E. Majorana and Y. Ogawa, "Mechanical thermal noise in coupled oscillators," *Physics Letters A*, vol. 233, no. 3, pp. 162–168, 1997, ISSN: 0375-9601. DOI: 10.1016/S0375-9601(97)00458-1.

[201] G. Cagnoli *et al.*, "Damping dilution factor for a pendulum in an interferometric gravitational waves detector," *Physics Letters A*, vol. 272, no. 1, pp. 39–45, 2000. DOI: https://doi.org/10.1016/S0375-9601(00)00411-4.

[202] S. Rowan *et al.*, "Investigation of mechanical loss factors of some candidate materials for the test masses of gravitational wave detectors," *Physics Letters A*, vol. 265, pp. 5–11, 2000. DOI: 10.1016/S0375-9601(99)00874-9.

[203] A. Schröter, "Mechanical losses in materials for future cryogenic gravitational wave detectors," Dissertation, Friedrich-Schiller-Universität Jena, 2008, Jena, 2008. [Online]. Available: http://uri.gbv.de/document/gvk:ppn:560947623 (visited on 07/16/2024).

[204] V. B. Braginsky, V. Mitrofanov, and V. I. Panov, *Systems with Small Dissipation*. The University of Chicago Press, 1985, ISBN: 9780226070735.

[205] T. Uchiyama *et al.*, "Mechanical quality factor of a cryogenic sapphire test mass for gravitational wave detectors," *Physics Letters A*, vol. 261, no. 1, pp. 5–11, 1999. DOI: 10.1016/S0375-9601(99)00563-0.

[206] E. Majorana, P. Rapagnani, and F. Ricci, "Test facility for resonance transducers of cryogenic gravitational wave antennas," *Measurement Science and Technology*, vol. 3, no. 5, pp. 501–507, May 1992. DOI: 10.1088/0957-0233/3/5/010.

[207] W. Duffy, "Acoustic quality factor of aluminum alloys from 50 mK to 300 K," *Journal of Applied Physics*, vol. 68, no. 11, pp. 5601–5609, 1990. DOI: 10.1063/1.346971.

[208] E. Coccia and T. Niinikoski, "Acoustic quality factor of an aluminium alloy for gravitational wave antennae below 1 K," *Lett. Nuovo Cimento*, vol. 41, pp. 242–246, 1984. DOI: 10.1007/BF02747011.

[209] C. Zener, "Internal Friction in Solids II. General Theory of Thermoelastic Internal Friction," *Phys. Rev.*, vol. 53, pp. 90–99, 1 Jan. 1938. DOI: 10.1103/PhysRev.53.90.

[210] R. Nawrodt, S. Rowan, J. Hough, M. Punturo, F. Ricci, and J. Vinet, "Challenges in thermal noise for 3rd generation of gravitational wave detectors," *General Relativity and Gravitation*, vol. 43, no. 2, pp. 593–622, 2011. DOI: 10.1007/s10714-010-1066-5.

[211] A. M. Gretarsson *et al.*, "Pendulum mode thermal noise in advanced interferometers: A comparison of fused silica fibers and ribbons in the presence of surface loss," *Physics Letters A*, vol. 270, no. 3, pp. 108–114, 2000. DOI: 10.1016/S0375-9601(00)00295-4.

[212] A. V. Cumming *et al.*, "Lowest observed surface and weld losses in fused silica fibres for gravitational wave detectors," *Classical and Quantum Gravity*, vol. 37, no. 19, p. 195 019, Sep. 2020. DOI: 10.1088/1361-6382/abac42.

[213] F. Piergiovanni, M. Punturo, and P. Puppo, *The thermal noise of the Virgo+ and Virgo Advanced Last Stage Suspension (The PPP Effect)*, Report No. VIR-015D-09, Apr. 2009. [Online]. Available: https://tds.virgo-gw.eu/ql/?c=2199 (visited on 07/16/2024).

[214] K. Somiya, *Suspension thermal noise reduction in a cryogenic interferometer*, 2011. [Online]. Available: https://www.academia.edu/44046909/Suspension_thermal_noise_reduction_in_a_cryogenic_interferometer (visited on 07/16/2024).

[215] F. Bondu, P. Hello, and J. Vinet, "Thermal noise in mirrors of interferometric gravitational wave antennas," *Physics Letters A*, vol. 246, no. 3, pp. 227–236, 1998. DOI: 10.1016/S0375-9601(98)00450-2.

[216] K. Komori *et al.*, "Direct approach for the fluctuation-dissipation theorem under nonequilibrium steady-state conditions," *Phys. Rev. D*, vol. 97, p. 102 001, 10 May 2018. DOI: 10.1103/PhysRevD.97.102001.

[217] C. J. Gorter and J. Mellink, "On the irreversible processes in liquid helium II," *Physica*, vol. 15, pp. 285–304, 1949. DOI: 10.1016/0031-8914(49)90105-6.

[218] X. Koroveshi, S. Grohmann, P. Rapagnani, and V. Mangano, *Experimental plans to validate the He-II based payload cooling concept*, Talk held at ECLOUD and GWDVac'22 Workshops, Portoferraio, Italy, 2022. DOI: 10.5445/IR/1000153742.

[219] E. S. Fisher and C. J. Renken, "Single-Crystal Elastic Moduli and the hcp → bcc Transformation in Ti, Zr, and Hf," *Phys. Rev.*, vol. 135, A482–A494, 2A Jul. 1964. DOI: 10.1103/PhysRev.135.A482.

[220] Core Optics and Suspensions working group, *Silicon suspensions for ET-LF*, Talk held in Einstein Telescope—ISB Workshop, L'Aquila, Italy (2022), Slideshow.

[221] S. Di Pace *et al.*, "Research Facilities for Europe's Next Generation Gravitational-Wave Detector Einstein Telescope," *Galaxies*, vol. 10, no. 65, pp. 1–36, 2022. DOI: 10.3390/galaxies10030065.

[222] COMSOL Multiphysics®, COMSOL AB, Stockholm, Sweden, Stockholm, Sweden. [Online]. Available: www.comsol.com.

[223] F. Travasso on behalf of Virgo Collaboration, "Status of the Monolithic Suspensions for Advanced Virgo," *Journal of Physics: Conference Series*, vol. 957, no. 1, p. 012 012, Feb. 2018. DOI: 10.1088/1742-6596/957/1/012012.

[224] S. Sunil Kumar and K. Ramamurthi, "Thermal contact conductance of pressed contacts at low temperatures," *Cryogenics*, vol. 44, no. 10, pp. 727–734, 2004, ISSN: 0011-2275. DOI: 10.1016/j.cryogenics.2004.04.004.

[225] M. Yovanovich, "Thermal contact correlations," in *16th Thermophysics Conference*, vol. 83, Palo Alto, CA: American Institute of Aeronautics and Astronautics, Jun. 1981, pp. 83–95. DOI: 10.2514/6.1981-1164.

[226] B. Mikić, "Thermal contact conductance; theoretical considerations," *International Journal of Heat and Mass Transfer*, vol. 17, no. 2, pp. 205–214, Feb. 1974. DOI: 10.1016/0017-9310(74)90082-9.

[227] W. Hesse, *Aluminium material data sheets* (Beuth Wissen). Beuth Verlag GmbH, 2011, ISBN: 9783410220473.

[228] thyssenkrupp Materials (UK) Ltd, *Stainless Steel 1.4404 Material Data Sheet*, Nov. 2017. [Online]. Available: https://www.thyssenkrupp-materials.co.uk/stainless-steel-316l-14404.html (visited on 01/25/2024).

[229] G. Spranz, *Cryogenic Data Mathematica Package*, Ing.-Büro Elmar Röther, Version 1.0, 2011, Karlrsruhe, Germany.

[230] P. Giarratano, V. Arp, and R. Smith, "Forced convection heat transfer to supercritical helium," *Cryogenics*, vol. 11, no. 5, pp. 385–393, 1971. DOI: 10.1016/0011-2275(71)90038-5.

[231] E. W. Lemmon, I. H. Bell, M. L. Huber, and M. O. McLinden, *NIST Standard Reference Database 23: Reference Fluid Thermodynamic and Transport Properties-REFPROP, Version 10.0*, Natl Std. Ref. Data Series (NIST NSRDS), National Institute of Standards and Technology, Gaithersburg, MD, 2018. DOI: 10.18434/T4/1502528.

[232] I. H. Bell, J. Wronski, S. Quoilin, and V. Lemort, "Pure and pseudo-pure fluid thermophysical property evaluation and the open-source thermophysical property library coolprop," *Industrial & Engineering Chemistry Research*, vol. 53, no. 6, pp. 2498–2508, 2014. DOI: 10.1021/ie4033999.

[233] J. Sindermann, "Extension of a numerical model for cryogenic payload cooldown in the Einstein Telescope," Bachelor's Thesis, Karlsruhe Institute of Technology, Karlsruhe, Germany, 2024.

[234] J. Dickmann, S. Kroker, Y. Levin, R. Nawrodt, and S. Vyatchanin, "Thermal noise of beam splitters in laser gravitational wave detectors," *Phys. Rev. D*, vol. 98, p. 082 002, 8 Oct. 2018. DOI: 10.1103/PhysRevD.98.082002.

[235] X. Luo, S. Hanke, K. Battes, and C. Day, "Monte carlo simulation of the thermal radiation heat load to the cryogenic mirror and vacuum system of the Einstein Telescope," *IOP Conference Series: Materials Science and Engineering*, vol. 1327, no. 1, p. 012 031, May 2025. DOI: 10.1088/1757-899X/1327/1/012031.

[236] S. J. Rowlinson, "Robust optical configurations for reducing the impact of spatial laser beam effects in gravitational wave detectors," Dissertation, The University of Birmingham, Birmingham, United Kingdom, May 2021. [Online]. Available: http://etheses.bham.ac.uk/id/eprint/11872 (visited on 01/17/2024).

[237] U. Wagner, "The LHC refrigerators with surface located cold boxes for the temperature range 300-4.5 K," *LHC Project Note 70*, 1996. [Online]. Available: https://cds.cern.ch/record/691805/ (visited on 07/16/2024).

[238] P. Lebrun, "Large cryogenic helium refrigeration system for the LHC," CERN, Geneva, Tech. Rep., Feb. 2003. [Online]. Available: https://cds.cern.ch/record/605468 (visited on 07/16/2024).

[239] S. Claudet, P. Lebrun, L. Tavian, and U. Wagner, "Exergy analysis of the cryogenic helium distribution system for the large hadron collider (LHC)," *AIP Conference Proceedings*, 2010.

[240] G. Gistau-Baguer, "High power refrigeration at temperatures around 2.0 K," in *Proceedings of the Sixteenth International Cryogenic Engineering Conference/International Cryogenic Materials Conference*, T. Haruyama, T. Mitsui, and K. Yamafuji, Eds., Oxford: Elsevier Science, 1997, pp. 189–194. DOI: https://doi.org/10.1016/B978-008042688-4/50044-2.

[241] P. Lebrun and L. Tavian, "Cooling with superfluid helium," in *Proceedings of the CAS-CERN Accelerator School: Superconductivity for Accelerators*, CERN, 2014. DOI: 10.5170/CERN-2014-005.453.

[242] S. Miwa, M. Mori, and T. Hibiki, "Two-phase flow induced vibration in piping systems," *Progress in Nuclear Energy*, vol. 78, pp. 270–284, Jan. 2015. DOI: 10.1016/j.pnucene.2014.10.003.

[243] B. Shapiro *et al.*, "Cryogenically cooled ultra low vibration silicon mirrors for gravitational wave observatories," *Cryogenics*, vol. 81, pp. 83–92, Jan. 2017, ISSN: 0011-2275. DOI: 10.1016/j.cryogenics.2016.12.004.

[244] A. Grado *et al.*, "Ultra high vacuum beam pipe of the Einstein Telescope project: Challenges and perspectives," *Journal of Vacuum Science & Technology B*, vol. 41, no. 2, p. 024 201, Feb. 2023. DOI: 10.1116/6.0002323.

[245] J. Friedel, "Process Studies of the Helium-Based Cooling System for the Einstein Telescope," Bachelor's Thesis, Karlsruhe Institute of Technology, Karlsruhe, Germany, 2021.

[246] J. Fydrych, "Cryogenic Transfer Lines," in *Cryostat Design*, J. Weisend II, Ed., Series Title: International Cryogenics Monograph Series, Switzerland: Springer International Publishing, 2016, pp. 241–274. DOI: 10.1007/978-3-319-31150-0_9.

[247] P. Dauguet, G. M. Gistau-Baguer, and P. Briend, “Two Large 18 KW (Equivalent Power at 4.5 K) Helium Refrigerators for Cern’s LHC Project, Supplied by Air Liquide,” in *Advances in Cryogenic Engineering*, Q.-S. Shu, Ed. Boston, MA: Springer US, 2000, pp. 1277–1284. DOI: 10.1007/978-1-4615-4215-5_41.

[248] J. Bösel, B. Chromec, and A. Meier, “Two Large 18 kW (Equivalent Power at 4.5 K) Refrigerators for CERN’s LHC Project Supplied by Linde Kryotechnik AG,” in *Advances in Cryogenic Engineering*, Q.-S. Shu, Ed. Boston, MA: Springer US, 2000, pp. 1285–1292. DOI: 10.1007/978-1-4615-4215-5_42.

[249] O. S. Brüning *et al.*, *LHC Design Report* (CERN Yellow Reports: Monographs). Geneva: CERN, 2004. DOI: 10.5170/CERN-2004-003-V-1.

[250] P. Lebrun, “Superconductivity and Cryogenics for Future High-Energy Accelerators,” CERN, Geneva, Tech. Rep. CERN-AT-2007-004, 2007. [Online]. Available: https://cds.cern.ch/record/1026936 (visited on 07/16/2024).

[251] T. R. Strobridge, “Cryogenic refrigerators — An updated survey,” National Bureau of Standards, Gaithersburg, MD, Tech. Rep., 1974, Edition: 0. DOI: 10.6028/NBS.TN.655.

[252] U. Wagner, “Refrigeration,” in *CAS - CERN Accelerator School: Superconductivity and Cryogenics for Accelerators and Detectors*, 2004. DOI: 10.5170/CERN-2004-008.295.

[253] M. Ruhemann, *The Separation of Gases* (International series of monographs on physics). Clarendon Press, 1949, pp. 112–140.

[254] R. Barron, *Cryogenic Systems* (McGraw-Hill series in mechanical engineering). McGraw-Hill, 1966, pp. 75–177, ISBN: 9780070038202.

[255] T. Maurer, *Kältetechnik für Ingenieure (German language)*, 2., aktualisierte und überarbeitete Auflage. Berlin: VDE Verlag, 2021, ISBN: 978-3-8007-5241-6.

[256] M. Andrés-Carcasona, A. Macquet, M. Martínez, L. M. Mir, and H. Yamamoto, “Study of scattered light in the main arms of the Einstein Telescope gravitational wave detector,” *Phys. Rev. D*, vol. 108, p. 102 001, 10 Nov. 2023. DOI: 10.1103/PhysRevD.108.102001.

[257] K. Thorne, “Light Scattering and Proposed Baffle Configuration for the LIGO,” LIGO Scientific Collaboration, Technical Note LIGO-T890017-x0, Jan. 1989. [Online]. Available: https://dcc.ligo.org/LIGO-T890017/public (visited on 07/16/2024).

[258] P. Fritschel and H. Yamamoto, “Scattered light noise due to the ETM coating ripple,” LIGO Scientific Collaboration, Technical Note LIGO-T1300354-v3, Jul. 2013. [Online]. Available: https://dcc.ligo.org/LIGO-T1300354/public (visited on 07/16/2024).

[259] T. Akutsu *et al.*, "Vacuum and cryogenic compatible black surface for large optical baffles in advanced gravitational-wave telescopes," *Opt. Mater. Express*, vol. 6, no. 5, pp. 1613–1626, May 2016. DOI: 10.1364/OME.6.001613.

[260] X. Koroveshi *et al.*, "Cryogenic payloads for the Einstein Telescope: Baseline design with heat extraction, suspension thermal noise modeling, and sensitivity analyses," *Phys. Rev. D*, vol. 108, p. 123 009, 12 Dec. 2023. DOI: 10.1103/PhysRevD.108.123009.

[261] V. D. Arp, R. D. McCarty, and D. G. Friend, "Thermophysical properties of Helium-4 from 0.8 to 1500 K with pressures to 2000 MPa," National Institute of Standards and Technology, Tech. Rep. 1334 (revised), Sep. 1998.

[262] C. Kittel, *Introduction to Solid State Physics*. John Wiley & Sons, Hoboken, 2018, ISBN: 978-1-119-45416-8.

[263] W. M. Hartmann, H. V. Culbert, and R. P. Huebener, "Enhancement of the Lattice Heat Capacity Due to Low-Frequency Resonance Modes in Dilute Aluminum-Silver Alloys," *Phys. Rev. B*, vol. 1, pp. 1486–1493, 4 Feb. 1970. DOI: 10.1103/PhysRevB.1.1486.

[264] A. L. Woodcraft, "Recommended values for the thermal conductivity of aluminium of different purities in the cryogenic to room temperature range, and a comparison with copper," *Cryogenics*, vol. 45, no. 9, pp. 626–636, 2005. DOI: 10.1016/j.cryogenics.2005.06.008.

[265] E. R. Bielert, A. P. Verweij, and H. H. J. Ten Kate, "Implementation of the superfluid helium phase transition using finite element modeling," *Cryogenics*, vol. 53, pp. 78–85, 2013. DOI: 10.1016/j.cryogenics.2012.06.002.

[266] J. Crank and P. Nicolson, "A practical method for numerical evaluation of solutions of partial differential equations of the heat-conduction type," *Math. Proc. Camb. Phil. Soc.*, vol. 43, no. 1, pp. 50–67, 1947. DOI: 10.1017/S0305004100023197.

[267] F. R. Schwartzberg *et al.*, *Cryogenic Materials Data Handbook (revised) 1970, volume II*. Denver, CO, 1970, Martin Marietta Corporation.

[268] R. Stewart and Eckels, *CryoComp for Windows Ver. 5.3*, Eckels Engineering Inc., 1993 – 2017.

[269] A. Bertolini, G. Cella, R. DeSalvo, and V. Sannibale, "Seismic noise filters, vertical resonance frequency reduction with geometric anti-springs: A feasibility study," *Nuclear Instruments and Methods in Physics Research Section A: Accelerators, Spectrometers, Detectors and Associated Equipment*, vol. 435, no. 3, pp. 475–483, 1999. DOI: 10.1016/S0168-9002(99)00554-9.

[270] A. Stochino, R. DeSalvo, Y. Huang, and V. Sannibale, "Improvement of the seismic noise attenuation performance of the monolithic geometric anti-spring filters for gravitational wave interferometric detectors," *Nuclear Instruments and Methods in Physics Research Section A: Accelerators, Spectrometers, Detectors and Associated Equipment*, vol. 580, no. 3, pp. 1559–1564, 2007. DOI: 10.1016/j.nima.2007.06.029.

[271] Busch Vacuum Solutions, *PANDA series*, Schauinslandstraße 1, 79689 Maulburg, Germany, 2022. [Online]. Available: https://www.buschvacuum.com/global/en/products/vacuum-pumps/booster/panda-puma/ (visited on 06/18/2024).

[272] Pfeiffer Vacuum GmbH, *OktaLine*, Berliner Strasse 43, 35614 Asslar, Germany, 2024. [Online]. Available: https://www.pfeiffer-vacuum.com/global/en/shop/categories/OKTALINE (visited on 06/18/2024).

[273] Leybold GmbH, *RUVAC WS / WSU series*, Bonner Str. 498, 50968 Köln, Germany, 2024. [Online]. Available: https://www.leyboldproducts.com/products/roots-vacuum-pumps/ruvac-ws-wsu/pumps/ (visited on 06/18/2024).

[274] Busch Vacuum Solutions, *COBRA NS 0070–0600 C Dry screw vacuum pumps*, Schauinslandstraße 1, 79689 Maulburg, Germany, 2021. [Online]. Available: https://www.buschvacuum.com/global/en/products/cobra-ns-0070-0600-c.html (visited on 05/22/2025).

[275] W. F. Vinen and D. Shoenberg, "Mutual friction in a heat current in liquid heliumn. II. IV. Critical heat currents in wide channels," *Proceedings of the Royal Society of London. Series A. Mathematical and Physical Sciences*, vol. 243, no. 1234, pp. 400–413, 1958. DOI: 10.1098/rspa.1958.0007.

[276] Witzenmann GmbH, *HYDRA® Präzisionsbälge*, Pforzheim, Germany, 2019.

[277] "EN 17527:2021 Helium cryostats – Protection against excessive pressure; German version," Deutsches Institut für Normung e. V., Berlin, Germany, Standard, 2022.

[278] A. Einstein, A. Engel, and E. Schucking, *The collected papers of Albert Einstein: writings, 1914-1917*, English translation of selected texts. Princeton: Princeton university press, 1997, ISBN: 978-0-691-01734-1.

[279] P. R. Amestoy, I. S. Duff, J.-Y. L'Excellent, and J. Koster, "A fully asynchronous multifrontal solver using distributed dynamic scheduling," *SIAM Journal on Matrix Analysis and Applications*, vol. 23, no. 1, pp. 15–41, 2001. DOI: 10.1137/S0895479899358194.

[280] COMSOL AB, *COMSOL Multiphysics® 6.0 Programming Reference Manual*, Stockholm, Sweden, 2021. [Online]. Available: https://doc.comsol.com/6.0/doc/com.comsol.help.comsol/COMSOL_ProgrammingReferenceManual.pdf (visited on 07/09/2024).

[281] C. M. Rhie and W. L. Chow, "Numerical study of the turbulent flow past an airfoil with trailing edge separation," *AIAA Journal*, vol. 21, no. 11, pp. 1525–1532, 1983. DOI: 10.2514/3.8284.

[282] W. Kast and H. Nirschl, "Pressure Drop in Flow Through Pipes," in *VDI Heat Atlas*, VDI e.V., Ed., 2nd ed., Springer Berlin, Heidelberg, 2010, ch. L1.2, pp. 1057–1064. DOI: 10.1007/978-3-540-77877-6.

[283] H. Blasius, "Das Aehnlichkeitsgesetz bei Reibungsvorgängen in Flüssigkeiten," in *Mitteilungen über Forschungsarbeiten auf dem Gebiete des Ingenieurwesens: insbesondere aus den Laboratorien der technischen Hochschulen*. Springer Berlin Heidelberg, 1913, pp. 1–41. DOI: 10.1007/978-3-662-02239-9_1.

[284] L. F. Moody and N. J. Princeton, "Friction factors for pipe flow," *Transactions of the American Society of Mechanical Engineers*, pp. 671–684, Nov. 1944. DOI: 10.1115/1.4018140.

Appendix

A.1 Refined PFD of a helium cooling system concept for the Einstein Telescope

The process flow diagram of the helium cooling system concept for ET presented in Section 4.2 is extended to consider the advanced cryogenic consumer requirements addressed in Section 4.3.1. Figure A.1 shows these extensions.

The temperature level of the 3rd (outer) thermal shield cooling in the test mass cryostat is specified to $T \approx 80\,\mathrm{K}$ to allow for a harmonized helium supply with the cryopump sections demanding similar conditions. Further, heat extraction from the 1st (innermost) shield at $T \approx 2\,\mathrm{K}$ is indicated via HXFS in the test mass cryostat. The depiction of corresponding additional supply- and return tube connections is omitted. The associated helium loop is analogous to the connection between V56 and V57 and is merged into the same pipe connections towards V54 and V55.

In the interferometer arm pipes, two additional consumers are specified. Firstly, actively cooled baffles with cooling power demand at $T \approx 10\,\mathrm{K}$ in HXBF are supplied with helium by the header at $T \approx 5\,\mathrm{K}$ via V60. Pre-cooling the flow warmed up due to parasitic heat loads in the transfer lines through HX41 is possible. Valve V62 enables merging the returning flow to the low-temperature return manifold. Secondly, the cryopump heat exchanger is split into HXCP-I and HXCP-II. The latter takes into account the cryopump sections for pumping hydrogen at $T \approx 3.7\,\mathrm{K}$. Alongside the baffles, it is provided with helium by the header at $T \approx 5\,\mathrm{K}$ via V61. In order to supply cooling power at the required final temperature, the helium flow is expanded in V63 to $p_{\mathrm{sat}}(T = 3.7\,\mathrm{K}) \approx 0.6\,\mathrm{bar(a)}$. This subatmospheric pressure level is enabled by means of the vacuum pump P60. In ET-HF, cryopumps can be supplied similarly to HXCP-I and HXCP-II from the ET-LF CSUs (cf. Figure 4.4). Analogous to EH40, EH60 heats the return flow to T_{amb} directly upstream. In order to increase operational process efficiency, it is conceivable to priorly utilize the cold flow upstream of EH60 in heat exchangers with low pressure drop to pre-cool a supply stream at $T \approx 5\,\mathrm{K}$ or provide

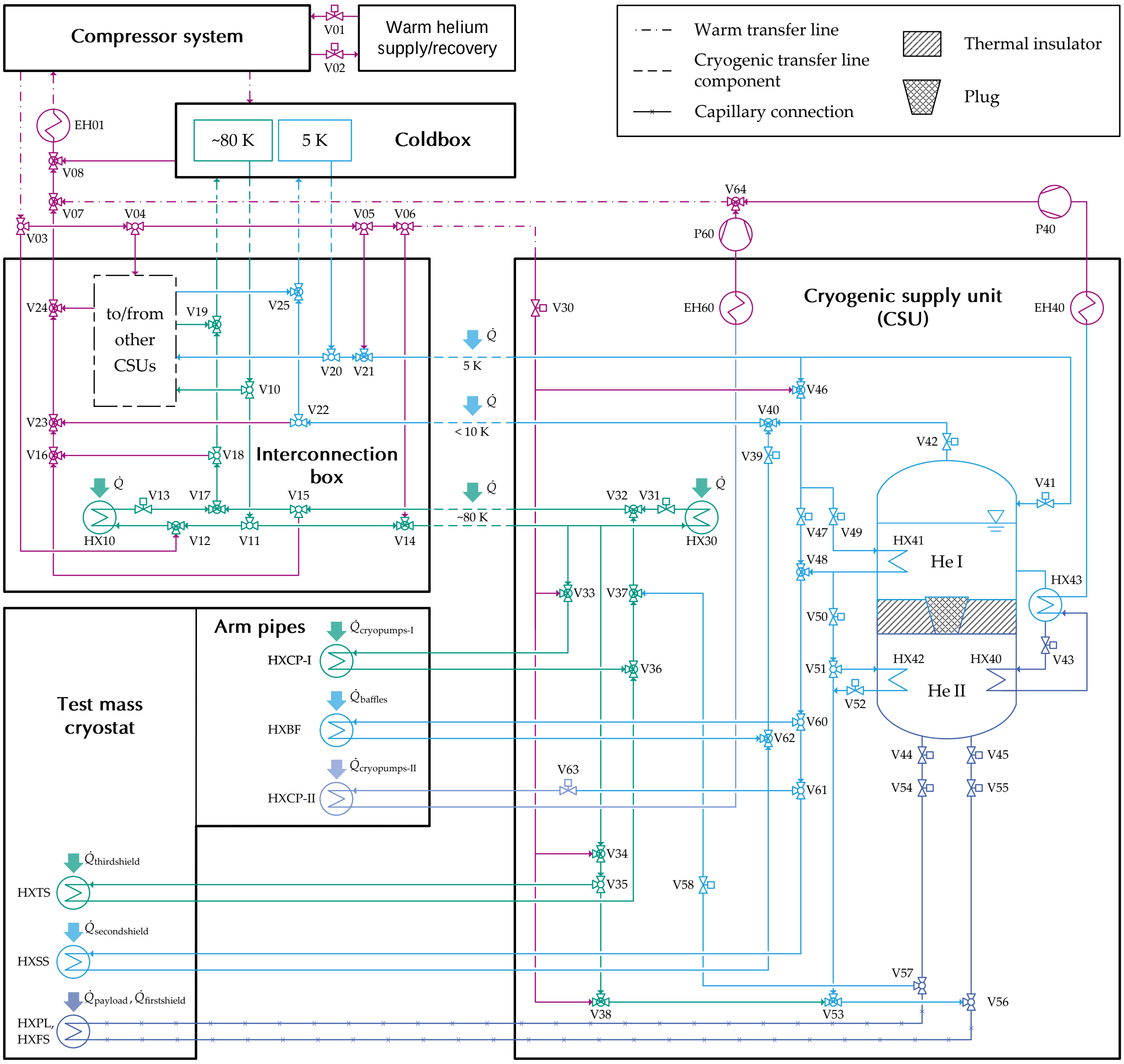

Figure A.1: Refined process flow diagram based on Figure 4.3 including cooling of cryopumps at $T \approx 3.7\,\mathrm{K}$, baffles at $T \geq 5\,\mathrm{K}$ and indication of heat extraction from the 3$^{\mathrm{rd}}$ thermal shield inside the test mass cryostat.

inner thermal shield cooling around the He I/He II supply vessel. Downstream of P60, the helium flow is fed into the warm return manifold via V64 at $p \approx 1.2\,\mathrm{bar(a)}$.

A.2 Liquefaction and equivalent refrigeration energy demands

Equation (4.4) enables the conversion of isothermal cooling power provided by the cryogenic helium infrastructure to equivalent refrigeration capacity specific to the cooling system. This is achieved by means of the actual liquefaction energy demand l_{liq} and helium mass flow $\dot{M}_{\mathrm{liq}}$, the virtual refrigeration energy demand l_{refr} and the specific enthalpy of vaporization Δh_{vap}. $\dot{M}_{\mathrm{liq}}$ in this context is calculated as

$$\dot{M}_{\mathrm{liq}}(T_{\mathrm{c}}) = \frac{\dot{Q}_{\mathrm{c}}(T_{\mathrm{c}})}{\Delta h_{\mathrm{vap}}\,(T_{\mathrm{c}})}\,, \tag{A.1}$$

via the values of $\dot{Q}_{\mathrm{c},i}$ listed in Table 4.5. The conversion to equivalent refrigeration capacity is only necessary for cooling powers to be provided at helium temperatures for which $p_{\mathrm{sat}} < 1.2\,\mathrm{bar(a)}$. At higher saturation pressures, the helium can still be drawn through the transfer lines and heat exchangers within the underground coldbox, which implies that for these streams, the cryoplant is operating as a refrigerator [252]. The correspondingly calculated values of $\dot{M}_{\mathrm{liq}}$ and the remaining parameters for determination of equivalent refrigeration capacity $\dot{Q}_{\mathrm{c,eq,refr}}$ are listed in Table 4.4. In turn, Table A.1 presents all fluid property values for calculation of l_{liq} and l_{refr} according to Equation (4.3) and $\dot{M}_{\mathrm{liq}}$ through Equation (A.1). It shall be noted here that insertion of Equations (A.1) and (4.2) leads to the simplified conversion equation

$$\dot{Q}_{\mathrm{c,eq,refr}} = \frac{l_{\mathrm{liq}}}{l_{\mathrm{refr}}} \cdot \dot{Q}_{\mathrm{c}}\,. \tag{A.2}$$

A.3 Minimum achievable test mass temperatures

Section 3.1.7.2 includes the consideration of silicon test mass suspensions with $d_{\mathrm{tm}} = 4.0\,\mathrm{mm}$ and $L_{\mathrm{tm}} = 0.8\,\mathrm{m}$. Albeit these dimensions do not comply with the envisaged ET-LF sensitivity goals, Figure A.2 shows the corresponding steady-state

Table A.1: State points and specific evaporation enthalpies for minimum liquefaction- and refrigeration work calculation (Equation (4.3)) and subsequent equivalent refrigeration capacity determination (Equation (4.4)).

T_{c} / K	Point	H / kJ kg^{-1}	s / J kg^{-1} K^{-1}	Δh_{vap} / kJ kg^{-1}
	①	0.480	0.337	
1.65	②$_{\mathrm{liq}}$	1538	41 225	22.67
	②$_{\mathrm{refr}}$	23.15	14 201	
	①	7.580	3042	
3.70	②$_{\mathrm{liq}}$	1538	32 575	22.66
	②$_{\mathrm{refr}}$	30.24	9181	

thermal modelling results obtained analogously to the data presented in Figure 3.18 in order to offer a comprehensive thermal evaluation of conceivable suspensions. Sapphire fiber configurations are added for comparison.

Generally, these TM suspension configurations yield lower values of $T_{\mathrm{TM,min}}$ due to larger diameters and shorter lengths. Further, the increased heat extraction efficiency through suspensions with these dimensions enhances the benefit of cooling the marionette with He II, indicated by the steeper curve gradients at $T_{\mathrm{MA}} = 2\,\mathrm{K}$ with respect to the results presented in Figure 3.18. As a consequence of the similar thermal conductivities of Silicon and Sapphire at temperatures $T \lesssim 10\,\mathrm{K}$, differences in $T_{\mathrm{TM,min}}$ between both materials decrease towards lower T_{MA} at equal suspension dimensions. This is particularly evident for the suspension configuration with highest thermal conductance ($L_{\mathrm{tm}} = 0.8\,\mathrm{m}$, $d_{\mathrm{tm}} = 4.0\,\mathrm{mm}$).

A.4 Extended numerical model information

In the scope of this thesis, two major numerical models are set up to investigate the thermal characteristics of the baseline design for cryogenic payloads in ET. Presented results are obtained via a steady-state model within COMSOL Multiphysics® (FEM) as well as a transient model in ANSYS Fluent® (FVM). This section aims to provide further details of both model settings and test mass cooldown results.

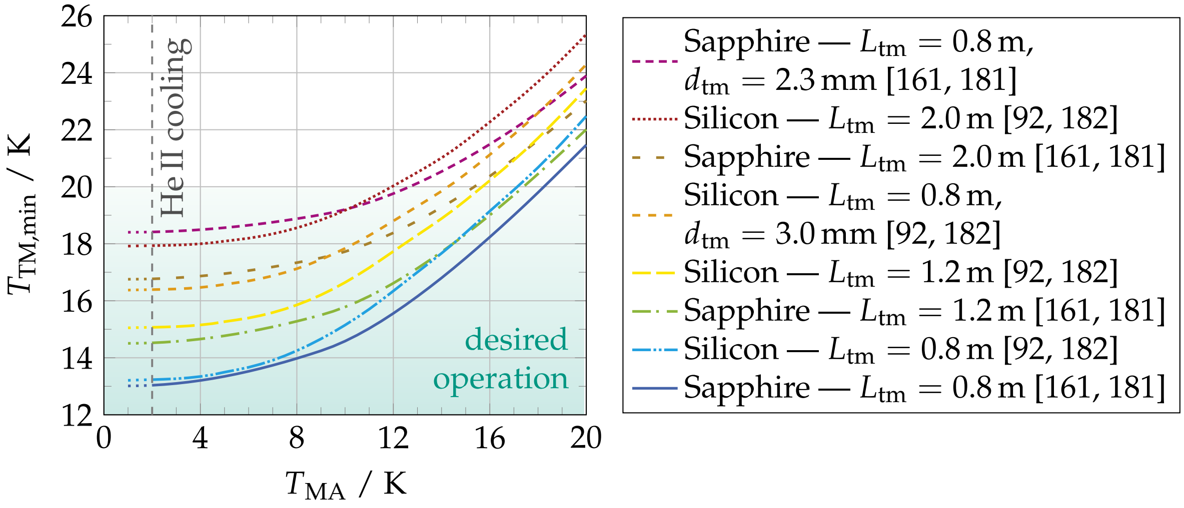

Figure A.2: Minimum reachable test mass temperature dependence on marionette interface temperature using different TM suspension fiber materials and lengths ($d_{\mathrm{tm}} = 4.0\,\mathrm{mm}$ unless stated otherwise).

A.4.1 Steady-state FEM thermal model

FEM numerical modelling relies on the spatial discretization of the considered geometry. The steady-state model is evaluated in 3D and therefore, volumetric elements are used to generate the domain mesh. Figure A.3 depicts the fully discretized model geometry for the case of a marionette composed of aluminum alloy 1200. The total meshed volume $V \approx 0.159\,\mathrm{m}^3$ is subdivided into $\sim 3.43 \cdot 10^6$ tetrahedral elements. All boundaries are constituted by the sum of $\sim 4.2 \cdot 10^5$ triangles. The dominating part of the elements is attributed to the TM suspension fibers, their anchors, and the corresponding platforms and ears as well as the surrounding of the suspension tube insertion length inside the marionette. This way, a discretization of the fine geometries with an average element skewness of ~ 0.67 is achieved. In longitudinal direction, each suspension fiber is subdivided into ~ 2500 elements along the total length $L = 1.365\,\mathrm{m}$ between anchors. The marionette surface area along the suspension tube insertion length is discretized into ~ 2800 triangles. Solving the thermal model described in Section 3.2.1 with this mesh requires approximately 20 min utilizing 8 processing cores clocking at $\sim 4.7\,\mathrm{GHz}$. Table A.2 lists the corresponding major solver settings.

Table A.2: Key FEM solver settings for the numerical steady-state thermal model in COMSOL Multiphysics®.

Setting	Expression/value
General solver	MUMPS [279]
Solver configuration	fully coupled [280]
Linear solver	direct [280]
Nonlinear method	automatic highly nonlinear (Newton) [280]
Initial damping factor	10^{-6}
Minimum damping factor	10^{-8}
Termination technique	iterations or tolerance
Number of iterations	1000
Tolerance factor	0.01
Termination criterion	solution [280]

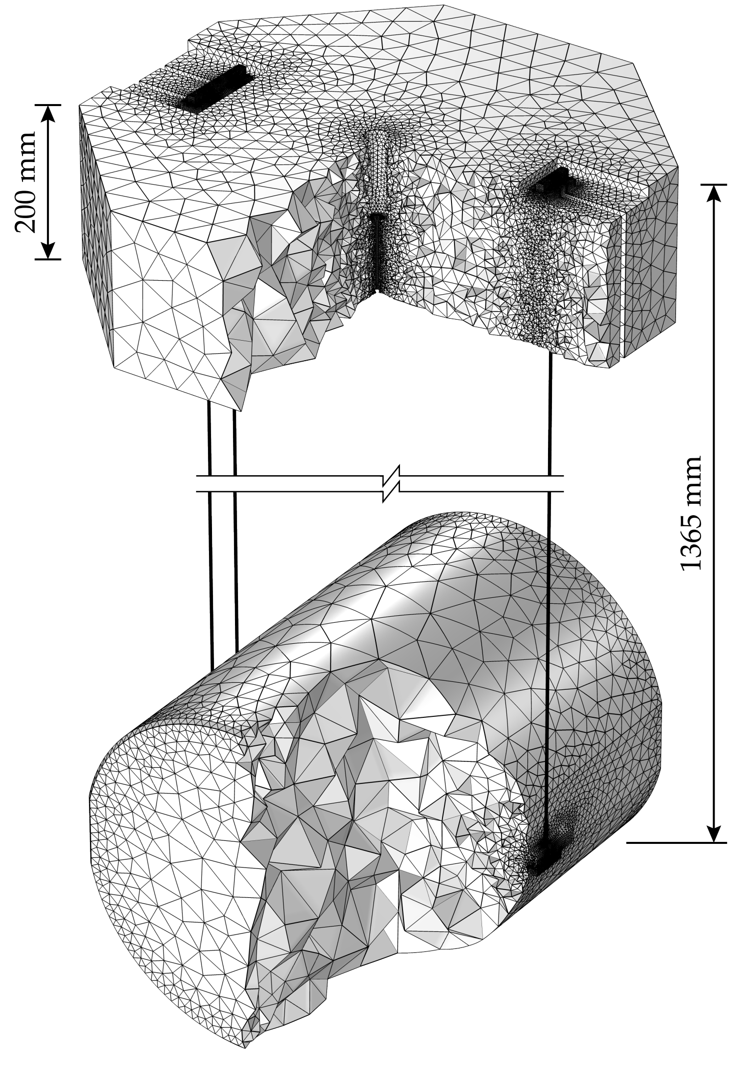

Figure A.3: Spatial discretization of the numerical steady-state thermal model for the results presented in Section 3.2.1 (Al 1200-marionette).

A.4.2 Transient FVM CFD model

The modelled 2D-geometry with rotational symmetry around the suspension tube longitudinal center axis is discretized using a variety of schemes as indicated in Figures A.4 and A.5. For a practical handling of the model geometry, the test mass (TM) is placed above the marionette, in the direction of the suspension tube. Rotational symmetry forces the TM to result in a torus. This change of shape with respect to the real geometry is accounted for via the chosen area of the TM in 2D as well as artificially reducing the surface area by multiplying the applied view factor $\varphi_{\mathrm{TM}\rightarrow\mathrm{sh}}$ with 0.875. Similarly, the rotation of the 2D suspension fiber geometry results in a tube. In order to provide an equal $A_{\mathrm{cross,HT}} \approx 28\,\mathrm{mm}^2$ in comparison to the sum provided by the actual four separate fibers, the width of the 2D fiber area is set to 19.7 µm.

The total amount of nodes generated for numerical evaluation via the finite volume method (FVM) in ANSYS Fluent® is $\sim 1.5 \cdot 10^5$. The suspension tube (ST) as well as the test mass suspension fiber are discretized via structured meshing methods. In longitudinal direction, the ST including helium domains is subdivided into ~1500 parts while the TM suspension fiber section exhibits $2 \cdot 10^4$ segments, avoiding exceedingly high skewness of the volumetric cells. At the ST bottom end environment, helium supply- and return domain merge into a flow reversal volume which is finely meshed

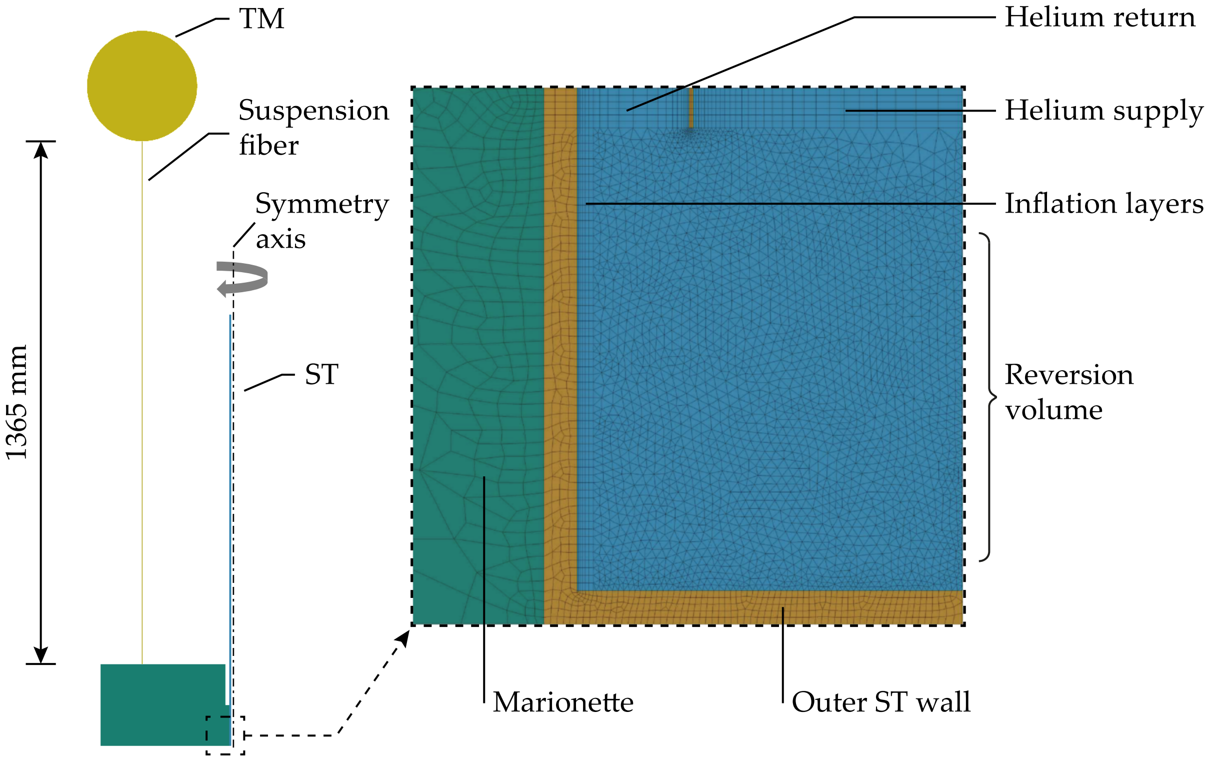

Figure A.4: Full geometry and ST spatial discretization details of the numerical transient CFD model for the results presented in Sections 3.1.4.5 and 3.2.2. Adapted from [233].

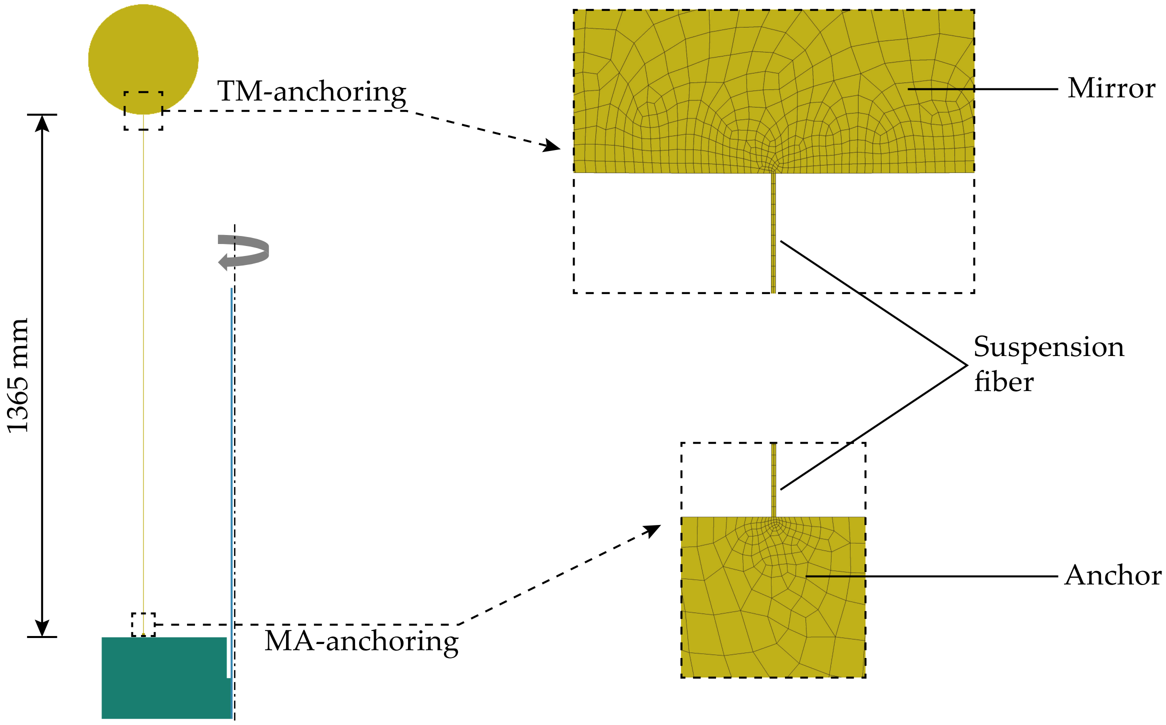

Figure A.5: Full geometry and TM suspension fiber anchoring spatial discretization details of the numerical transient CFD model for the results presented in Sections 3.1.4.5 and 3.2.2. Adapted from [233].

to take into account the large expected spatial gradients in flow velocity. Similarly, the regions in the TM- and MA bulk adjacent to the suspension fiber ends are finely meshed to allow sufficiently high resolution of thermal gradients. The rest of the marionette and test mass are discretized in an unstructured, coarser manner, in order to respect model computing efficiency. Solving the CFD model for the conditions described in Section 3.1.4.5 (MA and ST only) and Section 3.2.2 (MA, ST, suspension fibers and TM) with this mesh is achieved within a few hours, strongly depending on the cooldown duration as determined by the chosen boundary conditions, utilizing 8 processing cores clocking at ∼4.7 GHz. Table A.3 lists the corresponding major solver settings.

A.5 Test mass cooldown curves

For varied mass flows $\dot{M}_{\mathrm{He}}$, the average test mass temperature $\overline{T}_{\mathrm{TM}}(t)$ is evaluated for transient cooldown with the conditions stated in Tables 3.5 and 3.6 using the coupled numerical CFD model described in Section 3.2.2. Figure A.6 shows the corresponding results.

Table A.3: Key FVM solver settings for the numerical steady-state thermal model in ANSYS Fluent® [192].

Setting	Expression/value
Solver type	pressure-based
Pressure-velocity coupling scheme	coupled
Pressure-velocity coupling flux type	Rhie-Chow: distance based [281]
Near-wall treatment	scalable wall functions
Transient formulation	first order implicit
High order term relaxation	flow variables only
Flow courant number	10^{15}
Explicit relaxation factors:	
Momentum	0.25
Pressure	0.25
Under-relaxation factors:	
Density	0.175
Body forces	1.0
Turbulent kinetc energy	0.8
Turbulent dissipation rate	0.8
Turbulent viscosity	1.0
Energy	1.0
Spatial discretization:	
Gradient	least squares cell based
Pressure	second order
Density	second order upwind
Momentum	second order upwind
Turbulent kinetic energy	first order upwind
Turbulent dissipation rate	first order upwind
Energy	second order upwind

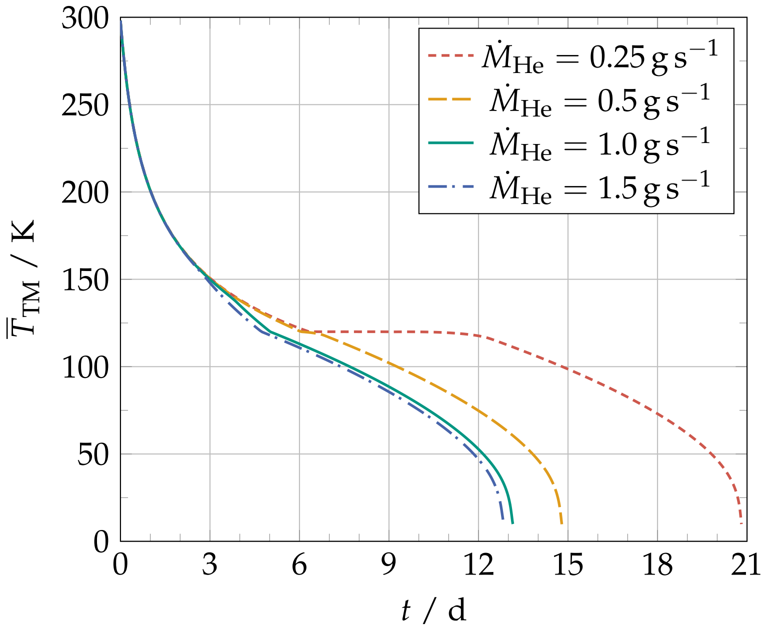

Figure A.6: Cooldown of an ET-LF silicon test mass installed within a thermal shield at $T = 5\,\mathrm{K}$ at different $\dot{M}_{\mathrm{He}}$ and conditions listed in Tables 3.5 and 3.6. Majority of curves evaluated by Sindermann [233].

For both $\dot{M}_{\mathrm{He}} = 1.5\,\mathrm{g\,s^{-1}}$ and $\dot{M}_{\mathrm{He}} = 1.0\,\mathrm{g\,s^{-1}}$, the qualitative curve trends are virtually identical to the one presented in Figure 3.12, yielding similar cooldown times of $\Delta t_{\mathrm{cooldown}} \approx 13\,\mathrm{d}$. The cutoff of radiative cooling due to $\epsilon_{\mathrm{TM,Si}}(\overline{T}_{\mathrm{TM}} < 120\,\mathrm{K}) = 0$ produces a minor slope discontinuity at $t \approx 4.5\,\mathrm{d}$. At lower mass flows, the lag in the decrease of T_{MA} with respect to T_{TM} becomes evident via a progressively enlarging plateau of $\overline{T}_{\mathrm{TM}}(t)$ caused by the temporary absence of heat extraction from the test mass by thermal conduction. For $\dot{M}_{\mathrm{He}} = 0.25\,\mathrm{g\,s^{-1}}$, this plateau extends between $t \approx 6\,\mathrm{d}$ and $t \approx 12\,\mathrm{d}$.

A.6 Friction coefficient

In accordance with the findings of Kast and Nirschl [282] for drawn brass and copper tubes, technically smooth surfaces are assumed for the determination of the friction coefficient ξ. Equation (A.3) shows the correspondingly defined function.

$$\xi(Re) = \begin{cases} \frac{64}{Re} & Re \leq 2320 \\ 0.04275 \cdot \tanh\left(\frac{Re-2660}{40.4491}\right) & 2320 < Re < 3000 \\ \frac{0.3164}{\sqrt[4]{Re}} & 3000 \leq Re \leq 10^5 \end{cases} \tag{A.3}$$

The laminar flow regime is described by the Hagen-Poiseuille law, whereas Blasius' correlation is applied in the turbulent flow regime [283]. The critical zone between both regimes (c.f. Moody and Princeton [284]) is modelled in a manner that ensures a smoothed transition for numerical computation of the differential equations (3.46) and (3.47) while avoiding underestimation of $\xi(Re \to 2320^+)$ as well as overestimation of $\xi(Re \to 3000^-)$ with respect to the established literature values. Figure A.7 displays the corresponding function graph.

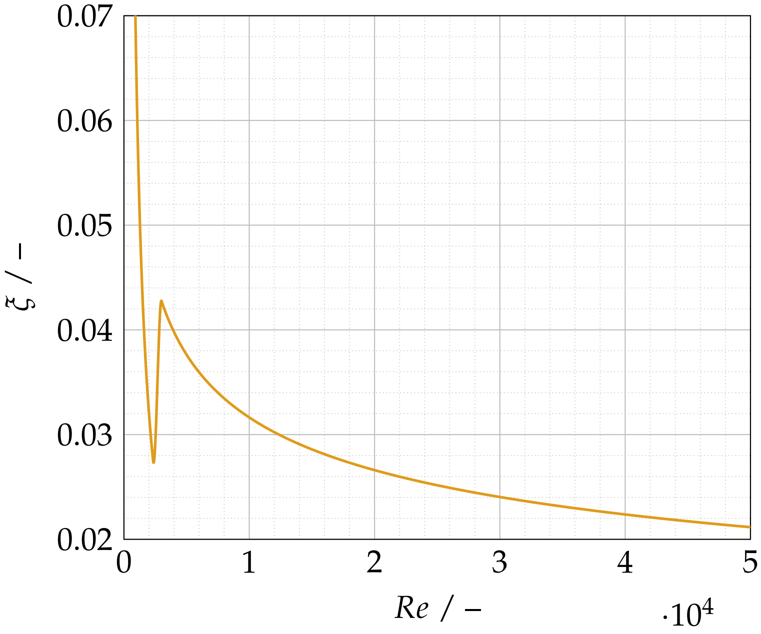

Figure A.7: Modelling of $\xi(Re)$ across the laminar- and turbulent flow regime as well as the critical zone for the range of Re relevant in this thesis.

Own publications

Peer-reviewed papers

[1] V. Ilardi, H. Silva, A. Dudarev, T. Koettig, P. Borges de Sousa, **L. N. Busch**, T. Kulenkampff, E. R. Bielert and H. H. J. ten Kate. "Development of light and highly radiation transparent cryostats for FCC detector magnets: first analyses of insulation materials". *IOP Conference Series: Materials Science and Engineering*, vol 502 p 012083, 2019.
DOI: 10.1088/1757-899X/502/1/012083.

[2] V. Ilardi, A. Dudarev, H. Silva, T. Koettig, **L. N. Busch**, P. Borges de Sousa and H. H. J. ten Kate. "Conceptual Design of the Cryostat for a Highly Radiation Transparent 2 T Superconducting Detector Solenoid for FCC–ee$^+$". *IEEE Transactions on Applied Superconductivity*, vol 30, no 4, p 1–5, 2020.
DOI: 10.1109/TASC.2020.2973588.

[3] V. Ilardi, **L. N. Busch**, A. Dudarev, T. Koettig, P. Borges de Sousa, J. Liberadzka, H. Silva and H. H. J. ten Kate. "Compression and thermal conductivity tests of Cryogel$^{\circledR}$ Z for use in the ultra-transparent cryostats of FCC detector solenoids". *IOP Conference Series: Materials Science and Engineering*, vol 756, p 012005, 2020.
DOI: 10.1088/1757-899X/756/1/012005.

[4] **L. Busch** and S. Grohmann. "Conceptual Layout of a Helium Cooling System for the Einstein Telescope". *IOP Conference Series: Materials Science and Engineering*, vol 1240 p 012095, 2021.
DOI: 10.1088/1757-899X/1240/1/012095.

[5] A. Utina, A. Amato, J. Arends, C. Arina, M. de Baar, M. Baars, P. Baer, N. van Bakel, W. Beaumont, A. Bertolini, M. van Beuzekom, S. Biersteker, A. Binetti, H. J. M. ter Brake, G. Bruno, J. Bryant, H. J. Bulten, **L. Busch**, P. Cebeci, C. Collette, S. Cooper, R. Cornelissen, P. Cuijpers, M. van Dael, S. Danilishin, D. Diksha, S. van Doesburg, M. Doets, R. Elsinga, V. Erends, J. van Erps, A. Freise,

H. Frenaij, R. Garcia, M. Giesberts, S. Grohmann, H. Van Haevermaet, S. Heijnen, J. V. van Heijningen, E. Hennes, J.-S. Hennig, M. Hennig, T. Hertog, S. Hild, H.-D. Hoffmann, G. Hoft, M. Hopman, D. Hoyland, G. A. Iandolo, C. Ietswaard, R. Jamshidi, P. Jansweijer, A. Jones, P. Jones, N. Knust, G. Koekoek, X. Koroveshi, T. Kortekaas, A. N. Koushik, M. Kraan, M. van de Kraats, S. L. Kranzhoff, P. Kuijer, K. A. Kukkadapu, K. Lam, N. Letendre, P. Li, R. Limburg, F. Linde, J.-P. Locquet, P. Loosen, H. Lueck, M. Martínez, A. Masserot, F. Meylahn, M. Molenaar, C. Mow-Lowry, J. Mundet, B. Munneke, L. van Nieuwland, E. Pacaud, D. Pascucci, S. Petit, Z. Van Ranst, G. Raskin, P. M. Recaman, N. van Remortel, L. Rolland, L. de Roo, E. Roose, J. C. Rosier, D. Ryckbosch, K. Schouteden, A. Sevrin, A. Sider, A. Singha, V. Spagnuolo, A. Stahl, J. Steinlechner, S. Steinlechner, B. Swinkels, N. Szilasi, M. Tacca, H. Thienpont, A. Vecchio, H. Verkooijen, C. H. Vermeer, M. Vervaeke, G. Visser, R. Walet, P. Werneke, C. Westhofen, B. Willke, A. Xhahi and T. Zhang. "ETpathfinder: a cryogenic testbed for interferometric gravitational-wave detectors". *Classical and Quantum Gravity*, vol 39 p 215008, 2022.
DOI: 10.1088/1361-6382/ac8fdb.

[6] X. Koroveshi, **L. Busch**, E. Majorana, P. Puppo, P. Rapagnani, F. Ricci, P. Ruggi and S. Grohmann. "Cryogenic payloads for the Einstein Telescope — Baseline design with heat extraction, suspension thermal noise modelling and sensitivity analyses". *Physical Review D*, vol 349 p 27–32, 2023.
DOI: 10.1103/PhysRevD.108.123009.

[7] **L. Busch**, G. Iaquaniello, P. Rosier, M. Stamm and S. Grohmann. "Low-noise thermal shielding around the cryogenic payloads in the Einstein Telescope". *IOP Conference Series: Materials Science and Engineering*, vol 1301 p 012013, 2024.
DOI: 10.1088/1757-899X/1301/1/012013.

[8] D. M. Aliaga, P. Richardson, B. Conroy, J. Acres, **L. Busch** and H. Derking. "Conceptual Design of a Cryo-Distribution System for STEP: Addressing Cooling Challenges and Enhancing Energy Efficiency". *IOP Conference Series: Materials Science and Engineering* (submitted 2025).

Other papers

[9] **L. Busch**, R. Lietzow and H. Neumann. "Heat load budgeting of a superconducting induction heater's commercial cryocooler-based cryostat". *Proceedings of the 46th Annual Meeting of the Deutscher Kaelte und Klimatechnischer Verein 2020*, vol 1 p 198–206, 2020.
ISBN: 9781713824237.

Talks

[10] **L. Busch**. "Heat load budgeting of a superconducting induction heater's commercial cryocooler-based cryostat". In *46th Annual Meeting of the Deutscher Kaelte und Klimatechnischer Verein 2020*, Online, November 2020.
DOI: 10.5445/IR/1000127903.

[11] **L. Busch** and S. Grohmann. "He-II cooling: Possibilities for ET". In *11th Einstein Telescope Symposium (ET 2020)*, Online, December 2020.
https://indico.in2p3.fr/event/20576/contributions/89060/
DOI: 10.5445/IR/1000162591.

[12] **L. Busch**, X. Koroveshi and S. Grohmann. "Helium-based cooling concept of the ET-LF interferometer". In *Gravitational Wave Advanced Detector Workshop (GWADW 2021)*, Online, May 2021.
https://agenda.infn.it/event/26121/contributions/136476/
DOI: 10.5445/IR/1000132799.

[13] **L. Busch** and S. Grohmann. "Conceptual layout of a helium cooling system for the Einstein Telescope". In *23rd Joint Cryogenic Engineering Conference and International Cryogenic Materials Conference (CEC/ICMC 2021)*, Online, July 2021.

[14] S. Grohmann, **L. Busch** and X. Koroveshi. "Cryogenics for the Einstein Telescope (ET)". In *European Cryogenics Course (2022)*, Twente, Netherlands, August 2022.
https://indico.cern.ch/event/1171258/.

[15] **L. Busch** and S. Grohmann. "Thermal design of the He-II suspension tube for ET-LF: Status and outlook". In *ECLOUD and GWDVac Workshops (2022)*, Portoferraio, Italy, September 2022.
https://agenda.infn.it/event/28336/contributions/177982/
DOI: 10.5445/IR/1000153741.

[16] **L. Busch**, G. Iaquaniello, P. Rosier, M. Stamm and S. Grohmann. "Low-noise thermal shielding around the cryogenic payloads in the Einstein Telescope". In *25th Joint Cryogenic Engineering Conference and International Cryogenic Materials Conference (CEC/ICMC 2023)*, Honolulu, United States, July 2023.
https://indico.cern.ch/event/1168385/contributions/5355793/.

Posters

[17] **L. Busch** and S. Grohmann. "Cool-down studies of the low-frequency interferometer in the Einstein Telescope". *Gravitational Wave Advanced Detector Workshop (GWADW 2022)*, Online, May 2022.
DOI: 10.5445/IR/1000162166.

[18] **L. Busch** and S. Grohmann. "Development status of the inner thermal shielding for the ET-LF cryogenic payloads". *13th Einstein Telescope Symposium (ET 2023)*, Online, May 2023.
DOI: 10.5445/IR/1000158784.

[19] **L. Busch** and S. Grohmann. "Development status of the inner thermal shielding for the ET-LF cryogenic payloads". *Gravitational Wave Advanced Detector Workshop (GWADW 2023)*, La Biodola, Italy, May 2023.
DOI: 10.5445/IR/1000162165.

[20] **L. Busch**, X. Koroveshi and S. Grohmann. "Cryogenic developments for the Einstein Telescope using superfluid helium". *Helmholtz Program Days Matter and the Universe (2023)*, Karlsruhe, Germany, September 2023.
DOI: 10.5445/IR/1000162297.

[21] **L. Busch** and S. Grohmann. "Developments towards the cryogenic helium infrastructure for ET". *XIV ET Symposium*, Maastricht, The Netherlands, May 2024.
https://indico.ego-gw.it/event/710/contributions/6442/.

Supervised theses

[22] Bachelor′s thesis: "Process studies of the helium-based cooling system for the Einstein Telescope".
Referee: Prof. Dr.-Ing. Steffen Grohmann.

[23] Bachelor′s thesis: "Numerical Modelling of the Helium Flow in the Marionette Suspension Tube of the Low-Frequency Interferometer in the Einstein Telescope".
Referee: Prof. Dr.-Ing. Steffen Grohmann.

[24] Bachelor′s thesis: "Extension of a Numerical Model for Cryogenic Payload Cool-Down in the Einstein Telescope".
Referee: Prof. Dr.-Ing. Steffen Grohmann.

[25] Master′s thesis: "Auslegung der Druckentlastungseinrichtungen einer Helium-Verflüssigungsanlage nach EN 17527 mithilfe eines neu zu entwickelnden Software-Tools".
Referee: Prof. Dr.-Ing. Steffen Grohmann.

[26] Master′s thesis: "Helium supply unit design for the experimental investigation of cryogenic mirror suspensions in gravitational-wave detectors".
Referee: Prof. Dr.-Ing. Steffen Grohmann.